Universidad Miguel Hernández de Elche
Instituto de Bioingeniería

Tesis Doctoral
Programa de Doctorado en Bioingeniería

Síntesis y caracterización de estructuras cerámicas porosas 3D multicapa obtenidas mediante el proceso sol-gel para aplicación en ingeniería de tejido óseo

Presentado por:
Nayarit Alexandra Mata Alayón

Directora:
Dra. Piedad N. De Aza Moya
Codirector:
Dr. Ángel Murciano Cases

Elche, 2021

INDICIOS DE CALIDAD

La Tesis Doctoral titulada "Síntesis y caracterización de estructuras cerámicas porosas 3D multicapa obtenidas mediante el proceso sol-gel para aplicación en ingeniería de tejido óseo", realizada por Dña. NAYARIT ALEXANDRA MATA ALAYÓN, con NIE: Y6573373X, bajo la dirección de los profesores Piedad N. De Aza Moya y Ángel Murciano Cases, se presenta bajo la modalidad de tesis por compendio de las siguientes publicaciones:

P. Ros-Tárraga, N.A. Mata, Á. Murciano, P. Velasquez, P.N. De Aza
Multilayer ceramic materials: A method to link bioactivity and durability
Ceramics International. 45, 23611-23618 (2019)
DOI: 10.1016/j.ceramint.2019.08.072
Factor de Impacto (2019): 3.830 (Q1)
Puesto que ocupa/N°de revistas en su área (2019): 2/28 (Materials Science, Ceramics)

N.A. Mata, P. Ros-Tárraga, P. Velasquez, A. Murciano, P.N. De Aza
Synthesis and characterization of 3D multilayer porous Si-Ca-P scaffolds doped with Sr ions to modulate in vitro bioactivity
Ceramics International. 46, 968-977 (2020)
DOI: 10.1016/j.ceramint.2019.09.058
Factor de Impacto (2020): 4.527 (Q1)
Puesto que ocupa/N°de revistas en su área (2020): 3/29 (Materials Science, Ceramics)

N.A. Mata, P. Ros-Tárraga, P. Velasquez, A. Murciano, P.N. De Aza
New iron-doped multilayer ceramic scaffold with noncontinuous bioactive behavior
Ceramics International. 46, 16388-16396 (2020)
DOI: 10.1016/j.ceramint.2020.03.198

d

Factor de Impacto (2020): 4.527 (Q1)
Puesto que ocupa/N°de revistas en su área (2020): 3/29 (Materials Science, Ceramics)

N.A. Mata, P. Ros-Tárraga, P. Velasquez, A. Murciano, P.N. De Aza
3D multiphasic porous scaffolds of calcium phosphates doping with silicon and magnesium
Boletín de la Sociedad Española de Cerámica y Vidrio. (2021)
DOI: 10.1016/j.bsecv.2021.03.004
Factor de Impacto (2020): 2.383 (Q1)
Puesto que ocupa/N°de revistas en su área (2020): 7/29 (Materials Science, Ceramics)

N.A. Mata, P. Velasquez, A. Murciano, P.N. De Aza
Multilayer Mg-pyrophosphate glass ceramic with discontinuous bioactivity. Physicochemical characterization
Ceramics International. 47, 14612-14620 (2021)
DOI: 10.1016/j.ceramint.2021.02.044
Factor de Impacto (2020): 4.527 (Q1)
Puesto que ocupa/N°de revistas en su área (2020): 3/29 (Materials Science, Ceramics)

N.A. Mata, M. Arango-Ospina, P. Velasquez, A. Murciano, P.N. De Aza, A.R. Boccaccini
Effect of Sr, Mg and Fe substitution on the physico-chemical and biological properties of Si-Ca-P multilayer scaffolds
Boletín de la Sociedad Española de Cerámica y Vidrio. (2021)
DOI: 10.1016/j.bsecv.2021.11.005
Factor de Impacto (2020): 2.383 (Q1)
Puesto que ocupa/N°de revistas en su área (2020): 7/29 (Materials Science, Ceramics)

La Dra. Dña Piedad N. De Aza Moya, directora y el Dr. D. Ángel Murciano Cases, codirector de la Tesis Doctoral titulada "Síntesis y caracterización de estructuras cerámicas porosas 3D multicapa obtenidas mediante el proceso sol-gel para aplicación en ingeniería de tejido óseo",

INFORMAN:

Que Dña. Nayarit Alexandra Mata Alayón, con NIE: Y6573373X, ha realizado bajo nuestra supervisión el trabajo titulado "Síntesis y caracterización de estructuras cerámicas porosas 3D multicapa obtenidas mediante el proceso sol-gel para aplicación en ingeniería de tejido óseo", conforme a los términos y condiciones definidos en su Plan de Investigación y de acuerdo al Código de Buenas Prácticas de la Universidad Miguel Hernández de Elche, cumpliendo los objetivos previstos de forma satisfactoria para su defensa pública como Tesis Doctoral.

Lo que firmamos para los efectos oportunos, en Elche a 22 de diciembre de 2021.

Dra. Dña Piedad N. De Aza Moya
Directora de la Tesis

Dr. D. Ángel Murciano Cases
Codirector de la Tesis

La Dra. Dña Piedad N. De Aza Moya, Coordinadora del Programa de Doctorado en Bioingeniería de la Universidad Miguel Hernández de Elche por Resolución Rectoral 3120/19, de 09 de diciembre de 2019.

INFORMA:

Que Dña. Nayarit Alexandra Mata Alayón, con NIE: Y6573373X, ha realizado bajo la supervisión de nuestro Programa de Doctorado el trabajo titulado "Síntesis y caracterización de estructuras cerámicas porosas 3D multicapa obtenidas mediante el proceso sol-gel para aplicación en ingeniería de tejido óseo", conforme a los términos y condiciones definidos en su Plan de Investigación y de acuerdo al Código de Buenas Prácticas de la Universidad Miguel Hernández de Elche, cumpliendo los objetivos previstos de forma satisfactoria para su defensa pública como Tesis Doctoral.

Lo que firmo para los efectos oportunos, en Elche a 22 de diciembre de 2021.

Dra. Dña Piedad N. De Aza Moya

Coordinadora del Programa de Doctorado en Bioingeniería

Índice general

Nomenclatura

Acrónimos

ADN   Ácido desoxirribonucleico.

ALP   Fosfatasa Alcalina.

BET   Método Brunauer-Emmet-Teller.

BJH   Método Barrett-Joyner-Halenda.

COD   Base de datos "*Crystallography Open Database*".

CPP   Pirofosfato de Calcio ($Ca_2P_2O_7$).

EAK   Péptido compuesto por ácido glutámico (E), alanina (A) y lisina (K).

EDX   Espectroscopía de Rayos-X de Energía Dispersiva.

ELK   Péptido compuesto por ácido glutámico (E), leucina (L) y lisina (K).

FTIR   Espectroscopía Infrarroja con Transformadas de Fourier.

HA   Hidroxiapatito ($Ca_{10}(PO_4)_6(OH)_2$).

ICP-OES Espectroscopía de Emisión por Plasma de Acoplamiento Inductivo.

ICSD   Base de datos "*Inorganic Crystal Structure Database*".

JCPDS Base de datos "*Joint Committee on Powder Diffraction Standards*".

LDH   Lactato Deshidrogenasa.

MG-63 Células de osteosarcoma línea MG-63.

RAD   Péptido compuesto por arginina (R), alanina (A) y ácido aspártico.

SBF   Suero Fisiológico Artificial.

SEM   Microscopía Electrónica de Barrido.

TCP   Fosfato Tricálcico ($Ca_3(PO_4)_2$).

TEOS   Tetraetil Ortosilicato ($Si(OC_2H_5)$).

TEP   Trietil Fosfato ($(C_2H_5)_3PO_4$).

TGF-$\beta3$ Factor de crecimiento transformante beta 3.

WST-8 Sal de tetrazolio soluble en agua.

XRD   Difracción de Rayos-X.

Índice de figuras

Índice de tablas

Resumen

El uso de injertos óseos se ha convertido en una práctica habitual en la regeneración de hueso enfermo, o hueso con problemas derivados de traumatismos. Estos injertos se han desarrollado en base a diferentes tipos de materiales, siendo los cerámicos los más destacados por su similitud con el componente mineral del hueso. Sin embargo, debido a la complejidad estructural y funcional del hueso, estructuras formadas por una única composición química, difícilmente pueden desempeñar la función de injerto óseo. Ante esta necesidad, en la presente Tesis Doctoral se propone el desarrollo de estructuras o andamios cerámicos, porosos, tridimensionales, multicapa, constituidos por un núcleo cuya composición química aporte resistencia mecánica y recubrimientos externos con composiciones que aporten bioactividad y biocompatibilidad.

El núcleo del andamio fue desarrollado con la siguiente composición química SiO_2-68CaO-25P_2O_5-6LiO$_2$ (% molar) y los recubrimientos externos con la siguiente composición química 29SiO_2-68CaO-3P_2O_5 (% molar). Adicionalmente, los recubrimientos externos fueron dopados con iones de zinc, estroncio, hierro y magnesio en diferentes concentraciones y configuraciones, para estimular la bioactividad y respuesta celular. Las técnicas empleadas para la obtención de los andamios multicapa fueron el proceso sol-gel y la técnica de réplica de esponja polimérica.

Gracias a la versatilidad del proceso sol-gel, se obtuvieron tres núcleos para los andamios, partiendo de la misma composición química y variando el tiempo de calentamiento de la disolución. El primer núcleo, constituido principalmente por una mezcla de las fases CPP y TCP, se obtuvo mediante el calentamiento, durante 30 minutos, de la disolución descrita anteriormente para el núcleo. Mientras que esta disolución, calentada durante 15 minutos y 1 hora, dió lugar al segundo y tercer núcleo, formados principalmente por las fases individuales de CPP y TCP, respectivamente. La caracterización física de estos núcleos, determinó que la resistencia a la compresión y macroporosidad varía entre 0.38-2.87 MPa y 42-77.6%, dependiendo de la proporción de cada fase cristalina y la cantidad de inmersiones de la esponja de poliuretano en las distintas disoluciones.

Posteriormente, con el primer núcleo, se desarrollaron andamios multicapa, recubiertos y dopados con zinc, estroncio e hierro. Los andamios dopados con 1% zinc, presentaron un aumento de la bioactividad *in vitro*, en comparación con el núcleo y el recubrimiento sin dopante. No obstante, dicha bioactividad disminuyó al aumentar el dopaje al 30% zinc. En base a estos resultados, se estudiaron diferentes concentraciones de dopaje, utilizando en este caso iones de estroncio. Con estos nuevos andamios, se determinó que el dopaje entre

1% y 10% aumenta la bioactividad del andamio. Por el contrario, los dopajes mayores al 10% provocan la pérdida de la bioactividad. Por último, se observó que en el caso particular de los andamios dopados con hierro, presentaban un comportamiento variable en el tiempo, en relación a la bioactividad, con dopaje del 1%, mientras que para dopaje del 3% presentaban un comportamiento continuo.

Seguidamente, se desarrollaron andamios multicapa dopados con 1%, 3% y 10 % de magnesio, empleando los núcleos constituidos individualmente por las fases de CPP y TCP. Con estos andamios, se realizó un estudio comparativo de la influencia de las fases cristalinas del núcleo en el comportamiento general de los andamios. Los resultados demostraron que los andamios elaborados con el núcleo de CPP presentaron un comportamiento bioactivo variable en el tiempo, con apatitos que precipitan y se disuelven continuamente. Mientras que los andamios elaborados con el núcleo de TCP presentaron bioactividad constante desde el día 3 de inmersión en SBF, independientemente del porcentaje de dopaje con magnesio.

Por último, una vez conocido el comportamiento individual de los iones dopantes, se desarrollaron nuevos andamios multicapa con dopaje simultáneo de hierro, estroncio y magnesio. Además se estudió la influencia de la disposición de los iones en las propiedades de los andamios. Para ello se desarrollaron dos andamios, el primero llamado 3J, con el 3% de los iones en el mismo recubrimiento externo, y el segundo llamado 3S, con el 3% de los iones en recubrimientos externos separados. Con estos andamios se realizaron ensayos de biocompatibilidad en presencia de células MG-63, mostrando un aumento de la viabilidad celular mayor al 100%, en comparación con el núcleo de CPP. Así como también una mejor adherencia y proliferación de las células en la superficie. No obstante, a pesar de que los andamios 3J y 3S no presentaron diferencias en cuanto a la respuesta celular, la bioactividad *in vitro* fue distinta, el andamio 3J fue bioactivo a los 21 días, mientras que el andamio 3S fue bioactivo a los 3 días.

En conclusión, en esta investigación debido al diseño multicapa y la introducción de iones que juegan un papel fundamental en la biología del hueso, se logró obtener andamios que unifican en una única estructura diferentes propiedades. Algunas de estas propiedades son la porosidad y resistencia a la compresión comparables a las del hueso trabecular, pero además bioactividad y biocompatibilidad. Todas estas características convierten a los andamios multicapa en futuras alternativas para aplicaciones en ingeniería de tejido óseo.

Abstract

The use of bone grafts has become a common practice in the regeneration of diseased bone, or bone with problems resulting from trauma. These grafts have been developed based on different types of materials, with ceramics being the most outstanding due to their similarity with the mineral component of bone. However, due to the structural and functional complexity of bone, structures consisting of a single chemical composition can hardly perform the function of a bone graft. In view of this need, this doctoral thesis proposes the development of porous, three-dimensional, multilayer ceramic structures or scaffolds, consisting of a core whose chemical composition provides mechanical strength and external coatings with compositions that provide bioactivity and biocompatibility.

The core of the scaffold was developed with the following chemical composition SiO_2-68CaO-$25P_2O_5$-$6LiO_2$ (% molar) and the external coatings with the following chemical composition $29SiO_2$-68CaO-$3P_2O_5$ (% molar). Additionally, the external coatings were doped with zinc, strontium, iron and magnesium ions in different concentrations and configurations to stimulate bioactivity and cellular response. The techniques used to obtain the multilayer scaffolds were the sol-gel process and the polymer sponge replication technique.

Thanks to the versatility of the sol-gel process, three cores for the scaffolds were obtained, starting from the same chemical composition and varying the heating time of the solution. The first core, consisting mainly of a mixture of tha CPP and TCP phases, was obtained by heating the solution described above for 30 minutes. While this solution, heated for 15 minutes and 1 hour, resulted in the second and third cores, formed mainly by the individual phases of CPP and TCP, respectively. The physical characterization of these cores determined that the compressive strength and macroporosity vary between 0.38-2.87 MPa and 42-77.6 %, depending on the proportion of each crystalline phase and the amount of immersions of the polyurethane sponge in the different solutions.

Afterwards, with the first core, multilayer scaffolds coated and doped with zinc, strontium and iron were developed. The scaffolds doped with 1% zinc showed an increase *in vitro* bioactivity compared to the core and undoped coating. However, this bioactivity decreased with increasing doping to 30% zinc. For this reason, different doping concentrations were subsequently studied, using in this case strontium ions. From these studies it was determined that doping between 1% and 10% increases the bioactivity of the scaffold. On the contrary, doping higher than 10% causes a loss of bioactivity. Finally, it

was observed that in the particular case of iron-doped scaffolds, they showed a variable behavior over time, in relation to bioactivity, with 1% doping, while for 3% doping they showed a continuous behavior.

Subsequently, multilayer scaffolds doped with 1%, 3% and 10% magnesium were developed, using the cores consisting of individual CPP and TCP phases. A comparative study of the influence of the crystalline phases of the core on the overall behavior of the scaffolds was carried out. The results showed that the scaffolds prepared with the CPP core exhibited time-varying bioactive with apatite´s precipitating and dissolving continuously. While the scaffolds elaborated with the TCP core presented constant bioactivity from day 3 of immersion in SBF, regardless of the percentage of doping with magnesium.

Finally, once the individual behavior of the dopant ions was known, new multilayer scaffolds with simultaneous doping of iron, strontium and magnesium were developed. In addition, the influence of ion disposition on the properties of the scaffolds was studied. For this purpose, two scaffolds were developed, the first called 3J, with 3% of the ions in the same external coating, and the second called 3S, with 3% of the ions in separate external coatings. Biocompatibility assays were performed with these scaffolds in the presence of MG-63 cells, showing an increase in cell viability greater than 100% compared to the CPP core. As well as improved cell adhesion and proliferation on the surface. However, although the 3J and 3S scaffolds showed no difference in cellular response, the *in vitro* bioactivity was different, the 3J scaffold was bioactive at 21 days, while the 3S scaffold was bioactive at 3 days.

In general, in this research, due to the multilayer design and the introduction of ions that play a fundamental role in the biology of bone, it was possible to obtain scaffolds that unify in a single structure different properties. Some of these properties are porosity and resistance to compression comparable to trabecular bone, but also bioactivity and biocompatibility. All these properties turn multilayer scaffolds into future alternatives for bone tissue engineering applications.

Capítulo 1

Introducción

En este capítulo se presentará una breve introducción sobre el contexto general que motivó la realización de la presente Tesis Doctoral, dirigida hacia el desarrollo de estructuras cerámicas para aplicaciones en ingeniería de tejido óseo. Posteriormente, se definirán los fundamentos básicos relacionados con la ingeniería de tejidos y los biomateriales, específicamente las biocerámicas, sus requerimientos y principios asociados a los métodos de síntesis empleados.

1.1   Contexto general

El sistema musculoesquelético forma parte del conjunto de sistemas que definen el funcionamiento del cuerpo humano, estando constituido por huesos, músculos, articulaciones y tejidos blandos [1, 2]. Este sistema es de vital importancia ya que proporciona la estructura que da forma y estabilidad al cuerpo, además realiza las funciones de soporte mecánico, permite el movimiento, protege a los órganos vitales e interviene en importantes procesos metabólicos [3-6].

Todas estas funciones, sin embargo, pueden verse afectadas en algún momento de nuestra vida, ya que este sistema, al igual que los otros sistemas del cuerpo, está expuesto a sufrir daños o enfermedades. Hoy en día se conocen alrededor de 150 trastornos o enfermedades asociados al sistema musculoesquelético, las cuales se pueden encontrar en cualquier parte del cuerpo [7-9]. Algunas de ellas son artritis, afecciones de la columna vertebral, osteoporosis, cáncer de hueso, y traumatismos, entre otras [7, 10, 11].

En la actualidad, estos diagnósticos son tan frecuentes que un estudio de 2019 sobre el impacto de todas las enfermedades, advierte que aproximadamente 1714 millones de personas en todo el mundo sufren alguno de estos trastornos, convirtiéndose en una de las principales causas de discapacidad en el mundo [12]. En este sentido, el aumento ha sido tan significativo, que en los países en desarrollo se produjo un incremento del 60% de estas enfermedades entre los años 1990 y 2010 [7].

Parte importante de este incremento, se atribuye al envejecimiento de la población mundial, debido al aumento de la esperanza de vida de las últimas décadas. Siguiendo esta tendencia, se considera que los trastornos musculoesqueléticos van a empeorar en los próximos años, ya que se estima que para el año 2050 el número de personas mayores de 60 años representará el 22% de la población mundial [9]. Esto constituye un aumento del 26% respecto a la población mayor de 60 años en el año 2019 [9].

A pesar de que la mayoría de las disfunciones se asocian al envejecimiento, los niños, adolescentes y adultos no están exentos de padecerlas. Algunos de los trastornos pueden ser congénitos, pero muchos otros, como las fracturas, pueden ser ocasionadas por traumatismos de diferentes tipos. Existen traumatismos provocados por lesiones deportivas, pero en su mayoría, por accidentes de tráfico. El incremento en el uso de vehículos a motor, no solo es un riesgo para la salud debido a que reduce la actividad física, sino que también aumenta la cantidad de accidentes, ocasionando traumatismos musculoesqueléticos [7, 11].

Todas estas alteraciones del sistema musculoesquelético, independientemente de la edad del paciente, suponen una serie de costes directos e indirectos [2]. Entre los costes directos se encuentran los asociados a hospitalización, cirugía, implantes y medicamentos, mientras que los costes indirectos se asocian a pérdida de trabajo, reducción de la movilidad y terapia física [3]. También existen costes intangibles que están relacionados con el dolor, el deterioro y la depresión que, en el futuro, pueden derivar en otros trastornos [3].

Un ejemplo de estas afecciones relacionadas con el hueso es la osteoporosis. Esta enfermedad se caracteriza por una disminución de la densidad ósea, que tiende a aumentar la fragilidad de los huesos y, por tanto, ocasionar su fractura [13]. En el mundo, la osteoporosis causa más de 9 millones de fracturas al año, es decir, una fractura cada 3 segundos [14]. En algunos países de la Unión Europea, dentro de los cuales se encuentran Francia, Alemania, Italia, España y Suecia, además de Reino Unido, en el año 2017, se produjeron 2.7 millones de fracturas, con un coste anual de 37.5 billones de euros [14]. Además, se calculó que los años de vida ajustados por discapacidad (número de años perdidos

debido a la enfermedad) es de 21 años, por cada 1000 individuos mayores de 50 años, siendo mayor que lo estimado por derrame cerebral y enfermedades pulmonares crónicas [14]. En este sentido, se espera que en la Unión Europea para el año 2030 las fracturas aumenten de 2.7 a 3.3 millones [14].

De todas las fracturas causadas por osteoporosis, la fractura de cadera es la más fácil de contabilizar, además representa la de mayor impacto económico [15]. Se estima que en el mundo ocurren 1.6 millones de fracturas de cadera cada año, siendo 610.000 en la Unión Europea y 45.000 en España [16].

Un análisis de los costes directos de la fractura de cadera en pacientes mayores de 65 años (los 12 meses siguientes a la fractura), realizados por regiones autónomas en España, muestra que tan solo en la Comunidad de Madrid se gasta aproximadamente 12.300 €, mientras que en la Comunidad Valenciana 8.000 € [17].

Todos estos costes sociales y económicos, generan gran inquietud, ya que la tendencia es que ésta y otras problemáticas aumenten en los próximos años, incluso, después de la pandemia causada por la COVID-19, que ha ocasionado la muerte de aproximadamente 2.5 millones de personas, en su mayoría de avanzada edad. Esta tendencia se puede justificar en base a dos motivos, en primer lugar, las lesiones musculoesqueléticas, durante la pandemia, pasaron a ser menos prioritarias para los sistemas de control y prevención [18]. Únicamente los pacientes con fracturas graves fueron operados, pero inmediatamente dados de alta, sin un adecuado tratamiento postoperatorio, aún cuando las personas con fracturas por fragilidad tienen alta probabilidad de sufrir una recaída [18]. En segundo lugar, la inmovilización hospitalaria debido a las consecuencias ocasionadas por la COVID-19, y los tratamientos con glucocorticoides, durante mucho tiempo, aumentan el riesgo de sufrir fragilidad ósea y fracturas [18].

El escenario actual solo suma razones para pensar que las fracturas serán mucho más frecuentes, además, si los sistemas de prevención no funcionan correctamente, solo queda plantear soluciones a las fracturas que se van produciendo.

En este sentido, el hueso tiene la capacidad de regenerarse por sí mismo [19], salvo en el caso de grandes fracturas o aquellas que afectan a personas mayores, donde muy difícilmente se auto-regenera. Cuando esto sucede, la única forma de reparar el daño es acudir a la utilización de implantes o injertos.

Los injertos naturales aunque son los candidatos idóneos, pueden ocasionar complicaciones como rechazo o transmisión de enfermedades (si provienen de otro paciente) o morbilidad (si proviene del mismo paciente) [20]. Por estas

razones, los injertos sintéticos se utilizan desde la antiguedad. Los primeros materiales no biológicos utilizados en el cuerpo fueron piezas dentales de nácar en la civilización maya, mientras que en Europa se utilizaban piezas de hierro [21]. A principio del siglo XX se utilizó el acero al vanadio para reparar fracturas y, posteriormente, el acero inoxidable y aceros aleados con cromo y cobalto para la fijación de fracturas [21].

Estos esfuerzos demuestran la búsqueda insistente, por parte de la humanidad, de soluciones a los problemas que afectan el funcionamiento normal del cuerpo. Este sentimiento no se aleja de la realidad actual, ya que gracias al avance de la sociedad y las nuevas tecnologías, se ha abierto la posibilidad de emplear mejores materiales e incluso crear nuevas disciplinas como la ingeniería de tejidos. En este sentido, el desarrollo de nuevas disciplinas ha permitido un mejor entendimiento de los procesos biológicos. Este conocimiento ha posibilitado que dentro de especialidades como la ciencia de materiales, se desarrollen implantes inspirados en los procesos naturales de regeneración ósea. Este concepto denominado biomimetismo ha impulsado el desarrollo de la presente Tesis Doctoral.

A continuación se realizará una breve introducción sobre la ingeniería de tejidos y cómo esta disciplina ha dado lugar al desarrollo de sustitutos biológicos, en concreto de injertos óseos.

1.2   Ingeniería de tejidos

La ingeniería de tejidos es una disciplina relativamente nueva que nació en el año 1987, mostrando un gran crecimiento desde la década de los noventa hasta la actualidad [22]. Esta disciplina combina dos términos muy importantes, la ingeniería y el tejido. La ingeniería hace referencia al conjunto de conocimientos y prácticas científicas destinadas al desarrollo, construcción y diseño de nuevas tecnologías [23]. Por su parte, el tejido se refiere al conjunto de células que cumplen una determinada función [23]. La unión de estas dos palabras describe una disciplina destinada a solucionar y mitigar los grandes problemas derivados del deterioro o daño en los tejidos u órganos del cuerpo. En términos generales se puede definir la ingeniería de tejido como un "*campo multidisciplinar que aplica los principios de la ingeniería y las ciencias de la vida para el desarrollo de sustitutos biológicos que restauren, mantengan o mejoren las funciones de los tejidos*" [23].

Las aplicaciones son diversas, abarcando desde tejidos como cartílago, hueso, piel, injertos vasculares y cardíacos, hasta órganos como hígado, pulmón, riñón y corazón [24]. A pesar de que el uso de sustitutos para mejorar defectos

en el cuerpo se utilizan desde hace muchos años, esta nueva disciplina propone la implementación de los avances en la ingeniería para obtener materiales más eficientes.

La ingeniería de tejido se basa en tres grandes componentes o pilares como son los andamios, células y factores de crecimiento [22, 25, 26], cuyas funciones serán detalladas a continuación:

- **Andamios**

Los andamios son las estructuras artificiales que sustituyen el tejido afectado y que sirven como molde tridimensional para las células [23]. Este andamio debe permitir la adhesión, proliferación y diferenciación de las células mientras cumple su función dentro del organismo [22, 26]. La matriz puede estar de forma permanente en el cuerpo o de forma provisional mientras se regenera el tejido. Los andamios también pueden ser vehículos para transportar dentro del organismo ciertos nutrientes y fármacos [22].

- **Células**

Las células son las responsables de formar los tejidos y órganos. Su presencia e interacción con el andamio determina el éxito de la recuperación del tejido o adaptación en el cuerpo. Existen diferentes tipos de células, dependiendo de su origen. Estas puedan provenir del mismo paciente (autólogas) o de otros pacientes (alogénicas o xenogénicas) [23, 25] y entre los distintos tipos se encuentran las células madres, células maduras diferenciadas o mixtas [22].

- **Factores de crecimiento**

Los factores biológicos o de crecimiento son biomoléculas que se encargan de regular las respuestas celulares, mediando en los mecanismos de señalización de las células [22]. Estas biomoléculas pueden acelerar o mejorar el proceso de sanación [25]. Alguno de estos factores pueden ser hormonas, citoquinas, ácidos nucleicos, entre otros [22].

1.2.1 Tejido óseo

Los huesos son el tejido más importante del sistema esquelético, pudiendo presentarse en diferentes formas como planos, largos, cortos e irregulares dependiendo de la zona del cuerpo [4]. Entre sus funciones se encuentran dar la

estructura al cuerpo, almacenar minerales, producir células sanguíneas, soportar los músculos, mantener la homeostasis tanto del calcio como del hierro y proteger órganos como el cerebro, la médula espinal, los pulmones y el corazón [4, 22, 27].

Anatómicamente, el hueso presenta una estructura jerárquica que va desde el nivel macro hasta el sub-nanométrico como se muestra en la Figura 1.1 [28]. A nivel macro se identifican dos estructuras, conocidas como hueso compacto o cortical y hueso trabecular o esponjoso, los cuales representan el 80% y el 20% del esqueleto, respectivamente [4, 19, 29]. El hueso compacto corresponde a la corteza externa del hueso y se encuentra mineralizado al 80-90%. Por su parte, el hueso trabecular o esponjoso se encuentra en el interior del hueso y se distingue por su estructura tipo red con un 80% de porosidad [5].
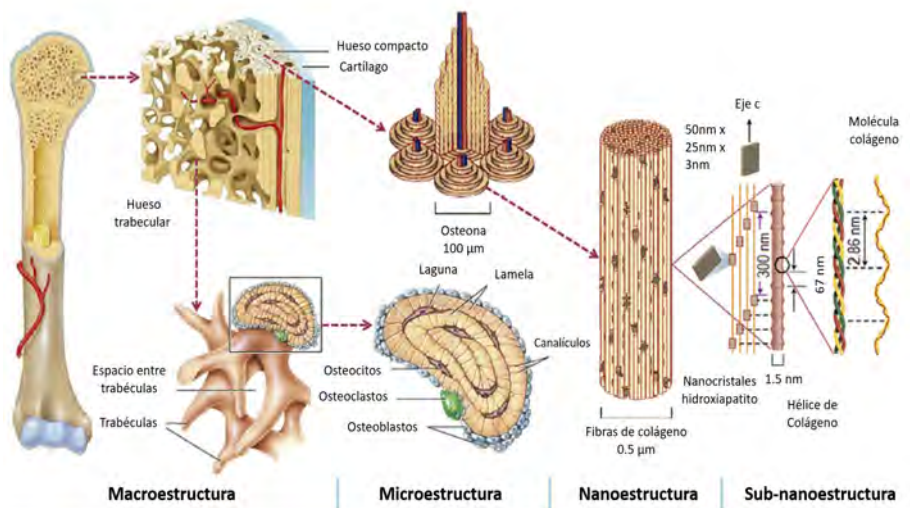
Figura 1.1: Estructura jerárquica del hueso [28].

A nivel microestructural se distinguen estructuras concéntricas llamadas osteonas, de 100 μm de diámetro, por las cuales pasan vasos sanguíneos y nervios [28, 30]. También se encuentran los tres tipos de células responsables en el metabolismo del hueso: osteoclastos, osteoblastos y osteocitos. Los osteoclastos son los responsables de la reabsorción del hueso viejo, mientras los osteoblastos son responsables de la formacón de hueso nuevo, dando lugar a un proceso de regeneración constante [5, 19, 30, 31]. Por su parte, los osteocitos son depósitos de células osteoblásticas, que se forman después de la mineralización y actúan como reguladores de la actividad de los osteoclastos y osteoblastos [5, 29-31].

Por último, a nivel nano y sub-nanométrico se observan con mayor detalle lamelas o fibras, las cuales están integradas por colágeno y cristales de HA [27-30]. El colágeno, principalmente tipo I, presenta una triple hélice de 1.5 μm de diámetro y 300 μm de largo. Mientras que los cristales de HA, preferencialmente orientados en el eje c, presentan una forma rectangular con dimensiones 50 nm x 25 nm x 3 nm [28]. Aunque en general el hueso está constituido en un 60% por HA y 20% por colágeno, existe en menor proporción otros elementos como se muestra en la Tabla 1.1 [27].

Tabla 1.1: Composición química del hueso (% en peso) [27].

Fase inorgánica	Fase orgánica
Hidroxiapatito ≈ 60	Colágeno ≈ 20
Agua ≈ 9	Proteínas ≈ 3
Carbonatos ≈ 4	Trazas: polisacáridos, lípidos, citoquinas.
Citratos ≈ 0.9	Células: osteoblastos, osteoclastos y osteocitos.
$Na^+ \approx 0.7$	
$Mg^{2+} \approx 0.5$	
$Cl^- \approx 0.13$	
Otros: K^+, F^-, Zn^{2+}, Fe^{2+}, Cu^{2+}, Sr^{2+}, Pb^{2+}	

La composición química del hueso, indica que los cristales de HA son los responsables en gran medida de la densidad ósea del hueso y, gracias a los procesos celulares, son capaces de regenerarse constantemente. El hueso compacto tiene una regeneración anual de 2.5%, mientras que el hueso trabecular del 25%. Esto permite que el esqueleto se renueve completamente cada 10 años [19].

La variación en la densidad ósea, acompañada de los procesos celulares, son mecanismos que se inician en los primeros años de vida, continuando en las diferentes etapas de crecimiento. En la Figura 1.2 [13], se observa que durante las etapas de la niñez y pubertad la densidad aumenta hasta alcanzar un punto máximo en los primeros años de la edad adulta. Este punto máximo de densidad ósea, puede verse influenciado por diversos factores como la genética, el sexo, la actividad física, la dieta, el peso del cuerpo y las hormonas [13]. Posteriormente, durante la mayor parte de la etapa adulta, la densidad del hueso se mantiene, hasta alcanzar la vejez, donde la densidad ósea comienza a disminuir debido a la degeneración de los procesos biológicos. Indipendientemente de los factores que afectan la densidad ósea, un hueso con baja densidad

es susceptible a las fracturas, y si estas superan un tamaño crítico, el hueso no es capaz de auto-regenerarse. Por ejemplo, el tamaño crítico del hueso largo es 4-7 cm [32], siendo necesario en fracturas de mayor tamaño recurrir a la utilización de injertos óseos.
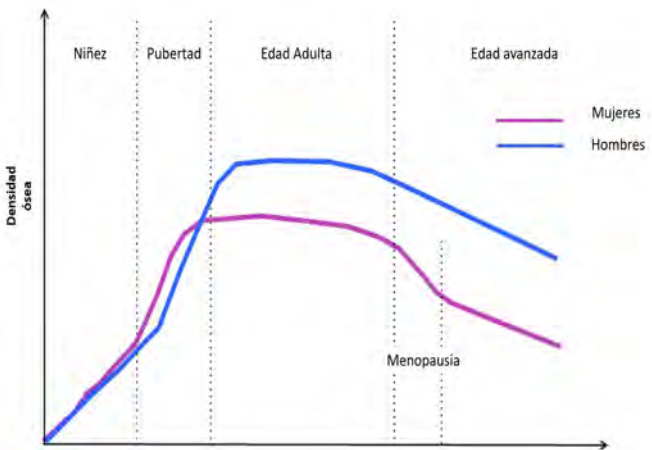
Figura 1.2: Variación de la densidad ósea en las diferentes etapas de la vida [13].

1.2.2 Injertos óseos

Hoy en día existen diferentes tipos de injertos para el hueso, y se pueden clasificar según su origen en: naturales y sintéticos [26, 33, 34]. Los injertos naturales, a su vez, dependiendo de su procedencia se pueden clasificar en: autoinjertos, aloinjertos o xenoinjertos [5, 20]. Por su parte, los injertos sintéticos pueden ser clasificados según el material que lo constituye en: materiales metálicos, cerámicos, poliméricos o compuestos [29, 35].

- Injertos naturales

El injerto ideal hasta el momento considerado como el "estándar de oro" por su capacidad de sanación es el autoinjerto [5, 20, 32, 36, 37]. Este tipo de injerto es el que proviene del tejido del mismo paciente y, por lo general, se extrae de la cresta ilíaca, costilla o cráneo [5, 36, 38]. Con este tipo de injerto se garantiza una correcta aceptación en el organismo con un 80-90% de éxito y se evita la transmisión de enfermedades [32]. Sin embargo, los inconvenientes son la limitación de disponibilidad del tejido y la necesidad de

realizar dos intervenciones quirúrgicas [5, 32, 36, 37, 39], ya que el paciente debe someterse a un procedimiento para extraer el tejido y otro para colocarlo en la zona afectada, aumentando así la posibilidad de infecciones y morbilidad [5, 38]. Adicionalmente, en muchos casos el paciente padece alguna enfermedad como osteoporosis o cáncer de hueso, o simplemente está sometido a algún tratamiento como quimioterapia, donde resulta imposible la extracción del tejido [5, 38]. Lo mismo ocurre si el paciente es pediátrico o si la zona afectada es de gran tamaño [5].

Otra alternativa son los aloinjertos, los cuales provienen del tejido de otro paciente de la misma especie, bien sea donación de pacientes vivos o cadáveres [5, 36, 37]. Estos ofrecen la facilidad de ser encontrados en diferentes formas y evitar los problemas asociados a la disponibilidad [5]. Antes de su utilización los injertos deben pasar por procesos de esterilización, descelurarización y desmineralización de forma controlada para evitar que pierdan colágeno, proteínas y algunos factores de crecimiento [5]. Para ello se utilizan técnicas como congelación, irradiación y criocongelación [5]. Todas estas técnicas disminuyen la posibilidad de transmisión de enfermedades, pero no en su totalidad, además, suelen disminuir las propiedades mecánicas originales del hueso [5, 32]. También existe un alto riesgo de rechazo que hay que prevenir mediante el suministro de inmunosupresores [5]. No solo las propiedades mecánicas se ven afectadas, sino que también en comparación con los autoinjerto, estos son menos osteoconductivo, osteoinductivo y no osteogénico [5, 36].

Por último, existe una tercera opción para injertos naturales, los xenoinjertos. Estas piezas provienen de una fuente animal, por lo general bovinos, porcinos y equinos [40]. Estos también son tratados antes de su utilización, pero no están exentos a ser portadores de virus infecciosos o de sufrir una respuesta inmunológica [37, 39]. Tampoco presentan propiedades osteoinductivas u osteogénicas y, por lo general, se reabsorben más rápido que los autoinjertos [37, 40].

- Injertos sintéticos

Los injertos sintéticos se clasifican según el tipo de material del cual están constituidos como metales, cerámicas, polímeros y compuestos [35]. Estos grupos de materiales se diferencian entre sí según el tipo de enlace entre los átomos y la estructura cristalina que forman, los cuales definen sus propiedades finales y por tanto sus aplicaciones.

Los injertos sintéticos son una excelente opción para minimizar los riesgos y limitaciones asociados con los injertos naturales [26, 34]. Estos injertos han ido

evolucionando, pasando de utilizar los materiales disponibles en los inicios de la humanidad [21], a aplicar las nuevas tecnologías, para desarrollar materiales adaptados según las necesidades.

1.3   Biomateriales

A lo largo de los años han surgido diferentes definiciones para los materiales empleados en aplicaciones médicas, pero de forma general se puede decir que "*un biomaterial es cualquier material, natural o fabricado por el hombre, que comprende la totalidad o parte de una estructura viva o un dispositivo biomédico que realiza, mejora o sustituye una función natural*" [21].

El uso de los biomateriales involucra un campo muy amplio. Algunas de las aplicaciones son prótesis de hueso, dentales, tendones, piel artificial, válvulas para el corazón, catéter de diálisis, lentes intraoculares, entre otros [21, 41, 42]. Dependiendo de la aplicación, los biomateriales son diseñados en diferentes formas y conformados por distintos tipos de materiales.

1.3.1   Tipos de materiales

Existen cuatro grandes grupos de materiales, clasificados en metales, cerámicas, polímeros y materiales compuestos [35]. En primer lugar, los materiales metálicos se caracterizan por su rigidez, resistencia y ductilidad [41]. Estas propiedades, permiten su maleabilidad durante su conformación y porteriormente, en servicio, tienen un comportamiento excelente soportando cargas [21, 39, 41]. Los metales más utilizados en biomedicina son los aceros inoxidables, aleaciones cobalto-cromo, titanio y sus aleaciones, metales pesados como zirconia-niobio y tungsteno [21, 35]. Estos materiales han sido empleados como tornillos para fijaciones de fracturas, placas craneales, prótesis de hueso, y en partes de órganos artificiales como marcapasos, catéteres y válvulas [21, 39, 41]. Sin embargo, una de las desventajas de los metales es que pueden ocasionar "*stress shielding*" debido a su alta resistencia mecánica. Este proceso natural se caracteriza por una reabsorción o pérdida del hueso adyacente al injerto, debido a la falta de exposición a las cargas mecánicas normales que ahora está soportando el injerto metálico [41]. Otros aspectos a tener en cuenta al momento de utilizar un material metálico, es su vulnerabilidad a la corrosión, y por tanto, a los productos derivados de su degradación, que no siempre son compatibles con el organismo [21, 41].

En segundo lugar, los materiales cerámicos destacan por su excelente biocompatibilidad, resistencia a la compresión, al desgaste y al ataque microbiano

[35, 41]. Existen diferentes composiciones químicas como HA, fosfatos cálcicos, silicatos de calcio, dióxido de zirconia, entre otros. En general sus aplicaciones están orientadas a usos ortopédicos y reemplazo de tejidos duros [43]. Dentro de las desventajas se encuentra la fragilidad, baja resistencia a tracción y dificultad para procesarlos homogéneamente [21].

Por otra parte, los materiales poliméricos son muy versátiles, ya que dependiendo del tipo de polímero se pueden obtener diversas propiedades. Por lo general, se caracterizan por su flexibilidad, resistencia a la fijación de proteínas y facilidad de fabricación en diferentes formas [41]. Estos pueden ser de origen natural como el colágeno, gelatina, actina, keratina, seda, celulosa, alginato entre otros o sintéticos como poliésteres, policarbonatos, polietilenos, politetrafluoroetileno, polimetacrilato, entre otros [21, 35]. Generalmente los polímeros son muy utilizados para la liberación controlada de fármacos, pero también en tejidos blandos, conectivos e implantes ortopédicos [43]. Algunas de las desvestajas de los polímeros es que no son tan resistentes como los metales, se deforman con el tiempo y se deterioran dependiendo del método de esterilización, pudiendo liberar sustancias tóxicas al organismo, generando una respuesta inflamatoria [21, 41].

Por último, se encuentran los materiales compuestos, los cuales son una combinación de materiales o fases, que difieren en forma, composición y volumen ($+5\%$) a una escala microscópica [21, 41]. De este modo se puede crear un nuevo material que reuna las características deseadas de cada material individual [21]. Sin embargo, es difícil obtener una buena estructura, ya que por lo general se requiere de una buena compatibilidad entre las fases, lo cual puede derivar en una disminución de las propiedades mecánicas [41]. Aunque de esta manera se puede obtener un material ajustado a las necesidades de ciertas aplicaciones, en muchos casos sigue prevaleciendo el uso de un solo tipo de material, debido principalmente al coste económico que esto supone [41].

1.3.2 Generaciones de biomateriales

A pesar de que el uso de los materiales en el cuerpo se remonta a tiempos prehistóricos, en los tiempos modernos gracias a los avances en la ciencia se ha obtenido un mayor entendimiento sobre las interacciones que existe entre los material y el organismo. A lo largo de los años, con cada innovación, fue posible establecer los requerimientos que debía presentar un material para estar en contacto con el cuerpo, de esta manera surgen las distintas generaciones de biomateriales.

- **Primera generación**

La primera generación de biomateriales surge entre los años 1950 y 1960
[42]. La característica principal de esta generación es la búsqueda de materia-
les **inertes**, es decir, materiales cuyas propiedades físicas permitieran sustituir
el tejido con la mínima respuesta inmune por parte del organismo [42, 44, 45].
En este momento histórico solo se disponían de materiales industriales que no
habían sido creado para fines médicos, como aceros inoxidables y aleaciones de
cobalto-cromo, siendo los primeros materiales metálicos usando en ortopedia
[44]. El titanio y sus aleaciones que eran utilizadas en el mundo de la aero-
náutica, empezaron a ser utilizados en la medicina. Las aleaciones de titanio
con níquel recibieron especial interés debido a sus propiedades mecánicas [44].
En relación a los materiales cerámicos, destacan la alumina y zirconia como
los más utilizados en este etapa [46-48]. Mientras que entre los materiales
poliméricos destacan la silicona, polietilenos, resinas acrílicas, poliuretanos,
polipropileno y polimetilmetacrilato [44].

El problema general que presentan estos materiales es que el organismo no
reconoce al material, terminando éste recubierto por un tejido fibroso que lo
encapsula e impide su integración en el organismo [44].

- **Segunda generación**

La segunda generación de biomateriales surge entre los años 1980 y 2000,
con el objetivo de eliminar los micro-movimientos que se producen en los mate-
riales de primera generación como consecuencia de la encapsulación con tejido
fibroso [42, 44]. En esta segunda generación surgen los materiales **bioactivos**,
los cuales son capaces de tener una interacción química controlada con el or-
ganismo [44, 45]. También apareció el concepto de materiales **reabsorbibles**,
que tienen la capacidad de degradarse mientras el tejido dañado se regenera
[42, 44, 45]. En esta generación tienen mayor importancia los materiales ce-
rámicos y poliméricos, ya que los materiales metálicos no son ni bioactivos ni
reabsorbibles [44]. Entre las cerámicas destacaron los compuestos de calcio y
fósforo, teniendo su mayor exponente en el HA, debido a su alta biocompa-
tibilidad y parecido con el componente mineral del hueso [45]. Se empezó a
entender la bioactividad como la capacidad de un material de formar una capa
de HA en su superficie, permitiendo la unión química con el tejido huésped [44,
49]. Las cerámicas de fosfatos cálcicos y los biovidrios fueron los materiales
más utilizados, destacando junto al HA mencionado anteriormente, los fosfa-
tos tricálcicos y fosfatos cálcicos amorfos [44, 45]. En relación a los biovidrios,

se observó que la presencia de silicio beneficia los procesos osteogénicos, por eso surgieron formulaciones de vidrios constituidos principalmente por una red de SiO$_2$, así como otro óxidos como Na$_2$O, CaO, P$_2$O$_5$, MgO y K$_2$O [44, 45].

Por su parte, dentro de los materiales poliméricos destacaron aquellos de origen natural o sintéticos capaces de degradarse. Los polímeros naturales tienen una bioactividad intrínseca, destacando de estos el quitosano, ácido hialurónico, colágeno, entre otros [44, 45]. Los polímeros sintéticos que destacaron fueron el poliglicólico, poliácido láctico, polidioxanona, policaprolactona, polihidroxibutirato, hidrogeles entre otros [44, 45]. Gracias a estos materiales mejora el problema del "*stress shielding*" ya que se degradan en el tiempo, transmitiendo carga al entorno [44]. En el caso de los polímeros degradables y no bioactivos, sufrían procesos de modificación de la superficie mediante la adsorción de proteínas y péptidos [44].

- **Tercera generación**

El objetivo de los materiales de la tercera generación es combinar la bioactividad y biodegradabilidad, estimulando, además, la regeneración del tejido a través de factores de señalización [44]. Estos factores deben modular respuestas específicas como el comportamiento célular, induciendo la adhesión, proliferación y diferenciación [44, 45]. En esta nueva generación de biomateriales también se incluye como objetivo la liberación controlada de fármacos, además de la funcionalización con proteínas, péptidos y otros factores que favorecen la interacción biológica. Algunas de las estratégias para lograr respuestas específicas comprenden la utilización de factores solubles como citoquinas y hormonas; factores insolubles como moléculas de la matriz extracelular; o estímulos externos como cargas mecánicas [45].

Cronológicamente la tercera generación de biomateriales surge al mismo tiempo que la ingeniería de tejido [44, 45]. A partir de este momento se empieza a considerar los andamios tridimensionales y su coexistencia con células y factores de crecimiento. Los materiales se consideran multifuncionales y deben ser biocompatibles, biodegradables, osteoconductivos, osteogénicos, osteoinductivos, resistentes mecánicamente y porosos para permitir la vascularización y paso de nutrientes, entre otras características [45].

Nuevos materiales, e incluso, los ya conocidos en la segunda generación de biomateriales, fueron tratados químicamente para mejorar sus propiedades. Los materiales polímericos y los cerámicos fueron procesados en distintas combinaciones. Por ejemplo, polímeros naturales como alginato, quitosano o sintéticos modificados con el (TGF)-β3 o proteínas y péptidos como RAD, ELK,

EAK [44]. Las cerámicas, sobre todo, los fosfatos cálcicos y biovidrios reforzados con polímeros, destacaron entre los nuevos materiales [44]. Los avances tecnológicos permitieron la aplicación de nuevas técnicas para la obtención de los andamios. De esta manera surgieron por ejemplo las espumas metálicas con aleaciones de titanio o tantalio, las cuales a través de tratamientos químicos favorecen la respuesta celular [44].

1.4   Biocerámicas

Los materiales cerámicos son sin lugar a duda uno de los grupos de materiales que más han aportado a la mejora en la calidad de vida de nuestra sociedad. Sus aplicaciones abarcan desde el área eléctrica, óptica, energética con los dieléctricos, semiconductores, piezoeléctricos, hasta aplicaciones médicas [48, 50]. El término de biocerámica incluye a las cerámicas, biovidrios y vitrocerámicos [48], englobando a todos los compuestos inorgánicos no metálicos como óxidos, sulfatos, nitratos, fosfatos, carbonatos y silicatos [50]. De este grupo, los fosfatos y silicatos destacan por sus múltiples aplicaciones.

1.4.1   Fosfatos cálcicos

Los fosfatos cálcios se definen como los compuestos formados por cationes de calcio unidos a grupos fosfatos, donde estos grupos se pueden presentar como orto- ($PO_4{}^{3-}$), meta- ($PO_3{}^-$), piro- ($P_2O_7{}^{4-}$) o poly- ($PO_3{}^{nn-}$) [27, 51]. En el mundo de los biomateriales, han despertando un gran interés debido a la gran similitud que presentan con el componente inorgánico o mineral del hueso. A pesar de que las primeras cerámicas empleadas como sustitutos óseos fueron bioinertes, como la zirconia y la alúmina, los primeros estudios centrados en la regeneración ósea plantearon la utilización de fosfatos cálcicos como HA, TCP o combinaciones de éstos [48, 52]. Sin embargo, en la actualidad se conoce un amplio abanico de materiales de fosfatos cálcicos cuya relación Ca/P varía desde 0.5 hasta 2 [27, 48]. Las características de los fosfatos cálcicos varían según su relación Ca/P, pero en general destacan por su biocompatibilidad, bioactividad, degradabilidad, osteoconductividad y osteoinductividad [27, 43, 48].

1.4.2   Silicatos

Los silicatos también juegan un papel importante como biocerámicas ya que el silicio es esencial en procesos metabólicos y en la formación y calcificación del tejido óseo [53, 54]. Los materiales que combinan calcio y silicio

estimulan la proliferación y adhesión celular, promoviendo la formación de hueso *in vivo* [55, 56]. Algunos de estos materiales son por ejemplo la wollastonita ($CaSiO_3$), silicato dicálcico (Ca_2SiO_4), akermanita ($Ca_2MgSi_2O_7$) y una amplia variedad de formulaciones vítreas. Principalmente, la liberación de silicio estimula la diferenciación de los osteoblastos y motiva la osteogénesis, osteointegración y osteoconductividad [39, 57].

1.4.3   Sustitución iónica

La incorporación de iones metálicos en materiales como silicatos y fosfatos cálcicos es una estrategia que surge para imitar, aún más, la estructura del hueso, pero también como respuesta para solucionar ciertos problemas. Muchos de estos elementos se encuentran naturalmente como trazas en el hueso, participando en procesos metabólicos, otros cumplen funciones terapéuticas o evitan infecciones microbianas [58]. Así entre estos elementos, podemos destacar:

- **Zinc**

El zinc (Zn^{2+}) es uno de los elementos esenciales en el cuerpo, que mayoritariamente se encuentra almacenado en los huesos [59]. Interviene en el metabolismo del hueso y funciona como cofactor de varias enzimas [53, 60]. El zinc detiene la resorción del hueso al inhibir la actividad de los osteoclastos, pero además, aumenta la actividad de la enzima ALP, favoreciendo la actividad de los osteoblastos y, en consecuencia, la formación de hueso [39, 53, 58, 60]. Al ser incorporado en los biomateriales destaca por mejorar la ***osteogénesis*** [39], pero también por mostrar efectos antiinflamatorios [53] y antimicrobianos [58].

- **Estroncio**

El estroncio (Sr^{2+}) es un elemento no esencial en el cuerpo, representando tan solo el 0.035% con respecto al total de calcio en los huesos [39, 59]. Sin embargo, debido a su similitud química con el calcio, actúa de forma similar y se define como un elemento "bone-seeking", es decir, con gran afinidad a la mineralización del hueso [39, 59]. Su principal efecto en los biomateriales es la ***osteogénesis***, al estimular la formación de hueso por la activación de los osteoblastos e inhibir la resorción, al frenar la actividad de los osteoclastos [39, 53, 58, 60]. Durante años el estroncio ha sido utilizado satisfactoriamente en tratamientos para la osteoporosis, ya que reduce las fracturas de vertebra en un 40% y de cadera en un 36% [39].

- **Hierro**

El hierro (Fe^{2+} o Fe^{3+}) es otro de los elementos importantes en nuestro organismo, no solo para el metabolismo del hueso sino también para una serie de procesos naturales como el transporte de oxígeno y nutrientes, síntesis de ADN, formación de vasos sanguíneos, respiración, proliferación y diferenciación celular, entre otros [58, 61]. La cantidad de hierro en el cuerpo es de 45 mg/kg en hombres y 35 mg/kg en mujeres [61]. En relación a su incorporación en los biomateriales, los investigadores tienen un creciente interés debido a la posibilidad de formar fases magnéticas, que permiten su utilización en hipertermia para el tratamiento contra el cáncer [58, 62]. Además de las propiedades magnéticas ha mostrado efectos positivos en relación a la biocompatibilidad de los materiales [58].

- **Magnesio**

El magnesio (Mg^{2+}) es uno de los iones metálicos esenciales de nuestro cuerpo, siendo el cuarto elemento más abundante [54, 59], encontrando en dientes y huesos el 65% del total [39]. Una deficiencia de magnesio puede ocasionar la reducción del hueso trabecular, generando problemas como osteoporosis y la posibilidad de fracturas [53, 59]. Adicionalmente, los biomateriales dopados con magnesio han destacado principalmente por impulsar la ***angiogénesis***, es decir, la formación de nuevos vasos sanguíneos [39]. También se ha observado que mejora la adhesión celular, debido a la interacción con la integrina de los osteoblastos [53], aumenta la capacidad para formar apatito y controla la reabsorción de materiales como el TCP [58].

- **Litio**

El litio (Li^+) es otro de los elementos no esencial en el organismo, pero genera efectos positivos en el mismo [59]. Desde hace años, el litio ha sido administrado para atender desordenes mentales como la depresión y bipolaridad. Recientemente se ha empezado a incorporar en los biomateriales, mostrando resultados beneficiosos en relación a la formación de hueso [39, 58, 59]. Se caracteriza principalmente por mejorar la ***osteogénesis*** [39], aumentar la masa ósea e incrementar la resistencia a la compresión de materiales como el TCP [63].

1.5   Andamios porosos tridimensionales

El hueso es un tejido difícil de imitar, al ser una estructura jerárquica compleja, formada por una fase orgánica y otra inorgánica, pero sobre todo, porque ocurren infinidad de procesos biológicos. Por este motivo, los requerimientos a tener en cuenta al momento de diseñar andamios que actúen como injerto óseo son amplios. Algunos de los más importantes se describen a continuación:

- **Porosidad:** debe poseer poros de diferentes tamaños, para permitir el desarrollo de las funciones vasculares, el transporte de oxígeno y nutrientes al interior y de desechos al exterior del andamio, para así mantener la actividad celular [32, 64-66]. El andamio debe presentar una porosidad similar a las del hueso trabecular (50-90%), con diferentes tamaños de poros (macro y micro).

- **Resistencia mecánica:** debe poseer propiedades mecánicas cercanas al hueso para permitir la correcta distribución de la carga [20, 32]. De lo contrario, se produciría el fenómeno conocido como "*stress shielding*", que se caracteriza por la reabsorción del hueso natural como se describió anteriormente [45].

- **Bioactividad:** capacidad inherente del material de participar en reacciones biológicas [27].

- **Biocompatibilidad:** adecuada respuesta con el hueso natural sin generar efectos tóxicos [20, 27, 32, 65].

- **Biodegradabilidad:** algunos andamios no solo estimulan la regeneración ósea, sino que también sirven de soporte mientras esto ocurre [20, 27, 65]. La velocidad de degradación debe ser coherente con la de regeneración del tejido y los compuestos liberados no deben generar efectos adversos en el organismo [20, 32].

- **Osteointegración:** capacidad de integrarse correctamente con el tejido huésped sin formar tejido fibroso en la interfase [27].

- **Osteoconducción:** capacidad de que las células se puedan adherir, proliferar, migrar y diferenciarse [64-66].

- **Osteoinducción/Osteogénico:** capacidad de inducir la formación de hueso nuevo mediante el reclutamiento de células y su diferenciación [27, 65].

- **Fabricación:** capaz de ser fabricado por técnicas que permitan obtener diferentes formas para atender todos los tipos de defectos [20, 64].

- **Comercialización:** capacidad de ser fabricado a costes aceptables para su comercialización [20, 64].

1.5.1 Síntesis de los andamios

La síntesis y preparación de andamios para aplicaciones en ingeniería de tejidos comprende un amplio número de técnicas y procesos como: evaporación de disolvente (solvent casting), liofilización (freeze-drying), electrohilado (electrospinning), saturación con gas (gas foaming), sol-gel, esterolitografía, impresión 3D, entre otros [64, 67]. No obstante, en el ámbito de esta Tesis Doctoral se desarrollará detalladamente tanto el proceso sol-gel, como la técnica de réplica de esponja polimérica, dado que son las técnicas empleadas en la obtención de los andamios porosos tridimensionales multicapa.

1.5.1.1 Fundamentos del proceso Sol-Gel

El proceso sol-gel es un técnica que permite obtener materiales cerámicos y vítreos, a través de la formación de una disolución denominada "sol", que posteriormente condensa para formar un "gel", a partir del cual se pueden obtener diferentes formas o estructuras.

El término "sol" hace referencia a la dispersión en un medio fluido de partículas coloidales de tamaño menor a 1000 nm, las cuales se obtienen a partir de un precursor inorgánico o alcóxido [68-70]. Por su parte, el término "gel" se refiere a una red tridimensional porosa, formada por la unión de las partículas coloidales, que atrapa en su interior una fase líquida [71]. Este gel puede ser manipulado de diferentes formas para evaporar o extraer el disolvente, hasta obtener aerogeles, xerogeles, cerámicas densas, fibras, recubrimientos, entre otros [72].

Esta técnica requiere de costes moderados debido a los reactivos utilizados, no siendo un factor limitante frente a la posibilidad de obtener materiales sólidos homogéneos y de gran pureza, con diferentes formas y a temperaturas relativamente bajas [69, 70, 73].

El proceso sol-gel conlleva una serie de etapas desde la mezcla de los reactivos hasta la obtención del producto final. Estas etapas serán descritas a continuación:

a) Hidrólisis y Condensación

El proceso se inicia con la mezcla del precursor líquido con agua, disolvente y catalizador, dando lugar a las reacciones de hidrólisis y condensación. Los precursores alcóxidos son los más populares debido a su elevada reactividad con componentes nucleofílicos [69, 74]. Poseen la forma $M(OR)_n$, donde M es el elemento metálico o catión con valencia n, O es oxígeno y R un radical alquilo [70, 74]. Este precursor al mezclarse con agua se hidroliza formando grupos M-OH, que posteriormente condensan dando como resultado los enlaces M-O-M [69, 70]. Ambas reacciones pueden ocurrir en presencia de un catalizador ácido (Figura 1.3) o básico (Figura 1.4) [68, 71, 75].

Las reacciones en medio ácido ocurren por la protonación del oxígeno del alcóxido como se muestra en la Figura 1.3. Esto genera cambios en la densidad de cargas, convirtiendo al átomo central del alcóxido en un electrófilo fácilmente atacable por agua durante la hidrólisis o por otros grupos hidrolizados durante la condensación [71].
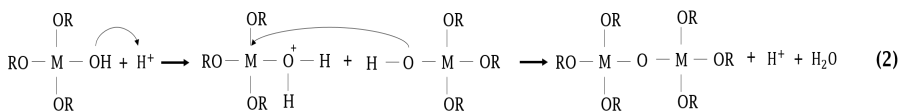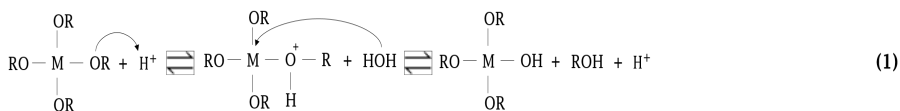
Figura 1.3: Reacción de hidrólisis (1) y condensación (2) en medio ácido [68, 71, 75].

Por su parte, las reacciones en medio básico ocurren por ataque nucleofílico al núcleo del precursor como se muestra en la Figura 1.4. Esto genera inestabilidad de cargas que termina con la ruptura del grupo alcoxi en el precursor [72].

En ambas Figuras se muestra que la reacción de hidrólisis ocurre solo en un grupo alquilo, no obstante, dependiendo de la cantidad de agua y catalizador, la hidrólisis puede ocurrir de forma completa en todos los grupos
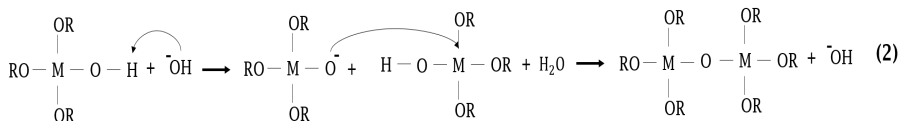
Figura 1.4: Reacción de hidrólisis (1) y condensación (2) en medio básico [68, 71, 75].

alquilo del precursor [74]. Igualmente, la reacción de condensación se muestra entre dos moléculas parcialmente hidrolizadas (condensación con salida de agua) pero también puede ocurrir entre una molécula hidrolizada y otra no hidrolizada (condensación con salida de un alcohol).

Los procesos de hidrólisis y condensación ocurren de forma simultánea, donde la velocidad de reacción depende de diferentes variables como: tipo de precursor, pH, tipo de disolvente, relación entre los grupos alcoxi y agua, presencia de electrolitos y temperatura [71, 76].

El precursor, según el tipo y longitud de sus ramificaciones, puede ocasionar una disminución en la velocidad de hidrólisis, debido a los efectos estéricos. La relación entre los grupos alcoxi y las moléculas de agua (R), también es un factor determinante [71]. A mayor cantidad de agua (menor R), los procesos de hidrólisis y condensación se aceleran, influenciando directamente las propiedades finales de los geles [71]. En relación al catalizador, a pH ácidos, la hidrólisis ocurre a una velocidad mayor que la condensación, produciendo geles poco entrecruzados. Por el contrario, a pH básico, la velocidad de condensación es mayor que la hidrólisis, produciendo geles altamente entrecruzado [75].

Por su parte, los disolventes, son especies necesarias para lograr la perfecta homogenización de los reactivos. Pueden utilizarse disolventes polares como el agua, alcoholes y formamida, o, disolventes no polares como tetrahidrofurano y dioxano [71].

En cuanto a los electrolitos o iones, estos pueden modificar la doble capa eléctrica entre las partículas, afectando la interacción entre ellas. Particularmente, disminuyen las fuerzas de repulsión y, por tanto, influyen en el proceso de gelificación. Muchos de los iones son contraiones del disolvente

o del catalizador, convirtiéndolos en variables que se deben cuidar para alcanzar la reproducibilidad del material [71].

Sin embargo, los iones pueden ser incorporados intencionalmente para la obtención de geles con iones dopantes que interrumpen los enlaces M-O-M, formando enlaces iónicos con los oxígenos de dos moléculas parcialmente hidrolizadas. Además de iones introducidos en la red, pueden formarse redes con dos elementos metálicos o cationes al mezclar dos precursores diferentes [70].

b) Gelificación.

En la etapa de gelificación las partículas del sol comienzan a condensar, formando aglomerados que continuamente aumentan de tamaño hasta formar una red tridimensional que retiene en su interior al disolvente [76]. Estas partículas condensan debido a las fuerzas de atracción de Van der Waals [69].

c) Maduración.

En la etapa de maduración continúan las reacciones químicas en el gel, como policondensación, sinéresis, engrosamiento y transformación de fases [75]. Estas reacciones provocan cambios en las propiedades del gel, principalmente una disminución de la porosidad, aumento del grosor entre las partículas y aumento de la resistencia [76].

d) Secado.

En la etapa de secado se elimina el líquido remanente en los poros del gel [76]. Es un proceso que debe realizarse de forma controlada ya que implica la contracción del gel. El secado se lleva a cabo por evaporación del disolvente o secado supercrítico. Dependiendo del tipo de secado se obtienen estructuras diferentes como aerogeles, xerogeles, entre otros [75].

e) Sinterizado.

La sinterización es la última etapa del proceso dependiendo del propósito final del gel. En esta etapa se produce principalmente la densificación del material, ocurriendo cambios químicos en la superficie, reorganización o eliminación de poros y cristalización [75, 76].

1.5.1.2 Fundamentos de la técnica de réplica de esponja polimérica

La técnica de réplica de esponja polimérica consiste en la utilización de una esponja, generalmente de poliuretano, que sirve como plantilla de sacrificio

para la obtención de materiales porosos de diferentes formas y tamaños. El método se inicia con la obtención de una barbotina o una disolución con la composición química deseada. La plantilla se impregna con esta disolución varias veces hasta cubrir por completo el material de la esponja. Finalmente se somete a un proceso de secado y posterior calentamiento o sinterizado, donde se elimina el material polimérico, obteniendo una pieza con la composición deseada y la forma de la plantilla [77-79].

Esta técnica comienza a ser utilizada alrededor del año 2000 para la obtención de materiales porosos en aplicaciones óseas. Tian et al. y Ramay et al. obtuvieron andamios porosos de HA utilizando esta técnica [79, 80]. Chen et al. por su parte, obtuvieron andamios porosos, resistentes y biodegradables de vitrocerámicas basados en la formulación del biovidrio 45S5 [77]. Posteriormente, a lo largo de los años, han surgido nuevas composiciones químicas que han permitido obtener distintos andamios porosos. También han surgido variaciones en la técnica para obtener estructuras más resistentes con porosidad controlada [78, 81].

Capítulo 2

Objetivos

En esta Tesis Doctoral se parte de la **hipótesis** de que andamios cerámicos multicapa formado por diferentes composiciones cerámicas, son una excelente alternativa para unificar en una estructura la mayor cantidad de requerimientos necesarios para un injerto óseo. Para demostrar esta hipótesis se estableció como ruta de síntesis la combinación de los métodos de réplica de esponja polimérica y el proceso sol-gel. En base a la hipótesis descrita se plantearon los siguientes objetivos.

El **objetivo general** de esta Tesis Doctoral es sintetizar y caracterizar nuevos andamios porosos tridimensionales multicapa, basados en un núcleo con composición perteneciente al sistema SiO_2-CaO-P_2O_5-LiO_2, y recubrimientos externos con composición dentro del sistema SiO_2-CaO-P_2O_5, dopado con iones de zinc, estroncio, hierro y magnesio.

Para alcanzar el objetivo general se plantean los siguientes **objetivo específicos**:

1. Obtener mediante el proceso sol-gel, combinado con la réplica de esponja polimérica el núcleo del andamio multicapa, con composición dentro del sistema SiO_2-CaO-P_2O_5-LiO_2.

2. Modificar el comportamiento del núcleo del andamio mediante recubrimientos con capas de composición pertenecientes al sistema SiO_2-CaO-P_2O_5.

3. Desarrollar estructuras multicapa con capacidad de liberar iones zinc, estroncio, hierro y magnesio en diferentes concentraciones.

4. Caracterizar mineralógica, química y físicamente los andamios multicapa.

5. Evaluar la bioactividad *in vitro* de los andamios multicapa mediante inmersión en SBF según la norma ISO/FDIS 23317.

6. Evaluar la influencia de las variables del procesado en las propiedades mineralógicas, físico-químicas y bioactividad *in vitro* del núcleo del andamio.

7. Evaluar la influencia de las fases cristalinas del núcleo en la bioactividad *in vitro* de andamios multicapa dopados con magnesio en diferentes concentraciones.

8. Obtener mediante el proceso sol-gel y réplica de esponja polimérica andamios multicapa con dopaje simultáneo, respecto a los moles de calcio de las capas externas, con estroncio (3%), hierro (3%) y magnesio (3%) en dos configuraciones diferentes. Los tres iones en la misma capa externa (Configuración 1) y los tres iones en capas externas separadas (Configuración 2).

9. Evaluar la influencia de la disposición de los tres iones dopantes (Configuración 1 y 2) en la bioactividad *in vitro* del andamio multicapa.

10. Evaluar la biocompatibilidad *in vitro* del núcleo y los andamios multicapa con los tres iones dopantes (Configuración 1 y 2) mediante ensayos de viabilidad, citotoxicidad, adhesión y proliferación de células de osteosarcoma MG-63.

Capítulo 3

Materiales y Métodos

En la presente Tesis Doctoral se desarrollaron diferentes andamios multicapa dopados con iones en varias concentraciones. En este capítulo se detallarán las formulaciones químicas empleadas para la conformación de cada andamio multicapa, describiendo posteriormente las técnicas de caracterización mineralógicas, física y química, así como la evaluación de la bioactividad y biocompatibilidad *in vitro*.

3.1 Formulaciones químicas de los andamios multicapa

Las formulaciones químicas utilizadas a lo largo de esta Tesis Doctoral se presentan en la Tabla 3.1. Estas formulaciones corresponden al núcleo del andamio, el recubrimiento externo original y las modificaciones debido al dopaje iónico, que dió lugar a la obtención de diferentes tipos de andamios multicapa.

3.2 Preparación de los andamios multicapa

Los andamios fueron preparados empleando las técnicas de sol-gel y réplica de esponja polimérica de acuerdo con los siguientes pasos:

1. Preparación de la disolución sol-gel con la composición deseada.

2. Inmersión de la esponja polimérica en la disolución.

Tabla 3.1: Formulaciones químicas de los andamios multicapa (% molar).

		SiO_2	P_2O_5	CaO	LiO_2	M_xO_y[a]
Andamios sin núcleo dopados con zinc	Andamio 1% Zn^{2+}	29	3	67.3	-	0.7
	Andamio 30% Zn^{2+}			52.3		14
Andamio multicapa	Núcleo	1	25	68	6	-
	Recubrimiento (R)	29	3	68	-	-
Andamio multicapa dopado con zinc	Núcleo	1	25	68	6	-
	R con 1% Zn^{2+} [b]	29	3	67.3	-	0.7
Andamios multicapa dopados con estroncio	Núcleo	1	25	68	6	-
	R con 1% Sr^{2+}			67.3		0.7
	R con 3% Sr^{2+}			66		2
	R con 10% Sr^{2+}	29	3	61	-	7
	R con 25% Sr^{2+}			51		17
	R con 50% Sr^{2+}			34		34
Andamios multicapa dopados con hierro	Núcleo	1	25	68	6	-
	R con 1% Fe^{3+}			67.3		0.3
	R con 3% Fe^{3+}	29	3	66	-	1
Andamios multicapa dopados con magnesio	Núcleo	1	25	68	6	-
	R con 1% Mg^{2+}			67.3		0.7
	R con 3% Mg^{2+}	29	3	66	-	2
	R con 10% Mg^{2+}			61		7
Andamios multicapa dopados con hierro, estroncio y magnesio	Núcleo	1	25	68	6	-
	R con 9% $(Fe^{3+}+Sr^{2+}+Mg^{2+})$[c]			63		2-2-1
	R con 3% Fe^{3+} [d]	29	3	67		1
	R con 3% Sr^{2+} [d]			66	-	2
	R con 3% Mg^{2+} [d]			66		2

[a] M_xO_y óxido del dopante (M = Zn, Sr, Fe o Mg), [b] Porcentaje del ion dopante respecto a los moles de calcio del recubrimiento, [c] Andamio formado por el núcleo y un solo recubrimiento dopado con Fe^{3+}, Sr^{2+} y Mg^{2+} (Configuración 1 - 3J) [d] Andamio formado por el núcleo y tres recubrimientos dopados con Fe^{3+}, Sr^{2+} y Mg^{2+} (Configuración 2 - 3S).

3. Centrifugación de la esponja para eliminar el exceso de líquido en los poros.

4. Secado en la estufa.

5. Sinterizado de las muestras: 55 horas hasta 950 °C, 8 horas a 950 °C y enfriamiento hasta temperatura ambiente.

Los pasos 2-4 se repiten dependiendo de la viscosidad de la disolución hasta cubrir por completo la estructura de la esponja polimérica.

Una vez obtenido el andamio que corresponde al núcleo, se procede a la obtención de los andamios multicapa. Para ello se repite el procedimiento descrito anteriormente pero ahora utilizando el núcleo previamente sinterizado en vez de la esponja de poliuretano. El proceso de sinterizado de las capas externas se realiza a 950 °C durante 3 horas.

Los reactivos utilizados para la preparación del sol-gel del núcleo fueron TEOS (98% - Sigma Aldrich) como fuente de silicio, TEP ($\geq$ 99.8% - Sigma Aldrich) como fuente de fósforo, carbonato de calcio ($CaCO_3 \geq$ 99.8%- Sigma Aldrich) y carbonato de litio (Li_2CO_3 99% - Sigma Aldrich). Los iones dopantes se añadieron a través de carbonato de zinc ($ZnCO_3$ - Sigma Aldrich), carbonato de estroncio ($SrCO_3$ 99% - Alfa Aesar), carbonato de magnesio ($MgCO_3$ - Acros organics) y sulfato de hierro (II) heptahidratado ($FeSO_4.7H_2O$ - Merck).

Los primeros andamios desarrollados en esta Tesis Doctoral fueron el núcleo y andamios basados en la formulación del recubrimiento externo dopados al 1% y 30% de zinc. Posteriormente se prepararon los andamios multicapa, constituidos por el núcleo y recubrimiento externo dopado al 1% de zinc, como se muestra en la Tabla 3.1. Estos andamios se obtuvieron utilizando esponjas de poliuretano con 20 poros por pulgada (ppi 20) y de forma cilíndrica, con 10 mm de diámetro y 5 mm de alto. La preparación de estos andamios se describe en la sección "*2.1. Materials preparation*" del Artículo 1.

Los siguientes andamios multicapa fueron los dopados entre 1% y 50% con estroncio, como se muestra en la Tabla 3.1. A partir de estos andamios se utilizaron esponjas de poliuretano ppi 20 de forma cilíndrica, con 12.7 mm de diámetro y 10 mm de alto. La preparación de estos andamios se describe en la sección "*2.1. Materials preparation*" del Artículo 2.

Seguidamente, se prepararon los andamios multicapa dopados al 1% y 3% de hierro, como se muestra en la Tabla 3.1. La preparación de estos andamios se describe en la sección "*2.1. Preparation of the scaffolds*" del Artículo 3.

Los andamios multicapa dopados con zinc, estroncio e hierro fueron obtenidos utilizando un núcleo cuya disolución sol-gel se calentó a 100 °C durante 30 minutos. Posteriormente, se varió el tiempo de calentamiento de la disolución a 15 minutos y 1 hora.

Los núcleos preparados con la disolución calentada durante 15 minutos y 1 hora, se utilizaron para preparar los andamios multicapa dopados al 1%, 3% y 10% de magnesio. La preparación de estos andamios se describe en la sección "*Experimental part*" del Artículo 4 y sección "*2. Materials and methods*" del Artículo 5.

Por último, se prepararon los andamios multicapa dopados con hierro, estroncio y magnesio en las configuraciones 1 y 2, como se muestra en la Tabla 3.1. La preparación de estos andamios se describe en la sección "*Scaffolds preparation*" del Artículo 6.

3.3   Caracterización de los andamios

Los andamios fueron caracterizados mineralógica, química y físicamente a través de diferentes técnicas. La caracterización de la macroestructura de los andamios se realizó mediante un microscopio óptico, mientras que la microestructura fue evaluada utilizando la técnica SEM-EDX. La caracterización mineralógica se realizó mediante XRD, analizando los difractogramas mediante el sotfware Math! 3 y las bases de datos: JCPDS, COD y ICSD. La composición química se estudió a través de espectroscopía Raman y FTIR. La porosidad de los andamios se estudió a través de diferentes técnicas de acuerdo con el tamaño del poro. Los macroporos se evaluaron mediante picnometría con agua según el principio de Arquimedes; los microporos a través de la técnica de porosimetría de mercurio y los mesoporos a través la adsorción-desorción de nitrógeno seguido del método BET y cálculos BJH. Por último, se estudió la resistencia mecánica de los andamios mediante la técnica de compresión simple.

Las condiciones de ensayo para cada una de las técnicas mencionadas, se detallan en la sección "*2.2. Materials characterization*" del Artículo 1 para los andamios dopados con zinc, en la sección "*2.2. Material characterization*" del Artículo 2 para los andamios dopados con estroncio, en la sección "*2.2. Characterization of the scaffolds*" del Artículo 3 para los andamios dopados con hierro, en la sección "*Experimental part*" del Artículo 4 y sección "*2. Materials and methods*" del Artículo 5 para los andamios dopados con magnesio y por último, la sección "*Scaffold characterization*" del Artículo 6 para los andamios dopados con hierro, estroncio y magnesio.

3.4   Bioactividad *in vitro* de los andamios

La bioactividad *in vitro* se estudió en base a la capacidad de los andamios para precipitar apatito en su superficie al estar en contacto con SBF. La formación de apatito en la superficie de los materiales ayuda a predecir la capacidad de unirse con el tejido óseo huésped [82].

Los ensayos se realizaron de acuerdo con la norma ISO/FDIS 23317:2017. Los andamios se sumergieron en el SBF durante diferentes intervalos de tiempo. Al finalizar, la superficie de los andamios se evaluó mediante SEM-EDX. Alicuotas del SBF resultante se analizaron mediante ICP-OES, para estudiar las variaciones iónicas entre las cerámicas y el SBF.

Los detalles de los ensayos se describen en la sección "*2.2.4. In vitro behaviour in bioactivity terms*" del Artículo 1 para los andamios dopados con zinc,

en la sección "*2.3. In vitro bioactivity evaluation*" del Artículo 2 para los anda-
mios dopados con estroncio, en la sección "*2.2.3. In vitro bioactivity evaluation
of the scaffolds*" del Artículo 3 para los andamios dopados con hierro, en la sec-
ción "*Experimental part*" del Artículo 4 y sección "*2. Materials and methods*"
del Artículo 5 para los andamios dopados con magnesio y por último, la sec-
ción "*In vitro bioactivity evaluation*" del Artículo 6 para los andamios dopados
con hierro, estroncio y magnesio.

3.5   Biocompatibilidad *in vitro* de los andamios

Los ensayos de biocompatibilidad se realizaron al núcleo y a las estructuras
multicapa dopadas con hierro, estroncio y magnesio con las configuraciones 1
y 2.

Estos ensayos se realizaron de forma directa e indirecta, utilizando la línea
celular de osteosarcoma MG-63. Los detalles sobre el cultivo, crecimiento y
siembra de las células se describen en la sección "*Cell culture*" del Artículo 6.

El ensayo indirecto consistió en el cultivo de las células con medio de
cultivo celular previamente en contacto con el andamio partículado, en con-
centraciones de 10 mg/ml y 100 mg/ml durante 24 y 96 horas. Se evaluó el
pH y la liberación de los iones en los medios de cultivo celular en contacto
con el material, mediante ICP-OES. Después de 1 y 3 días de cultivo de las
células con los distintos medios, se evaluó la viabilidad celular mediante el
ensayo WST-8 y la citotoxicidad mediante el análisis de la enzima LDH. Los
detalles de estos ensayos se describen en la sección "*Indirect cell culture*" del
Artículo 6.

Por su parte, el ensayo directo consistió en la siembra directa de las células
en la superficie de los andamios. Las muestras se incubaron durante 1, 3, 7,
14 y 21 días. Después de cada período se evaluó la viabilidad celular mediante
el ensayo WST-8. La citotoxicidad se evaluó mediante el ensayo LDH después
de 7, 14 y 21 días. Por último, se evaluó la morfología de las células de forma
visual mediante el microscopio de fluorescencia y SEM. Los detalles de estos
ensayos se describen en la sección "*Direct cell culture*" del Artículo 6.

Capítulo 4

Resultados

En este capítulo se realizará una descripción global de los resultados obtenidos en el desarrollo de la presente Tesis Doctoral. Para ello, los resultados se presentan siguiendo el progreso de los andamios multicapa.

4.1 Andamios dopados con zinc

Este estudio comienza con la obtención del núcleo y la evaluación de varios andamios para seleccionar la composición adecuada para los recubrimientos externos.

Estos primeros resultados se presentan en el **Artículo 1**, que se inicia con la caracterización del núcleo (llamado 3D-CaLi) como se evidencia en la Figura 1 (pág. 77). Dicha caracterización muestra que la microestructura del núcleo es homogénea y está formada por granos hexagonales, los cuales, están constituidos principalmente por las fases CPP y TCP. Adicionalmente, en relación a las propiedades físicas, esta estructura presentó una resistencia a la compresión de 1.0-1.7 MPa y 74% de porosidad.

Seguidamente, se desarrollaron nuevos andamios para determinar las formulaciones químicas adecuadas para el recubrimiento externo del núcleo. Estas nuevas formulaciones presentan mayor porcentaje de silicio y menor porcentaje de fósforo respecto al núcleo (andamio 3D-Ca). Adicionalmente, estas formulaciones fueron dopadas con iones de zinc al 1% y 30% respecto a los moles totales de calcio (andamios 3D-Ca 1%-Zn y 3D-Ca 30%Zn). Finalmente, se obtuvieron los andamios con la macro- y microestructura mostrada en la

Figura 2 (pág. 78), en las cuales se pueden observar los poros interconectados, adquiridos de la esponja de poliuretano.

Los andamios 3D-Ca, 3D-Ca 1%-Zn y 3D-Ca 30%Zn, presentaron las fases cristalinas identificadas en los difractogramas de la Figura 3 (pág. 78). En particular, los andamios 3D-Ca y 3D-Ca 1%-Zn estaban constituidos por una fase de silicato de calcio amorfo junto con otras fases identificadas como cristobalita (SiO_2 - tetragonal) y tridimita (SiO_2 - triclínico), mientras que en el andamio 3D-Ca 30%Zn se identificaron las fases de hardystonita ($Ca_2ZnSi_2O_7$), cuarzo (SiO_2 - trigonal) y wollastonita-2M ($CaSiO_3$).

Posteriormente, se evaluó la bioactividad *in vitro* de estos andamios como se observa en la Figura 4 (pág. 79). En estas imágenes se evidencia que el andamio 3D-Ca desde el primer día presentó precipitados esféricos en su superficie, los cuales fueron aumentando hasta los 7 días de inmersión en SBF. Estos precipitados esféricos presentaron una morfología tipo varillas (rod-like shape), con relación Ca/P cercana al carbohidroxiapatito. Por su parte, en el andamio 3D-Ca 1%-Zn los precipitados formaron una capa contínua tan solo 1 día después de la inmersión en SBF. La morfología de estos precipitados fue tipo hoja (blade-like shape), con una relación Ca/P después de 7 días similar al HA. Por el contrario, el andamio 3D-Ca 30%Zn no presentó ningún precipitado en su superficie en los tiempos evaluados.

Una vez conocida la bioactividad de estos andamios, se decidió recubrir el núcleo con capas de la composición 3D-Ca 1%-Zn, debido al aumento de la bioactividad observada anteriormente. Una vez obtenido este nuevo andamio multicapa (3D-CaLiZn), se realizó la caracterización microestructural como se muestra en la Figura 5 (pág. 80). En estas imágenes, se observan fragmentos del recubrimiento sobre la microestructura del núcleo previamente caracterizado. En el análisis de las fases cristalinas de este andamio presentado en la Figura 6 (pág. 80), se determinó que la fase predominante es la fase de TCP, seguido por las fases de tridimita y silicato de calcio con zinc.

Por último, se realizó la evaluación de la bioactividad *in vitro* del núcleo y del andamio multicapa como se muestra en la Figura 7 (pág. 81). Este estudio concluyó que el núcleo del andamio no presenta bioactividad durante el tiempo de estudio, mientras que el andamio 3D-CaLiZn después de 1 día de inmersión empezó a presentar precipitados. Después de 14 días, se observó que el precipitado cubría la totalidad de la superficie del andamio y, un estudio más detallado, reveló que alguno de estos presentaban una morfología de esfera hueca como se observa en la Figura 7-j (pág. 81).

4.2 Andamios dopados con estroncio

En el **Artículo 2** se desarrollaron nuevos andamios multicapa, basados en la misma composición química del núcleo anterior (**Artículo 1**) y con recubrimientos externos dopados con iones de estroncio. Se utilizaron diferentes concentraciones de dopante para determinar su influencia en la bioactividad *in vitro*.

La Figura 1 (pág. 87) de este artículo, muestra la macroestructura de los nuevos andamios, donde es posible observar sus dimensiones y poros interconectados. Seguidamente, en la Figura 2 (pág. 88) se observa la microestructura del núcleo y de los andamios recubiertos y dopados. En el caso del núcleo, se evidencia que éste presenta granos hexagonales, con una relación Ca/P que varía desde el borde hasta el centro entre 1.2-1.3, así como también pequeños cristales con relación Ca/P de 1.6 y bastones con relación Ca/P de 1.2. Por su parte, en la superficie de los andamios con los recubrimientos, se observa una nueva capa sobre los granos hexagonales. A medida que aumenta el porcentaje de dopante, se forman partículas distribuidas por toda la superficie. A su vez, el análisis por EDX indica, la presencia de silicio y estroncio en estas partículas superficiales.

El análisis por XRD, cuyos difractogramas se muestran en la Figura 3 (pág. 89), confirman nuevamente que el núcleo está constituido principalmente por las fases de CPP y TCP, además de las fases de fosfato cálcico con litio $(LiCa(PO_4)$ y $Ca_{9.95}Li_{1.05}(PO_4)_7)$, cristobalita y cloroapatito $(Ca_5(PO_4)_3Cl)$. En cambio, en los andamios con los recubrimientos, aparecen nuevas fases como Sr_2SiO_4 y $[(Ca_{1.65}Sr_{0.35})(SiO_4)]$, cambiando la intensidad de los picos de las fases del núcleo, observándose una disminución de los picos de la fase CPP.

Adicionalmente, en la Figura 4 (pág. 89) se muestran los espectros obtenidos mediante FTIR, en los cuales se identificaron las bandas de los grupos Si-O-Si, $PO_4{}^{3-}$ y $P_2O_7{}^{4-}$ para el caso del núcleo. Por su parte, en los andamios con los recubrimientos sin y con estroncio, se evidenció una disminución de las bandas correspondientes al grupo $P_2O_7{}^{4-}$ y aparición de las bandas del grupo Si-O-2NBO, que corresponde a las vibraciones de grupos Si-O con dos oxígenos del tetraedro SiO_4, no unidos debido a la presencia de elementos alcalinotérreos como calcio y estroncio.

En relación a la porosidad de los andamios, en la Figura 5 (pág. 90) se muestran las curvas obtenidas mediante la técnica de porosimetría de mercurio. En ellas se observa que el núcleo presenta una distribución de tamaño de poro bimodal, con la mayoría de los poros alrededor de las 80 μm. En general,

el núcleo presentó una microporosidad (< 300 μm) del 41.9% y macroporosidad (> 300 μm) del 71.9%, obtenida mediante el principio de Arquimedes. Por su parte, el andamio recubierto y sin dopaje (andamio C/EL-0Sr), presentó una distribución de tamaño de poros más amplia (entre 108 y 0.5 μm), con una microporosidad del 52.5% y una macroporosidad del 64.2%. Mientras que el andamio recubierto y dopado con estroncio al 50% (C/EL-50Sr, muestra representativa de los andamios dopados), presentó una distribución amplia de poros entre 189 y 3.8 μm, con una microporosidad del 40.8% y macroporosidad del 69.4%.

Para completar la caracterización física de los andamios, se estudió la resistencia a la compresión, obteniendo una resistencia del núcleo de 0.9-1.6 MPa, y los núcleos con los recubrimientos una resistencia de 0.9-1.8 MPa.

Finalmente, la evaluación de la bioactividad *in vitro* mostró nuevamente que el núcleo del andamio no es bioactivo y al recubrirlo con la segunda composición, sin dopaje, el andamio presenta bioactividad a partir de los 14 días (Figura 6 (pág. 91)), con una relación Ca/P de 1.67. Posteriormente, al dopar la muestra con estroncio al 1%, la bioactividad aumenta, apareciendo precipitados de apatita tan solo a 3 días, y una relación Ca/P de 1.66. Sin embargo, al aumentar el porcentaje de dopaje en más del 25%, la bioactividad desaparece. Con excepción del andamio dopado al 50% de estroncio, el cual después de 7 días presentó un precipitado en su superficie que podría corresponder a un apatito, debido a la relación (Ca+Sr)/P de 1.7, pero al disolverse posteriormente, se pierde el carácter bioactivo del andamio.

4.3   Andamios dopados con hierro

Los andamios multicapa desarrollados anteriormente con estroncio (**Artículo 2**), permitieron determinar la cantidad de dopaje idónea para aumentar la bioactividad *in vitro*. Es por ello, que partiendo de esta información, en el **Artículo 3** se desarrollaron nuevos andamios multicapa, pero esta vez dopados con hierro, en las concentraciones de 1% y 3%.

En la Figura 1 (pág. 99) de este artículo, se presentan las microestructuras observadas mediante SEM. En estas imágenes se advierten las capas agrietadas del recubrimiento externo de los andamios dopados al 1% (andamio C/EL-1Fe) y 3% (andamio C/EL-3Fe) sobre la microestructura característica del núcleo.

Seguidamente, en la Figura 2 (pág. 99) se muestran los difractogramas obtenidos por XRD, donde se identificó que los núcleos recubiertos y dopados con hierro presentaron una nueva fase de fosfato cálcico dopado con hierro

$(Ca_{9.93}Fe_{1.167}(PO_4)_7)$. Adicionalmente, se observó un aumento de los picos correspondientes a la fase de cristobalita, y disminución de los picos de la fase de CPP presente en el núcleo.

En relación a las propiedades físicas de los andamios, se estudiaron distintos tipos de porosidad: mesoporos (entre 2-50 nm), microporos (< 300 μm) y macroporos (> 300 μm). El resultado del estudio de los mesoporos se observa en la Figura 3 (pág. 100), donde se presentan las isotermas obtenidas mediante adsorción y desorción de nitrógeno. En este caso, tanto el núcleo como los andamios C/EL-1Fe y C/EL-3Fe, presentaron una distribución de mesoporos entre 3 nm y 10 nm, siendo la mayoría de los mesoporos alrededor de 3 nm aproximadamente.

En segundo lugar, se realizó el estudio de los microporos, mediante la técnica de porosimetría de mercurio, cuyo resultado se muestra en la Figura 4 (pág. 100). Según estas curvas, el núcleo del andamio presentó poros entre 123 μm y 10 μm, con una microporosidad total del 30.6%, mientras que los andamios C/EL-1Fe y C/EL-3Fe, entre 150 μm y 0.5 μm, con una microporosidad del 51.3% y 54.1%, respectivamente. Por último, a través del principio de Arquimedes se determinó la macroporosidad, en este caso, el núcleo presentó un 77.6%, mientras que los andamios C/EL-1Fe y C/EL-3Fe presentaron una macroporosidad del 57.4% y 51.9%, respectivamente.

En cuanto a la resistencia a la compresión de estos andamios, se obtuvo para el núcleo una resistencia de 0.9-1.6 MPa, para el andamio C/EL-1Fe 0.4-1.2 MPa y para el andamio C/EL-3Fe 1-1.5 MPa.

Finalmente, se realizó la evaluación de la bioactividad *in vitro*. Los resultados del núcleo se muestran en la Figura 5 (pág. 101), en la cual se observa que este fue no bioactivo entre 3 y 28 días. Por su parte, el andamio C/EL-1Fe cuya evaluación de bioactividad se presenta en la Figura 6 (pág. 102), mostró que durante las primeras horas del ensayo (6 y 9 horas), el recubrimiento se disuelve hasta revelar la microestructura del núcleo. No obstante, después de 1 día se observó la formación de los primeros precipitados, los cuales continuaron creciendo hasta los 13 días. Estos precipitados presentaron una morfología globular característica del apatito, con una relación Ca/P de 1.35-1.71. Sin embargo, después de los 18 días gran parte de los precipitados se disolvieron, revelando nuevamente la microestructura del núcleo. Este comportamiento de precipitación y disolución se repitió nuevamente, ya que a los 23 días se formó una nueva capa de precipitado y a los 28 días se disolvió.

Por el contrario, el andamio C/EL-3Fe presentó un comportamiento distinto, como se evidencia en la Figura 7 (pág. 103). Si bien hasta el tercer día el comportamiento fue similar al anterior, después de 8 días se formaron

precipitados en la superficie, los cuales se mantuvieron hasta los 28 días del ensayo, presentando una relación Ca/P de 1.25-1.75.

Por último, en la Figura 8 (pág. 103) se muestran las curvas de la concentración iónica en el SBF durante el tiempo de contacto con los diferentes andamios. Para el caso del núcleo, de forma general, ocurrió una ligera disminución de calcio en el medio, demostrando la adsorción de este ion en la superficie del material. Por el contrario, la concentración de fósforo aumentó en el SBF debido a la liberación de este ion del material, mientras que la concentración de silicio no varió con el tiempo, permaneciendo aproximadamente cercana a cero.

En cuanto al intercambio iónico de los andamios C/EL-1Fe y C/EL-3Fe, en general, ambos presentaron una disminución de la concentración de calcio en el SBF. Por su parte, las concentraciones de fósforo y silicio presentaron un comportamiento opuesto entre ellos. Es decir, una liberación de fósforo acompañado de adsorción de silicio y viceversa. Adicionalmente, comparando el estudio realizado por SEM, se observó que los precipitados de apatito aparecen cuando ocurre una liberación de silicio y, en consecuencia, adsorción de fósforo. Es por ello que el andamio C/EL-1Fe, al presentar precipitación y disolución de apatito, en las curvas de concentración iónica se evidenció un comportamiento oscilatorio entre el fósforo y el silicio. Por el contrario, el andamio C/EL-3Fe, al mostrar precipitados estables a partir de los 8 días, presentó adsorción de fósforo y liberación de silicio hasta alcanzar prácticamente la estabilidad durante el resto del ensayo.

4.4 Andamios dopados con magnesio

Hasta el momento, los andamios multicapa dopados con zinc, estroncio e hierro poseen un núcleo común constituido principalmente por las fases de CPP y TCP. Este núcleo de composición inicial SiO_2-68CaO-25P_2O_5-6LiO$_2$ (% molar), se obtuvo mediante la inmersión sucesiva (20-30 veces) de la esponja de poliuretano en la disolución preparada por los reactivos mencionados anteriormente, y calentada a 100 °C durante 30 minutos.

Sin embargo, se quiso estudiar la influencia en las propiedades del núcleo, de algunas variables implicadas en el proceso sol-gel. Para ello, se seleccionaron variables como el tiempo de calentamiento de la disolución antes de la inmersión de la esponja y la cantidad de recubrimientos.

En el **Artículo 4** se muestra el desarrollo de los nuevos núcleos, partiendo de la misma composición química empleada anteriormente y calentando

la disolución durante 1 hora y 15 minutos a 100 °C. La disolución calentada durante 1 hora fue utilizada para recubrir 10 veces la esponja de poliuretano, obteniendo el llamado núcleo A. Mientras que la disolución calentada durante 15 minutos fue utilizada para recubrir 30 veces la esponja, obteniendo el llamado núcleo B.

Una vez sinterizadas estas estructuras se procedió con su caracterización, cuyos resultados se muestran en la Figura 2 (pág. 111) de este artículo. En esta figura se observa que el núcleo A está constituido principalmente por la fase TCP, y las fases minoritarias de CPP, cristobalita y fosfatos de litio y cloro. Así mismo, su observó que su microestructura es una superficie lisa donde se distinguen algunos bordes de granos hexagonales. El análisis por EDX confirmó la presencia de silicio y cloruros, además de una relación Ca/P en la superficie de 1.06 y 1.40.

Por el contrario, el núcleo B está constituido principalmente por la fase CPP y las fases minoritarias de cristobalita y fosfato de litio. En consecuencia, su microestructura está formada por granos hexagonales de diferentes tamaños, y cuyo análisis por EDX demostró la presencia de silicio en algunos puntos de la superficie, con una relación Ca/P de 0.93 y 1.09.

Adicionalmente, en la Figura 3 (pág. 112) se presentan los espectros Raman de ambos núcleos, donde se identificaron las vibraciones de los grupos químicos presentes en cada muestra. En el núcleo A se identificaron las bandas vibracionales del grupo PO_4^{3-}. Mientras que en el núcleo B se identificaron las vibraciones características de los grupos P-O-P y PO_3.

Una vez conocidas las características principales de los núcleos, se estudió la influencia de las fases cristalinas de ambos núcleos en las propiedades finales de los andamios multicapa. Para ello se desarrollaron andamios multicapa dopados al 1%, 3% y 10% de magnesio utilizando como base ambos núcleos (A y B).

En primer lugar, se realizó la caracterización de los andamios multicapa obtenidos a partir del núcleo A, recubiertos y dopados al 1% (CoreA-1Mg), 3% (CoreA-3Mg) y 10% (CoreA-10Mg) de magnesio.

En la Figura 4 (pág. 113) se muestran los difractogramas obtenidos para estos andamios (CoreA-XMg), en los cuales se evidencia la formación de una nueva fase cristalina de fosfato cálcio dopado con magnesio ($Ca_{10.115}Mg_{0.385}(PO_4)_7$). Así mismo, también se observó la disminución de la fase de CPP y cloroapatito.

En la Figura 5 (pág. 114) se observa la microestructura de estos andamios estudiada por SEM. En la superficie de los andamios CoreA-1Mg y CoreA-3Mg

se observa placas separadas del recubrimiento sobre la superficie del núcleo, mientras que en la superficie del andamio CoreA-10Mg se observa, en toda la superficie, partículas del recubrimiento.

En cuanto a las propiedades físicas de los andamios, se evaluó la porosidad mediante la técnica de porosimetría de mercurio para el núcleo A y el andamio CoreA-10Mg, como muestra representativa (Figura 6 (pág. 114)). En las curvas se observa que el núcleo A presentó una microporosidad de 57.46% con poros entre 250 μm y 1.7 μm, mientras que el andamio CoreA-10Mg presentó una microporosidad de 65.49% y poros entre 173 μm y 0.5 μm. En relación a la macroporosidad y resistencia a la compresión, el núcleo A presentó un 72.50% con 0.38-1.84 MPa y el andamio CoreA-10Mg 53.29% con 0.40-2.00 MPa.

Finalmente, se evaluó la bioactividad *in vitro* comenzando por el núcleo A, como se muestra en la Figura 7 (pág. 115). En estas imágenes se observa que a partir del día 7, se empieza a disolver la microestructura inicial revelando una estructura con lamelas, sobre la cual empieza a precipitar apatito después de 14 días. Ambas microestructuras (estructura con lamelas y precipitados) siguieron evolucionando hasta los 28 días del ensayo.

Por su parte, los tres andamios dopados con magnesio, presentaron precipitados de apatito en la superficie a los 3 días de inmersión en SBF, permaneciendo hasta los 28 días, como se muestra en la Figura 8 (pág. 116).

Una vez conocido las propiedades y comportamiento *in vitro* de los andamios con el núcleo A, se procedió al estudio de los mismos andamios pero ahora con el núcleo B. Dichos resultados se presentan en el **Artículo 5**.

En la Figura 1 (pág. 124) de este artículo se observan los difractogramas de los andamios dopados con 1% (3D-[Ca/P/Si]-1Mg), 3% (3D-[Ca/P/Si]-3Mg) y 10% (3D-[Ca/P/Si]-10Mg) de magnesio. En estos andamios nuevamente se identificó la fase de fosfato cálcico dopado con magnesio ($Ca_{10.115}Mg_{0.385}(PO_4)_7$).

A continuación, en la Figura 2 (pág. 124) se muestran los espectros obtenidos por FTIR del núcleo B y el andamio 3D-[Ca/P/Si]-10Mg, como muestra representativa de todos los andamios. En estos espectros se identificaron vibraciones de los grupos Si-O-Si, PO_4^{3-}, $P_2O_7^{4-}$, PO_2 y PO.

Seguidamente, se realizó el estudio de la microestructura de los andamios como se muestra en las imágenes de la Figura 3 (pág. 125). En ellas se observa que el núcleo está formado por granos hexagonales, en cuyos bordes se logra identificar una fase vítrea de unión entre cada grano. En cambio, en los andamios multicapa se observan las capas del recubrimiento para el anda-

mio 3D-[Ca/P/Si]-1Mg y a medida que aumenta el porcentaje de dopante se forman partículas de diferentes tamaños y morfologías.

Por su parte, las curvas obtenidas mediante porosimetría de mercurio se observan en la Figura 4 (pág. 125). En este caso el núcleo B presentó poros entre 0.1 μm y 0.004 μm, con una microporosidad total de 23.76 %. Por el contrario, el andamio 3D-[Ca/P/Si]-10Mg presentó una distribución de poros entre 200 μm y 35 μm, y entre 33 μm y 4.5 μm, con una microporosidad de 49.50 %. Por último, la macroporosidad y resistencia a la compresión del núcleo B fue 42% y 2.87 MPa, mientras que el andamio 3D-[Ca/P/Si]-10Mg presentó 34% y 3.38 MPa.

En la Figura 5 se presentan los resultados de la evaluación de la bioactividad *in vitro* del núcleo (pág. 126). Estos resultados muestran que durante el tiempo de ensayo ocurrió degradación de la fase vítrea entre los granos hexagonales, lo que ocasionó el redondeamiento de los bordes. Además, a los 28 días se observó precipitados de silicio en la superficie.

Por otro lado, los distintos comportamientos de los andamios 3D-[Ca/P/Si]-XMg, se observan en la Figura 6 (pág. 127). En este caso, el andamio 3D-[Ca/P/Si]-1Mg presentó precipitados de apatito a los 3 días, sin embargo, se disuelven después de 7 días y se vuelven a formar a partir de los 21 días.

Por su parte, el andamio 3D-[Ca/P/Si]-3Mg después de 7 días revela la microestructura del núcleo. No obstante, a los 14 días se forman precipitados en la superficie, los cuales se disuelven a los 21 días y aparecen de nuevo a los 28 días junto con la revelación de una estructura formada por lamelas.

El andamio 3D-[Ca/P/Si]-10Mg hasta los 7 días se comporta de forma similar al andamio 3D-[Ca/P/Si]-3Mg. Posteriormente, a los 14 y 21 días se forman precipitados con forma de algodón (cotton-like) y después de 28 días desaparecen.

Para finalizar, se realizó el estudio de la variación de los iones en el SBF, cuyas curvas se muestran en la Figura 7 (pág. 128). Para el caso del núcleo, se observó adsorción de calcio y liberación de fósforo al SBF, mientras que el comportamiento de los andamios 3D-[Ca/P/Si]-XMg fue de liberación y adsorción de calcio durante el ensayo, junto con el comportamiento inverso entre el fósforo y el silicio.

4.5 Andamios dopados con hierro, estroncio y magnesio

Una vez estudiada la interacción de los iones por separado en los andamios multicapa (**Artículo 2, 3 y 4**), se procedió a desarrollar nuevos andamios multicapa con el dopaje simultáneo de los iones hierro, estroncio y magnesio. En función de los resultados obtenidos anteriormente, se realizó un dopaje al 3% para cada ion. Adicionalmente, se estudió el efecto de la disposición de los iones dopantes en las propiedades de los andamios multicapa.

En este estudio, se utilizó el núcleo B y los recubrimientos externos se colocaron en dos configuraciones diferentes. En la primera configuración llamada andamio 3J, 3% de los iones de hierro, estroncio y magnesio se colocaron en la misma capa, mientras que en la configuración 2, llamada andamio 3S, 3% de los iones se colocaron en capas separadas.

Los resultados de caracterización, evaluación de la bioactividad y biocompatibilidad *in vitro* de estos andamios multicapa se presentaron en el **Artículo 6**.

En la Figura 1 (pág. 136) de este artículo, se observan los difractogramas del núcleo y los andamios 3J y 3S. Estos resultados confirman que el núcleo está formado principalmente por la fase cristalina de CPP, sin embargo, presentó un leve desplazamiento hacia grados 2θ mayores.

Por su parte, los andamios 3J y 3S mantienen los picos de la fase CPP pero muchos más desplazado hacia la derecha. Esto indica la sustitución de iones de menor tamaño en la red cristalina, como por ejemplo iones de magnesio, esta hipótesis fue confirmada al identificarse la fase de pirofosfato de magnesio ($Mg_2P_2O_7$). También se formaron nuevas fases como silicatos de calcio sustituidos por magnesio, hierro y estroncio ($Ca_{0.1}Fe_{0.6}Mg_{1.3}(SiO_3)_2$ y $Ca_{0.9}Mg_{0.71}Fe_{0.25}(SiO_3)_2$, $Ca_{1.65}Sr_{0.35}(SiO_4)$) y fases de fosfatos cálcicos dopados con hierro, magnesio y litio ($Ca_{9.333}Fe_{1.167}(PO_4)_7$, $Ca_{10.115}Mg_{0.385}(PO_4)_7$, $CaLi(PO_4)$), además de un aumento en los picos de la fase de cristobalita.

Por otro lado, en la Figura 2 (pág. 136) se presentan las microestructuras obtenidas por SEM. Nuevamente se observa en el núcleo los granos típicos de este material, y al recubrirlo, se observan las placas del recubrimiento. En el caso del andamio 3J se puede observar debajo del recubrimiento la microestructura del núcleo, mientras que en el andamio 3S, debajo de las placas del recubrimiento se observa la microestructura del recubrimiento anterior.

En relación a las propiedades física de los andamios, se evaluó la porosidad y la resistencia a la compresión cuyos resultados se muestran en la Figura 3

(pág. 137). En estas curvas se observa que el núcleo presentó una porosidad de 65%, que va disminuyendo con la cantidad de recubrimientos y una resistencia a la compresión de 1.00 ± 0.47 MPa que aumenta hasta 2.74 ± 0.52 MPa en el andamio 3S.

Posteriormente, se evaluó la bioactividad *in vitro* como se muestra en la Figura 4 (pág. 137). En este tipo de andamios se observó que el andamio 3J presentó precipitados de apatito en la superficie después de los 21 días, mientras que el andamio 3S presentó los precipitados desde el día 3.

Los resultados de la variación iónica en SBF se muestra en la Figura 5 (pág. 138). En general, se observó adsorción de calcio y liberación de fósforo, silicio, litio y estroncio. Mientras que la concentración de los iones de hierro y magnesio se mantuvo igual durante el tiempo de estudio, a excepción del andamio 3S después de 21 días cuando experimentó adsorción de magnesio.

Por último, se realizaron los ensayos de biocompatibilidad *in vitro* con células de osteosarcoma MG-63. En este sentido, se realizaron ensayos indirectos en los cuales se estudió la influencia de los iones liberados por los andamios particulados, en el comportamiento de las células. Además, se realizaron ensayos directos de las células en contacto con la superficie de los andamios.

En cuanto a los resultados, el ensayo indirecto mostró que los iones liberados por el núcleo disminuyen el pH del medio, provocando posteriormente la disminución de la viabilidad celular, pero sin efectos citotóxicos, como se muestra en las Figuras 6-9 (pág. 139-141). Por su parte, el análisis de los iones liberados en el medio de cultivo celular (Figura 7 (pág.140)), demostró que el núcleo presenta una fuerte liberación de fósforo y litio y en menor proporción silicio.

Por el contrario, la viabilidad celular de los andamios 3J y 3S aumentó ligeramente respecto al control (células en contacto con medio de cultivo celular original). Del análisis de la variación iónica destaca la liberación de silicio, ya que la variación del resto de los iones no fue significativa en el tiempo de ensayo.

Por otro lado, en el ensayo directo, se observó que la viabilidad celular de los andamios 3J y 3S después de 14 y 21 días aumentó significativamente respecto al núcleo, con un aumento porcentual de más del 100%, como se muestra en la Figura 10 (pág. 141). Adicionalmente, el ensayo de citotoxicidad, cuyos resultados se presentan en la Figura 11 (pág. 142), muestran que el núcleo después de 21 días induce la disminución del número de células, que no ocurre en el caso de los andamios 3J y 3S.

Finalmente, se evaluó la morfología de las células, a través de las imágenes

de microscopía de fluorescencia presentadas en la Figura 12 (pág. 142) y SEM presentada en la Figura 13 (pág. 143). En primer lugar, en los resultados de fluorescencia después de 3 días, se observaron células de forma redonda, algunas individuales y otras formando aglomerados en la superficie del núcleo. Por el contrario, en los andamios 3J y 3S se observaron mayor cantidad de células en la superficie, algunas de ellas expandidas. Además, después de 7 días, en el caso del núcleo, las células continuaron aglomeradas en la superficie, pero en los andamios 3J y 3S, se formaron nuevas colonias de células.

Por último, en el estudio por SEM, se observa que después de 3 días hay células en la superficie del núcleo, pero más en la superficie de los andamios 3J y 3S. Como consecuencia, en la superficie de los andamios 3J y 3S, después de 14 días se formó una capa densa y contínua de células, la cual se densificó mucho más después de 21 días. En el núcleo también se formó una capa contínua de células pero después de los 21 días.

Capítulo 5

Discusión

En este capítulo se realizará una discusión general de los resultados descritos anteriormente, resaltando las características más importantes de los andamios y su contribución en el área de ingeniería de tejido óseo.

Esta disciplina, en la actualidad, se centra cada vez más en buscar opciones que imiten el hueso tanto estructural como funcionalmente, garantizando la restauración de sus funciones y mejorando la calidad de vida de las personas. Es por este motivo, que la presente Tesis Doctoral se ha basado en el desarrollo de andamios multicapa, que surgen como una alternativa de injerto sintético. Estos andamios pretenden cumplir con gran parte de los requerimientos necesarios, para su aplicación en regeneración ósea, evitando así los inconvenientes asociados a los injertos naturales. Además, se propone el uso de una metodología recientemente adaptada, que permite obtener andamios tridimensionales, porosos multicapa, combinando la versatilidad del proceso sol-gel y la técnica de réplica de esponja polimérica.

Partiendo de estas metodologías, el proceso de conformación de los andamios multicapa, se inició con el estudio de varias composiciones químicas, dentro del sistema SiO_2-CaO-P_2O_5-XMO, hasta definir la composición adecuada para el núcleo y los recubrimientos externos. Posteriormente, en función de las propiedades físicas y la bioactividad *in vitro*, se identificó el andamio con la composición SiO_2-$68CaO$-$25P_2O_5$-$6LiO_2$ (% molar) como la opción idónea para el núcleo y la composición $29SiO_2$-$68CaO$-$3P_2O_5$ (% molar) para los recubrimientos externos.

En relación al núcleo, las características más importantes para su selec-

ción fueron la resistencia a la compresión y la porosidad, que destacaron en comparación con otros andamios cerámicos. Por ejemplo, andamios de HA obtenidos mediante réplica de esponja polimérica, presentaron una resistencia a la compresión entre 0.29 y 0.03 MPa, para una porosidad entre 69% y 86% [80, 83, 84].

Adicionalmente, el núcleo presentó estabilidad química debido a las fases cristalinas que lo conforman. A pesar de estar constituido por la fase TCP, conocida por su bioactividad *in vitro* [85], también se identificó la fase CPP, que inhibe la cristalización de apatito *in vitro* debido a los enlaces P-O-P del grupo pirofosfato de su estructura [86, 87]. Este pirofosfato, se conoce por ser un fuerte regulador de la mineralización en el cuerpo, que en presencia de ALP y según la necesidad del cuerpo, se hidroliza y da lugar a grupos fosfatos que producen la mineralización del hueso [88, 89].

Finalmente, la resistencia a la compresión, porosidad y estabilidad química de esta estructura, lo convirtieron en un excelente candidato para el núcleo, ya que al no degradarse rápidamente, funciona como soporte mucho más tiempo para las capas del recubrimiento externo.

Por su parte, las capas externas seleccionadas, destacaron por presentar bioactividad. Esta diferencia respecto al núcleo se debe a la alta concentración de silicio y la disminución de la fase inhibidora. Principalmente, el silicio y sus fases amorfas, benefician la bioactividad debido al intercambio iónico con el SBF, que genera puntos de nucleación para el apatito, según el mecanismo propuesto por Hench [90].

Adicionalmente, la composición química de los recubrimiento se modificó incorporando iones dopantes. Inicialmente se utilizó zinc en dos concentraciones (1% y 30% Zn) y se escogió la composición dopada con menor cantidad debido a la bioactividad mostrada en los tiempos iniciales (incluso mayor respecto a la misma composición sin iones dopantes). Esto demostró que los iones introducidos en la red, aceleran la disolución y generan más puntos de nucleación para la precipitación de apatito. Sin embargo, altas concentraciones de zinc, inhibe la bioactividad al modificar los ángulos de los enlaces P-O-P y formar la fase cristalina $Ca_2ZnSi_2O_7$, que presenta poca disolución y, por tanto, interfiere en el intercambio iónico.

Finalmente, con la estructura del núcleo y la composición dopada con zinc se obtuvo el primer andamio multicapa que combina la estabilidad del núcleo y al mismo tiempo la bioactividad *in vitro*. De esta manera se garantiza una correcta integración del andamio con el tejido huésped, pero también durabilidad mientras se regenera el hueso en la zona afectada. Esto representa un

gran avance, ya que muchos andamios de diferentes tipos de materiales, presentan un excelente comportamiento bioactivo pero se degradan rápidamente, perdiendo efectividad para las aplicaciones de sustitución ósea [91]. Además, estos primeros resultados, destacan de otros andamios realizados, ya que pocos estudios han explorado la obtención de andamios multicapa [92, 93] y, ninguno, utilizando esta metodología.

Posteriormente, a partir de este primer andamio multicapa se empezaron a desarrollar nuevos andamios utilizando otros dopantes. Por ejemplo, el dopaje con estroncio, permitió definir las concentraciones adecuadas para modular la bioactividad. Con esto se logró demostrar que el andamio multicapa sin dopaje presenta bioactividad a los 14 días, mientras que al dopar al 1%, 3% y 10% la bioactividad aparece después de 3 y 7 días. Sin embargo, un dopaje al 25% y 50% disminuyen el comportamiento bioactivo.

Estas variaciones en la bioactividad se atribuyeron a la distorsión en la red cristalina que se genera al sustituir iones de calcio por iones de estroncio con radio iónico mayor [94, 95]. Como consecuencia, esta distorsión provoca la inestabilidad que permite el intercambio iónico con el SBF y desencadena la nucleación de apatito [95, 96]. Sin embargo, al aumentar la concentración de dopante, ocurre igual que con los iones de zinc, se forman fases cristalinas que dificultan su disolución y creación de puntos de nucleación [96].

Una vez conocido las concentraciones de dopante para alcanzar la bioactividad, se realizaron los andamios multicapa dopados con hierro (1% y 3%), observándose dos comportamientos bioactivos diferentes: el andamio dopado al 1% presentó bioactividad variable y el andamios dopado al 3% bioactividad estable en el tiempo. Este comportamiento se atribuye a la diferencia en la cantidad de la fase $Ca_{9.93}Fe_{1.167}(PO_4)_7$, que conduce a un intercambio iónico diferente, logrando estabilizar los precipitados de apatito.

A pesar de que estos comportamientos no fueron confirmados en ensayos *in vivo*, se considera que ambos andamios pueden ser utilizados en diferentes situaciones según el tipo de paciente. Para ello hay que tener en cuenta las diferentes etapas de crecimiento del tejido óseo [97, 98]. En los primeros años de vida los huesos se encuentran poco mineralizados (poca densidad ósea) y van aumentando la densidad debido a los procesos biológicos que se llevan a cabo en la niñez y juventud. Una vez en la etapa adulta, se alcanza el punto máximo de mineralización y, al envejecer, empieza a disminuir la densidad ósea al igual que los procesos biológicos [13, 99-101].

En consecuencia, al ser diferente el hueso de un niño al de un adulto, se puede considerar que el injerto para un niño no debe mineralizarse tan rápido

como el de un adulto. Es por ello que se plantea el uso del andamio con bioactividad variable para el caso de pacientes en edad de crecimiento, ya que se ajusta mejor al hueso adyacente y, junto con los procesos biológicos, alcanzará la mineralización en el momento correcto. Por el contrario, el andamio con bioactividad estable puede ser más apropiado para pacientes adultos, con un hueso completamente mineralizado.

Hasta este punto, se habían desarrollados varios andamios multicapa y se establecieron las cantidades de dopaje iónico para modular la bioactividad *in vitro*. Estos andamios tienen en común que fueron construidos partiendo del mismo núcleo. Sin embargo, posteriormente, gracias a la versatilidad del proceso sol-gel, se pudieron obtener núcleos con diferentes fases cristalinas, partiendo de la misma composición química y variando una de las variables del procesado.

De esta forma, se determinó que el tiempo de calentamiento de la disolución antes de sumergir la esponja de poliuretano, es una de la variables determinante en la formación de las fases cristalinas. El tiempo de calentamiento empleado originalmente fue de 30 minutos y dió como resultado la formación de núcleos con un mezcla de las fases CPP y TCP. Posteriormente, al disminuir el tiempo a 15 minutos se obtuvieron núcleos formados por la fase de CPP y, al aumentar a 1 hora, se obtuvieron núcleos formados por la fase TCP.

Esta diferencia en la formación de una fase cristalina o mezcla de ambas, se debe a la concentración de iones calcio disponibles durante el proceso de condensación de las moléculas hidrolizadas. Esta disponibilidad de calcio está relacionada con la cantidad de agua remanente y depende del tiempo de calentamiento. A menor tiempo de calentamiento se forman dos fases visibles en la disolución, una fase aceitosa que contiene las moléculas hidrolizadas y condensadas, y una fase líquida que corresponde al agua remanente. De esta forma, las moléculas de agua disuelven y solvatan los iones calcio, evitando su interacción con la fase aceitosa y, por tanto, favoreciendo la formación de moléculas con poco calcio como CPP. Por el contrario, si el tiempo de calentamiento es mayor, gran parte del agua se evapora permitiendo la interacción de todas las moléculas con el calcio, favoreciendo la formación de las moléculas de TCP que requieren mayor cantidad de calcio. En definitiva, la ausencia o presencia de calcio determina la formación de las fases, como también fue observado por Zyman et al. [102].

Estos procesos permitieron, por lo tanto, obtener tres núcleos con propiedades totalmente diferentes. Por ejemplo, la resistencia a la compresión, ya que el núcleo de CPP es más resistente que el núcleo de TCP. La bioactividad

también fue diferente en cada núcleo, siendo el núcleo de TCP más bioactivo que el de CPP y la mezcla de ambas fases.

En vista de que la bioactividad es diferente en cada núcleo, se procedió a estudiar andamios multicapa empleando ambos tipos de núcleos y con recubrimientos externos dopados con magnesio.

Estos nuevos andamios a pesar de tener los mismos recubrimientos externos, presentaron una bioactividad *in vitro* diferente. Los andamios con el núcleo de TCP, presentaron bioactividad estable desde el tercer día, mientras que los andamios con el núcleo de CPP, presentaron bioactividad solo en algunos días del ensayo. Esto evidencia que el núcleo de TCP al no presentar el efecto inhibidor del pirofosfato, potencia la bioactividad de los recubrimientos externos. Por su parte, los andamios con el núcleo de CPP también presentaron bioactividad, pero menor en comparación al caso anterior, debido al efecto inhibidor del pirofosfato.

Sin embargo, en los andamios con el núcleo de CPP se observó bioactividad variable (precipitación y disolución de apatito), pudiendo ser atribuido a la fase vítrea observada entre los granos hexagonales de la microestructura. Esto quiere decir, que si bien la bioactividad se activa debido al intercambio iónico del silicio, que genera los primeros puntos de núcleación, la fase vítrea posteriormente comienza a liberar cadenas de $P_2O_7^{4-}$. Estas cadenas de polifosfato generan efecto quelante con los cationes divalentes [103], es decir, reaccionan con el calcio del apatito recientemente precipitado, produciendo la ruptura de la estructura y su disolución. Estos procesos de liberación de silicio y fósforo se producen de forma opuesta y continua en el tiempo, produciendo el efecto de bioactividad variable en la superficie del andamio. Este comportamiento fue corroborado por las curvas de concentración iónica durante el desarrollo del ensayo.

Por último, y una vez conocida la influencia de los tipos de núcleo y las concentraciones de dopaje adecuada, se desarrollaron nuevos andamios multicapa, con dopaje simultáneo de los iones de hierro, estroncio y magnesio. La concentración de dopante seleccionada fue 3% para cada ion, debido a la bioactividad mostrada en los andamios con dopaje individual y, además, para garantizar que el total de los tres iones no superase el 10%, que es el dopaje límite, a partir del cual los andamios pierden la bioactividad. Adicionalmente, estos iones se colocaron en dos formas diferentes (configuración 3J y 3S) para estudiar la influencia de la disposición en el comportamiento general del andamio.

Al realizar los primeros ensayos de caracterización, se identificó que a pesar de que los andamios 3J y 3S presentaban la misma composición química, se

evidenció por XRD que los iones se organizaron formando diferentes fases cristalinas o en distintas proporciones. La causa principal de esta distribución se debe a los tratamientos térmicos realizados a cada andamio, en los cuales se promueve la difusión atómica.

En general, en el procedimiento planteado para la obtención de los andamios multicapa, se estableció que después de cada recubrimiento realizado sobre la base del andamio (núcleo), se debe realizar un tratamiento térmico de sinterización. Como resultado, los andamios con los tres iones dopantes en la misma capa sufrieron un proceso de sinterización, mientras que los andamios con los tres iones en capas separadas sufrieron tres procesos de sinterización (uno por cada capa). Esto significa que los átomos del andamio con los iones dopantes en capas separadas estuvieron expuestos por más tiempo a los procesos de difusión y, por tanto, a un reordenamiento diferente. Además, este andamio al tener dos recubrimientos más respecto al andamio 3J, presentaba mayor cantidad de átomos de silicio, calcio y fósforo.

La mayor cantidad de recubrimientos no solo afectó en las fases cristalinas, sino también en las propiedades físicas como la porosidad y resistencia a la compresión. Los andamios con la configuración 3S al tener mayor cantidad de recubrimientos, presentó menor porosidad, ya que al colocar cada capa se fueron cerrando los poros originales del núcleo. Sin embargo, al disminuir la porosidad aumentó la resistencia a la compresión.

Por otro lado, respecto a la bioactividad *in vitro*, los andamios presentaron comportamientos diferentes. El andamio con la configuración 3J presentó los primeros precipitados de apatito después de 21 días, mientras que el andamio 3S a tan solo 3 días. Esta diferencia se debe a la mayor cantidad de silicio que posee el andamios 3S, al tener dos capas más respecto al andamio 3J. Además de poseer mayor cantidad de fases de TCP y menos CPP, como resultado del reordenamiento llevado a cabo en los procesos de sinterizado.

Como resultado, tanto las fases de silicio como el TCP contribuyen con la rápida precipitación de apatito, debido a los mecanismos previamente descritos, que permiten superar el efecto inhibidor del CPP. En consecuencia, el andamio 3J al presentar más fase CPP que TCP (en comparación con el andamio 3S), su mecanismo de bioactividad *in vitro* se relentiza y queda condicionado únicamente al asociado con la liberación de silicio, según el mecanismo de Hench [90].

Finalmente, se realizó el estudio de biocompatibilidad *in vitro* de los andamios, empleando células de osteosarcoma MG-63. Los ensayos de viabilidad indirectos, donde se estudió la influencia de los iones liberados por los andamios, demostraron que el núcleo tiende a disminuir la viabilidad de las células,

debido principalmente a la disminución del pH. Esta acidificación del medio, se asocia con la ruptura de los enlaces del grupo P-O-P de la molécula de CPP, debido al ataque de las moléculas de agua, formando los grupos $2PO_4^{3-}$ y H^+, siendo este último el responsable de la disminución del pH. Este comportamiento concuerda con los resultados obtenidos en las curvas de concentración iónica del SBF durante el ensayo.

Posteriormente, los ensayos directos de las células en contacto con la superficie de los andamios, indicaron que la viabilidad celular de los andamios 3J y 3S, después de 14 y 21 días, aumentó significativamente respecto al núcleo. Este aumento de aproximadamente 100%, se asocia a la liberación de iones como el silicio y el estroncio principalmente, así como la presencia de los iones de magnesio y hierro.

Adicionalmente, los ensayos de citotoxidad no revelaron efectos negativos de los andamios a excepción del núcleo después de 21 días, pudiendo ser el resultado de la acidificación prolongada del medio. Sin embargo, estos inconvenientes se atribuyen a la alta concentración de moléculas de pirofosfato, ya que otros autores han reportado excelente biocompoatibilidad del CPP a menores concentraciones [104, 105].

En cuanto a la morfología de las células en la superficie, para el caso del núcleo, se observaron pocas células y muchas de ellas redondeadas y aglomeradas. Esta falta de adherencia y proliferación de las células en la superficie se debe, además de a la acidificación local, a la falta de precipitados de apatito que favorezcan la interacción con las células, como también fue observado por Benerjee et al. [85].

Por el contrario, en la superficie de los andamios 3J y 3S, se observó que las células se adhirieron y proliferaron. Muchas de ellas se expandieron desde los primeros días del ensayo, llegando a formar después de 14 días, una capa densa y continúa de células cubriendo toda la superficie. Esta buena interacción entre las células y el material es atribuido principalmente al silicio, conocido por aumentar la proliferación y diferenciación celular [106]. Sin embargo, también se debe considerar el aporte de los iones de hierro, estroncio y magnesio que anteriormente han mostrado biocompatibilidad y efecto positivos en la morfología, proliferación y viabilidad celular [62, 107-109].

En general, se observó una buena interacción de las células con los andamios 3J y 3S, independientemente de la colocación de los iones. Esto quiere decir, que la disposición de los iones en las capas externas solo influyó en la distribución de las fases cristalinas y, por lo tanto, en la velocidad de la bioactividad *in vitro*.

Por otro lado, en relación al núcleo, a pesar de que no mostró un buen desempeño, debido a los efectos negativos, se pudo demostrar que los recubrimientos externos del andamio aportan bioactividad y biocompatibilidad. Pudiendo, incluso, superar el aporte negativo del núcleo y aumentar significativamente la viabilidad del andamio. Además, se espera que *in vivo*, en un medio dinámico, el núcleo no provoque la acidificación prolongada, que afecta a las células, y se regularice el efecto inhibidor del pirofosfato al estar en presencia de la ALP.

Para finalizar, volviendo a las propiedades físicas de los andamios, se observó que cada tipo de estructura presentó una porosidad, distribución de poros y resistencia a la compresión diferentes según el tipo de núcleo y recubrimiento externo. Todos los andamios presentaron características apropiadas en comparación con el hueso trabecular y su estructura jerárquica. En general, todos presentaron macro-, micro- y mesoporos responsables de ciertos procesos durante el crecimiento del hueso. Por ejemplo, los macroporos son necesarios para la colonización y migración de las células a través del andamio, así como también para el suministro de nutrientes, eliminación de residuos y formación de nuevos vasos sanguíneos [40, 52, 110-112]. Por su parte, la meso- y microporosidad permite la retención de proteínas que facilitan la interacción entre el material y las células [52, 110].

En cuanto a la resistencia a la compresión, desde el inicio se evidenció que los andamios obtenidos en este estudio presentan una resistencia superior a otros andamios realizados por técnicas similares [113-115]. Adicionalmente, los valores reportados en este estudio fueron cercanos al límite inferior o dentro del rango reportado para la resistencia a la compresión del hueso trabecular. Según Gibson et al. dicho valor se encuentra entre 0.2 y 4 MPa [116], mientras que Caeiro et al. reporta entre 1.5 y 9.3 MPa, según la zona del cuerpo [117].

Finalmente, en función de lo abordado anteriormente, se puede decir que todos los andamios desarrollados en la presente Tesis Doctoral, presentaron las características requeridas, agrupadas en un sola estructura gracias al diseño multicapa. Especialmente, los andamios multicapa con dopaje simultáneo de los tres iones, destacaron al mostrar los primeros indicios positivos en relación al comportamiento celular. Aunque todavía se debe profundizar en los aspectos biológicos *in vitro*, estos andamios representan una excelente alternativa para futuras aplicaciones en ingeniería de tejido.

Capítulo 6

Conclusiones y Proyecciones Futuras

En este capítulo se expondrán las conclusiones más importantes derivadas de la presente Tesis Doctoral, que responden a los objetivos planteados para esta investigación.

Por último, se presentarán algunas de las proyecciones futuras que se originaron a partir de este estudio, con el objetivo de orientar la investigación a niveles más avanzados de caracterización y así, lograr en el futuro la aplicación clínica de estos materiales.

6.1   Conclusiones

Una de las primeras y más importantes conclusiones derivadas de esta Tesis Doctoral fue la posibilidad de obtener andamios con un diseño innovador, partiendo de una nueva metodología. Esta metodología, plantea combinar el ya usado y conocido método de réplica de esponja polimérica, con el proceso sol-gel modificado, que permite obtener materiales cerámicos a temperaturas relativamente bajas. Adicionalmente, con este método fue posible desarrollar un nuevo diseño de andamios multicapa, combinando en una sola estructura dos o más composiciones químicas diferentes. Esto permitió convertir un núcleo sin bioactividad y biocompatibilidad, pero poroso y con resistencia mecánica cercana al hueso trabecular, en un andamio con todas estas propiedades,

cuyas capas externas aportan o aumentan la bioactividad y la respuesta celular. Estos andamios con diseño multicapa reúnen características que andamios de composición individual no serían capaz de presentar.

Adicionalmente, se confirmó la versatilidad del proceso sol-gel, no solo en la obtención de los andamios multicapa, sino también en la posibilidad de obtener materiales con distintas fases cristalinas, partiendo de la misma composición química. Se concluyó que el tiempo de calentamiento de la disolución sol-gel es una de las variables determinante para la formación de las fases cristalinas.

De esta forma fue posible obtener tres núcleos constituidos por las fases de TCP, CPP y mezcla de ambas. En general, los núcleos se diferenciaron por sus características físicas, pero sobre todo por la diferencia en la bioactividad *in vitro*. Se confirmó que la fase de TCP produce bioactividad, y al actuar como núcleo del andamio multicapa, contribuye al aumento de la bioactividad proporcionada por los recubrimientos externos. Por el contrario, se confirmó el efecto inhibidor *in vitro* de la fase CPP, aunque sigue siendo considerado una buena opción, ya que se espera que *in vivo*, en presencia de la ALP, se produzca su hidrólisis de acuerdo con la necesidad de mineralización del cuerpo. Se concluyó que los núcleos no solo sirven como soporte mecánico para los recubrimientos externos, sino que también influyen en la bioactividad general del andamio.

En relación a los recubrimientos externos, se comprobó que aportan bioactividad debido a la alta concentración de silicio. Adicionalmente, se determinó que la incorporación de los iones dopantes, en bajas concentraciones, aumenta mucho más la bioactividad, debido a la inestabilidad creada en la red cristalinas. Por el contrario, altas concentraciones de iones dopantes, contribuyen a la formación de fases cristalinas estables, que no se disuelven y, en consecuencia, limitan la bioactividad. En base a estos resultados, se concluyó que la cantidad adecuada de iones dopantes en los recubrimientos externos, para garantizar la bioactividad, es entre 1% y 10%.

Por otro lado, en cuanto a las propiedades físicas de los andamios multicapa, se observó que los recubrimientos externos también aportan en el aumento de las propiedades mecánicas, pero disminuyendo la porosidad total.

Otro de los resultados importantes obtenidos en este estudio, fue que los andamios dopados con hierro y magnesio, presentaron tanto comportamiento bioactivo estable como variable en el tiempo. Estos comportamientos se deben a las fases cristalinas que se forman con los iones dopantes o debido a la fase vítrea del núcleo. En base a estos comportamiento, surgió la idea de que estos andamios pueden ser utilizados según la edad del paciente y el grado de mineralización del hueso. Además, este comportamiento de bioactividad variable,

es un resultado innovador que, hasta donde alcanza nuestro conocimiento, no ha sido reportado anteriormente.

Finalmente, los últimos andamios obtenidos en esta investigación (andamios multicapa con dopaje simultáneo), fueron el resultado de todos los hallazgos obtenidos a partir de los andamios anteriores. Se logró desarrollar andamios con dopaje de hierro, estroncio y magnesio en dos configuraciones diferente. Con estos andamios se comprobó que gracias a la diferencia en la cantidad de tratamientos térmicos, los iones se reordenaron de forma distinta. Se concluyó que este cambio en la proporción y tipo de fases, influyen en la bioactividad, siendo el andamio con los tres iones dispuestos en recubrimientos separados, el que presenta bioactividad más temprana, por tener más capas de silicio respecto al andamio con los tres iones en un solo recubrimiento.

Sin embargo, a pesar de la diferencia en la bioactividad, la respuesta celular fue igual en ambos andamios, concluyéndose que los recubrimientos externos aumentan en más del 100% la viabilidad celular. Además, superficialmente mejoran la adherencia y proliferación en comparación con el núcleo, debido principalmente a la liberación de silicio y la presencia de los iones dopantes.

Por último, de acuerdo con todas las características obtenidas por los andamios multicapa, se concluye que estos materiales presentan un gran potencial en el área de ingeniería de tejido óseo y, por lo tanto, es de gran interés la continuidad de su investigación.

6.2 Proyecciones Futuras

En función de los resultados obtenidos y siguiendo con el objetivo final de utilizar estos materiales en aplicaciones de ingeniería de tejido óseo, a continuación se presentan algunos aspectos a considerar en futuros trabajos de investigación.

- En primer lugar, sería adecuado estudiar y optimizar el proceso de obtención de los andamios para lograr desarrollar piezas a mayor escala.

- En segundo lugar, sería idóneo estudiar la factibilidad de sustituir el ácido clorhídrico usado en la preparación del sol-gel, por otros tipos de ácidos y, así, disminuir las posibles complicaciones asociadas con la acidificación *in vitro*.

- En cuanto a las propiedades de los andamios, es necesario realizar un estudio detallado sobre la velocidad de degradación en diferentes medios.

- Por otro lado, sería conveniente realizar un estudio profundo sobre la cinética de formación de las fases cristalinas y amorfas, para entender mejor los mecanismos de interacción e intercambio iónico del material con el medio.

- En relación a los ensayos de bioactividad, en esta investigación únicamente se realizaron en un medio estático. Por esta razón, sería adecuado realizar ensayos en un medio dinámico, para confirmar la bioactividad de los andamios y el comportamiento variable y estable observado en algunos de los materiales.

- La influencia de los iones dopantes en el material también requiere de mayor indagación. Es necesario realizar ensayos en presencia de bacterias, para evaluar posibles efectos antibacterianos aportado por los iones.

- En cuanto a la biocompatibilidad de los andamios, es necesario que sea estudiada de forma más amplia. Sería idóneo realizar ensayos como: evaluación de la diferenciación celular, posibilidad de formar nódulos de mineralización y expresión de marcadores celulares de superficie, para evaluar mejor la interacción entre el material y las células.

- Por último, se plantea la realización de estudios *in vivo*, específicamente en modelos animales para corroborar la efectividad de los andamios multicapa.

Capítulo 7

Conclusions

One of the first and most important conclusions derived from this research was the possibility of obtaining scaffolds with an innovative design, based on a new methodology. This methodology proposes to combine the already used and well known polymeric sponge replication method with the modified sol-gel process, which allows obtaining ceramic materials at relatively low temperatures. Additionally, with this method it was possible to develop a new multilayer scaffold design, combining in a single structure two or more different chemical compositions. This made it possible to convert a core without bioactivity and biocompatibility, but porous and with mechanical strength close to trabecular bone, into a scaffold with all these properties, whose outer layers provide or increase bioactivity and cellular response. These scaffolds with multilayer design bring together features that scaffolds with individual scaffolds of individual composition would not be able to present.

Additionally, the versatility of the sol-gel process was confirmed not only in obtaining multilayer scaffolds, but also in the possibility of obtaining materials with different crystalline phases, starting from the same chemical composition. It was concluded that the heating time of the sol-gel solution is one of the determining variables for the formation of the crystalline phases.

In this way, it was possible to obtain three cores consisting of TCP, CPP and a mixture of both phases. In general, the cores were differentiated by their physical characteristics, but above all by the difference in *in vitro* bioactivity. It was confirmed that the TCP phase produces bioactivity, and by acting as the core of the multilayer scaffold, contributes to the increased bioactivity

provided by the external coatings. On the contrary, the *in vitro* inhibitory effect of the CPP phase was confirmed, although it is still considered a good option, since *in vivo*, in the presence of ALP, its hydrolysis is expected to occur according to the body's need for mineralization. Finally, it was concluded that the cores not only serve as mechanical support for the external coatings, but also influence the overall bioactivity of the scaffold.

In relation to the external coatings, it was found that they provide bioactivity due to the high concentration of silicon. Additionally, it was determined that the incorporation of dopant ions, in low concentrations, increases bioactivity, due to the instability created in the crystalline network. In contrast, high concentrations of dopant ions, contribute to the formation of stable crystalline phases, which do not dissolve and, consequently, limit bioactivity. Based on these results, it was concluded that the appropriate amount of dopant ions in external coatings, to ensure bioactivity, is between 1 % and 10 %.

On the other hand, regarding the physical properties of the multilayer scaffolds, it was observed that the external coatings also contribute to the increase of the mechanical properties, but decreasing the total porosity of the scaffolds.

Other important results obtained in this study were that the iron and magnesium doped scaffolds, presented stable and time-varying bioactive behavior. These behaviors are due to the crystalline phases formed with the dopant ions or due to the glassy phase of the core. Based on these behaviors, it was suggested that these scaffolds can be used according to the age of the patient and the degree of bone mineralization. Moreover, this variable bioactivity behavior is an innovative result that, to the best of our knowledge, has not been reported before.

Finally, the last scaffolds obtained in this research (multilayer scaffolds with simultaneous doping), were the result of all the findings obtained from the previous scaffolds. In this case, it was possible to develop scaffolds with iron, strontium and magnesium doping in two different configurations. With these scaffolds it was found that due to the difference in the number of heat treatments, the ions were rearranged differently. It was concluded that this change in the proportion and type of phases, influences the bioactivity, being the scaffold with the three ions arranged in separate coatings, the one that presents earlier bioactivity, because it has more silicon layers with respect to the scaffold with the three ions in a single coating.

However, despite the difference in bioactivity, the cellular response was equal in both scaffolds and, concluding that the external coatings increase cell viability by more than 100 %. In addition, superficially both scaffolds improve

adhesion and proliferation compared to the core, mainly due to the release of silicon and the presence of dopant ions.

Finally, according to all the characteristics obtained by the multilayer scaffolds, it is concluded that these materials present a great potential in the area of bone tissue engineering and, therefore, it is of great interest the continuity of their research.

Bibliografía

[1] Blyth, F. M. y Noguchi, N., «Chronic musculoskeletal pain and its impact on older people,» *Best Practice and Research: Clinical Rheumatology*, vol. 31, n.º 2, págs. 160-168, 2017.

[2] Ingram, M. y Symmons, D. P. M., «The burden of musculoskeletal conditions,» *Medicine*, vol. 46, n.º 3, págs. 152-155, 2018.

[3] Pawelec, K. M., «Introduction to the challenges of bone repair,» en *Bone Repair Biomaterials*, K. M. Pawelec y J. A. Planell, eds., Segunda ed, Woodhead Publishing, 2019, cap. 1, págs. 1-13.

[4] Bilgiç, E., Boyacıoğlu, Ö., Gizer, M., Korkusuz, P. y Korkusuz, F., «Architecture of bone tissue and its adaptation to pathological conditions,» en *Comparative Kinesiology of the Human Body*, A. Salih e I. E. Şimşek, eds., Academic Press, 2020, cap. 6, págs. 71-90.

[5] Brown, J. L. y Laurencin, C. T., «Bone Tissue Engineering,» en *Biomaterials Science*, W. R. Wagner, S. E. Sakiyama-Elbert, G. Zhang y M. J. Yaszemski, eds., Cuarta Ed, Academic Press, 2019, cap. 2.6.6, págs. 1373-1388.

[6] Li, G. y Niu, W., «Challenges toward musculoskeletal injuries and diseases,» en *Nanoengineering in Musculoskeletal Regeneration*, M. Razavi, ed., Academic Press, 2020, cap. 1, págs. 1-41.

[7] Briggs, A. M., Cross, M. J., Hoy, D. G., Sànchez-Riera, L., Blyth, F. M., Woolf, A. D. y March, L., «Musculoskeletal Health Conditions Represent a Global Threat to Healthy Aging: A Report for the 2015 World Health Organization World Report on Ageing and Health,» *Gerontologist*, vol. 56, S243-S255, 2016.

[8]   Briggs, A. M., Woolf, A. D., Dreinhöfer, K., Homb, N., Hoy, D. G., Kopansky-Giles, D., Åkesson, K. y March, L., «Reducing the global burden of musculoskeletal conditions,» *Bulletin of the World Health Organization*, vol. 96, n.º 5, págs. 366-368, 2018.

[9]   Briggs, A. M., Shiffman, J., Shawar, Y. R., Åkesson, K., Ali, N. y Woolf, A. D., «Global health policy in the 21st century: Challenges and opportunities to arrest the global disability burden from musculoskeletal health conditions,» *Best Practice Research Clinical Rheumatology*, vol. 34, n.º 5, 2020.

[10] «The Burden of Musculoskeletal Diseases in the United States,» *The United States Bone and Joint Initiative (USBJI)*, vol. 3, 2016.

[11] Gosselin, R. A., Conway, D. J., Phillips, J. J. y Coughlin, R. R., «Diseases of the Musculoskeletal System,» en *Hunter's Tropical Medicine and Emerging Infectious Diseases*, E. T. Ryan, David R. Hil, T. Solomon, N. E. Aronson y T. P. Endy, eds., Décima Edi, Elsevier, 2020, cap. 13, págs. 114-119.

[12] Cieza, A., Causey, K., Kamenov, K., Hanson, S. W., Chatterji, S. y Vos, T., «Global estimates of the need for rehabilitation based on the Global Burden of Disease study 2019: a systematic analysis for the Global Burden of Disease Study 2019,» *The Lancet*, vol. 396, n.º 10267, págs. 2006-2017, 2020.

[13] Iuliano, S. e Hill, T. R., «Dairy foods and bone accrual during growth and development,» en *Milk and Dairy Foods*, D. I. Givens, ed., Academic Press, 2020, cap. 11, págs. 299-322.

[14] Borgström, F. y col., «Fragility fractures in Europe: burden, management and opportunities,» *Archives of Osteoporosis*, vol. 15, n.º 1, 2020.

[15] Kanis, J. A., Odén, A., McCloskey, E. V., Johansson, H., Wahl, D. A. y Cooper, C., «A systematic review of hip fracture incidence and probability of fracture worldwide,» *Osteoporosis International*, vol. 23, n.º 9, págs. 2239-2256, 2012.

[16] Ojeda-Thies, C. y col., «Spanish National Hip Fracture Registry (RNFC): analysis of its first annual report and international comparison with other established registries,» *Osteoporosis International*, vol. 30, págs. 1243-1254, 2019.

[17] Bartra, A., Caeiro, J.-R., Mesa-Ramos, M., Etxebarría-Foronda, I., Montejo, J., Carpintero, P., Sorio-Vilela, F., Gatell, S. y Canals, L., «Cost of osteoporotic hip fracture in Spain per Autonomous Region,» *Revista Española de Cirugía Ortopédica y Traumatología*, vol. 63, n.º 1, págs. 56-68, 2019.

[18] Napoli, N., Elderkin, A. L., Kiel, D. P. y Khosla, S., «Managing fragility fractures during the COVID-19 pandemic,» *Nature Reviews Endocrinology*, vol. 16, n.º 9, págs. 467-468, 2020.

[19] Spruyt, D., Gillet, C. y Rasschaert, J., «Bone and bone marrow; interactions,» *Encyclopedia of Endocrine Diseases*, vol. 4, págs. 31-39, 2018.

[20] Jones, J. R., Lee, P. D. y Hench, L. L., «Hierarchical porous materials for tissue engineering,» *Philosophical Transactions of the Royal Society A: Mathematical, Physical and Engineering Sciences*, vol. 364, n.º 1838, págs. 263-281, 2006.

[21] Raghavendra, G. M., Varaprasad, K. y Jayaramudu, T., «Biomaterials: Design, Development and Biomedical Applications,» en *Nanotechnology Applications for Tissue Engineering*, S. Thomas, Y. Grohens y N. Ninan, eds., William Andrew Publishing, 2015, págs. 21-44.

[22] Belleghem, S. M. V., Mahadik, B., Snodderly, K. L. y Fisher, J. P., «Overview of Tissue Engineering Concepts and Applications,» en *Biomaterials Science*, W. R. Wagner, S. E. Sakiyama-Elbert, G. Zhang y M. J. Yaszemski, eds., Cuarta Ed, Academic Press, 2020, cap. 2.6.2, págs. 1289-1316.

[23] Verma, P. y Verma, V., «Concepts of tissue engineering,» en *Animal Biotechnology*, Ashish S. Verma y A. Singh, eds., Segunda ed, Academic Press, 2020, cap. 15, págs. 295-307.

[24] Chandra, P. K., Soker, S. y Atala, A., «Tissue engineering: current status and future perspectives,» en *Principles of Tissue Engineering*, R. Lanza, R. Langer, J. P. Vacanti y A. Atala, eds., Quinta ed., Academic Press, 2020, cap. 1, págs. 1-35.

[25] Dzobo, K., Thomford, N. E., Senthebane, D. A., Shipanga, H., Rowe, A., Dandara, C., Pillay, M. y Motaung, K. S. C. M., «Advances in regenerative medicine and tissue engineering: Innovation and transformation of medicine,» *Stem Cells International*, 2018.

[26] Alonzo, M., Alvarez Primo, F., Anil Kumar, S., Mudloff, J. A., Dominguez, E., Fregoso, G., Ortiz, N., Weiss, W. M. y Joddar, B., «Bone tissue engineering techniques, advances, and scaffolds for treatment of bone defects,» *Current Opinion in Biomedical Engineering*, vol. 17, pág. 100 248, 2021.

[27] Eliaz, N. y Metoki, N., «Calcium phosphate bioceramics: A review of their history, structure, properties, coating technologies and biomedical applications,» *Materials*, vol. 10, n.º 4, 2017.

[28] Wang, X., Xu, S., Zhou, S., Xu, W., Leary, M., Choong, P., Qian, M., Brandt, M. y Xie, Y. M., «Topological design and additive manufacturing of porous metals for bone scaffolds and orthopaedic implants: A review,» *Biomaterials*, vol. 83, págs. 127-141, 2016.

[29] Polo-Corrales, L., Latorre-Esteves, M. y Ramirez-Vick, J. E., «Scaffold design for bone regeneration,» *Journal of Nanoscience and Nanotechnology*, vol. 14, n.º 1, págs. 15-56, 2014.

[30] Martinez-Marquez, D., Delmar, Y., Sun, S. y Stewart, R. A., «Exploring macroporosity of additively manufactured titanium metamaterials for bone regeneration with quality by design: A systematic literature review,» *Materials*, vol. 13, n.º 21, págs. 1-44, 2020.

[31] Wubneh, A., Tsekoura, E. K., Ayranci, C. y Uludağ, H., «Current state of fabrication technologies and materials for bone tissue engineering,» *Acta Biomaterialia*, vol. 80, págs. 1-30, 2018.

[32] Li, J. J., Kaplan, D. L. y Zreiqat, H., «Scaffold-based regeneration of skeletal tissues to meet clinical challenges,» *Journal of Materials Chemistry B*, vol. 2, n.º 42, págs. 7272-7306, 2014.

[33] Wang, W. y Yeung, K. W., «Bone grafts and biomaterials substitutes for bone defect repair: A review,» *Bioactive Materials*, vol. 2, n.º 4, págs. 224-247, 2017.

[34] Ho-Shui-Ling, A., Bolander, J., Rustom, L. E., Johnson, A. W., Luyten, F. P. y Picart, C., «Bone regeneration strategies: Engineered scaffolds, bioactive molecules and stem cells current stage and future perspectives,» *Biomaterials*, vol. 180, págs. 143-162, 2018.

[35] Bose, S. y Bandyopadhyay, A., «Introduction to Biomaterials,» en *Characterization of Biomaterials*, A. Bandyopadhyay y S. Bose, eds., Academic Press, 2013, cap. 1, págs. 1-9.

[36] Dimitriou, R., Jones, E., McGonagle, D. y Giannoudis, P. V., «Bone regeneration: current concepts and future directions,» *BMC Medicine*, vol. 9, n.º 1, pág. 66, 2011.

[37]   Dorozhkin, S. V., «Biocomposites and hybrid biomaterials based on calcium orthophosphates,» *Biomatter*, vol. 1, n.º 1, págs. 3-56, 2011.

[38]   Przekora, A., «The summary of the most important cell-biomaterial interactions that need to be considered during in vitro biocompatibility testing of bone scaffolds for tissue engineering applications,» *Materials Science and Engineering C*, vol. 97, págs. 1036-1051, 2019.

[39]   Bose, S., Fielding, G., Tarafder, S. y Bandyopadhyay, A., «Understanding of dopant-induced osteogenesis and angiogenesis in calcium phosphate ceramics,» *Trends in Biotechnology*, vol. 31, n.º 10, págs. 594-605, 2013.

[40]   Vallet-Regi, M., *BioCeramics with Clinical Applications*. Chichester, UK: John Wiley Sons, 2014.

[41]   Kuhn, L. T., «Biomaterials,» en *Introduction to Biomedical Engineering*, J. D. Enderle, S. M. Blanchard y J. D. Bronzino, eds., Segunda Ed, Academic Press, 2005, cap. 6, págs. 255-312.

[42]   Ratner, B. D., Hoffman, A. S., Schoen, F. J. y Lemons, J. E., «Biomaterials Science : An Evolving , Multidisciplinary Endeavor,» en *Biomaterials Science: An Introduction to Materials in Medicine*, B. D. Ratner, A. S. Hoffman, F. J. Schoen y J. E. Lemons, eds., Tercera ed, Academic Press, 2013, págs. xxv-xxxix.

[43]   Nikolova, M. P. y Chavali, M. S., «Recent advances in biomaterials for 3D scaffolds: A review,» *Bioactive Materials*, vol. 4, págs. 271-292, 2019.

[44]   Navarro, M., Michiardi, A., Castan, O. y Planell, J. A., «Biomaterials in orthopaedics,» *Journal of the Royal Society Interface*, vol. 5, págs. 1137-1158, 2008.

[45]   Yu, X., Tang, X., Gohil, S. V. y Laurencin, C. T., «Biomaterials for Bone Regenerative Engineering,» *Advanced Healthcare Materials*, vol. 4, n.º 9, págs. 1268-1285, 2015.

[46]   De Aza, P. N., De Aza, A. H. y De Aza, S., «Crystalline Bioceramic Materials,» *Boletin de la Sociedad Espanola de Ceramica y Vidrio*, vol. 44, n.º 3, págs. 135-145, 2005.

[47]   Pina, S., Reis, R. L. y Oliveira, J. M., «Ceramic biomaterials for tissue engineering,» en *Fundamental Biomaterials: Ceramics*, S. Thomas, P. Balakrishnan y M. Sreekala, eds., Woodhead Publishing, 2018, cap. 4, págs. 95-116.

[48]   Yang, Y., Kang, Y., Sen, M. y Park, P., «Biomaterials for tissue engi-
       neering,» en *Biomaterials for Tissue Engineering Applications*, J. Bur-
       dick y R. Mauck, eds., Vienna: Springer, 2011, cap. 7, págs. 1-564.

[49]   Ben-Nissan, B., «Biomimetics and Bioceramics,» *Learning from Nature
       How to Design New Implantable Biomaterialsis*, vol. 171, págs. 89-103,
       2004.

[50]   Dorozhkin, S. V., «Current state of bioceramics,» *Journal of Ceramic
       Science and Technology*, vol. 9, n.º 4, págs. 353-370, 2018.

[51]   Vasant, S. R. y Joshi, M. J., «A review on calcium pyrophosphate and
       other related phosphate nano bio-materials and their applications,»
       Reviews on Advanced Materials Science, vol. 49, n.º 1, págs. 44-57,
       2017.

[52]   Ginebra, M. P., Espanol, M., Maazouz, Y., Bergez, V. y Pastorino, D.,
       «Bioceramics and bone healing,» *EFORT Open Reviews*, vol. 3, n.º 5,
       págs. 173-183, 2018.

[53]   Hoppe, A., Güldal, N. S. y Boccaccini, A. R., «A review of the biological
       response to ionic dissolution products from bioactive glasses and glass-
       ceramics,» *Biomaterials*, vol. 32, n.º 11, págs. 2757-2774, 2011.

[54]   Shepherd, J. H., Shepherd, D. V. y Best, S. M., «Substituted hydrox-
       yapatites for bone repair,» *Journal of Materials Science: Materials in
       Medicine*, vol. 23, n.º 10, págs. 2335-2347, 2012.

[55]   Ribas, R. G., Schatkoski, V. M., Montanheiro, T. L. d. A., Mene-
       zes, B. R. C. de, Stegemann, C., Leite, D. M. G. y Thim, G. P.,
       «Current advances in bone tissue engineering concerning ceramic and
       bioglass scaffolds: A review,» *Ceramics International*, vol. 45, n.º 17,
       págs. 21 051-21 061, 2019.

[56]   Ros-Tárraga, P., Mazón, P., Rodríguez, M. A., Meseguer-Olmo, L.
       y De Aza, P. N., «Novel resorbable and osteoconductive calcium sili-
       cophosphate scaffold induced bone formation,» *Materials*, vol. 9, n.º 9,
       págs. 1-15, 2016.

[57]   Arango-Ospina, M., Nawaza, Q. y Boccaccini, A. R., «Silicate-based
       nanoceramics in regenerative medicine,» en *Nanostructured Biomate-
       rials for Regenerative Medicine*, V. Guarino, M. Iafisco y S. Spriano,
       eds., primera ed, Woodhead Publishing, 2019, cap. 9, págs. 255-273.

[58] Schatkoski, V. M., Larissa do Amaral Montanheiro, T., Canuto de Menezes, B. R., Pereira, R. M., Rodrigues, K. F., Ribas, R. G., Morais da Silva, D. y Thim, G. P., «Current advances concerning the most cited metal ions doped bioceramics and silicate-based bioactive glasses for bone tissue engineering,» *Ceramics International*, vol. 47, n.º 3, págs. 2999-3012, 2021.

[59] Lin, S. H., Zhang, W. J. y Jiang, X. Q., «Applications of Bioactive Ions in Bone Regeneration,» *The Chinese journal of dental research : the official journal of the Scientific Section of the Chinese Stomatological Association (CSA)*, vol. 22, n.º 2, págs. 93-104, 2019.

[60] Boanini, E., Gazzano, M. y Bigi, A., «Ionic substitutions in calcium phosphates synthesized at low temperature,» *Acta Biomaterialia*, vol. 6, n.º 6, págs. 1882-1894, 2010.

[61] Lieu, P. T., Heiskala, M., Peterson, P. A. y Yang, Y., «The roles of iron in health and disease,» *Molecular Aspects of Medicine*, vol. 22, n.º 1-2, págs. 1-87, 2001.

[62] Singh, R. K., Srivastava, M., Prasad, N. K., Awasthi, S., Dhayalan, A. y Kannan, S., «Iron doped β-Tricalcium phosphate: Synthesis, characterization, hyperthermia effect, biocompatibility and mechanical evaluation,» *Materials Science and Engineering C*, vol. 78, págs. 715-726, 2017.

[63] Zhao, C. Q., Xu, X. C., Lu, Y. J., Wu, S. Q., Xu, Z. Y., Huang, T. T. y Lin, J. X., «Doping lithium element to enhance compressive strength of β-TCP scaffolds manufactured by 3D printing for bone tissue engineering,» *Journal of Alloys and Compounds*, vol. 814, 2020.

[64] Thavornyutikarn, B., Chantarapanich, N., Sitthiseripratip, K., Thouas, G. A. y Chen, Q., *Bone tissue engineering scaffolding: computer-aided scaffolding techniques*, 2-4. 2014, vol. 3, págs. 61-102.

[65] Bose, S., Roy, M. y Bandyopadhyay, A., «Recent advances in bone tissue engineering scaffolds,» *Trends in Biotechnology*, vol. 30, n.º 10, págs. 546-554, 2012.

[66] Zhu, T., Cui, Y., Zhang, M., Zhao, D., Liu, G. y Ding, J., «Engineered three-dimensional scaffolds for enhanced bone regeneration in osteonecrosis,» *Bioactive Materials*, vol. 5, n.º 3, págs. 584-601, 2020.

[67] Roseti, L., Parisi, V., Petretta, M., Cavallo, C., Desando, G., Bartolotti, I. y Grigolo, B., «Scaffolds for Bone Tissue Engineering: State of the art and new perspectives,» *Materials Science and Engineering C*, vol. 78, págs. 1246-1262, 2017.

[68] Singh, L. P., Bhattacharyya, S. K., Kumar, R., Mishra, G., Sharma, U., Singh, G. y Ahalawat, S., «Sol-Gel processing of silica nanoparticles and their applications,» *Advances in Colloid and Interface Science*, vol. 214, págs. 17-37, 2014.

[69] Carballo Suárez, L. y Galindo V., H., «Estudio de los procesos Sol-gel para la obtención de un aglutinante apropiado para el peletizado de alúmina. 1. Ensayos de una técnica de peletizado,» *Ingeniería e Investigación*, vol. 48, págs. 57-63, 2001.

[70] Phulé, P. y Wood, T., «Ceramics and Glasses, Sol–Gel Synthesis of,» en *Encyclopedia of Materials: Science and Technology*, K. J. Buschow, R. W. Cahn, M. C. Flemings, B. Ilschner, E. J. Kramer, S. Mahajan y P. Veyssière, eds., Elsevier, 2001, págs. 1090-1095.

[71] Schubert, U., «Part One Sol – Gel Chemistry and Methods,» en *The Sol-Gel Handbook: Synthesis, Characterization and Applications*, D. Levy y M. Zayat, eds., Wiley-VCH Verlag GmbH Co. KGaA, 2015, págs. 1-28.

[72] Owens, G. J., Singh, R. K., Foroutan, F., Alqaysi, M., Han, C. M., Mahapatra, C., Kim, H. W. y Knowles, J. C., «Sol-gel based materials for biomedical applications,» *Progress in Materials Science*, vol. 77, págs. 1-79, 2016.

[73] Zarzycki, J., «Past and Present of Sol-Gel Science and Technology,» *Journal of Sol-Gel Science and Technology*, vol. 8, n.º 1-3, págs. 17-22, 1997.

[74] Brinker, C. y Scherer, G., *Sol-Gel Science*, Academic P. Academic Press, 1990.

[75] Landau, M. V., «Sol-Gel Process,» en *Handbook of Heterogeneous Catalysis*, G. Ertl, H. Knözinger, F. Schüth y J. Weitkamp, eds., Weinheim, Germany: Wiley-VCH Verlag GmbH Co. KGaA, 2008, cap. 2.3.4.

[76] Hench, L. L. y West, J. O. N. K., «The Sol-Gel Process,» *Chem. Rev.*, vol. 90, n.º 1, págs. 33-72, 1990.

[77] Chen, Q. Z., Thompson, I. D. y Boccaccini, A. R., «45S5 Bioglass®-derived glass-ceramic scaffolds for bone tissue engineering,» *Biomaterials*, vol. 27, n.º 11, págs. 2414-2425, 2006.

[78] Imani, S. M., Rabiee, S. M., Goudarzi, A. M. y Dardel, M., «A novel modification for polymer sponge method to fabricate the highly porous composite bone scaffolds with large aspect ratio suitable for repairing critical-sized bone defects,» *Vacuum*, vol. 176, pág. 109 316, 2020.

[79] Tian, J. y Tian, J., «Preparation of porous hydroxyapatite,» *Journal of Materials Science*, vol. 36, págs. 3061-3066, 2001.

[80] Ramay, H. R. y Zhang, M., «Preparation of porous hydroxyapatite scaffolds by combination of the gel-casting and polymer sponge methods,» *Biomaterials*, vol. 24, n.º 19, págs. 3293-3302, 2003.

[81] Wang, C., Chen, H., Zhu, X., Xiao, Z., Zhang, K. y Zhang, X., «An improved polymeric sponge replication method for biomedical porous titanium scaffolds,» *Materials Science and Engineering C*, vol. 70, págs. 1192-1199, 2017.

[82] Kokubo, T. y Takadama, H., «How useful is SBF in predicting in vivo bone bioactivity?» *Biomaterials*, vol. 27, n.º 15, págs. 2907-2915, 2006.

[83] Kim, H. W., Knowles, J. C. y Kim, H. E., «Hydroxyapatite porous scaffold engineered with biological polymer hybrid coating for antibiotic Vancomycin release,» *Journal of Materials Science: Materials in Medicine*, vol. 16, n.º 3, págs. 189-195, 2005.

[84] Miao, X., Lim, G., Loh, K. y Boccaccini, A. R., «Preparation and characterisation of calcium phosphate bone cement,» *Mater. Process. Prop. Perform.*, vol. 3, págs. 319-324, 2004.

[85] Banerjee, S. S., Bandyopadhyay, A. y Bose, S., «Biphasic resorbable calcium phosphate ceramic for bone implants and local alendronate delivery,» *Advanced Engineering Materials*, vol. 12, n.º 5, págs. 148-155, 2010.

[86] Fleisch, H. y Bisaz, S., «Mechanism of calcification: Inhibitory role of pyrophosphate,» *Nature*, vol. 195, n.º 4844, pág. 911, 1962.

[87] Fleisch, H., Maerki, J. y Russell, R. G. G., «Effect of Pyrophosphate on Dissolution of Hydroxyapatite and Its Possible Importance in Calcium Homeostasis.,» *Experimental Biology and Medicine*, vol. 122, n.º 2, págs. 317-320, 1966.

[88] Grover, L. M., Wright, A. J., Gbureck, U., Bolarinwa, A., Song, J., Liu, Y., Farrar, D. F., Howling, G., Rose, J. y Barralet, J. E., «The effect of amorphous pyrophosphate on calcium phosphate cement resorption and bone generation,» *Biomaterials*, vol. 34, n.º 28, págs. 6631-6637, 2013.

[89] Orriss, I. R., Arnett, T. R. y Russell, R. G. G., «Pyrophosphate: A key inhibitor of mineralisation,» *Current Opinion in Pharmacology*, vol. 28, págs. 57-68, 2016.

[90]   Hench, L. L., «Bioceramics: from concept to clinic. J Am Ceram Soc. 1993;72:93-98.,» *Journal of the American Ceramic Society*, vol. 74, págs. 1487-1510, 1991.

[91]   Chen, Q., Zhu, C. y Thouas, G. A., «Progress and challenges in biomaterials used for bone tissue engineering: bioactive glasses and elastomeric composites,» *Progress in Biomaterials*, vol. 1, n.º 1, pág. 2, 2012.

[92]   Jun, I. K., Song, J. H., Choi, W. Y., Koh, Y. H., Kim, H. E. y Kim, H. W., «Porous hydroxyapatite scaffolds coated with bioactive apatite-wollastonite glass-ceramics,» *Journal of the American Ceramic Society*, vol. 90, n.º 9, págs. 2703-2708, 2007.

[93]   Neto, A. S., Brazete, D. y Ferreira, J. M., «Cuttlefish bone-derived biphasic calcium phosphate scaffolds coated with sol-gel derived bioactive glass,» *Materials*, vol. 12, n.º 7, 2019.

[94]   Hesaraki, S., Gholami, M., Vazehrad, S. y Shahrabi, S., «The effect of Sr concentration on bioactivity and biocompatibility of sol-gel derived glasses based on CaO-SrO-SiO2-P2O5 quaternary system,» *Materials Science and Engineering C*, vol. 30, n.º 3, págs. 383-390, 2010.

[95]   Fredholm, Y. C., Karpukhina, N., Brauer, D. S., Jones, J. R., Law, R. V. e Hill, R. G., «Influence of strontium for calcium substitution in bioactive glasses on degradation, ion release and apatite formation,» *Journal of the Royal Society Interface*, vol. 9, n.º 70, págs. 880-889, 2012.

[96]   Maçon, A. L., Lee, S., Poologasundarampillai, G., Kasuga, T. y Jones, J. R., «Synthesis and dissolution behaviour of CaO/SrO-containing sol–gel-derived 58S glasses,» *Journal of Materials Science*, vol. 52, n.º 15, págs. 8858-8870, 2017.

[97]   Del Rio, L., Carrascosa, A., Pons, F., Gusinyé, M., Yeste, D. y Domenech, F. M., «Bone mineral density of the lumbar spine in white mediterranean Spanish children and adolescents: Changes related to age, sex, and puberty,» *Pediatric Research*, vol. 35, n.º 3, págs. 362-366, 1994.

[98]   Lafita, J., «Fisiología y fisiopatología ósea,» *Anales del Sistema Sanitario de Navarra*, vol. 26, n.º 3, págs. 7-17, 2003.

[99]   Davies, J. H., Evans, B. A. y Gregory, J. W., «Bone mass acquisition in healthy children,» *Archives of Disease in Childhood*, vol. 90, n.º 4, págs. 373-378, 2005.

[100] Levine, M. A., «Assessing bone health in children and adolescents.,» *Indian journal of endocrinology and metabolism*, vol. 16, n.º 2, págs. 205-212, 2012.

[101] Saggese, G., Baroncelli, G. I. y Bertelloni, S., «Puberty and bone development,» *Best Practice and Research: Clinical Endocrinology and Metabolism*, vol. 16, n.º 1, págs. 53-64, 2002.

[102] Zyman, Z. Z., Goncharenko, A. V. y Rokhmistrov, D. V., «Phase evolution during heat treatment of amorphous calcium phosphate derived from fast nitrate synthesis,» *Processing and Application of Ceramics*, vol. 11, n.º 2, págs. 147-153, 2017.

[103] Gao, H., Tan, T. y Wang, D., «Dissolution mechanism and release kinetics of phosphate controlled release glasses in aqueous medium,» *Journal of Controlled Release*, vol. 96, n.º 1, págs. 29-36, 2004.

[104] Alsubhe, E., Anastasiou, A. D., Mehrabi, M., Raif, E. M., Hassanpour, A., Giannoudis, P. y Jha, A., «Analysis of the osteogenic and mechanical characteristics of iron (Fe2+/Fe3+)-doped β-calcium pyrophosphate,» *Materials Science and Engineering C*, vol. 115, pág. 111 053, 2020.

[105] Anastasiou, A. D. y col., «β-pyrophosphate: A potential biomaterial for dental applications,» *Materials Science and Engineering C*, vol. 75, págs. 885-894, 2017.

[106] Han, P., Wu, C. y Xiao, Y., «The effect of silicate ions on proliferation, osteogenic differentiation and cell signalling pathways (WNT and SHH) of bone marrow stromal cells,» *Biomaterials Science*, vol. 1, n.º 4, págs. 379-392, 2013.

[107] Gu, Y., Zhang, J., Zhang, X., Liang, G., Xu, T. y Niu, W., «Three-dimensional Printed Mg-Doped β-TCP Bone Tissue Engineering Scaffolds: Effects of Magnesium Ion Concentration on Osteogenesis and Angiogenesis In Vitro,» *Tissue Engineering and Regenerative Medicine*, vol. 16, n.º 4, págs. 415-429, 2019.

[108] Xing, M., Wang, X., Wang, E., Gao, L. y Chang, J., «Bone tissue engineering strategy based on the synergistic effects of silicon and strontium ions,» *Acta Biomaterialia*, vol. 72, págs. 381-395, 2018.

[109] Vahabzadeh, S. y Bose, S., «Effects of Iron on Physical and Mechanical Properties, and Osteoblast Cell Interaction in β-Tricalcium Phosphate,» *Annals of Biomedical Engineering*, vol. 45, n.º 3, págs. 819-828, 2017.

[110] Perez, R. A. y Mestres, G., «Role of pore size and morphology in musculo-skeletal tissue regeneration,» *Materials Science and Engineering C*, vol. 61, págs. 922-939, 2016.

[111] Hing, K. A., «Bioceramic bone graft substitutes: Influence of porosity and chemistry,» *International Journal of Applied Ceramic Technology*, vol. 2, n.º 3, págs. 184-199, 2005.

[112] Karageorgiou, V. y Kaplan, D., «Porosity of 3D biomaterial scaffolds and osteogenesis,» *Biomaterials*, vol. 26, n.º 27, págs. 5474-5491, 2005.

[113] Ros-Tárraga, P., Murciano, A., Mazón, P., Gehrke, S. A. y De Aza, P. N., «New 3D stratified Si-Ca-P porous scaffolds obtained by sol-gel and polymer replica method: Microstructural, mineralogical and chemical characterization,» *Ceramics International*, vol. 43, n.º 8, págs. 6548-6553, 2017.

[114] Ros-Tárraga, P., Murciano, Á., Mazón, P., Gehrke, S. A. y De Aza, P. N., «In vitro behaviour of sol-gel interconnected porous scaffolds of doped wollastonite,» *Ceramics International*, vol. 43, n.º 14, págs. 11 034-11 038, 2017.

[115] Gervaso, F., Scalera, F., Kunjalukkal Padmanabhan, S., Sannino, A. y Licciulli, A., «High-performance hydroxyapatite scaffolds for bone tissue engineering applications,» *International Journal of Applied Ceramic Technology*, vol. 9, n.º 3, págs. 507-516, 2012.

[116] Gibson, L. y Ahsby, M., *Cellular solids: Structure and properties*, Segunda ed. Cambridge: Cambridge University Press, 1999, págs. 429-452.

[117] Caeiro, J., González, P. y Guede, D., «Biomecánica y hueso (y II): ensayos en los distintos niveles jerárquicos del hueso y técnicas alternativas para la determinación de la resistencia ósea,» *Revista de Osteoporosis y Metabolismo Mineral*, vol. 5, n.º 2, págs. 99-108, 2013.

Anexos

Apéndice A

Artículo 1

CCC RightsLink®

Home

Help

Email Support

Sign in

Create Account

Multilayer ceramic materials: A method to link bioactivity and durability

Author: Patricia Ros-Tárraga,Nayarit A. Mata,Ángel Murciano,Pablo Velasquez,Piedad N. De Aza

Publication: Ceramics International

Publisher: Elsevier

Date: 1 December 2019

Journal Author Rights

Please note that, as the author of this Elsevier article, you retain the right to include it in a thesis or dissertation, provided it is not published commercially. Permission is not required, but please ensure that you reference the journal as the original source. For more information on this and on your other retained rights, please visit: https://www.elsevier.com/about/our-business/policies/copyright#Author-rights

BACK   CLOSE WINDOW

Multilayer ceramic materials: A method to link bioactivity and durability

Patricia Ros-Tárraga[a,*], Nayarit A. Mata[b], Ángel Murciano[c], Pablo Velasquez[b], Piedad N. De Aza[b]

[a] *Grupo de Regeneración y Reparación de Tejidos: Ortobiología, Biomateriales e Ingeniería de Tejidos, UCAM-Universidad Católica San Antonio de Murcia, Avda. Los Jerónimos 135, Guadalupe, 30107, Murcia, Spain*
[b] *Instituto de Bioingeniería, Universidad Miguel Hernández, Avda. Ferrocarril s/n, Elche, Alicante, 03202, Spain*
[c] *Departamento de Materiales, Óptica y Tecnología Electrónica, Universidad Miguel Hernández, Avda. Universidad s/n, Elche, Alicante, 03202, Spain*

ABSTRACT

The goal of this work is to develop multilayer scaffolds with a high durability core and bioactive external layers. Different ceramics were analysed by Scanning Electron Microscope fitted with Energy-Dispersive X-Ray Spectroscopy, X-Ray Diffraction and they were subjected to *in vitro* testing using simulated body fluid. A non-bioactive porous ceramic scaffold, composed fundamentally of calcium pyrophosphate and tricalcium phosphate, constituted the core of the final multilayer ceramic. Otherwise, a highly bioactive ceramic, composed fundamentally of a major amorphous calcium silicate phase with traces of Zn in its composition, constituted the external layers of the final multilayer ceramic. When the multilayer ceramic was analysed, the mineralogical phases changed compared with core ceramic individually, and it was demonstrated that bioactive external layers provided this capacity to the core ceramic, constituted by a material that was initially non-bioactive.

1. Introduction

Nowadays, bone defects are usually treated using metallic elements as prosthesis, plates and screws, that is, first generation biomaterials, which have some drawbacks. These materials release toxic metallic ions, have a low bioresorption rate and induce chronic pain, among others. Furthermore, differences between the mechanical properties of these surgical materials and natural bone tissue induce the stress shielding phenomenon, which causes bone loss as a result of dimished physiological bone loading that affects long-term functional outcomes [1,2]. For all these reasons, it is necessary to study different biomaterials, such as polymers, ceramics and composites. In the last 50 years, ceramics have been used in medical-surgical areas, like traumatology, odontology and maxillofacial surgery, to replace and repair damaged hard tissues. They offer satisfactory results thanks to their biocompatibility, bioactivity and osteoconductivity. This good performance of ceramics is directly related with their chemical composition and their interaction with the microenvironment.

In bone development, calcium, phosphorus (as phosphate and pyrophosphate groups) and silicon are three of the most important inorganic elements. Calcium, along with phosphate groups, is the most important component of the mineralised matrix. Calcium acts as a signal transduction molecule for cell behaviour, migration, proliferation, and differentiation of osteoblasts during *in vivo* bone formation.

However, it has been demonstrated that calcium levels up to 300 mg/L are cytotoxic for cells [3]. Silicon is able to regulate the expression of osteoblastic genes in osteoblasts and human bone marrow-derived mesenchymal stem cells (BMSCs). Nevertheless, other important ions exist for bone tissue regeneration, such as copper, zinc, magnesium and strontium. Zinc is related with *in vitro* osteoblastic activity stimulation and *in vivo* bone resorption inhibition [4], for which concentration is very important. High concentrations of Zn inhibit the crystallization of hydroxyapatite [5], whereas slow Zn release promotes bone formation and accelerates patient recovery [6]. Another inorganic element that plays an essential role in skeletal mineralization is pyrophosphate (PPi). Given its ability to inhibit the precipitation of hydroxyapatite, excess PPi induces a decreased in skeletal mineralization, while extracellular PPi deficiency leads to the formation of excess hydroxyapatite in the skeleton [7–10]. Biological enzymes, such as alkaline phosphatase (ALP), present in active osteoblasts, can hydrolyse pyrophosphate groups, promoting the loss of the inhibitory capacity of pyrophosphates and supersaturating the extra-cellular fluid with phosphates groups, capable of initiating mineralization [11]. Materials that present the pyrophosphate phase in their composition have been developed in recent years. Examples of these materials are bioactive calcium pyrophosphate glass-ceramics [12,13] and 3D sol-gel glasses [14].

One of the main difficulties for developing 3D scaffolds with potential applications in bone tissue engineering is to obtain a bioactive

75

material, which provides structural support during the healing process. Usually when a biomaterial is stiff and resistant, it has no bioactivity and its reabsorption rate is very low. However when a biomaterial is bioactive, its mechanical strength is poor [15]. Therefore, in order to gradually replace the material with newly grown bone tissue, it is necessary to strike a balance between bioactivity and durability, understanding last one as permanence time in the body. For this reason, it is necessary to develop more complex materials, such as multilayer materials, that comprise layers with different chemical compositions. The scaffolds core could be made from materials with pyrophosphate, which provides a greater durability and adequate structural support for repairing damaged tissue, and the external layers could be composed of a bioactive and osteoinductive material [16]. As far as our knowledge is concerned, no such material has been studied to date. Therefore, the goal of this work is to develop multilayer scaffolds with a high durability core and bioactive external layers. For this reason, the physicochemical and mineralogical characterization of different ceramics was evaluated to fulfil the above-mentioned goal and to select the adequate chemical composition for the core and the external layers.

2. Materials and methods

2.1. Materials preparation

Different ceramics were prepared by the sol-gel method to study their microstructure, chemical and mineralogical composition, and their *in vitro* bioactivity. Table 1 summarizes the composition of each ceramic where, in order to simplify the writing, each composition was labelled as 3D-Ca, 3D-Ca 1%-Zn, 3D-Ca 30%-Zn and 3D-CaLi ceramics.

All the ceramic samples were obtained following these general steps: i) preparing the initial sol-gel solution using the adequate reactants; ii) immersing polyurethane sponges of $0.39 \, cm^3$ (1 cm diameter, 0.5 cm high) in the sol-gel solution, removing the excess by centrifugation (the number of immersions depends on the topography and manageability required), getting a new layer in each immersion, as it is described in the previous literature [16]); iii) drying samples for 15 min at 180 °C after each immersion; iv) the green 3D structures, or core ceramics, were sintered by heat treatment for 55 h until 950 °C was reached, they were maintained at this temperature for 8 h, and were slowly cooled for about 24 h.

Once the four general stages used in the development of ceramics have been described, the preparation of the specific solutions needed for the different ceramics is described below.

- **3D-Ca ceramics**

The 3D-Ca ceramics were prepared using 29.4 wt% SiO_2 – 67.8 wt% CaO – 2.9 wt% P_2O_5 as the sol-gel composition, with 10.9 mL of Si$(OC_2H_5)_4$, 1.6 mL of $(C_2H_5)_3PO_4$ (TEOS, Aldrich-Tetraethyl Orthosilicate, and TEP, Aldrich-Trietyl Phosphate, respectively) and 11.3 g of calcium carbonate ($CaCO_3$ Sigma) as reactants.

- **3D-Ca 1%-Zn ceramics**

The 3D-Ca 1%-Zn ceramics were prepared using 29.4 wt% SiO_2 – 67.3 wt% CaO – 2.8 wt% P_2O_5 – 0.5 wt% ZnO as the sol-gel composition, with TEOS, TEP, $CaCO_3$ and zinc carbonate ($ZnCO_3$, Sigma-Aldrich) as reactants. It was necessary to dissolve 4.2 g of $CaCO_3$ in 10 mL of distilled water and chlorhydric acid drop by drop (HCl, Applichem Panreac), to obtaine a homogeneous solution with a pH between 2 and 3. Simultaneously, a sol-gel solution was prepared by mixing 10.9 mL of TEOS, 1.6 mL of TEP, 5 mL of ethanol 97°, 12 mL of distilled water and, after 30 s, 0.1 g of $ZnCO_3$ and 7,0 g of $CaCO_3$, getting a solution with a pH between 2 and 3. Once the two solutions were available, both were mixed, obtaining a final homogeneous solution with a pH between 2 and 3.

- **3D-Ca 30%-Zn ceramics**

The 3D-Ca 30%-Zn ceramics were prepared using 30.8 wt% SiO_2 – 52.3 wt% CaO – 3.0 wt% P_2O_5 – 13.9 wt% ZnO as the sol-gel composition, with TEOS, TEP, $CaCO_3$ and zinc carbonate ($ZnCO_3$, Sigma-Aldrich) as reactants. It was necessary to dissolve 2.3 g of $CaCO_3$ in 10 mL of distilled water and chlorhydric acid drop by drop (HCl, Applichem Panreac), to obtain a homogeneous solution with a pH between 2 and 3. Simultaneously, a sol-gel solution was prepared by mixing 10.9 mL of TEOS, 1.6 mL of TEP, 5 mL of ethanol 97°, 12 mL of distilled water and, after 30 s, 3.4 g of $ZnCO_3$ and 6.0 g of $CaCO_3$, getting a solution with a pH between 2 and 3. Once the two solutions were available, both were mixed, obtaining a final homogeneous solution with a pH between 2 and 3.

- **3D-CaLi ceramics**

Stratified porous scaffolds of 3D-CaLi, which will be the core of the multilayer ceramic, were prepared using 1.4 wt%SiO_2 – 26.0 wt%P_2O_5 – 69.5 wt%CaO – 3.1 wt%Li_2O as the sol-gel composition, with 0.4 mL of Si$(OC_2H_5)_4$, 10.2 mL of $(C_2H_5)_3PO_4$, 5 mL of C_2H_5OH, 20 mL of distilled water, 0.5 g of lithium carbonate (Li_2CO_3, Sigma-Aldrich) and 8.0 g of calcium carbonate, as reactants. After mixing them all, HCl was added drop by drop to obtain a homogeneous solution with a pH of 3. Having dissolved all the $CaCO_3$, the solution was heated until almost all the water had evaporated, which gave an emulsion, which acted as the initial sol-gel solution.

- **Multilayer ceramics with a 3D-CaLi core and 3D-Ca 1%-Zn external layers: 3D-CaLiZn**

The new class of multilayer ceramics with a 3D-CaLi core and 3D-Ca 1%-Zn external layers, hereinafter referred to as 3D-CaLiZn, were prepared to improve the physico-chemical properties of both independent ceramics. Firstly, a 3D-CaLi ceramic was obtained following the above described procedure. After sintering the ceramic, it was immersed in a 3D-Ca 1%-Zn sol-gel solution, prepared following the above described procedure.

Finally, the 3D-CaLi core covered with 3D-Ca 1%-Zn was subjected to a second sintering using the same heat treatment used before: 55 h until 950 °C was reached and maintained for 8 h, followed by slow cooling.

2.2. Materials characterization

After obtaining all the ceramics, they were physically, chemically and mineralogically characterized by an optical microscope, a Scanning Electron Microscope (SEM) and X-Ray Diffraction (XRD). Finally, the *in vitro* behaviour was studied using simulated body fluid (SBF) and SEM-EDX (SEM fitted with Energy-Dispersive X-Ray Spectroscopy).

2.2.1. Macroscopic and microscopic morphology of the sintered bioceramics

The macroscopic morphology structure was examined under a

Table 1
Chemical compositions of the different ceramics sintered in this work.

| Ceramic		wt% SiO_2	wt% P_2O_5	wt% CaO	wt% Li_2O	wt% ZnO
3D-Ca		29.3	2.9	67.8	–	–
3D-Ca 1%-Zn		29.4	2.8	67.3	–	0.5
3D-Ca 30%-Zn		30.8	3.0	52.3	–	13.9
3D-CaLi		1.4	26.0	69.5	3.1	–
3D-CaLiZn	Core – 3D-CaLi	1.4	26.0	69.5	3.1	–
	External layers – 3D-Ca 1%-Zn	29.4	2.8	67.3	–	0.5
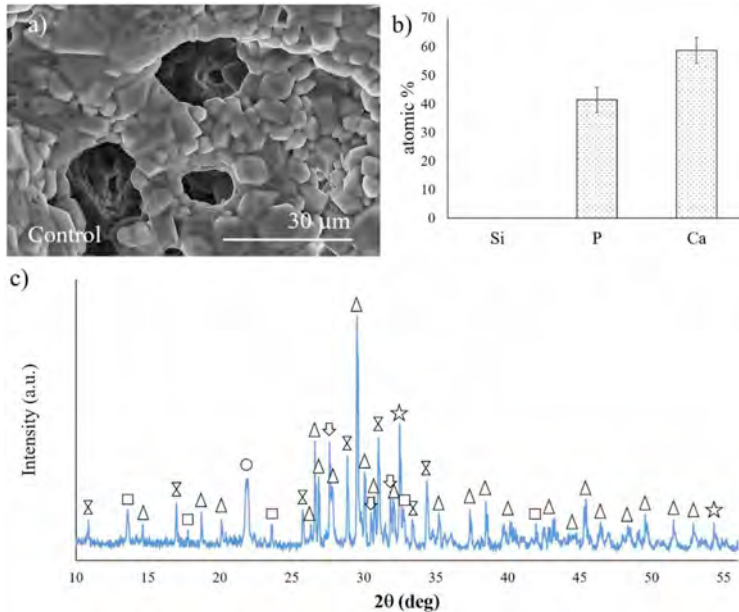
Fig. 1. a) SEM micrograph of the microstructure; b) EDX results of Si, P and Ca; and c) XRD pattern, of the 3D-CaLi ceramics.

Nikon SMZ1500 stereomicroscope equipped with a Nikon DXM1200F digital camera. Otherwise, microscopic morphology was analysed by SEM-EDX.

2.2.2. Mineralogical characterization by X-Ray Diffraction

The XRD patterns were obtained in a Bruker-AXS D8 Advance automated diffractometer using CuKα 1.2 radiation (1.54056 Å). Data were collected in the Bragg-Brentano (θ/2θ) vertical geometry (in the flat reflection mode) at 0.05° steps, by counting 6 s per step. The X-ray tube was operated at 40 kV and 30 mA, as described in the previous literature [16]. The diffractograms of samples were compared with the database provided by the Joint Committee on Powered Diffraction Standards (JCPDS) and with the database provided by the Crystallography Open Database (COD), using the Power Diffraction Match! 3 version 33.6.2.121 software.

2.2.3. Mechanical properties of the core

The compression strength of foams was measured by a Microtest SCM3000 mechanical tester at a crosshead speed of 1.00 mm/min. Samples were cylindrical shaped and measured 7.0 mm in high with a 7.5 mm diameter. During the compression test, load was applied until the densification of the porous samples started to occur.

2.2.4. In vitro behaviour in bioactivity terms

The materials' potential bioactivity was evaluated *in vitro* by immersing samples in Kokubo's [17] SBF at a ratio of 3:1 (ceramic mass, in mg: SBF volume, in mL). The samples in SBF were incubated at 37 ± 0.5 °C in a shaking water bath for 1, 3, 7 and 14 days. After these time periods, samples were dried at 50 °C for 24 h. The newly-formed Ca–P precipitate on the ceramic surface was chemically identified by SEM-EDX (SEM-Hitachi S–3500 N and the INCA system, Oxford Instruments Analytical, UK), by covering samples with palladium after each soaking time in SBF, as described in the previous literature [16].

3. Results and discussion

In order to select the chemical composition of the core and the external layers of the multilayer ceramic, the microstructure and *in vitro* bioactivity of different ceramics were studied.

First of all, the material which would constitute the core of the multilayer material, the 3D-CaLi ceramic, was analysed to study its microstructure, and its chemical and mineralogical composition.

Fig. 1a shows the SEM microstructure of the 3D-CaLi ceramic. It shows a homogeneous distribution of hexagonal shaped grains, which was attributable to the presence of calcium pyrophosphate and tricalcium phosphate (TCP), as the previous literature describes [18,19]. An interconnected porosity is also observed, which is necessary for new tissue ingrowth an vascularization constructs [20]. The EDX results (Fig. 1b) showed an absence of silicon and a predominance of calcium and phosphorus, with Ca/P ratios of about 1.32 ± 0.06, which corresponds to an intermediate Ca/P ratio value between TCP and calcium pyrophosphate [21]. These results were corroborated with the results obtained with the samples' XRD patterns, shown in Fig. 1c. The 3D-CaLi ceramics are composed fundamentally by calcium pyrophosphate, and tricalcium phosphate (COD-96-100-1557 and COD-96-151-7239, respectively). It has other mineralogical phases, such as calcium and lithium orthophosphate (COD-96-722-2995), dicalcium silicate (COD-96-154-6028), cristobalite (COD-96-900-8111) and dilithium oxide (COD-96-151-4095). All these results are in accordance with the reactants used in the initial sol-gel solution, from which the 3D-CaLi ceramic was obtained.

Once the 3D-CaLi ceramic was characterized, the microstructure and *in vitro* bioactivity of the different ceramics were studied to select the adequate chemical composition for the external layers, which will constitute the bioactive portion of the final multilayer ceramic.

Different scaffolds were fabricated by the sol-gel and polymer replication methods, getting the final ceramics observed in Fig. 2. They all showed uniform dimensions and interconnected porosity. Fig. 2 a-h display the ceramics with different compositions: 3D-Ca and 3D-Ca 1%-Zn, with some plugged channel pores and wide struts. However, Fig. 2 i-

77
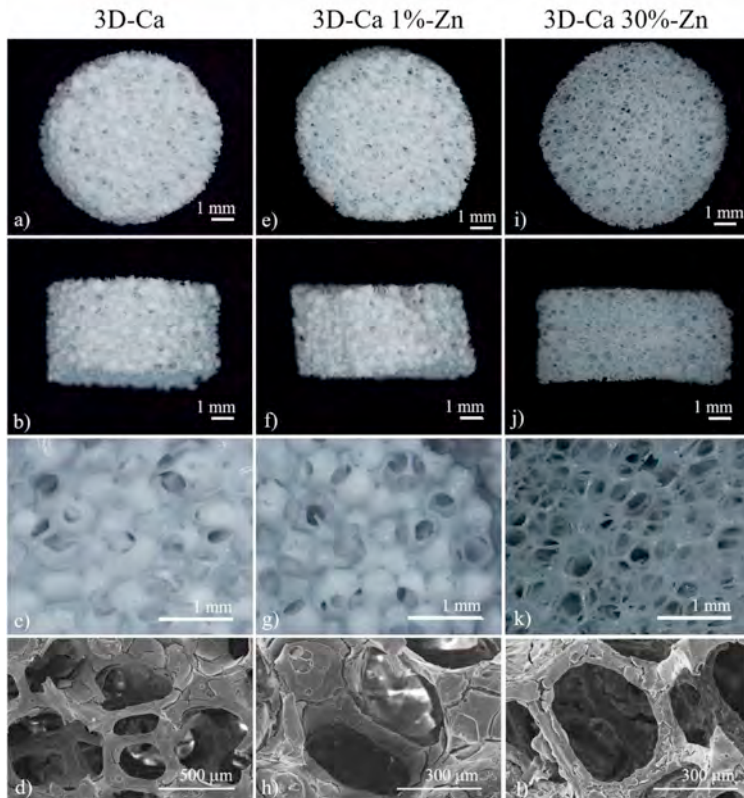
Fig. 2. Macroscopic structure of the different stratified 3D porous scaffolds: (a–c) 3D-Ca, (e–g) 3D-Ca 1%-Zn and (i–k) 3D-Ca 30%-Zn; microscopic structure of d) 3D-Ca, h) 3D-Ca 1%-Zn and l) 3D-Ca 30%-Zn.
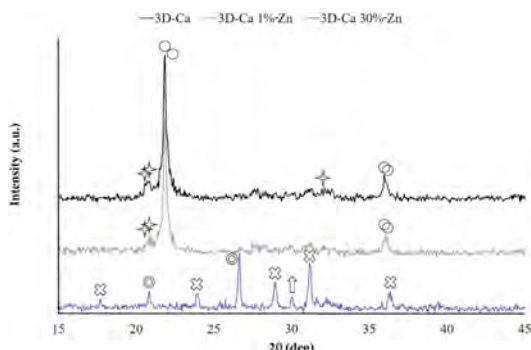

Fig. 3. XRD patterns of the 3D-Ca, 3D-Ca 1%-Zn and 3D-Ca 30%-Zn ceramics. ○ = cristobalite; ✦ = *tridymite*; ◎ = *Quartz*; ⇧ = *wollastonite-2M*; ⋈ = *hardystonite*.

l show the 3D-Ca 30%-Zn ceramics, with all their pores completely opened and with thicker struts. These observations were confirmed when samples were observed by SEM.

Dipping thickness depends on the viscosity of the sol solution. When the Zn concentration was increased, the viscosity of the initial solution decreased, reducing the plugging of pores and increasing the number of

opened pores.
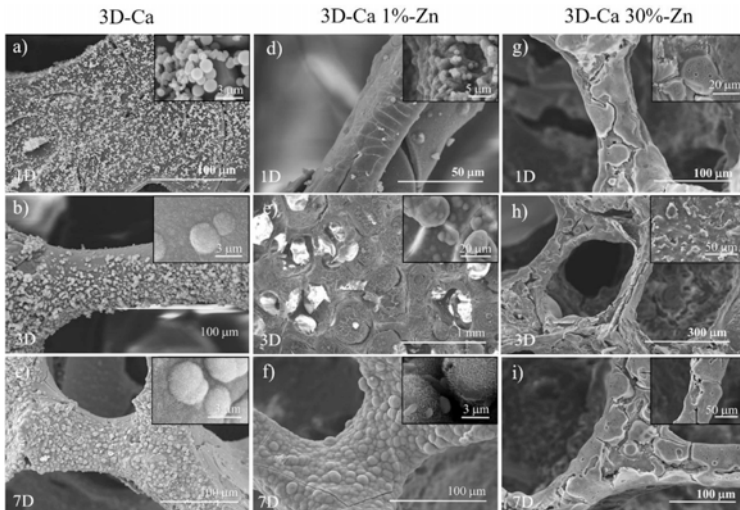
The mineralogical compositios of the 3D-Ca, 3D-Ca 1%-Zn and 3D-Ca 30%-Zn ceramics are shown in Fig. 3. The 3D-Ca and 3D-Ca 1%-Zn ceramics are composed fundamentally by a major amorphous calcium silicate phase with small amounts of silica (cristobalite and tridymite – JCPDS 82–1403 and JCPDS 70–8142, respectively). However, the 3D-Ca 30%-Zn ceramics has a completely different mineralogical composition. It is composed fundamentally by hardystonite (JCPDS 72–1603) and quartz (JCPDS 86–1560), and small amounts of wollastonite-2M (JCPDS 84–0655).

As a result of using the sol-gel method, polymorphous phases of SiO_2 appeared in all the ceramics. In this technique, Si–O–Si bonds were established to stabilize the 3D structure. Although cristobalite is a SiO_2 high temperature phase (over 1470 °C), it appeared in the 3D-Ca and 3D-Ca 1%-Zn ceramics. This fact is due to the presence of phosphorus traces in these samples. This ion induces the crystallization of high temperature SiO_2 phases at low temperatures [22].

In addition, Zn ions are a primary network modifier. This ion decreases the structure's local symmetry by increasing the number of non-bridging oxygen (NBO) atoms [5]. Accordingly, a high Zn concentration induces changes in the phases composition of 3D-Ca 30%-Zn, where hardystonite appears as the majority phase in samples. This new phase could be good because it has been demonstrated that bone marrow mesenchymal stem cells adhere well to this ceramic, and its implantation *in vivo* has shown rapid new bone growth compared to other materials, such as β-TCP [23].

78

Table 2
Summary of the physical parameters of different SiO_2–CaO–P_2O_5 ceramics and glasses.

Material	Pore size (μm)	Porosity (%)	Compressive strength (MPa)	Reference
SiO_2–CaO–P_2O_5 – 3D-CaLi	400–700	74	1.0–1.7	Present work
SiO_2–CaO–P_2O_5	250–400	90–95	0.18–0.40	[16]
SiO_2–CaO-$(Mg/Na/K)_yO_x$	200–400	90–95	0.02–0.03	[24]
Si-αTCP	300–1000	80	0.72	[25]
HA	420–560	86	0.21	[26]
HA	490–1130	69–86	0.03–0.29	[27]
HA	200–400	70–77	0.55–5	[28]
45S5 Bioglass®	510–720	89–92	0.27–0.42	[29]
Glass-reinforced HA	420–560	85–97.5	0.01–0.175	[30]
70S30C bioactive glass	Up to 600	70–95	0.5–2.5	[31]
HA + βTCP	200–400	73	9.8	[47]

Fig. 4. SEM micrographs of the 3D-Ca, 3D-Ca 1%-Zn and 3D-Ca 30%-Zn stratified porous scaffolds after immersion in SBF: a-c) 3D-Ca after 1,3 and 7 days; d-f) 3D-Ca 1%-Zn after 1,3 and 7 days; g-i) 3D-Ca 30%-Zn after 1,3 and 7 days.

Very few reports are available about the mechanical properties of different polycrystalline porous SiO_2–CaO–P_2O_5 scaffolds obtained by polymer replica methods [16,24,25]. To the best of our knowledge, Table 2 summarizes the characteristics of highly porous bioactive ceramic and glass foams developed for bone tissue engineering, including pore size, pore structure, and compressive strength data. In general, compressive strength varies significantly with scaffold porosity. For example, the compressive strength of HA scaffolds, synthesized by the polymer-sponge method, decreased from 0.29 to 0.03 MPa when porosity increased from 69% to 86% [26–28]. It is obvious that today's 45S5 Bioglass-based foams are generally stronger than HA-based foams with similar porosities [29–31]. The bonding strength herein developed between the core and external layers is chemical bonding which allows the multilayer ceramic material to behave like one/a single body. The handling of the 3D ceramic is strong enough (compressive strength ~ 1.0–1.7 MPa) to keep the external layer attached to the core during the mechanical test.

Fig. 4a–c show the surface morphologies of the 3D-Ca multilayer porous scaffolds after different immersion times in SBF. After 1 day of immersion in SBF (Fig. 4a), the first changes to the material's surface in the 3D-Ca ceramics were observed, along with the presence of spherical particles that covered its entire surface. At this point, the EDX analysis revealed slight silicon presence and Ca/P ratios were about 1.79 ± 0.07, which were higher than those in the stoichiometric

hydroxyapatite (HA), which is 1.67. When the immersion time came to 3 days (Fig. 4b), the calcium phosphate particles formed a compact layer covering the whole ceramic surface. This layer was formed as a result of the size and number of precipitate particles increasing, which join one another. At this time, silicon was lower than after 1 day of SBF immersion and the Ca/P ratios were enhanced with values of 1.84 ± 0.12, which is higher than before. Finally, after 7 days of immersion, particles continued to grow, acquiring rod-like shape, and creating a massive compact precipitate plaque over the ceramic's surface (Fig. 4c). When the atomic percentage was calculated at that time, Ca/P ratios exceeded 2.04 ± 0.34. This Ca/P approximately corresponded to a carbonated hydroxyapatite (CHA, Ca/P of 2.15) [32], which is the main component of the bone mineral phase. This CHA corresponds to an hydroxyapatite with carbonate groups substituting the hydroxyl and phosphate groups [33].

3D-Ca 1%-Zn *in vitro* bioactivity (Fig. 4 d-f) showed a similar behaviour to the 3D-Ca samples, but with one remarkable difference: a thin continuous plaque appeared after only 1 day of immersion in SBF (Fig. 4d). This fact indicates that 3D-Ca 1%-Zn ceramics have a really high bioactivity, higher than some other bioactive materials described in the literature [34–37]. The precipitate morphology also differed from one of 3D-Ca. In this case, the precipitate had a blade-like morphology and not a rod-like one. The EDX results gave Ca/P ratios that went from 1.24 ± 0.13 after 1 day of SBF immersion to 1.66 ± 0.30 after 7 days

79
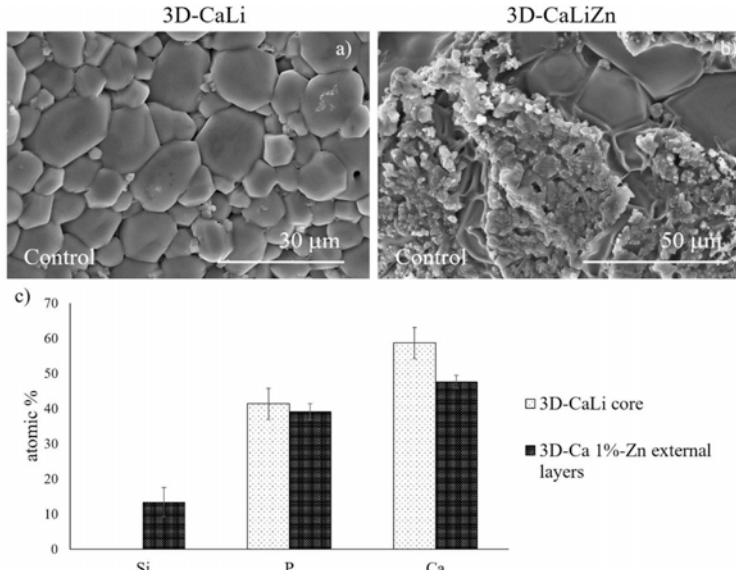
Fig. 5. SEM micrographs of the a) 3D-CaLi, b) 3D-CaLiZn ceramics and c) EDX results of Si, P and Ca of the 3D-CaLiZn ceramics (3D-CaLi core and 3D-Ca 1%-Zn external layers).
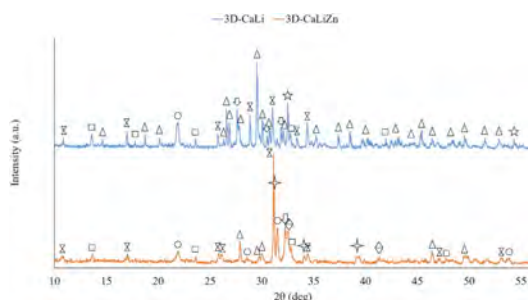

Fig. 6. X-Ray Diffraction patterns of the 3D-CaLi and 3D-CaLiZn ceramics.○ = cristobalite; $\times$ = tricalcium phosphate; □ = calcium and lithium orthophosphate; △ = calcium pyrophosphate; ⇩ = dicalcium silicate; ✢ = tridimite; ♦ = zinc modified calcium silicate (Ca 1/2Si 0.8Zn); ☆ = dilithium oxide.

of immersion. The initial precipitate was assigned to an octacalcium phosphate (Ca/P = 1.33) after 1 day of immersion, passed through an amorphous calcium phosphate (Ca/P = 1.5) after 3 days of immersion and, finally, after 7 days, the obtained precipitate was hydroxyapatite (Ca/P = 1.67), as described in the literature [38]. It is necessary to highlight that this small quantity of Zn is capable of changing the sample's bioactivity velocity, speeding up the initiation of the nucleation and crystallization of the hydroxyapatite layer, and is able to modify the precipitate morphology.

The 3D-Ca 30%-Zn samples did not show any precipitate on its surface after any SBF immersion time (Fig. 4 g-i), and the EDX results were invariable in time. These samples were not bioactive at any study time, which falls in line with the previous literature [5,39–42]. When the Zn concentration in solution is high enough, it slows down the HA formation process. This behaviour is due to the Zn^{2+} ions modifying chain P–O–P bond angles because the Zn^{2+} atomic radius is smaller than the Ca^{2+} one, which indicates that the places where Zn enters instead of Ca are not capable of forming HA and the material's

bioactivity is delayed. The higher the Zn concentration, the more likely Zn will occupy the Ca places and, therefore, no precipitate is formed. Furthermore, Zn^{2+} ions modify chain P–O–P bond angles, interfering with the HA precipitation. Finally, as see with the XRD results, Zn can react with Ca, Si and O, forming a new crystal phase of $Ca_2ZnSi_2O_7$, which has been proved to have a low dissolution, altering the ion exchange with SBF.

After demonstrating the high bioactivity of the 3D-Ca 1%-Zn ceramic, the composite multilayer ceramic, with a core constituted by the 3D-CaLi composition and the external layers by the bioactive 3D-Ca 1%-Zn composition was studied. The objective was to develop structures with a controlled time of remaining in the human body, in accordance with bone tissue regeneration stages but by maintaining, at the same time, an excellent bioactivity, allowing thus a direct contact implant-bone.

Fig. 5a and b shows the SEM micrographs of the 3D-CaLi (core) and the 3D-CaLiZn (core coated by bioactive layers) ceramics microstructures, respectively. The surface morphology of the multilayer 3D-CaLiZn shows the presence of hexagonal shaped grains, characteristic of the 3D-CaLi ceramics, constituting which was called the ceramic core. On this core, it was possible to see fragmented plaques that corresponded with the external 3D-Ca 1%-Zn composition layers. Its heterogeneous and fragmented presence was due to the shrinkage that ceramics underwent after the second sintering treatment. This external plaque modify not only the ceramic's chemical composition, but also the surface's roughness, which is an essential characteristic for cell adhesion and proliferation [43].

The EDX results (Fig. 5c) supported the SEM observations. When the EDX data were collected in the 3D-CaLi core zones, they showed that silicon was absent due to the low Si concentration used to prepare it. Otherwise, when the EDX data were collected on the external plaques (3D-Ca 1% Zn), they showed that silicon was present, as expected. The external layers were too thin and the presence of Zn was too slight in the sol-gel initial composition, so EDX was unable to detect it. Finally, the Ca/P ratios were different. In 3D-CaLi, the Ca/P ratios were about 1.32 ± 0.06, which corresponds to an intermediate Ca/P ratio value
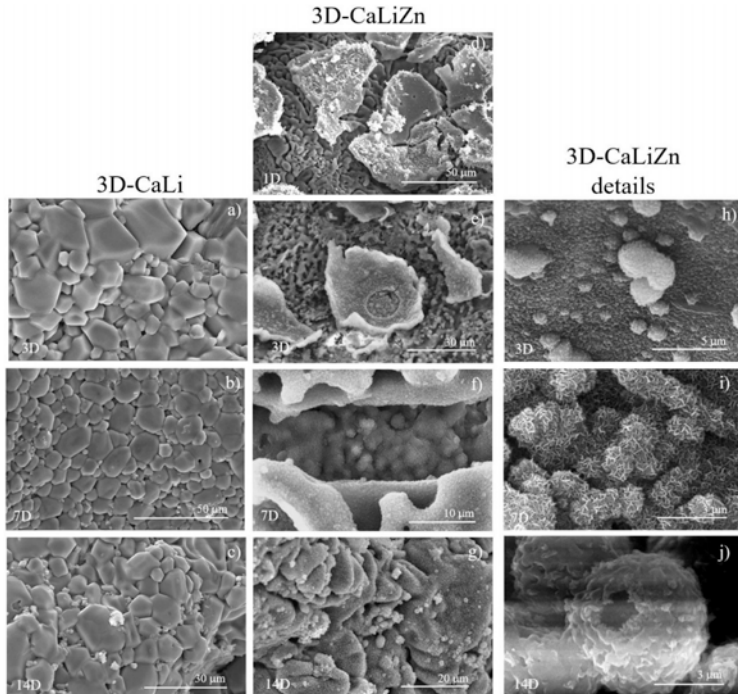
Fig. 7. SEM micrographs of the 3D-CaLi and 3D-CaLiZn multilayer porous scaffolds after different immersion times in SBF: a-c) 3D-CaLi after 3,7 and 14 days; d-g) 3D-CaLiZn after 1, 3, 7 and 14 days; h-j) 3D-CaLiZn detail micrographs after 3, 7 and 14 days.

between TCP and calcium pyrophosphate [21]. However, it decreased in the 3D-CaLiZn samples, with values of 1.22 ± 0.02.

The mineralogical composition of the 3D-CaLi and 3D-CaLiZn ceramics is shown in Fig. 6. The 3D-CaLiZn ceramics have a different distribution of mineralogical phases compared to the 3D-CaLi ceramics (shown and described in Fig. 1). In the 3D-CaLiZn multilayer ceramics, tricalcium phosphate is also the predominant phase, but has fewer less intense peaks. Furthermore, phases such as tridimite (COD-96-900-0521) and zinc modified calcium silicate (COD-96-810-0091) appears. These results reveal that the second sintering process of the final mul-tilayer ceramic modified the mineralogical pattern compared to the core alone (3D-CaLi), changing its behaviour.

The bioactive behaviour of both the core (3D-CaLi) and the core coated with bioactive layers (3D-CaLiZn) was evaluated by SEM images. Fig. 7 shows the SEM micrographs of 3D-CaLi and 3D-CaLiZn scaffolds after being soaked in SBF for 3, 7 and 14 days.

Any surface modification and precipitate were observed in 3D-CaLi scaffolds after any immersion time in SBF (Fig. 7a–c). These results mean that the 3D-CaLi ceramics were not bioactive at any study time. By considering that the 3D-CaLi ceramics are fundamentally composed by calcium pyrophosphate and tricalcium phosphate, as the DRX results showed, these results agree with the previous literature, which has demonstrated that pyrophosphate molecules contain P–O–P bonds that block the formation and/or growth of HA critical nuclei and crystals [10,44].

Instead, the 3D-CaLiZn ceramics exhibited a completely different behaviour when immersed in SBF. After 1 day of immersion (Fig. 7d), only the 3D-Ca 1%-Zn external layers showed spherical precipitates, which were scattered heterogeneously over the surface of the ceramics. However, the 3D-CaLi core had a different morphology, despite not presenting any type of precipitate. It was difficult to delimit the

characteristic grains observed in the 3D-CaLi ceramics. When the SBF immersion time was increased to 3 days, all the 3D-CaLiZn ceramic surface showed precipitates on it (Fig. 7e). No defined spherical pre-cipitate exists, but the whole surface was modified. After 7 days of SBF immersion (Fig. 7f), spherical precipitates were seen in the 3D-CaLi core, but the formed plaque was too thin to obtain reliable EDX results. Finally, when the samples were immersed in SBF for 14 days (Fig. 7g), all the surface samples were covered by a calcium phosphate pre-cipitate, but were still too thin. The detailed micrographs (Fig. 7h–j), show the variation in the spherical precipitate morphology, as well as the increase in its size and number at different SBF immersion times, even hollow spheres were observed after 14 days of immersion. The addition of external 3D-Ca 1%-Zn layers on the 3D-CaLi core modified the *in vitro* behaviour of the 3D-CaLi ceramic, making it bioactive. Small amounts of Zn accelerated the bioactivity in the 3D-Ca ceramics, as shown in Fig. 4d. However, in this last case, it was capable of inducing the precipitation of a calcium phosphate component on a non-bioactive material. By bearing in mind the strong metal ion chelating capacity of some ions, such as Ca^{2+} and Zn^{2+} [45,46], the 3D-Ca 1%-Zn external layers were added, creating the 3D-CaLiZn ceramics. Zn and Ca ions compete for pyrophosphate binding sites, which allows enough Ca ions in the ceramic-SBF interphase to initiate the nucleation and crystal-lization of HA precipitate on the ceramic surface.

4. Conclusions

This work demonstrates that it is possible to develop a new class of multilayerporous materials by the sol-gel process. This new material is composed of a high durability core and a highly bioactive external coating. The ceramic, which will constitute the core of the final mul-tilayer ceramic (3D-CaLi), was elaborated based on quaternary system

81

SiO$_2$–P$_2$O$_5$–CaO–Li$_2$O, and its mineralogical analysis revealed the presence of calcium pyrophosphate and tricalcium phosphate phases fundamentally. In bioactivity terms, the study of its *in vitro* behaviour, demonstrated that the 3D-CaLi ceramics were not bioactive at any study time.

The external bioactive layers were elaborated based on quaternary system SiO$_2$–P$_2$O$_5$–CaO–ZnO. It has been demonstrated that certain quantities of a cation, such as Zn^{2+}, induce major changes in behaviour in ceramics. Initially, a 1% addition of Zn was able to accelerate the bioactivity of a bioactive ceramic (3D-Ca), keeping its mineralogical composition. However, when 30% Zn was added, bioactivity was inhibited and the whole mineralogical composition changed. When the 3D-Ca 1%-Zn solution was added, as external layers, to a non-bioactive ceramic (3D-CaLi), the multilayer 3D-CaLiZn ceramic was obtained, which was capable of modifying the mineralogical phases of the individual 3D-CaLi ceramic, and of inducing the precipitation of calcium phosphate species on the surface of the ceramic's core. In short, large quantities of Zn inhibit a material's bioactivity, but small quantities are capable to provide this capacity to a non-bioactive material.

Conflicts of interest

None.

Funding

References

[1] P.J. Denard, P. Raiss, R. Gobezie, T.B. Edwards, E. Lederman, Stress shielding of the humerus in press-fit anatomic shoulder arthroplasty: review and recommendations for evaluation, J. Shoulder Elb. Surg. 27 (2018) 1139–1147.

[2] D.L. Millis, Responses of Musculoskeletal Tissues to Disuse and Remobilization, Canine Rehabilitation and Physical Therapy, second ed., Elsevier, 2014, pp. 92–153.

[3] L. Malaval, F. Liu, P. Roche, J.E. Aubin, Kinetics of osteoprogenitor proliferation and osteoblast differentiation in vitro, J. Cell. Biochem. 74 (1999) 616–627.

[4] F. Barrère, C.A. van Blitterswijk, K. de Groot, Bone regeneration: molecular and cellular interactions with calcium phosphate ceramics, Int. J. Nanomed. 1 (2006) 317–332.

[5] R. Veres, A. Vulpoi, K. Magyari, C. Ciuce, V. Simon, Synthesis, characterisation and in vitro testing of macroporous zinc containing scaffolds obtained by sol–gel and sacrificial template methods, J. Non-Cryst. Solids 373–374 (2013) 57–64.

[6] S. Kapoor, A. Goel, A.F. Correia, M.J. Pascual, H.-Y. Lee, H.-W. Kim, J.M. Ferreira, Influence of ZnO/MgO substitution on sintering, crystallisation, and bio-activity of alkali-free glass-ceramics, Mater. Sci. Eng. C 53 (2015) 252–261.

[7] Y. Zhou, C. Wu, J. Chang, Bioceramics to regulate stem cells and their micro-environment for tissue regeneration, Mater. Today 24 (2018) 41–56.

[8] W.N. Addison, F. Azari, E.S. Sørensen, M.T. Kaartinen, M.D. McKee, Pyrophosphate inhibits mineralization of osteoblast cultures by binding to mineral, up-regulating osteopontin, and inhibiting alkaline phosphatase activity, J. Biol. Chem. 282 (2007) 15872–15883.

[9] N.J. Lakhkar, I.-H. Lee, H.-W. Kim, V. Salih, I.B. Wall, J.C. Knowles, Bone formation controlled by biologically relevant inorganic ions: role and controlled delivery from phosphate-based glasses, Adv. Drug Deliv. Rev. 65 (2013) 405–420.

[10] H. Fleisch, R. Russell, F. Straumann, Effect of pyrophosphate on hydroxyapatite and its implications in calcium homeostasis, Nature 212 (1966) 901–903.

[11] L.M. Grover, A.J. Wright, U. Gbureck, A. Bolarinwa, J. Song, Y. Liu, D.F. Farrar, G. Howling, J. Rose, J.E. Barralet, The effect of amorphous pyrophosphate on calcium phosphate cement resorption and bone generation, Biomaterials 34 (2013) 6631–6637.

[12] T. Kasuga, Bioactive calcium pyrophosphate glasses and glass-ceramics, Acta Biomater. 1 (2005) 55–64.

[13] T. Kasuga, Development of phosphate glass-ceramics for biomedical applications, J. Ceram. Soc. Jpn. 115 (2007) 455–459.

[14] S. Thakur, S. Garg, G. Kaur, O.P. Pandey, Effect of strontium substitution on the cytocompatibility and 3-D scaffold structure for the xSrO–(10 − x) MgO–60SiO 2–20CaO–10 P 2 O 5 (2≤ x≤ 8) sol–gel glasses, J. Mater. Sci. Mater. Med. 28 (2017) 89.

[15] Q. Chen, C. Zhu, G.A. Thouas, Progress and challenges in biomaterials used for bone tissue engineering: bioactive glasses and elastomeric composites, Prog. Biomater. 1 (2012) 2.

[16] P. Ros-Tárraga, A. Murciano, P. Mazón, S.A. Gehrke, N. Piedad, New 3D stratified Si-Ca-P porous scaffolds obtained by sol-gel and polymer replica method: micro-structural, mineralogical and chemical characterization, Ceram. Int. 43 (2017) 6548–6553.

[17] T. Kokubo, H. Takadama, How useful is SBF in predicting in vivo bone bioactivity? Biomaterials 27 (2006) 2907–2915.

[18] H.-S. Ryu, H.-J. Youn, K.S. Hong, B.-S. Chang, C.-K. Lee, S.-S. Chung, An improvement in sintering property of β-tricalcium phosphate by addition of calcium pyrophosphate, Biomaterials 23 (2002) 909–914.

[19] R. Detsch, H. Mayr, G. Ziegler, Formation of osteoclast-like cells on HA and TCP ceramics, Acta Biomater. 4 (2008) 139–148.

[20] P. Ros-Tárraga, P. Mazón, M. Rodríguez, L. Meseguer-Olmo, P. De Aza, Novel resorbable and osteoconductive calcium silicophosphate scaffold induced bone formation, Materials 9 (2016) 785.

[21] S.R. Vasant, M. Joshi, A review on calcium pyrophosphate and other related phosphate nano bio-materials and their applications, Rev. Adv. Mater. Sci. 48 (2017) 44–57.

[22] S. Padilla, J. Roman, A. Carenas, M. Vallet-Regı, The influence of the phosphorus content on the bioactivity of sol–gel glass ceramics, Biomaterials 26 (2005) 475–483.

[23] H. Mohammadi, M. Hafezi, N. Nezafati, S. Heasarki, A. Nadernezhad, S. Ghazanfari, M. Sepantafar, Bioinorganics in bioactive calcium silicate ceramics for bone tissue repair: bioactivity and biological properties, J. Ceram. Sci. Tehcnol. 5 (2014) 1–12.

[24] P. Ros-Tárraga, Á. Murciano, P. Mazón, S.A. Gehrke, N. Piedad, In vitro behaviour of sol-gel interconnected porous scaffolds of doped wollastonite, Ceram. Int. 43 (2017) 11034–11038.

[25] P. De Aza, M. Rodríguez, S. Gehrke, J. Maté-Sánchez de Val, J. Calvo-Guirado, A Si-αTCP scaffold for biomedical applications: an experimental study using the rabbit tibia model, Appl. Sci. 7 (2017) 706.

[26] H.-W. Kim, J.C. Knowles, H.-E. Kim, Hydroxyapatite porous scaffold engineered with biological polymer hybrid coating for antibiotic Vancomycin release, J. Mater. Sci. Mater. Med. 16 (2005) 189–195.

[27] X. Miao, G. Lim, K. Loh, A.R. Boccaccini, Preparation and characterisation of calcium phosphate bone cement, Mater. Process. Prop. Perform. (MP3) 3 (2004) 319–324.

[28] H.R. Ramay, M. Zhang, Preparation of porous hydroxyapatite scaffolds by combination of the gel-casting and polymer sponge methods, Biomaterials 24 (2003) 3293–3302.

[29] Q.Z. Chen, I.D. Thompson, A.R. Boccaccini, 45S5 Bioglass®-derived glass–ceramic scaffolds for bone tissue engineering, Biomaterials 27 (2006) 2414–2425.

[30] S. Callcut, J. Knowles, Correlation between structure and compressive strength in a reticulated glass-reinforced hydroxyapatite foam, J. Mater. Sci. Mater. Med. 13 (2002) 485–489.

[31] J.R. Jones, L.L. Hench, Factors affecting the structure and properties of bioactive foam scaffolds for tissue engineering, J. Biomed. Mater. Res. Part B: Applied Biomaterials: An Off. J. Soc. Biomater., Jpn. Soc. Biomater. Aust. Soc. Biomater. Korean Soc. Biomater. 68 (2004) 36–44.

[32] A. Fabig, B. Herrmann, Trace elements in buried human bones: intra-population variability of Sr/Ca and Ba/Ca ratios–diet or diagenesis? Naturwissenschaften 89 (2002) 115–119.

[33] E. Landi, G. Celotti, G. Logroscino, A. Tampieri, Carbonated hydroxyapatite as bone substitute, J. Eur. Ceram. Soc. 23 (2003) 2931–2937.

[34] R.L. Siqueira, P.F.S. Alves, T. da Silva Moraes, L.A. Casemiro, S.N. da Silva, O. Peitl, C.H.G. Martins, E.D. Zanotto, Cation-doped bioactive ceramics: in vitro bioactivity and effect against bacteria of the oral cavity, Ceram. Int. 45 (2019) 9231–9244.

[35] A. Yazdanpanah, F. Moztarzadeh, Synthesis and characterization of Barium–Iron containing magnetic bioactive glasses: the effect of magnetic component on structure and in vitro bioactivity, Colloids Surfaces B Biointerfaces 176 (2019) 27–37.

[36] S. Arabyazdi, A. Yazdanpanah, A.A. Hamedani, A. Ramedani, F. Moztarzadeh, Synthesis and characterization of CaO-P2O5-SiO2-Li2O-Fe2O3 bioactive glasses: the effect of Li2O-Fe2O3 content on the structure and in-vitro bioactivity, J. Non-Cryst. Solids 503 (2019) 139–150.

[37] B.A. Allo, A.S. Rizkalla, K. Mequanint, Hydroxyapatite formation on sol–gel derived poly (ε-caprolactone)/bioactive glass hybrid biomaterials, ACS Appl. Mater. Interfaces 4 (2012) 3148–3156.

[38] C. Liu, Y. Huang, W. Shen, J. Cui, Kinetics of hydroxyapatite precipitation at pH 10 to 11, Biomaterials 22 (2001) 301–306.

[39] J. Ma, B. Huang, X. Zhao, C. Wang, H. Zhang, Effect of zinc substitution for calcium on the structure, dissolution behavior and apatite formation of CaO–ZnO–SiO2–P2O5 bioceramics, Mater. Lett. 206 (2017) 154–157.

[40] R.C. Lucacel, O. Ponta, V. Simon, Short-range structure and in vitro behavior of ZnO–CaO–P2O5 bioglasses, J. Non-Cryst. Solids 358 (2012) 2803–2809.

[41] H. Zreiqat, Y. Ramaswamy, C. Wu, A. Paschalidis, Z. Lu, B. James, O. Birke, M. McDonald, D. Little, C.R. Dunstan, The incorporation of strontium and zinc into a calcium–silicon ceramic for bone tissue engineering, Biomaterials 31 (2010) 3175–3184.

[42] A.K. Jaiswal, H. Chhabra, S.S. Kadam, K. Londhe, V.P. Soni, J.R. Bellare, Hardystonite improves biocompatibility and strength of electrospun poly-caprolactone nanofibers over hydroxyapatite: a comparative study, Mater. Sci. Eng. C 33 (2013) 2926–2936.

[43] P. Mazón, D. García-Bernal, L. Meseguer-Olmo, F. Cragnolini, N. Piedad, Human mesenchymal stem cell viability, proliferation and differentiation potential in response to ceramic chemistry and surface roughness, Ceram. Int. 41 (2015) 6631–6644.

[44] N.C. Blumenthal, Mechanisms of inhibition of calcification, Clin. Orthop. Relat. Res. (1989) 279–289.

[45] A. Kreżel, W. Maret, The biological inorganic chemistry of zinc ions, Arch. Biochem. Biophys. 611 (2016) 3–19.

[46] T.J. Greenfield, M. Julve, R.P. Doyle, Exploring the biological, catalytic, and magnetic properties of transition metal coordination complexes incorporating pyrophosphate, Coord. Chem. Rev. 384 (2019) 37–64.

[47] H.R. Ramay, M. Zhang, Biphasic calcium phosphate nanocomposite porous scaffolds for load-bearing bone tissue engineering, Biomaterials 25 (2004) 5171–5180.

82

Apéndice B

Artículo 2

Synthesis and characterization of 3D multilayer porous Si–Ca–P scaffolds doped with Sr ions to modulate in vitro bioactivity

Author: Nayarit A. Mata,Patricia Ros-Tárraga,Pablo Velasquez,Angel Murciano,Piedad N. De Aza

Publication: Ceramics International

Publisher: Elsevier

Date: January 2020

Journal Author Rights

BACK

CLOSE WINDOW

Synthesis and characterization of 3D multilayer porous Si–Ca–P scaffolds doped with Sr ions to modulate *in vitro* bioactivity

Mata Nayarit A.[a,*], Ros-Tárraga Patricia[b], Velasquez Pablo[a], Murciano Angel[c], De Aza Piedad N.[a]

[a] *Instituto de Bioingeniería, Universidad Miguel Hernández, Avda. Ferrocarril S/n, Elche, Alicante, 03202, Spain*
[b] *Grupo de Investigación en Regeneración y Reparación de Tejidos, Universidad Católica San Antonio de Murcia, Guadalupe, Murcia, Spain*
[c] *Departamento de Materiales, Óptica y Tecnología Electrónica, Universidad Miguel Hernández, Avda. Universidad S/n, Elche, Alicante, 03202, Spain*

A B S T R A C T

In this study, multilayer ceramic scaffolds were prepared by sol-gel and polymeric replication methods. The objective was to fabricate scaffolds based on two different compositions: a core with composition SiO_2–$25P_2O_5$–$68CaO$–$6Li_2O$ (mol%) to confer mechanical resistance and external layers with composition $29SiO_2$–$3P_2O_5$-(68-x)CaO-xSrO (mol%) (x = 0, 0.7, 2, 7, 17 and 34) to provide modulated bioactivity. The obtained scaffolds were characterized by X-ray diffraction (XRD), Fourier Transform Infrared Spectroscopy (FTIR), Scanning Electron Microscopy with Energy Dispersive X-Ray Spectroscopy (SEM-EDX) and Mercury Porosimetry Techniques. *In vitro* bioactivity was evaluated by soaking samples in simulated body fluid (SBF). The results revealed that the core was not bioactive, but bioactivity could be modulated when the core was covered with external layers. The samples doped with 0.7 and 7 mol% SrO showed bioactivity after 3 days in SBF, while the sample doped with 2 mol% SrO displayed bioactivity after 14 days. The samples doped with 17 and 34 mol% SrO presented no bioactivity, rather precipitates on the surface after 14 days and 7 days, respectively, which could correspond to a modified apatite. Variation in bioactivity with increasing dopant concentrations is attributed to the fact that a certain amount of Ca^{2+} ions substituted for Sr^{2+} can distort the network at different levels. This makes the material more unstable, which favors the ion exchange needed for hydroxyapatite nucleation.

1. Introduction

One of the most important clinical challenges of recent times has been to find alternatives to combat the increase in structural bone damage caused by trauma and diseases, which especially affect the elderly. Until recently, natural implants like autografts, homografts and xenografts, were the best option. However, autograft implants are limited by not only poor donor area availability, but also by the possibility of causing morbidity. The use of homograft and xenograft implants is limited by the high risk of transmitting diseases and rejections [1,2]. For this reason, tissue engineering has led to research to find new alternatives that imitate the human bone, like synthetic implants [3].

Currently, the ideal implant must act as a temporally template while bone regeneration occurs. This means that the scaffold should be bioactive, biodegradable at the same bone regeneration rate, osteoinductive and osteoconductive, and must promote osseointegration. The scaffold must be porous and present surface properties to allow cell proliferation and vascular ingrowth, and to promote cell fixation

[1,3,4]. In line with all sense, ceramic materials stand out for presenting some of these requirements, especially calcium phosphates [5]. The excellent biocompatibility of this ceramic type is due to chemical similarity with biological bone, constituted in approximately 60% by calcium phosphate called hydroxyapatite [4]. The structure of this biological apatite contains trace elements or ions that perform a fundamental function in angiogenesis and bone metabolism. Even these can be important enzyme cofactors during bone tissue growth. Some such ions are Na^+, Mg^{2+}, K^+, CO_3^{2-}, Cl^- and F^-, and they enter the apatite by ion substitution for Ca^{+2} [3,6].

In order to create a material that better resembles biological bone, recent studies have used calcium phosphate, which has been previously studied to dope them with ions and to promote a special function in the scaffold [7–10]. One of these elements is strontium (Sr), which corresponds to 0.335% in relation to the total calcium content in the human body [7]. Strontium has been used to treat osteoporosis for several years given its ability to decrease bone resorption and to promote bone growth [11]. The Sr^{2+} ion has been replaced in some calcium

85

phosphate ceramic scaffolds, which demonstrates its cooperative role with calcium. Both ions suppress the activity of osteoclasts and promote the functions of osteoblasts [10]. The effects of Sr on osteoblast have been experimentally demonstrated *in vitro* and are attributed to the increased expression of alkaline phosphate activity, collagen type I and osteocalcin [12].

Another of the molecules found in mineralized tissue, such as teeth and bones, is pyrophosphate, which represents 0.5% of the total phosphate content [13]. Its chemical structure consists of two inorganic phosphate molecules joined by a hydrolysable ester [14]. Previous studies have shown that pyrophosphate is an important regulator of the bone mineralization process, and very much depends on the performance of other enzymes [15,16]. According to requirements, pyrophosphate can be released extracellularly or be formed from ATP breaking down due to the action of enzyme NPP1. This pyrophosphate prevents mineralization by binding strongly to the surface of hydroxyapatite crystals, which, as a result, blocks nucleation points for future crystals. However, in the presence of the TNAP enzyme, pyrophosphate is hydrolyzed into two phosphate molecules that will subsequently promote bone formation and mineralization. In general, the relationship between pyrophosphate and phosphates is a factor that regulates the bone mineralization process [17].

This pyrophosphate and the doped calcium phosphate were synthesized previously and used as ceramic implants. Some methods employed to fabricate scaffolds include rapid prototype, electrospinning, gas foaming, freezing-drying, gel casting replica, polymer foam replication, impregnate sintering, solvent casting, particulate leaching, 3D printing, etc. [3,18]. The polymer sponge replica method is one of the most widely used because it allows scaffolds with high interconnected porosity to be obtained. This method consists in impregnating a polymeric sponge with ceramic slurry, which is subsequently dried and sintered to eliminate organic material and to promote densification [18–20]. However, the majority of the ceramic that presents biocompatibility, when fabricated by these methods, results in very porous scaffolds without adequate mechanical strength to function as bone implants [20]. The most recent idea is to create a multilayer or stratified material, where the internal scaffold layers consist of chemical formulations that provide mechanical resistance, while outer layers confer bioactivity and biocompatibility [21].

The objective of this work was to obtain 3D porous ceramic scaffolds with multiplex layers. A 3D scaffold with composition SiO_2–$25P_2O_5$–$68CaO$–$6Li_2O$ (mol%) (referred to as the core from this point onward) was coated with layers with composition $29SiO_2$–$3P_2O_5$–$68CaO$ (mol%). The external scaffold layers were doped with Sr^{2+} ions at different concentrations (0%, 1%, 3%, 10%, 25% and 50%) in relation to the total Ca^{2+} moles.

2. Materials and methods

2.1. Material preparation

Multilayer 3D scaffolds were made by combining the sol-gel and polymeric sponge replication methods. The solution of the core with composition SiO_2–$25P_2O_5$–$68CaO$–$6Li_2O$ (mol%) was prepared in two stages. In the first stage, hydrolysis commenced by mixing 0.38 mL of Si (OC_2H_5) (TEOS, Aldrich - Tetraethyl Orthosilicate 98%), 10.2 mL of $(C_2H_5)_3PO_4$ (TEP, Aldrich - Triethyl Phosphate $\geq$ 99.8%), 20 mL of distilled water, 5 mL of ethanol 97° and 10 mL of hydrochloric acid (HCl 37%, Ensure). The mixture was stirred for 30 min to promote the reaction. Subsequently in the second reaction stage, 0.5 g of lithium carbonate (Li_2CO_3, Sigma-Aldrich 99%) was added to reinforce mechanical properties, as were 8.04 g of calcium carbonate ($CaCO_3$, Sigma $\geq$99%). The pH of the final solution was adjusted between 2 and 3 with HCl, added drop by drop. Finally, the solution was heated to 100 °C for 30 min until an oil solution capable of wetting sponges was achieved.

Polyurethane sponges (20 ppi, 12.7 mm diameter, 10 mm high)

were submerged in the sol-gel solution and dried in an oven at 140 °C for 20 min. Once the first layer had dried, the process was repeated about 30 times until all the sponge bridges were covered. Then it was sintered at a heating rate of 18.5 °C/h to reach 950 °C, which was maintained for 8 h.

After obtaining the manipulable scaffold core, the sol-gel solution of the external layers was made, whose composition was $29SiO_2$–$3P_2O_5$–$68CaO$ (mol%). This solution was obtained by mixing 11.03 mL of TEOS, 1.63 mL of TEP, 20 mL of distilled water, 5 mL of ethanol 97°, 10 mL of HCl and 11.33 g of $CaCO_3$. The pH of the solution was adjusted between 2 and 3 by the addition of HCl, added drop by drop. For the samples coated with the external composition doped with Sr^{2+}, the original calcium carbonate moles were replaced with strontium carbonate ($SrCO_3$, Alfa Aesar 99%) according to the corresponding substitution percentage. The amounts of strontium carbonate added in each solution were 0.17 g, 0.50 g, 1.67 g, 4.18 g and 8.36 g, which correspond to 1%, 3%, 10%, 25% and 50% of calcium molar substitution, respectively. For all the above solutions, the remaining moles (necessary to complete the original CaO moles) were added as calcium carbonate.

Afterward, the core was coated with each previous solution and dried at 200 °C for 5 min. This process was repeated 5 times to not eliminate the core scaffold porosity. Finally, scaffolds were resintered at a heating rate of 92.5 °C/h to reach 950 °C, which was maintained for 3 h. The composition and label of the final scaffolds are found in Table 1.

2.2. Material characterization

The morphology of the ceramic scaffolds was characterized by Scanning Electron Microscopy with Energy Dispersive X-Ray Spectroscopy (SEM-EDX) by a Hitachi S–3500 N with INCA system by Oxford Instruments Analytical.

The composition and crystalline phases were evaluated by X-Ray Diffraction (XRD, Bruker- AXR D8 Advance) using Cu-K$_\alpha$ radiation (1.5418740 Å) with Bragg-Bretano thetha-2thetha geometry and secondary graphite monochromator. Data were collected between 21° and 36° (2θ) at 0.02 steps, counting 8 s per step. The X-Ray tube was operated at 40 kV and 30 mA. The diffractograms of samples were compared with the Crystallography Open Database (COD) and the Inorganic Crystal Structure Database (ICSD). All diffractograms were analyzed by the version 3.7.1.132 of the Match! software.

Chemical composition was evaluated by Fourier Transform Infrared Spectroscopy (FTIR, spectrometer Thermo Scientific Nicolet iS5 equipped with an iD5 ATR accessory). Spectra were collected between $550 \, cm^{-1}$ - $1450 \, cm^{-1}$ at room temperature and a resolution of $4 \, cm^{-1}$ using 64 scans.

The porosity and pore distribution of the 3D scaffolds were evaluated by the Mercury Porosimetry Technique (Poremaster 60 GT Quantachrome instruments) at a pressure range between 66.6 bar and 4104.84 bar.

The mechanical strength of both the core and the core coated with

Table 1
Composition (mol%) of scaffolds.

|	Core				External layers			
	SiO_2	P_2O_5	CaO	Li_2O	SiO_2	CaO	P_2O_5	SrO
Core	1	25	68	6	–	–	–	–
C/EL-0Sr	1	25	68	6	29	68	3	–
C/EL-1Sr	1	25	68	6	29	67.3	3	0.7
C/EL-3Sr	1	25	68	6	29	66	3	2
C/EL-10Sr	1	25	68	6	29	61	3	7
C/EL-25Sr	1	25	68	6	29	51	3	17
C/EL-50Sr	1	25	68	6	29	34	3	34

86
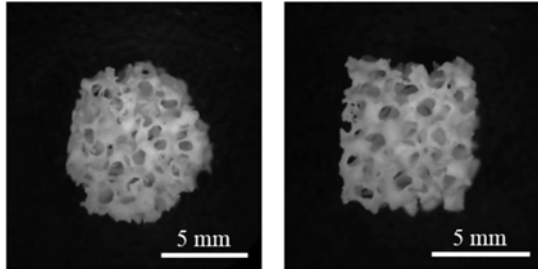
Fig. 1. Optical images of the representative ceramic 3D scaffolds obtained by the sol-gel and polymer replication methods.

the outer layers was evaluated by the compressive strength of the scaffolds by a Microtest SCM3000 mechanical tester. Tests were carried out by applying loads to 25 cylindrical scaffolds of the core and core coated (8.5 mm diameter, 7.0 mm high) at a speed of 1.00 mm/min until the scaffold completely broke.

2.3. In vitro bioactivity evaluation

In order to evaluate bioactivity, scaffolds were soaked in simulated body fluid (SBF), which was prepared according Kokubo's guidelines [22]. All the samples soaked in SBF were immersed in a water bath at 37 °C for 3 days, 7 days and 14 days. After each time, samples were characterized by SEM-EDX.

3. Results

3.1. Sample characterization

The ceramic scaffolds fabricated by the sol-gel and polymer replication methods were observed under an optical microscope. Fig. 1 shows how the scaffolds looked, which presented a cylindrical shape and interconnected pores.

The microstructure of all different scaffold types was studied by SEM-EDX (Fig. 2). Fig. 2 (a) shows the microstructure of the core of scaffolds, which presents hexagonal grains (●) and a Ca/P ratio varying from the edge to the middle of these grains. At the edges of the hexagonal grains, the Ca/P ratio is 1.3, and is 1.2 in the middle. On the surface, the presence of small crystals was observed (*) with a Ca/P ratio of 1.6, and rods (→) with a ratio of 1.2. Fig. 2 (b) shows the C/EL-0Sr scaffold microstructure with the previous hexagonal grains present in the core, but now coated with a new layer with a Ca/P ratio of 1.2 (♦). Another structure observed on the sample surface was bright precipitates which, when analyzed by EDX, were seen to be formed only by silicon (▼). The following figures (Fig. 2(c–e)) show the microstructure of the Sr-doped scaffolds. In these cases when the percentage of Sr ions rises, the amount of silicon precipitates on the surface increases. The EDX results demonstrated that the silicon content in the bright precipitates varied from 7.76 wt% of Si to 19.09 wt% of Si for samples C/EL-0Sr and C/EL-50Sr, respectively. The amount of Sr was not detected in samples C/EL-1Sr and C/EL-3Sr because it went below the SEM-EDX detection limit. However, Sr content varied from 3.30 wt% of Sr to 28.06 wt% of Sr in samples C/EL-10Sr and C/EL-50Sr, respectively.

Fig. 3 shows the diffractions patterns of the core, samples C/EL-0Sr and samples C/EL-25Sr and C/EL-50Sr, as being representative of all the doped scaffolds. The XRD pattern of the core showed characteristic peaks of the following phases: calcium diphosphate ($Ca_2P_2O_7$) (COD 96-100-1557), beta tricalcium phosphate (β-$Ca_3(PO_4)_2$) (COD 96-151-7239), $LiCa(PO_4)$ (COD 96-722-2995), $Ca_{9.95}Li_{1.05}(PO_4)_7$ (COD 96-152-6054), cristobalite (SiO_2) (COD 96-900-8228) and chlorapatite ($Ca_5(PO_4)_3Cl$) (COD 96-210-5266). Sample C/EL-0Sr presented the

same phases as the core, but showed a modified crystallinity for some phases. A decrease in the peaks corresponding to the $Ca_2P_2O_7$ phase and an increase in the peaks of phases β-$Ca_3(PO_4)_2$, $LiCa(PO_4)$, $Ca_{9.95}Li_{1.05}(PO_4)_7$, and SiO_2 can be seen.

Furthermore, the diffraction patterns of samples C/EL-25Sr and C/EL-50Sr, also shown in Fig. 3, presented the characteristic peaks of the phases found in the core and a two new phases containing Sr. These phases corresponded to strontium silicate (Sr_2SiO_4) (ICSD 35667) [23] and nonstoichiometric calcium/strontium silicate ($Ca_{1.65}Sr_{0.35}$) (SiO_4) (COD 96-153-5820). In both samples, a decrease in the peaks corresponding to phase $Ca_2P_2O_7$ took place, as well as a drop in the crystallinity of sample C/EL-50Sr compared to sample C/El-25Sr. Particularly, sample C/EL-50Sr showed a low expression of the peaks corresponding to phases $Ca_2P_2O_7$, β-$Ca_3(PO_4)_2$, $LiCa(PO_4)$, $Ca_{9.95}Li_{1.05}(PO_4)_7$, but an increase in the peaks corresponding to phases Sr_2SiO_4, ($Ca_{1.65}Sr_{0.35}$) (SiO_4), $Ca_5(PO_4)_3Cl$ and SiO_2.

Fig. 4 presents the FTIR spectra of all the samples, while Table 2 shows the vibration modes assigned to each observed signal. In the spectrum to the core, different signals were observed between 1000 cm^{-1} and 1185 cm^{-1}, which correspond to the superposition of the asymmetrical stretching of the groups Si–O–Si and PO_4^{3-}, that usually present vibrational modes between 1000-1300 cm^{-1} [24–28] and 1000-1100 cm^{-1} [24], respectively. The presence of group Si–O–Si was also corroborated by the 800 cm^{-1} signal, which corresponds to symmetrical stretching or bending vibration, previously reported between 760 cm^{-1} and 850 cm^{-1} [24,28]. Likewise, the signals observed at 938 cm^{-1} and 969 cm^{-1}, and those at 584 cm^{-1} and 668 cm^{-1}, correspond to the symmetrical stretching and bending vibration of group PO_4^{3-}, that are reported in 900–970 cm^{-1} [24] and 520-660 cm^{-1} [4,24,29], respectively. Finally, the presence of the pyrophosphate group ($P_2O_7^{4-}$) was observed given the signals at 1208 cm^{-1} [30], 919 cm^{-1} [30] and 724 cm^{-1} [9,30].

The samples coated with outer layers (with and without Sr ions) presented diminished intensity for the signals between 1027 cm^{-1} and 1200 cm^{-1}. However, signals remained around 1000 cm^{-1}, which could be attributed to the presence of groups Si–O–Si and PO_4^{3-}. A diminished intensity of the peaks corresponding to the pyrophosphate group was observed and a signal at 848 cm^{-1} appeared, which could be attributed to the vibration of group Si–O–2NBO [24,25]. This group corresponded to the stretching modes of Si–O with two non bonding oxygens per SiO_4 tetrahedron, due to the presence of alkaline earth elements, such as Ca and Sr. Another group identified was Si-O-NBO at 900 cm^{-1}, which is usually reported between 890 and 975 cm^{-1} [24,25].

Fig. 5 presents the curves obtained by the Mercury Porosimetry Technique, and Table 3 shows the total porosity and specific surface area obtained by the core, sample C/EL-0Sr and C/EL-50Sr, as being representative of all the doped scaffolds. Fig. 5 (a) shows how the core presents two regions of intruded volume. The first region shows a bigger intruded mercury volume, which corresponded to a range of pore diameters between 125 µm and 15 µm. The second region displays a smaller intruded mercury volume, which corresponded to a pore diameter that varied between 2.7 µm and 0.5 µm. Fig. 5 (b) shows that the core had a bimodal pore size distribution with more pores around 80 µm, as well as a second group of pores, with a diameter around 2 µm. In general, the Mercury Porosimetry Technique allows information to be obtained about pores smaller than 300 µm. For the core, total porosity was 41.9% (< 300 µm), with a specific surface area of 0.71 m²/g (see Table 3). Additionally, Archimedes' principle allows the porosity corresponding to pores bigger than 300 µm to be obtained. In this case, the core's total porosity was 71.9%.

Scaffold C/EL-0Sr presented a bigger intruded mercury volume compared to the core, which fell within the 108 µm–0.5 µm pore diameter range, as shown in Fig. 5 (a). This sample had a bigger total porosity of 52.5% (< 300 µm) and a wider pore size distribution. Fig. 5 (b) depicts how the sample presented four pore diameter peaks

87
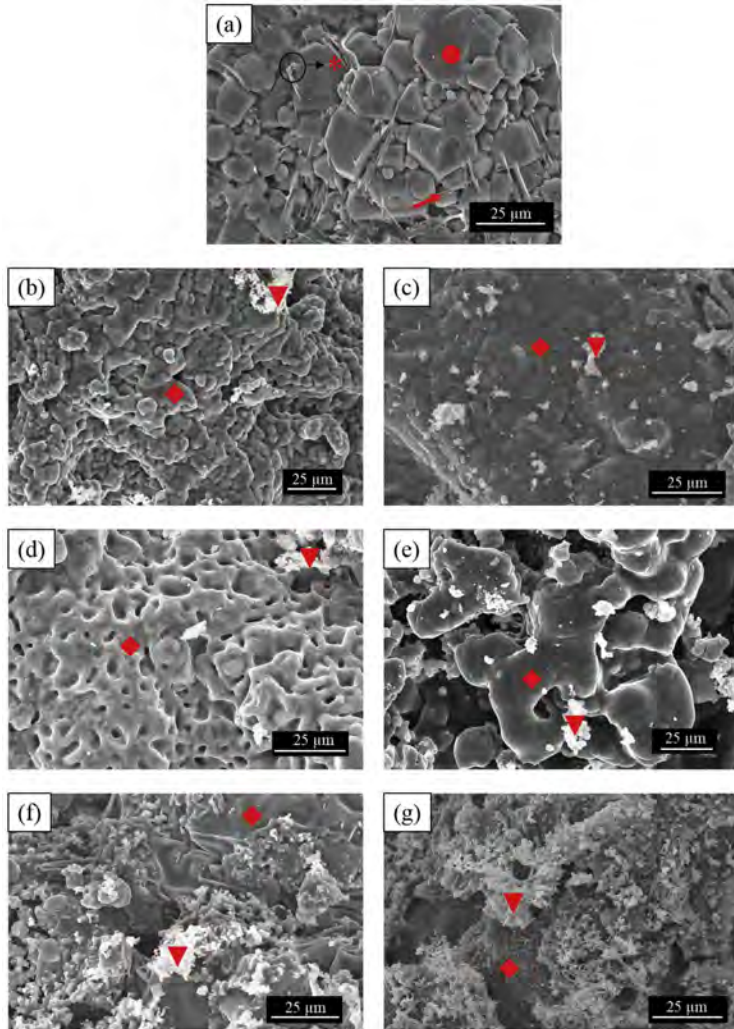
Fig. 2. SEM images of scaffolds: (a) Core; (b) C/EL-0Sr; (c) C/EL-1Sr; (d) C/EL-3Sr; (e) C/EL-10Sr; (f) C/EL-25Sr; (g) C/EL-50Sr. Identified morphologies: hexagonal grain (●), small crystals (*), rods (→), external layer (♦) and bright precipitates (▼).

corresponding to 46.2 μm, 15 μm, 9.5 μm and 3.3 μm. However, the sample also had a specific surface area of 0.32 m^2/g, which represents a decrease compared to the core. According to the Archimedes results, this sample's total porosity was 64.2% (> 300 μm).

Finally, sample C/EL-50Sr had a similar amount of intruded volume to the core, with pore diameter values ranging between 189 μm and 3.8 μm. Unlike the core however, the sample showed a wider pore size distribution with peaks at 101 μm, 46.8 μm and 30 μm: see Fig. 5 (b). This sample had a total porosity of 40.8% (< 300 μm) and its specific surface area was 1.83 m^2/g. The Archimedes results revealed that this sample's total porosity was 69.4% (> 300 μm).

Regarding the scaffolds' compressive strength, Table 3 presents the values obtained for the core and the core coated with outer layers. The core presented a range of compressive strength values between 0.9 and 1.6 MPa, while the core coated with the doped and undoped layers presented a range of values between 0.9 and 1.8 MPa.

3.2. In vitro bioactivity

In relation to the *in vitro* bioactivity results, Fig. 6 shows the obtained SEM images corresponding to the core and sample C/EL-0Sr. Fig. 7 provides the Sr-doped samples.

Fig. 6(a–c) depicts the core's morphology after SBF immersion at 3 days, 7 days and 14 days, respectively. After the SBF immersions, the sample still presented hexagonal grains, small crystals and rods, which were observed before being soaked in SBF (Fig. 2 (a)).

Fig. 6(d–f) shows sample C/EL-0Sr's morphology after SBF immersion at 3 days, 7 days and 14 days, respectively. Fig. 6 (d) reveals that after 3 immersion days, no morphological changes were observed compared to the same sample being soaked in SBF before (Fig. 2 (b)). After 7 days in SBF (Fig. 6 (e)) the sample presented a dissolution of the original precipitates, which covered the core's hexagonal grains and revealed bright precipitates on the surface, which contained silicon as

88
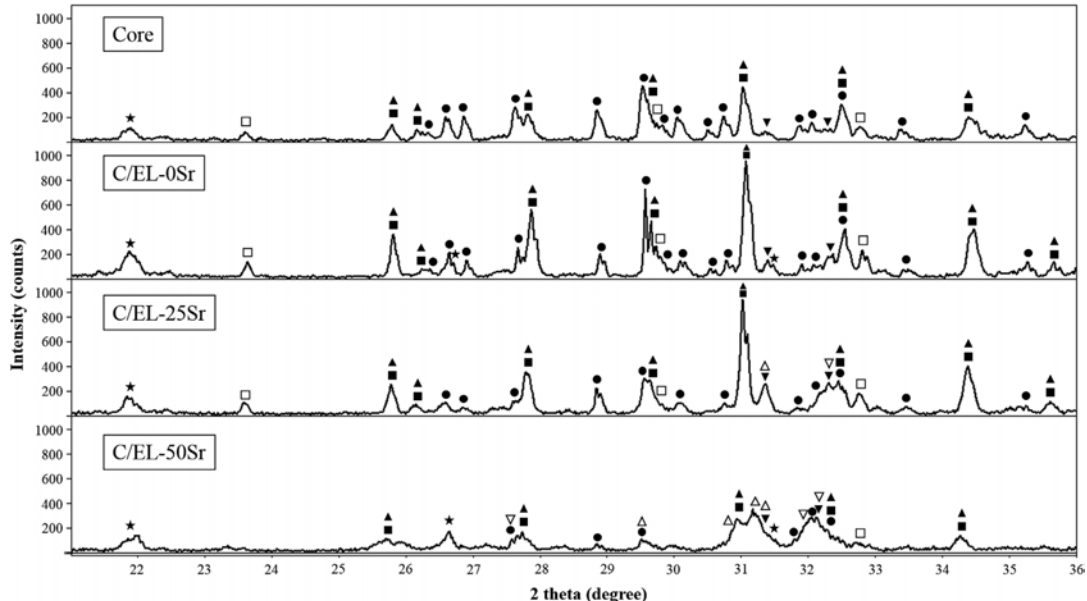
Fig. 3. The XRD diffraction patterns of the core and scaffolds C/EL-0Sr, C/EL-25Sr and C/EL-50Sr (● $Ca_2P_2O_7$, ■ β-$Ca_3(PO_4)_2$, □ $LiCa(PO_4)$, ▲ $Ca_{9.95}Li_{1.05}(PO_4)_7$, ▼ $Ca_5(PO_4)_3Cl$, ★ SiO_2, △ Sr_2SiO_4 and ▽ $(Ca_{1.65}Sr_{0.35})$ (SiO_4)).
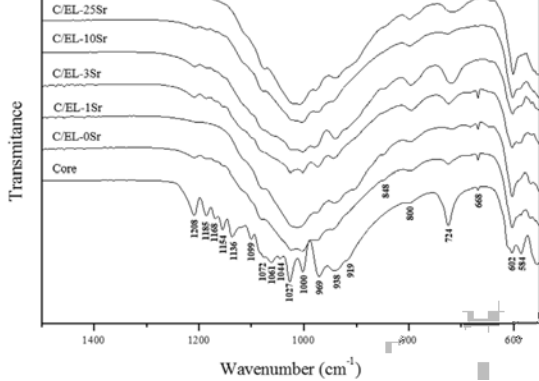
Fig. 4. The scaffold's FTIR spectra.

Table 2
The scaffold's FTIR vibrational modes.

Wavenumber (cm^{-1})	Vibrations
1000–1185	Si–O–Si asymmetrical stretching
1000–1099	PO_4^{3-} asymmetrical stretching
1208	$P_2O_7^{4-}$
938/969	PO_4^{3-} symmetrical stretching
919	$P_2O_7^{4-}$
900	Si-O-NBO stretching
800	Si–O–Si symmetrical stretching or bending
848	Si–O–2NBO stretching
724	$P_2O_7^{4-}$
584/602/668	PO_4^{3-} bending

corroborated by EDX.

However after 14 days in SBF, Ca–P precipitates with globular morphology formed on the sample's surface (see Fig. 6 (f)). EDX gave a Ca/P ratio of 1.67, which corresponded to hydroxyapatite [31].

Fig. 7 shows the changes in the Sr-doped scaffolds after being soaked in SBF. Fig. 7(a–c) presents the surface morphology of sample C/EL-1Sr soaked in SBF. After 3 days in SBF (Fig. 7 (a)), the sample presented precipitates with a globular morphology and a Ca/P ratio of 1.66, which corresponded to the Ca/P ratio of hydroxyapatite. This Ca/P ratio did not change after 7 days and 14 days (Fig. 7(b–c)), which means that hydroxyapatite continuously precipitated. After 3 days however, the globular morphology size was 4.8 μm. After 7 days and 14 days, these individual globules joined and formed larger precipitates, as indicated by the red arrow (above) in Fig. 7(a–c). The hydroxyapatite that precipitated at 3 days was covered with a second precipitate, as revealed by EDX, and corresponded to NaCl crystals (▲). However, these crystals progressively dissolved for longer immersion times.

Fig. 7(d–f) shows sample C/EL-3Sr after being soaked in SBF. After 3 days of immersion in SBF (Fig. (d)), the sample displayed no morphological modifications compared to its initial state (Fig. 2 (d)). However after 7 days and 14 days in SBF, Ca–P precipitates with a globular morphology appeared on the surface (Fig. 7(e–f)). EDX gave a Ca/P ratio of 1.6 for both these times, which corresponded to the hydroxyapatite ratio. Like sample C/EL-1Sr, the globular morphology was united and formed larger precipitates, as shown by the red arrows in Fig. 7(e–f).

Fig. 7(g–i) illustrates sample C/EL-10Sr after being soaked in SBF. After 3 days in SBF, the sample presented precipitates on the surface, similarly to the hydroxyapatite observed in previous samples. The EDX analysis revealed that besides these precipitates containing Ca and P, they also presented Sr and Si. In this case, the (Ca + Sr)/P ratio had to be considered because 10 mol% of Ca^{2+} ions were substituted for Sr^{2+}. On the precipitate surface, this ratio was 1.64, which indicated the existence of hydroxyapatite substituted for Sr. EDX also confirmed the presence of 5.50 wt% of Si, which was maintained by the

89
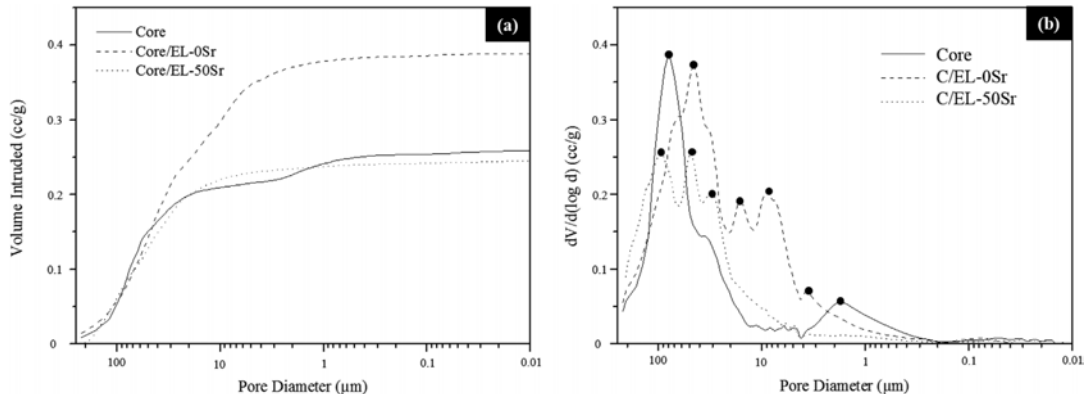
Fig. 5. Mercury porosimetry curves: (a) Cumulative and (b) Differential intrusion vs. pore diameter in scaffolds.

microstructure after immersion in SBF. Notwithstanding after 7 days and 14 days of SBF immersion (Fig. 7(h–i)), the Ca/P ratio was 1.60 for both times, which corresponded to the hydroxyapatite ratio obtained in previous samples. In these cases, EDX did not detect any Sr or Si on the surface, which could be due to these ions being released from the sample or the thick hydroxyapatite layer not allowing these ions to migrate from the material to the outside. The precipitate presented a globular morphology after 7 days of immersion. After 14 days, the different globular morphologies were joined to form the only precipitate-like plates on the surface, as seen in Fig. 7(h–i).

Fig. 7(j–l) shows sample C/EL-25Sr after being soaked in SBF. After 3 days in SBF (Fig. 7 (j)), this sample presented initial coating dissolution (Fig. 2 (f)) and the characteristic hexagonal grain of the core was noted after 7 days (Fig. 7(k)). Nevertheless after 14 days in SBF (Fig. 7 (l)), surface precipitates formed and the EDX analysis revealed that the surface of the sample content was 13.3 wt% of Si. Finally, Fig. 7(m–o) shows sample C/EL-50Sr after being soaked in SBF. After 3 days (Fig. 7 (m)), the sample showed the initial coating dissolution observed in Fig. 2 (g). However, precipitates formed on the sample's surface after 7 days in SBF (Fig. 7 (n)). EDX revealed the presence of Sr and, as well as sample C/EL-10Sr, it was necessary to consider the (Ca + Sr)/P ratio. This ratio was 1.7, which indicates that the precipitate could correspond to a type of hydroxyapatite modified by the presence of Sr. After 14 days in SBF, the whole precipitate on the surface was dissolved, as shown in Fig. 7 (o), and the characteristic hexagonal grains of the core surrounded by rods with a Ca/P ratio of 1 appeared (Fig. 7 (o)).

4. Discussion

In this study, ceramic scaffolds with composition SiO_2–CaO–P_2O_5 were manufactured by the sol-gel and polymer sponge replica methods. The combination of these methods has been previously used by other researchers to obtain porous scaffolds for future tissue engineering applications. However, in this work, two new variants were

incorporated into the manufacturing process that have been studied separately to date. The first variant was to create multilayer scaffolds composed of two different compositions (core + outer layers), while the second involved doping outer layers with Sr ions at different concentrations.

4.1. The scaffolds' porosity and compressive strength

In the scaffolds' design, porosity was one of the factors to control because macroporosity (pore size > 100 μm) [5] and microporosity (pore size < 10 μm) [5] play an important role in the cellular processes that promote bone growth. The polymer sponge replication method allowed interconnected porous to be obtained, whose size varied between 200 μm and 3 nm depending on the type of sponge [20]. However, when this method was combined with the sol-gel method, thanks to the quick gelation of the sol solution, pores can progressively close after each coating. For this reason, it is necessary to control the number of coatings and to create a compromise between the appropriate pore size and the number of coatings required to create a hard core after sintering. Fig. 5 shows that the scaffold core presents two average groups of different pore sizes: one up to 80 μm and another up to 2 μm. Part of this porosity is observed in Fig. 2 (a). Some correspond to the micropores formed when the hexagonal grains came into contact with the rods.

Furthermore, the curve of sample C/EL-0Sr, which corresponded to the core after coating, showed the formation of more pores with different sizes ranging from 108 μm to 0.5 μm. This indicated that the coating was not completely smooth and presented certain roughness, as shown in Fig. 2 (b). The specific surface area reduced compared to the core because the whole initial microstructure was covered with the new layers that filled the micropores. Finally, for the sample doping done with the maximum amount of Sr (C/EL-50Sr), pore size was between 189 μm and 3.8 μm, but the number of pores lowered compare to C/EL-0Sr. This decrease was attributed to the silicon agglomerates, as observed in Fig. 2 (g), which covered the previously rough coating

Table 3
Total porosity, surface area and compressive strength.

Sample	Porosity (%) < 300 μm[a]	Porosity (%) > 300 μm[b]	Surface Area (m²/g)	Compressive strength (MPa)
Core	41.9	71.9	0.71	0.9–1.6
C/EL-0Sr	52.5	64.2	0.32	0.9–1.8
C/EL-50Sr	40.8	69.4	1.83	

[a] Obtained by the Mercury Porosimetry Technique.
[b] Obtained by Archimedes principle.

90
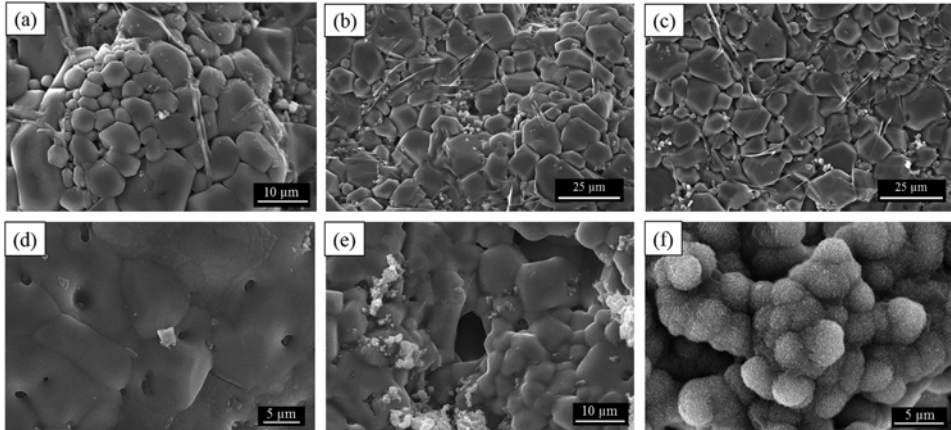
Fig. 6. SEM images of the core (above) and sample C/EL-0Sr (below) soaked in SBF for: (a,d) 3 days, (b,e) 7 days and (c,f) 14 days, respectively.

observed in sample C/El-0Sr. Consequently, these agglomerates caused the specific surface area to increase. A similar result was obtained by Hesaraki et al. [8], who observed how the specific surface area augmented when increasing the amount of Sr ion doping in glasses with composition $CaO–SiO_2–P_2O_5$. They suggested that this was due to the stress induced in the network while ions were being substituted. The ionic radius of Ca^{+2} was 1.00 Å and it was 1.13 Å for Sr^{+2}. Therefore, introducing larger ions created stress for the network and reduced particulate size and, consequently, increased the specific surface area.

Regarding the scaffolds' porosity, the total porosity corresponding to pores < 300 μm and > 300 μm was between 52.5% and 40.8%, and between 71.9% and 64.2%, respectively. In short, the porosity of the three analyzed scaffolds lay between 1 and 20 μm, which is important for the cell development, orientation and directionality of cellular in-growth [18]. Macropores of around 100 μm (detected by the Mercury Porosimetry Technique) and over 300 μm (detected by Archimedes principles) are necessary for nutrient supply, the waste removal of cells and for regenerating mineralized bone [18,32,33].

Another aspect considered while evaluating scaffolds was resistance to compression. The core provided a resistance around 0.9–1.6 MPa and the external layers increased the scaffolds' resistance to 0.9–1.8 MPa. The herein fabricated scaffold displayed greater resistance to compression than in other studies. For example by the sol-gel technique, other authors have obtained a resistance of 0.18–0.40 MPa and 0.02–0.03 MPa in system $SiO_2–CaO–P_2O_5$ and system $SiO_2–CaO–(Mg/Na/K)_yO_x$, respectively [19,20]. Regarding the influence of the dopant on the material's strength, Feng et al. [34] observed reduced compression resistance when doping β-TCP with more than 2.5 wt% of ZnO. Conversely, the resistance to compression of the material synthesized in the present study fell within the same range of values, regardless of the amount of dopant employed.

Human bone has a complex hierarchical structure that can be divided into cortical and trabecular bone in macro terms. Material obtained during present investigation is structurally comparable to trabecular bone or sponge, whose compressive strength is 0.2–4 MPa. In comparison, synthesized material's compressive strength came closer to the lower limit than to the upper limit of trabecular bone. However, as discussed by Chen et al. [35], a scaffold must have adequate mechanical resistance to allow it to be manipulated when it is applied but the scaffold's resistance does not need to equal bone because the cell culture and the new tissue to be formed *in vitro* will increase mechanical strength over time.

4.2. The scaffolds' chemical and mineralogical characterization

The scaffolds' chemical and mineralogical composition was evaluated by XRD, FTIR and SEM-EDX. Phases were identified for the core, sample C/EL-0Sr and doped samples C/EL-25Sr and C/EL-50Sr, which represent the intermediate and maximum amounts of the doped Sr ions. The XRD patterns of these samples are provided in Fig. 3. As observed, one of the phases present in the core was calcium diphosphate, constituted by two calcium ions joined to a pyrophosphate group ($P_2O_7^{4-}$). Pyrophosphate is a natural molecule found in the human body and an important regulator of the bone mineralization process. Some researchers have shown that pyrophosphate inhibits crystallization *in vitro,* but not *in vivo* [13], mainly because if the TNAP enzyme is present *in vivo*, it is able to hydrolyze the pyrophosphate molecule and form two phosphate groups to promote bone mineralization. The relation between pyrophosphate and phosphates is a determining factor during bone growth and the enzymes of the body act according to the organism's requirements. Pyrophosphate is able to prevent soft tissue calcification, and can cause diseases and abnormalities in bone tissue if it is lacking or found in excess [17].

The remaining phosphorus introduced into the material formed the tricalcium phosphate phase ($Ca_3(PO_4)_2$) and two additional phases containing lithium, one of which was stoichiometry ($LiCa(PO_4)$) and the other was non stoichiometry ($Ca_{9.95}Li_{1.05}(PO_4)_7$). The chloroapatite ($Ca_5(PO_4)_3Cl$) phase was also identified in the core, whose formation was attributed to hydrochloric acid (HCl) being added while preparing the sol-gel solution. Chloropatite is a material that began to be studied only quite recently given its ability to transform into hydroxyapatite when immersed with water [36]. Fahami et al. have demonstrated that the Zeta potential of chloropatite is negative at pH 5, 7.4 and 9, and a negative Zeta potential is a factor that favors osseointegration, apatite nucleation and bone regeneration. Likewise, they obtained bioactivity after a 14-day incubation in SBF [37]. Finally, one phase with silicon that corresponded to cristobalite (SiO_2) was identified.

The FTIR curves (Fig. 4) corroborate the presence of the phases identified by XRD. The signals at 724 cm^{-1}, 919 cm^{-1} and 1208 cm^{-1} confirm the presence of the pyrophosphate group, present in the calcium diphosphate phase. Another vibrational mode detected in the core group was PO_4^{3-}, which formed the tricalcium phosphate, chlorapatite or lithium-calcium phases. One group Si–O–Si was also detected, which may belong to the cristobalite phase.

Given the presence of different phases in the core, the microstructure observed by SEM (Fig. 2 (a)) corresponded to a combination of this. Generally, the tricalcium phosphate phase has shown a

91
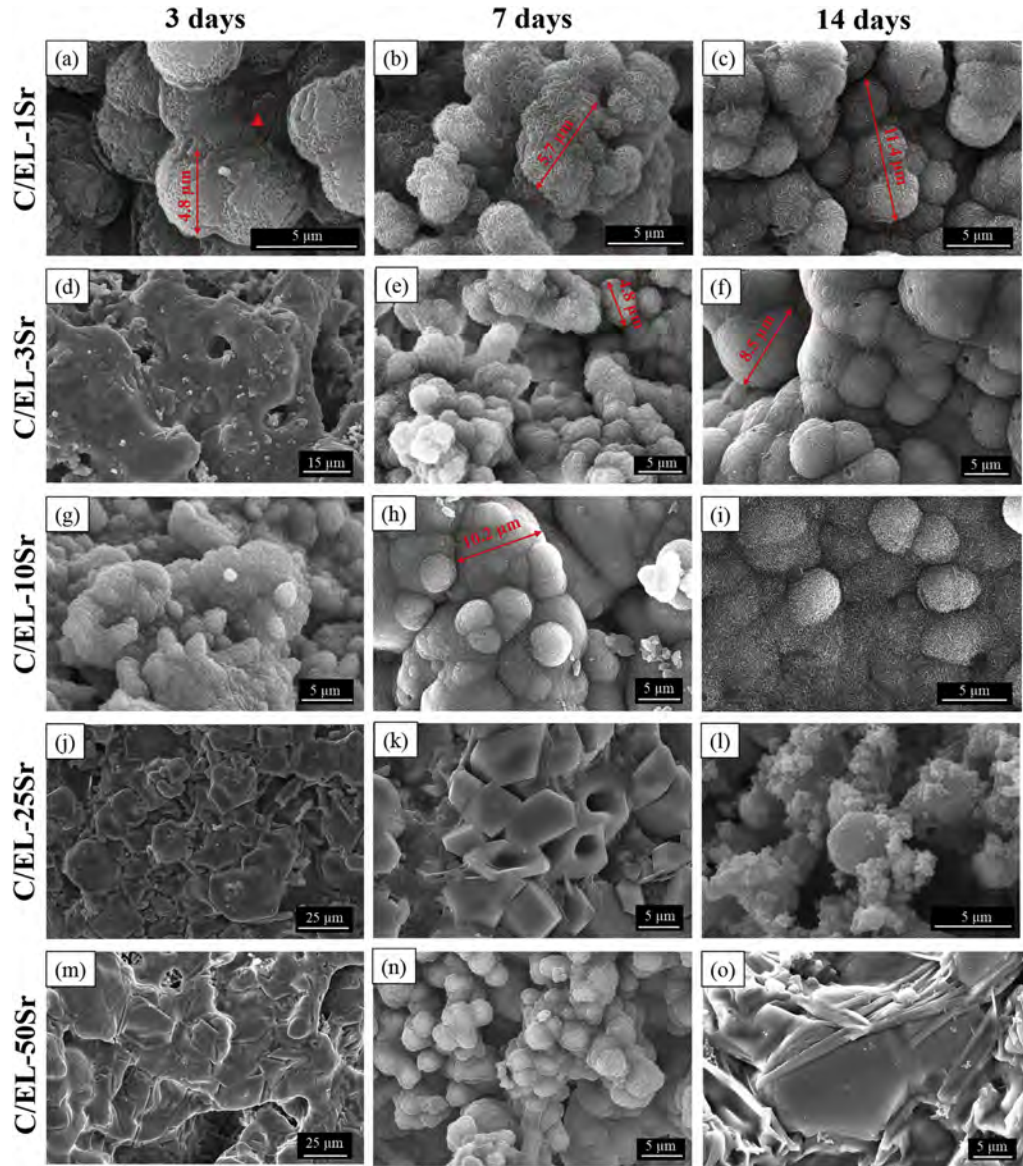
Fig. 7. The SEM images of C/EL-1Sr, C/EL-3Sr, C/EL-10Sr, C/EL-25Sr and C/EL-50Sr soaked in SBF for: (a,d,g,j,m) 3 days, (b,e,h,k,n) 7 days and (c,f,i,l,o) 14 days.

hexagonal grain [38] with a Ca/P ratio of 1.5. In this study however, the grain observed by SEM presented a different Ca/P ratio in the middle and on the edges of the hexagonal grains. This means that the structure was not pure beta tricalcium phosphate, but comprised a combination of the other phases.

Conversely, sample C/EL-0Sr showed a decrease in the peaks of phase $Ca_2P_2O_7$ and an increase in the peaks of phases β-$Ca_3(PO_4)_2$, LiCa (PO_4) and $Ca_{9.95}Li_{1.05}(PO_4)_7$. This behavior is attributed to the new interactions that took place during the second sintering process between the ions present in the core and the new ions added to the outer layers, which resulted in a new combination of phases. Phase $Ca_2P_2O_7$

had a Ca/P ratio of 1 and phase β-$Ca_3(PO_4)_2$ had a Ca/P ratio of 1.5. Therefore during the first core sintering, the phase with the lowest Ca/P ratio would be preferentially formed in relation to those phases that needed a larger quantity of Ca ions per P. However, by coating the core with the outer layers, which contained more Ca ions, the diffusion of these ions could occur during the sintering process and favor the formation of phase β-$Ca_3(PO_4)_2$. This was why a decrease in phase $Ca_2P_2O_7$ and an increase in phase β-$Ca_3(PO_4)_2$ occurred, including the phases of β-$Ca_3(PO_4)_2$ modified by the presence of lithium, which formed stoichiometric phase $LiCa(PO_4)$ and nonstoichiometric phase $Ca_{9.95}Li_{1.05}(PO_4)_7$, respectively. An increase in the peaks corresponding

92

to SiO_2 also took place as a result of incorporating the outer layers, whose composition provided a larger amount of Si.

The diffractograms of samples C/EL-25Sr and C/EL-50Sr showed the presence of the previously identified phases, and of two new phases that contained Sr. For the Sr-doped samples, a different behavior was observed than for sample C/EL-0Sr. Phases $Ca_2P_2O_7$ and β-$Ca_3(PO_4)_2$, which decreased and increased in sample C/EL-0Sr, both decreased in this case. On this occasion, ions were organized differently, which favored the formation of phases $Ca_5(PO_4)_3Cl$, Sr_2SiO_4 and $(Ca_{1.65}Sr_{0.35})$ (SiO_4). Likewise, loss of crystallinity was observed from sample C/EL-25Sr to sample C/EL-50Sr, which indicates that adding a bigger amount of Sr distorts the network of the initially obtained material by producing a bigger quantity of amorphous phase.

Other studies have reported accomplishing the formation of strontium silicate phases in bioglasses with compositions SiO_2–P_2O_5–CaO and SiO_2–P_2O_5–CaO–Na_2O with doping between 0-36 and 0–23.08%, respectively [27,29]. Both studies have shown that increasing doping enhances the bioactivity, except for the maximum doping performed by Macon et al. This sample corresponded to composition $60SiO_2$–$4P_2O_5$–$36SrO$ (%mol) and the SEM evaluation indicated the presence of a mixture of particle morphology, i.e. needle-like and glassy particles. This sample could be the equivalent to C/EL-50Sr, and like the sample of Macon et al., XRD evidenced amorphousness compared to sample C/EL-25Sr. Likewise, the SEM analysis (Fig. 2(c–g)) showed that as the amount of Sr increased in the samples, the scaffolds' surface presented a more irregular morphology.

The EDX analysis performed on the surface of the doped samples (Fig. 2(c–g)) showed that agglomerates contained Si and Sr, and that as the amount of Sr rose, the agglomerates distributed over the entire surface increased. This could be due to more phases Sr_2SiO_4 and $(Ca_{1.65}Sr_{0.35})$ (SiO_4) forming, or to amorphous phases forming that would have been created in the material as a result of the distortion caused by Sr in the material's network.

As for the FTIR of the coated samples (Fig. 4), the spectrum showed that the peaks corresponding to the pyrophosphate groups decreased, as did the intensity of the overlapping peaks of groups PO_4 and Si–O–Si between 1000 and 1200 cm^{-1}. The latter could be attributed to the lower phosphorus oxide content on the outer layers and to an increase in the amount of silicon oxide. Therefore, the larger amount of peaks within that range was attributed to group Si–O–Si. Another modification observed in sample C/EL-0Sr was the appearance of a peak at 848 cm^{-1}, which was attributed to the existence of group Si–O–2NBO that corresponded to nonbonding alkaline earth metals like Ca. Additionally, when this sample was doped with Sr, a new peak appeared around 900 cm^{-1}, which was attributed to the vibrations in group Si-O-NBO due, in this case, to the bigger amount of alkaline earth metals like Sr.

4.3. Scaffolds' in vitro characterization

Samples were immersed in SBF to evaluate the material's ability to transform into apatite precipitates and to, therefore, demonstrate their bioactivity *in vitro*. The scaffold's core presented no bioactivity for any of the times it came into contact with SBF, which confirms that the presence of pyrophosphate group inhibited the crystallization of hydroxyapatite *in vitro* [16]. However, for the core coated with the layers of different chemical compositions (sample C/EL-0Sr), the material displayed bioactivity after 14 days in SBF. The appearance of apatite precipitates on the surface could be attributed to the following factors: (i) an increase in the amorphous phase; (ii) an increase in the chlorapatite phase; and/or (iii) a decrease in the phase containing group pyrophosphate. Although the material presented no bioactivity in less than 14 days, this does not necessary mean a negative aspect because this study enabled the material's bioactivity to be modulated by doping the formulation of the outer layers with Sr ions at different concentrations.

In the Sr-doped scaffolds, samples C/EL-1Sr and C/EL-10Sr showed bioactivity after only 3 days in SBF, while sample C/EL-3Sr, which represented an intermediate doping concentration compared to the aforementioned samples, presented bioactivity after 7 days. Sample C/EL-25Sr presented no hydroxyapatite precipitates after 3 and 7 days in SBF (Fig. 7 (j) and (k)). On the contrary, the material that initially coated the core (Fig. 2 (f)) was dissolved, and it was possible to observe the core's characteristic microstructure. After 14 days immersed in SBF, precipitates similar to hydroxyapatite appeared on the surface which, when analyzed by EDX, were seen to be formed mainly by Si. Finally, the behavior of sample C/EL-50Sr was similar to that of sample C/EL-25Sr because after 3 days in SBF (Fig. 7 (m)), the dissolution of the material that initially coated the core took place (Fig. 2 (g)). After 7 days in SBF (Fig. 7 (n)), hydroxyapatite precipitates appeared on the surface and EDX showed that they were formed by Ca, Sr and P, and that hydroxyapatite could be doped with Sr. However, this precipitate was unstable because it disappeared after 14 days in SBF (Fig. 7 (o)).

The accelerated bioactivity of the scaffold's outer layers with small amounts of Sr (sample C/EL-1Sr compared to sample C/EL-0Sr) was due to the substitution of Ca^{2+} ions for Sr^{2+}, which caused distortions in the network. This distortion made the material less stable and allowed ions to be more easily released and exchanged with SBF, and to thus create new hydroxyapatite nucleation points. For example, Shahrabi et al. argues that bioglasses doped with Sr release more Si ions to the environment when they are immersed in SBF and, therefore, accelerate bioactivity [28]. According to the general mechanism of bioactivity, Si–O–Si bands must break and form two Si–OH groups by releasing one of these to the medium, while another Si–OH group remains at the interface by creating nucleation points of hydroxyapatite [39,40]. This means that depending on the dopant concentration, different phases form and Si is released in SBF to a greater or lesser extent, which modified the material's bioactivity. This would explain the iterative behavior observed in the other doped samples, as well as the differences found in previous studies in the effect that Sr had on the material's bioactivity. Macon et al. [27] and Fredholm et al. [29] obtained an accelerated formation of hydroxyapatite layers by increasing the percentage of doped Sr in samples. Heseraki et al. [8] reported a delay in apatite layer formation, and suggested that the energy required to break the Sr–O bond of group Si–O–Sr exceeded that required to break Ca–O from group Si–O–Ca [8].

The *in vitro* tests carried out in this research work allowed the bioactivity of polycrystalline ceramic materials to be interpreted according to two new variants. First, the concept of "layers of bioactive formulations" in the SiO_2–CaO–P_2O_5 system was created, which can be incorporated into mechanically resistant ceramic scaffolds that do not have bioactivity. Second, it was demonstrated that these bioactive layers' bioactivity is modulated by adding doping elements at different concentrations, which allows to adjust the precipitation time of hydroxyapatite in already known formulations.

5. Conclusions

Ceramic scaffolds with multiplex layers were fabricated by the sol-gel and polymer sponge replica methods. The scaffold consists of a core with composition SiO_2–$25P_2O_5$–$68CaO$–$6Li_2O$ (mol%) and outer layers with composition $29SiO_2$–$3P_2O_5$–(68-x)CaO-xSrO (x = 0, 0.7, 2, 7, 17, 34) (mol%).

The fabricated scaffolds had adequate porosity and mechanical strength to be used in the bone tissue engineering field. In relation to the samples' bioactivity, the core's chemical formulation was not bioactive, although it was possible to coat it with layers of bioactive chemical formulation in the SiO_2–CaO–P_2O_5 system, and bioactivity was achieved after 14 days in SBF. The outer layer's bioactivity was modulated by doping with Sr ions at different concentrations. The variation in the bioactive behavior of the samples doped with SrO indicates that the network is distorted at certain dopant concentrations,

93

and the capacity of dissolution and ion exchange with the medium can be modified and, consequently, the ability to precipitate hydroxyapatite on the surface can vary.

Specifically, samples C/EL-1Sr and C/EL-10Sr were very interesting as they were bioactive only after 3 days in SBF, and also for their composition presenting Sr ions, which will provide *in vivo* benefits.

Funding source

Declarations of interest

None.

References

[1] I. Denry, L.T. Kuhn, Design and characterization of calcium phosphate ceramic scaffolds for bone tissue engineering, Dent. Mater. 32 (2016) 43–53.
[2] J.R. Jones, P.D. Lee, L.L. Hench, Hierarchical porous materials for tissue engineering, Philos. Trans. R. Soc. A Math. Phys. Eng. Sci. 364 (2006) 263–281.
[3] J.J. Li, D.L. Kaplan, H. Zreiqat, Scaffold-based regeneration of skeletal tissues to meet clinical challenges, J. Mater. Chem. B 2 (2014) 7272–7306.
[4] N. Eliaz, N. Metoki, Calcium phosphate bioceramics: a review of their history, structure, properties, coating technologies and biomedical applications, Materials 10 (2017) 1-104.
[5] S.V. Dorozhkin, Bioceramics of calcium orthophosphates, Biomaterials 31 (2010) 1465–1485.
[6] S.V. Dorozhkin, Biocomposites and hybrid biomaterials based on calcium orthophosphates, Biomatter 1 (2011) 3–56.
[7] S.M. Rabiee, N. Nazparvar, M. Azizian, D. Vashaee, L. Tayebi, Effect of ion substitution on properties of bioactive glasses: a review, Ceram. Int. 41 (2015) 7241–7251.
[8] S. Hesaraki, M. Gholami, S. Vazehrad, S. Shahrabi, The effect of Sr concentration on bioactivity and biocompatibility of sol-gel derived glasses based on CaO-SrO-SiO2-P2O5 quaternary system, Mater. Sci. Eng. C Mater. Biol. Appl. 30 (2010) 383–390.
[9] S. Kannan, F. Goetz-Neunhoeffer, J. Neubauer, J.M.F. Ferreira, Cosubstitution of zinc and strontium in beta-tricalcium phosphate: synthesis and characterization, J. Am. Ceram. Soc. 94 (2011) 231–236.
[10] S. Thakur, S. Garg, G. Kaur, O.P. Pandey, Effect of strontium substitution on the cytocompatibility and 3-D scaffold structure for the xSrO-(10-x) MgO-60SiO(2)-20CaO-10 P2O5 (2 < = x < = 8) sol-gel glasses, J. Mater. Sci. Mater. Med. 28 (2017) 89–102.
[11] S. O'Donnell, A. Cranney, G.A. Wells, J.D. Adachi, J.Y. Reginster, Strontium ranelate for preventing and treating postmenopausal osteoporosis, Cochrane Database Syst. Rev. (2006) 31.
[12] S. Panzavolta, P. Torricelli, L. Sturba, B. Bracci, R. Giardino, A. Bigi, Setting properties and in vitro bioactivity of strontium-enriched gelatin-calcium phosphate bone cements, J. Biomed. Mater. Res. A 84A (2008) 965–972.
[13] R.E. Wuthier, R.G.G. Russell, S. Bisaz, H. Fleisch, Relationship between pyrophosphate, amorphous calcium phosphate and other factors in sequence of calcification in-vivo Calcified Tissue, Researcher 10 (1972) 198–206.
[14] R.A. Terkeltaub, Inorganic pyrophosphate generation and disposition in pathophysiology, Am. J. Physiol. Cell Physiol. 281 (2001) C1–C11.
[15] H. Fleisch, J. Maerki, R.G.G. Russell, Effect of pyrophosphate on dissolution of hydroxyapatite and its possible importance in calcium homeostasis, Proc. Soc. Exp. Biol. Med. 122 (1966) 317–320.
[16] H. Fleisch, R.G.G. Russell, S. Bisaz, P.A. Casey, R.C. Muhlbauer, Influence of Pyrophosphate Analogues (Diphosphonates) on Precipitation and Dissolution of Calcium Phosphate in Vitro and in Vivo, Calcified Tissue Research, S, 1968, pp.
1–10.
[17] I.R. Orriss, T.R. Arnett, R.G.G. Russell, Pyrophosphate: a key inhibitor of mineralisation, Curr. Opin. Pharmacol. 28 (2016) 57–68.
[18] M. Vallet-Regí, Bio-Ceramics with Clinical Applications, New York, (2014).
[19] P. Ros-Tarraga, A. Murciano, P. Mazon, S.A. Gehrke, P.N. De Aza, In vitro behaviour of sol-gel interconnected porous scaffolds of doped wollastonite, Ceram. Int. 43 (2017) 11034–11038.
[20] P. Ros-Tarraga, A. Murciano, P. Mazon, S.A. Gehrke, P.N. De Aza, New 3D stratified Si-Ca-P porous scaffolds obtained by sol-gel and polymer replica method: microstructural, mineralogical and chemical characterization, Ceram. Int. 43 (2017) 6548–6553.
[21] I.K. Jun, J.H. Song, W.Y. Choi, Y.H. Koh, H.E. Kim, Porous hydroxyapatite scaffolds coated with bioactive apatite-wollastonite glass-ceramics, J. Am. Ceram. Soc. 90 (2007) 2703–2708.
[22] T. Kokubo, H. Takadama, How useful is SBF in predicting in vivo bone bioactivity? Biomaterials 27 (2006) 2907–2915.
[23] K. Persson, Materials Data on Sr2SiO4 (SG: 62), Materials Project, 2014, https://doi.org/10.17188/1192715.
[24] H. Aguiar, J. Serra, P. Gonzalez, B. Leon, Structural study of sol-gel silicate glasses by IR and Raman spectroscopies, J. Non-Cryst. Solids 355 (2009) 475–480.
[25] Y.C. Fredholm, N. Karpukhina, R.V. Law, R.G. Hill, Strontium containing bioactive glasses: glass structure and physical properties, J. Non-Cryst. Solids 356 (2010) 2546–2551.
[26] S. Solgi, M. Khakbiz, M. Shahrezaee, A. Zamanian, M. Tahriri, S. Keshtkari, M. Raz, K. Khoshroo, S. Moghadas, A. Rajabnejad, Synthesis, characterization and in vitro biological evaluation of sol-gel derived Sr-containing nano bioactive glass, Silicon 9 (2017) 535–542.
[27] A.L.B. Macon, S.H. Lee, G. Poologasundarampillai, T. Kasuga, J.R. Jones, Synthesis and dissolution behaviour of CaO/SrO-containing sol-gel-derived 58S glasses, J. Mater. Sci. 52 (2017) 8858–8870.
[28] S. Shahrabi, S. Hesaraki, S. Moemeni, M. Khorami, Structural discrepancies and in vitro nanoapatite formation ability of sol-gel derived glasses doped with different stimulator ions, Ceram. Int. 37 (2011) 2737–2746.
[29] Y.C. Fredholm, N. Karpukhina, D.S. Brauer, J.R. Jones, R.V. Law, R.G. Hill, Influence of strontium for calcium substitution in bioactive glasses on degradation, ion release and apatite formation, J. R. Soc. Interface 9 (2012) 880–889.
[30] S. Raynaud, E. Champion, D. Bernache-Assollant, P. Thomas, Calcium phosphate apatites with variable Ca/P atomic ratio I. Synthesis, characterisation and thermal stability of powders, Biomaterials 23 (2002) 1065–1072.
[31] P. Velasquez, Z.B. Luklinska, L. Meseguer-Olmo, J. de Val, R.A. Delgado-Ruiz, J.L. Calvo-Guirado, M.P. Ramirez-Fernandez, P.N. de Aza, TCP ceramic doped with dicalcium silicate for bone regeneration applications prepared by powder metallurgy method: in vitro and in vivo studies, J. Biomed. Mater. Res. A 101 (2013) 1943–1954.
[32] V. Karageorgiou, D. Kaplan, Porosity of 3D biomaterial scaffolds and osteogenesis, Biomaterials 26 (2005) 5474–5491.
[33] K.A. Hing, Bioceramic bone graft substitutes: influence of porosity and chemistry, Int. J. Appl. Ceram. Technol. 2 (2005) 184–199.
[34] P. Feng, P.P. Wei, C.J. Shuai, S.P. Peng, Characterization of mechanical and biological properties of 3-D scaffolds reinforced with zinc oxide for bone tissue engineering, PLoS One 9 (2014) e87755.
[35] Q.Z.Z. Chen, I.D. Thompson, A.R. Boccaccini, 45S5 Bioglass (R)-derived glass-ceramic scaffolds for bone tissue engineering, Biomaterials 27 (2006) 2414–2425.
[36] X. Chen, R. Hill, N. Karpukhina, Chlorapatite glass-ceramics, Int. J. Appl. Glass Sci. 5 (2014) 207–216.
[37] A. Fahami, G.W. Beall, T. Betancourt, Synthesis, bioactivity and zeta potential investigations of chlorine and fluorine substituted hydroxyapatite, Mater. Sci. Eng. C Mater. Biol. Appl. 59 (2016) 78–85.
[38] E. Champion, Sintering of calcium phosphate bioceramics, Acta Biomater. 9 (2013) 5855–5875.
[39] A.H. De Aza, P. Velasquez, M.I. Alemany, P. Pena, P.N. De Aza, In situ bone-like apatite formation from a Bioeutectic((R)) ceramic in SBF dynamic flow, J. Am. Ceram. Soc. 90 (2007) 1200–1207.
[40] I.M. Martinez, L. Meseguer-Olmo, A. Bernabeu-Esclapez, P.A. Velasquez, P.N. De Aza, In vitro behavior of alpha-tricalcium phosphate doped with dicalcium silicate in the system Ca2SiO4-Ca-3(PO4)(2), Mater. Char. 63 (2012) 47–55.

94

Apéndice C

Artículo 3

New iron-doped multilayer ceramic scaffold with noncontinuous bioactive behavior

Author: N.A. Mata,P. Ros-Tárraga,P. Velasquez,A. Murciano,P.N. De Aza

Publication: Ceramics International

Publisher: Elsevier

Date: July 2020

© 2020 Elsevier Ltd and Techna Group S.r.l. All rights reserved.

Journal Author Rights

Please note that, as the author of this Elsevier article, you retain the right to include it in a thesis or dissertation, provided it is not published commercially. Permission is not required, but please ensure that you reference the journal as the original source. For more information on this and on your other retained rights, please visit: https://www.elsevier.com/about/our-business/policies/copyright#Author-rights

BACK   CLOSE WINDOW

New iron-doped multilayer ceramic scaffold with noncontinuous bioactive behavior

N.A. Mata[a],[*], P. Ros-Tárraga[a], P. Velasquez[a], A. Murciano[b], P.N. De Aza[a]

[a] *Instituto de Bioingeniería, Universidad Miguel Hernández, Avda. ferrocarril s/n, Elche, Alicante, 03202, Spain*
[b] *Departamento de Materiales, Óptica y Tecnología Electrónica, Universidad Miguel Hernández, Avda. Universidad s/n, Elche, Alicante, 03202, Spain*

ABSTRACT

New multilayer porous ceramic scaffolds, constituted by a core covered with external layers, are proposed as future bone tissue implants. The core with composition SiO_2 - $25P_2O_5$ – $68CaO$–$6Li_2O$ (mol%) provided suitable compressive strength (0.9–1.6 MPa) to act as an initial support during bone tissue regeneration. The external layers with composition $29SiO_2$ - $3P_2O_5$ - $(68-x)$ CaO - xFe_2O_3 (mol%) (x = 0.3 and 1) (samples C/EL-1Fe and C/EL-3Fe, respectively) conferred a bioactive character to scaffolds. The surfaces of both samples showed apatite precipitates after coming into contact with simulated body fluid (SBF). Sample C/EL-1Fe exhibited non-continuous bioactive behavior, with precipitates of apatite that precipitated and dissolved between days 1 and 28. Sample C/EL-3Fe showed precipitates after 8 days that remained until the end of the study time. This variation in material, achieved by modifying the amounts of iron in external layers, represents an important advance in the ability to control an implant's bioactivity in line with requirements of future applications.

1. Introduction

In recent years, the number of research works about developing ceramic materials to be used as bone substitution implants has increased. Ceramic materials are proven excellent candidates thanks to the similarity of their properties to human bone, and the possibility of mimicking the functions performed by this complicated tissue [1–3]. Human bone is a hierarchical structure formed by several structural levels. Levels begin with macrostructures, whose main components are cortical and cancellous bone, until nanostructures are formed by molecules [4,5]. This tissue is the framework that supports the body, facilitates movements, protects organs and participates in important biological mechanisms [6]. For all these reasons, it is so important to find alternatives to replace and repair the bone tissue affected by trauma or defect during aging.

Currently, the biggest challenge in manufacturing implants is combining different properties that initially seem to act in opposite ways. For example, the mechanical strength of ceramic scaffolds must come close to bone strength, and its porosity should allow cell growth. Additionally, the external surface that comes into contact with the organism must be bioactive and biocompatible [7].

Given this combination of requirements, the development of porous ceramic scaffolds constituted by multiplex layers is proposed to provide different functions. The feasibility of this multilayer system has been demonstrated by manufacturing porous 3D scaffolds with compositions in the SiO_2–CaO–P_2O_5 system and using ion doping, such as zinc and strontium, to potentiate natural bone processes [8,9]. Traces of these elements are found in the human body and play an important role in bone metabolism. Both stimulate new bone formation, while zinc has anti-inflammatory effects and strontium possesses an osteogenic expression [10,11].

The present work proposes using a new multilayer system with external layers doped with small percentages of iron. This element is a micronutrient that forms part of several biological processes, such as oxygen transport and DNA synthesis, among others. It is also an essential component of some metalloproteins, and is present in small amounts in teeth and bones [12,13]. Previously, iron has been doped in biomaterials, e.g. hydroxyapatite, and shown improvements in bactericidal and mineralization properties [12,14]. Other researchers have studied the influence of iron and its concentration on $β$-$Ca_3(PO_4)_2$, Vahabzadeh et al. reported effects on physico-mechanical properties, and the *in vitro* proliferation and differentiation of osteoblasts [15]. Singh et al. demonstrated that an adequate amount of iron produces hyperthermia and biocompatibility effects [16]. Finally, the iron incorporated in mesoporous silicate bioactive glass enhanced mitochondrial activity and the expression of osteogenic genes [17].

In this case, the resistant core is coated by external layers with a composition in the SiO_2–CaO–P_2O_5 system, and doped with 1% and 3%

Table 1
Reagents used in the sol-gel preparation for the core and scaffolds' external layers[a].

Sample	Core				External layers			
	TEOS (ml)	TEP (ml)	CaCO$_3$ (g)	Li$_2$CO$_3$ (g)	TEOS (ml)	TEP (ml)	CaCO$_3$ (g)	FeSO$_4$.7H$_2$O (g)
C/EL-1Fe	0.36	11.4	8.38	0.5	10.29	1.75	11.22	0.31
C/EL-3Fe							10.99	0.94

[a] All the preparations were carried out with 20 ml of distilled water, 5 ml of ethanol and 10 ml of HCl to obtain 10 g of sol.

of iron in relation to the total moles of calcium. This new material was characterized and *in vitro* bioactivity was studied.

2. Materials and methods

2.1. Preparation of the scaffolds

The multilayer 3D scaffolds were made by sol-gel and polymeric sponge replication methods. First, the ceramic scaffold core was made with composition SiO$_2$ - 25P$_2$O$_5$ – 68CaO–6Li$_2$O (mol%). To do so, the reagents shown in Table 1 were mixed in the following order: (1) triethyl phosphate (TEP, Aldrich $\geq$ 99.8%); (2) distilled water; (3) ethanol 97°; (4) tetraethyl orthosilicate (TEOS, Aldrich 98%); (5) hydrochloric acid (HCl 37%, Ensure); (6) lithium carbonate (Li$_2$CO$_3$, Sigma-Aldrich 99%); (7) calcium carbonate (CaCO$_3$, Sigma $\geq$99%). The mixture's pH was adjusted to between 2 and 3 by adding HCl drop by drop. Polyurethane sponges (20 ppi), with a 12.7 mm diameter and 10 mm high, were immersed 20 times in the solution and dried in an oven at 140 °C for 20 min after each immersion. Subsequently, sponges were sintered by heat treatment for 50 h until 950 °C, maintained for 8 h and slowly cooled to room temperature.

Second, the external layer's solutions were prepared with composition 29SiO$_2$ - 3P$_2$O$_5$ - (68-x) CaO - xFe$_2$O$_3$ (mol%) (x = 0.3 and 1). Table 1 shows the reagents and quantities used to prepare sol-gel, and they follow the same above-presented order. The mixture's pH was adjusted to between 2 and 3 by adding HCl drop by drop. The core was coated by this new solution and dried at 200 °C for 5 min. This process was repeated 5 times and resintered for 10 h until 950 °C, maintained for 3 h and, finally, slowly cooled to room temperature.

2.2. Characterization of the scaffolds

2.2.1. Chemical and mineralogical characterization of the scaffolds

The microstructural characterization of scaffolds was evaluated by Scanning Electron Microscopy with Energy Dispersive X-Ray Spectroscopy (SEM-EDX, Hitachi S–3500 N with INCA system by Oxford Instruments Analytical).

The composition and crystalline phases were evaluated by X-Ray Diffraction (XRD, Bruker, AXR D8 Advance) with a secondary graphite monochromator using Cu-K$_\alpha$ radiation (1.5418740Å). The X-Ray tube operated at 40 kV and 30 mA. Data were collected between 10° and 38° (2θ) at 0.02 steps by counting 8 s per step. All the diffractograms were compared to the Crystallography Open Database (COD) and were analyzed using the version 3.8.2.148 of the Match! software.

2.2.2. Physical characterization of the scaffolds

Mesopores (pores between 2 and 50 nm) were evaluated using the nitrogen adsorption and desorption technique performed at 77.3 K (Quantachrome, QuadraSorb instruments) followed by the Brunauer-Emmet-Teller (BET) method and the Barrett-Joyner-Halenda (BJH) calculation to obtain the specific surface area, the mesopore volume and the pore size distribution.

Pores smaller than 300 μm were evaluated by the Mercury Porosimetry Technique (Poremaster 60 GT Quantachrome instruments). Those larger than 300 μm were evaluated by picnometry with H$_2$O by Archimedes principle.

The core's mechanical strength was previously evaluated by a simple compression test [9] and the same technique was herein used to obtain the compressive strength of samples C/EL-1Fe and C/EL-3Fe. Tests were carried out by applying loads to the cylindrical scaffolds (8.5 mm diameter, 7.0 mm high) at a speed of 1.00 mm/min until the scaffold completely broke using a Microtest SCM3000 mechanical tester. In all, 25 samples of each composition (C/EL-1Fe and C/EL-3Fe) were tested.

2.2.3. In vitro bioactivity evaluation of the scaffolds

In vitro bioactivity was evaluated by soaking samples in simulated body fluid (SBF) at different times [18]. These samples came into contact with SBF and were subsequently submerged in a water bath at 37 °C from 6 h to 28 days. The test was carried out with samples C/EL-1Fe and C/EL-3Fe using the core without external layers as the control.

After each testing time, samples were evaluated morphologically by SEM-EDX, while the resulting SBF was assessed by inductively coupled plasma optical emission spectrometry (ICP-OES, Perkin-Elmer Optima 2000™) to monitor any variations in the concentrations of the silicon, phosphorus and calcium ions.

3. Results

3.1. Characterization of the scaffolds

Fig. 1 shows the morphologies of the samples observed by SEM. Fig. 1 (A-C) depicts the microstructures formed on the scaffold's cores, constituted by hexagonal grains over the entire surface. In Fig. 1 (D-F) and Fig. 1 (G-I), which correspond to samples C/EL-1Fe and C/EL-3Fe, we can identify the layers of the external coatings (▲) on top of the microstructures constituting the core (●). Specially, sample C/EL-3Fe presented a higher coating coverage, which makes it difficult to identify the core's microstructures. We can also see how a cracked rough coating formed in both cases instead of a continuous smooth layer such as the core.

Fig. 2 shows the diffractograms of the core, as well as samples C/EL-1Fe and C/EL-3Fe, with the corresponding phases identified by XRD. The core presented the following phases: calcium diphosphate (Ca$_2$P$_2$O$_7$) (COD 96-100-1557); beta tricalcium phosphate (β-Ca$_3$(PO$_4$)$_2$) (COD 96-151-7239); LiCa(PO$_4$) (COD 96-722-2995), Ca$_{9.95}$Li$_{1.05}$(PO$_4$)$_7$ (COD 96-152-6054); cristobalite (SiO$_2$) (COD 96-900-8228). Samples C/EL-1Fe and C/EL-3Fe presented the same phases identified in the core, and also phase Ca$_{9.33}$Fe$_{1.167}$(PO$_4$)$_7$ (COD 96-400-2456). The layers external to samples C/EL-1Fe and C/EL-3Fe increased the intensity of the peaks corresponding to the cristobalite phase. Also, in both samples, the intensity of the peaks of the calcium diphosphate phase diminished.

Fig. 3 shows the nitrogen adsorption and desorption isotherms with pore size distribution curves of the core and samples C/EL-1Fe and C/EL-3Fe. The curves show that all three materials presented mesopores between 3 nm and 10 nm. The parameters obtained by this technique are shown in Table 2. The specific surface area and the volume of the mesopore increased from the core to the C/EL-3Fe sample and the diameter of the pore obtained by the DJH calculation was around 3 nm.

Fig. 4 shows the curves obtained by the Mercury Porosimetry

98
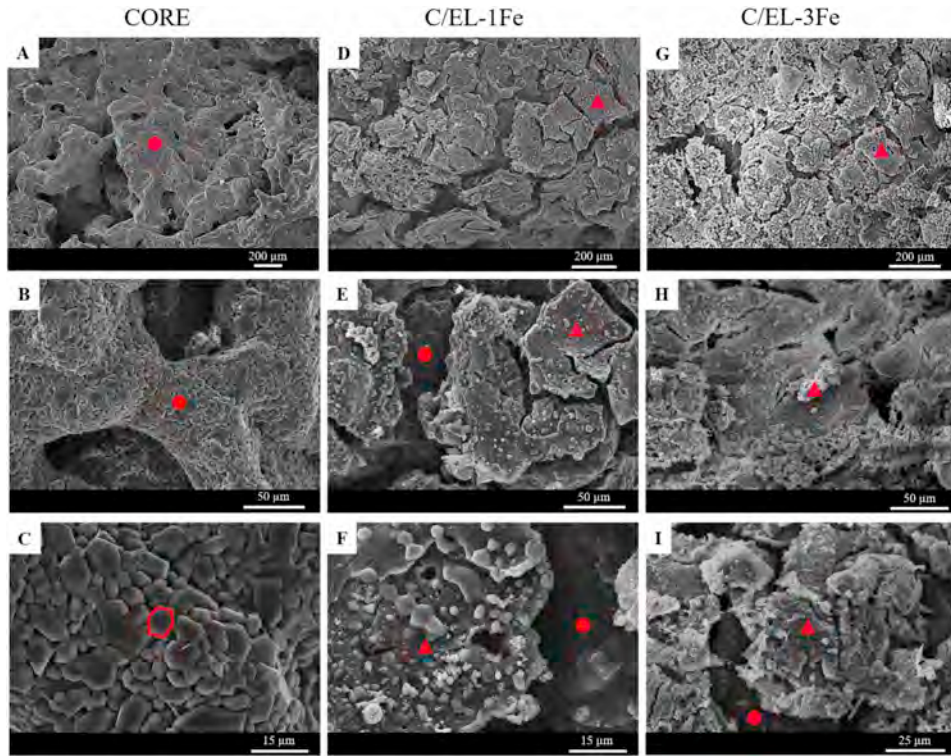
Fig. 1. SEM images of scaffolds: (A–C) core, (D–F) C/EL-1Fe and (G–I) C/EL-3Fe. Identified structure: (●) core and (▲) external layers.

Technique. The three samples displayed single mode conduct in relation to pore size, with the core between 123 μm and 10 μm, and samples C/EL-1Fe and C/EL-3Fe between 150 μm and 0.5 μm. The scaffolds with external coatings showed a bigger amount of intruded mercury, which meant more pores compared to the core. Table 3 presents the total porosity obtained by this technique, where the core presented 30.6%, as well as increases of 51.3% and 54.1% for samples C/EL-1Fe and C/EL-3Fe, respectively.

By Arquimedes principle, total porosity above 300 μm was determined and is presented in Table 3. The core presented a porosity of 77.6%, and decreases of 57.4% and 51.9% were seen for samples C/EL-1Fe and sample C/EL-3Fe, respectively.
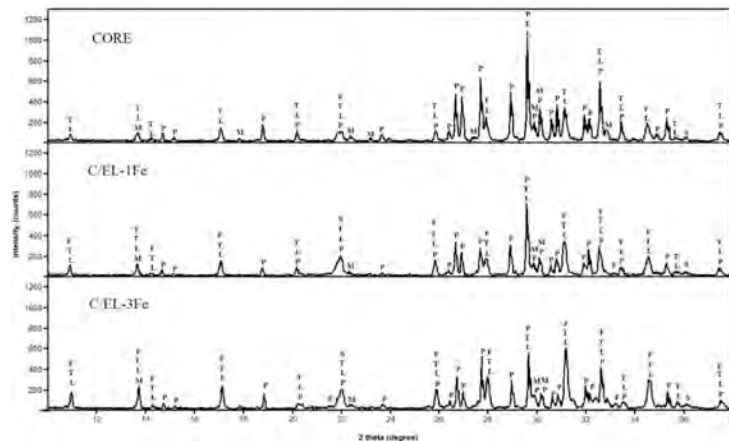
Fig. 2. XRD diffraction patterns of the core, sample C/EL-1Fe and sample C/EL-3Fe (T: β-Ca$_3$(PO$_4$)$_2$, L: Ca$_{9.95}$Li$_{1.05}$(PO$_4$)$_7$, P: Ca$_2$P$_2$O$_7$, S: SiO$_2$, M: LiCa(PO$_4$), F: Ca$_{9.33}$Fe$_{1.167}$(PO$_4$)$_7$).

99
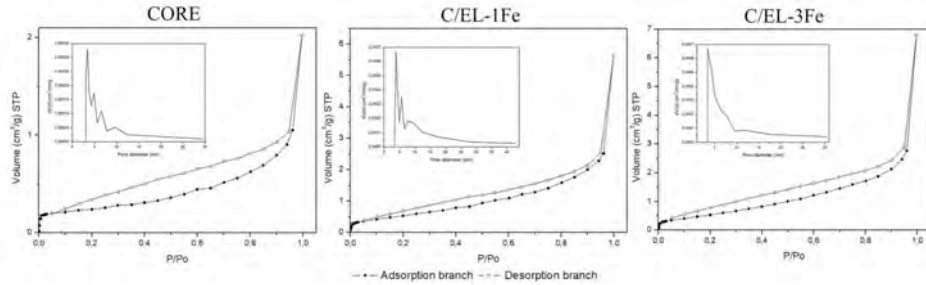
Fig. 3. Nitrogen adsorption-desorption isotherm with pore size distribution of the core and samples C/EL-1Fe and C/EL-3Fe.

Table 2
Parameters obtained by nitrogen adsorption-desorption technique.

Sample	Specific surface area (m²/g)	Mesopore volume (cm³/g)	Mesopore diamater (nm)
Core	0.835	0.0016	3.41
C/EL-1Fe	2.146	0.0039	3.83
C/EL-3Fe	2.265	0.0043	3.42
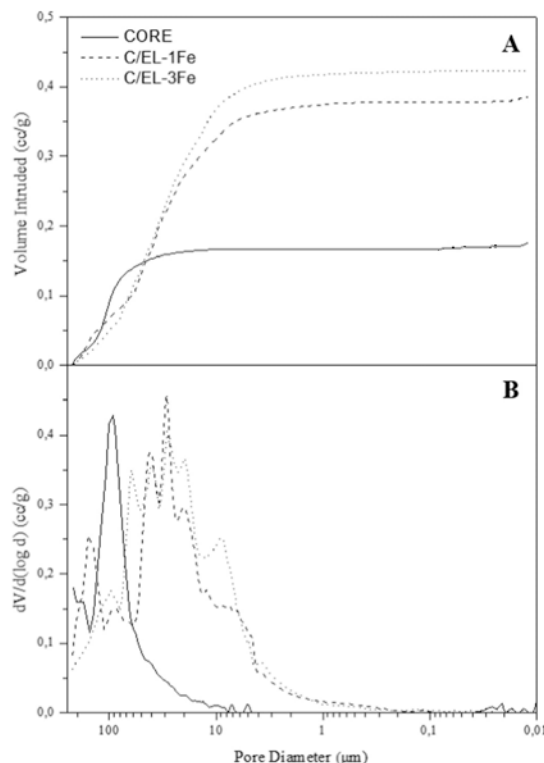
Fig. 4. Mercury porosimetry curves: (A) cumulative and (B) differential intrusion vs. pore diameter in scaffolds.

Finally, Table 3 also provides the scaffolds' compressive strength results. The scaffold's core had a compressive strength of 0.9–1.6 MPa [9], sample C/EL-1Fe had a value of 0.4–1.2 MPa and sample C/EL-3Fe gave a value of 1–1.5 MPa.

3.2. In vitro bioactivity evaluation of the scaffolds

The evaluation of the scaffolds' *in vitro* bioactivity was done by SEM-EDX to observe microstructural changes, and by ICP-OES to obtain the ion exchange between samples and SBF. Fig. 5 shows the images of the core obtained by SEM after immersion in SBF at 3, 7 and 28 days. The results revealed that regardless of the time during which the core remained in contact with SBF, the microstructure of the hexagonal grains remained the same as that observed before the evaluation began (Fig. 1 (A-C)).

Figs. 6 and 7 are the SEM images obtained after immersion in SBF at different times for samples C/EL-1Fe and C/EL-3Fe, respectively.

Fig. 6 illustrates that after the sample C/EL-1Fe surface had been in contact with SBF for 6 h and 9 h, the initially observed microstructure was presented (Fig. 1 (D-F)). Part of the external layer was observed at 6 h (Fig. 6A) and, subsequently, hexagonal grains of the core became evident at 9 h (Fig. 6B), but with undefined edges. However, a precipitate began to form on the surface after 1 day (Fig. 6C). This precipitate continued to grow after 3, 8 and 13 days (Fig. 6 (D-F)). The EDX analysis revealed that these precipitates had a Ca/P ratio of 1.30–1.35 on day 1, 1.24–1.30 on day 3, 1.24–1.37 on day 8 and 1.35–1.71 on day 13. After being in contact with SBF for 18 days, the Ca–P precipitates observed on day 13 disappeared. This left the microstructure of the core visible again with some small globular precipitates (Fig. 6G). After 23 days, the precipitate reappeared (Fig. 6H) and disappeared again on day 28 (Fig. 6I).

Fig. 7 shows the results of sample C/EL-3Fe. In this case, and as in the previous sample, the external layer dissolved and revealed the core's microstructure after 6 h (Fig. 7A) and 9 h (Fig. 7B). Later after 1 day (Fig. 7C), new precipitates appeared on the surface. The EDX analysis showed that the precipitate that formed on day 1 has a Ca/P ratio of 1.41–1.74. Unlike the previous case however, the presence of silicon on the surface was revealed. Fig. 7D shows that after 3 days, the precipitate disappeared and part of the hexagonal grains dissolved to reveal a laminar structure. After 8 days (Fig. 7E) of being in contact with SBF, precipitates formed again on the surface and remained with time, even after 28 days (Fig. 7I). The EDX analysis revealed that the Ca/P ratio for this precipitate was 1.25–1.75.

Fig. 8 depicts the curves of the ICP-OES performed with SBF after being contact with the core, and samples C/EL-1Fe and C/EL-3Fe at different times. The core's curves showed a lower calcium concentration in SBF because the sample adsorbed this ion. On the contrary, the ionic phosphorus concentration slightly increased in SBF because the sample released this ion. Finally, the ionic silicon concentration remained at around zero throughout the study period.

For samples C/EL-1Fe and C/EL-3Fe, an initial increase and a later decrease in the ionic concentration of calcium took place between 6 h and 1 day. With time however, these samples generally displayed lowering ionic concentrations of calcium in SBF and, consequently, this ion was adsorbed by these samples.

100

Table 3
Scaffold's porosity and compressive strength.

Sample	Porosity (%) < 300 μm[a]	Porosity (%) > 300 μm[b]	Compressive strength (MPa)
Core	30..6	77.6	0.9–1.6
C/EL-1Fe	51.3	57.4	0.4–1.2
C/EL-3Fe	54.1	51.9	1–1.5

[a] Obtained by the Mercury Porosimetry Technique.
[b] Obtained by Archimedes principle.

The silicon concentration rose in both samples. Particularly, sample C/EL-1Fe presented rapid silicon release until 13 days of being in contact with SBF, and then silicon dropped. In sample C/EL-3Fe, a rapid release in silicon took place after 8 days of being contact with SBF, from which point the ionic concentration slightly increased for the other study times.

Finally, the ionic phosphorus concentration differed in both samples. After 1 day, the phosphorus concentration in SBF lowered with sample C/EL-1Fe, and the lowest ionic phosphorous concentration in SBF was observed at 13 days. From this point, the phosphorus concentration in SBF increased up to 28 days, and exceeded the initial values of this ion concentration in SBF. With sample C/EL-3Fe, the phosphorus concentration slightly lowered from the time it came into contact with SBF up to 1 day. Between days 1 and 3, the phosphorus concentration rose and lowered until 8 days. This concentration remained practically constant until day 23, when it lowered slightly after 28 days.

Another piece of information obtained from the curves of the doped samples revealed an opposing behavior between the ion concentrations of silicon and phosphorus. An increase in the concentration of one represented a decrease in the other ion, and behavior was specular.

4. Discussion

The objective of this research was to develop materials with similar properties and characteristics to human bone to be used as an implant. The scaffold herein obtained was manufactured with $CaO–P_2O_5–SiO_2$ system compositions using iron as a dopant on external layers. The scaffold's core presented a calcium diphosphate phase, which inhibits *in vitro* bioactivity [19], but provides mechanical resistance to act as a bone implant and to confer the porosity needed to allow new bone growth processes. It also demonstrated the possibility of modulating the sample's bioactivity by coating the core with external layers using the composition in the same system, but by doping with different concentrations of strontium ions [9]. The bioactive character of outer layers was due to the modifications made by the dopant when it entered the material's crystalline network and produced different crystalline phases, which subsequently determined the sample's ionic exchange with SBF.

In the present work, the modifications of the crystalline network were made by adding iron as a dopant. The ionic substitution was made in relation to the initial calcium moles and modifications differed depending on the dopant's size. The cationic size of Fe^{3+} is 0.64 Å [20] and that of Ca^{2+} is 1.00 Å [20]. Therefore, a large ion was substituted for a smaller one. The characterization techniques herein used sought to understand the changes that iron produced in the material's crystalline network to understand the variations made in our samples' bioactivity.

4.1. Characterization of the scaffolds

The microstructural characterization carried out by SEM showed that samples C/EL-1Fe (Fig. 1 (D-F)) and C/EL-3Fe (Fig. 1 (G-I)) presented plates of the material on top of the core's microstructure. These plates corresponded to the external layers on the scaffold's core. In both samples, the formation of fragments of the coating distributed along the surface took place, which meant that a continuous layer did not form on top of the core. This can be attributed to the contraction undergone by the ceramic material during drying and sintering.

The obtained XRD diffractograms showed the modifications made in the phases of the core with external layers. The intensity of the cristobalite phase peaks increased because the outer layers had 29% mol of SiO_2. Moreover, the calcium diphosphate phase peaks decreased and the nonstoichiometric phase $Ca_{9.93}Fe_{1.167}$ $(PO_4)_7$ appeared. The reduction in the calcium diphosphate phase was attributed to the diffusion processes that occurred between the core and the external layer, where a new iron-containing phase was favored.

The chemical characterization of scaffolds revealed that the external layer doped with small amounts of iron maintained the ceramic material's polycrystalline character. As far as we know, no other fully crystalline materials with compositions in system $CaO–P_2O_5–SiO_2–Fe_2O_3$ have been reported. Several studies, like that by Wu et al., have shown that mesoporous bioactive glass scaffolds can be obtained with a molar ratio of 5Fe/10Ca/5P/80Si and 10Fe/5Ca/5P/80Si, whose characterization by XRD indicates that the material is formed predominantly by an amorphous phase [17]. Baino et al. developed sol-gel ceramic materials with compositions $60SiO_2–38CaO–2Fe_2O_3$ and $60SiO_2–30CaO–10Fe_2O_3$. By XRD, they found that only the composition with $10Fe_2O_3$ presented crystalline phases, while the others displayed only an amorphous phase [21].

In relation to the pores, the evaluation of mesopores showed that the three materials presented a type IV(a) isotherm with a H3-type hysteresis loop [22]. Although mesopores are between 2 nm and 50 nm, the materials of this study presented a size distribution between 3 nm and 10 nm. As well as a low specific surface area and mesopore volume compared to other work that use the sol-gel method but for bioactive glass [23].

The total microporosity (< 300 μm) in the scaffold's core was 30.6%. In the core with external layers, this porosity rose to 51.3% and 54.1% in samples C/EL-1Fe and C/EL-3Fe, respectively. This was because coatings had a rough surface above the core that allowed greater mercury intrusion. The porosimetry curves showed that the three samples had a unique pore distribution, but samples C/EL-1Fe and C/EL-3Fe displayed a wide pore distribution as a result of the rough surface above the core.

The macroporosity (> 300 μm) in the core was 77.6%, which
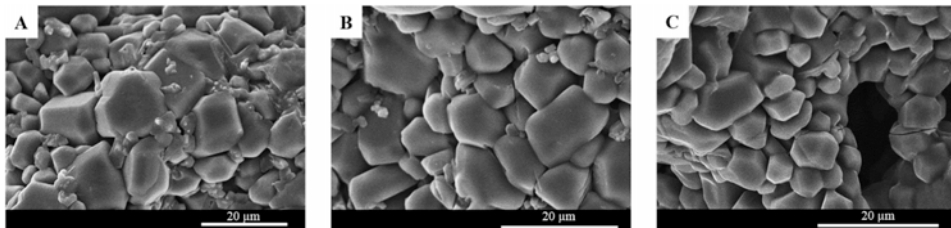
Fig. 5. SEM images of the core soaked in SBF for: (A) 3 days, (B) 7 days; (C) 28 days.

101
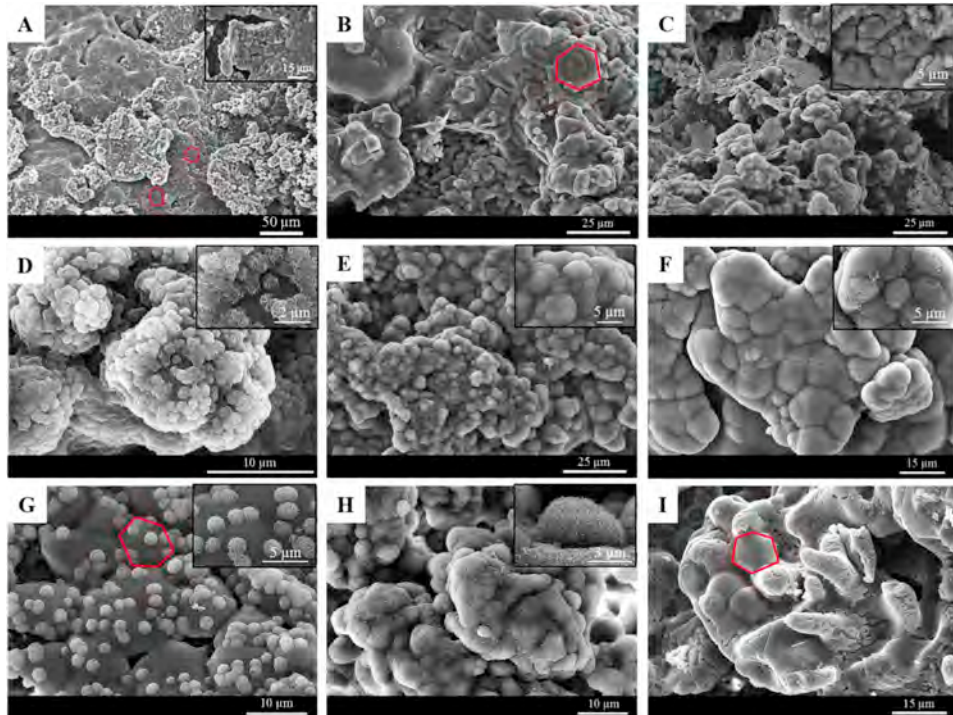
Fig. 6. SEM images of sample C/EL-1Fe soaked in SBF for: (A) 6 h; (B) 9 h; (C) 1 day; (D) 3 days; (E) 8 days; (F) 13 days; (G) 18 days; (H) 23 days; (I) 28 days.

dropped to 57.4% and 51.9% in the core with external layers in samples C/EL-1Fe and C/EL-3Fe, respectively. This was because each outer coating layer increased the thickness of the initial strut in the polyurethane sponge.

Scaffolds presented adequate meso-, micro- and macroporosity to act as ideal implants. Macroporosity is necessary for colonization and angiogenesis to occur in bone growth, and for scaffold bioresorption. Microporosity is also required to promote protein adsorption, cell adhesion and permeability [24]. Some studies indicate that bone growth occurs in scaffolds with pores exceeding 100 μm [25], while others mention that the optimal pore size is 300 μm [26]. In relation to micropores, between 1 μm and 3 μm are required for interaction between cells and the surface, and between 3 μm and 12 μm for cell migration through scaffolds [27].

Finally, a slight decrease in compressive strength compared to the core was observed for sample C/EL-1Fe, although an increase occurred for sample C/EL-3Fe with a similar compression resistance range to the core (Table 3). This resistance corresponds to one of the highest compression resistance values reported to date for scaffolds manufactured using sol-gel and polymer sponge: 0.18–0.40 MPa in SiO_2–CaO–P_2O_5 scaffolds [28], 0.02–0.03 MPa in SiO_2–CaO–$(Mg/Na/K)_yO_x$ scaffolds [29]; 0.51 MPa in hydroxyapatite scaffolds [30].

4.2. In vitro bioactivity evaluation of scaffolds

Bioactivity is understood as a material's ability to form apatite precipitates on the surface with a similar chemical composition to the hydroxyapatite found in human bone. The formation of this precipitate is related to the ion exchange that takes place between the sample and SBF. For this reason, samples' bioactivity was studied using surface characterization by SEM-EDX and SBF ions by ICP-OES.

The results of the *in vitro* bioactivity evaluation of the core revealed that its initial morphology presented no modifications and, consequently, no bioactivity (Fig. 5). This behavior can be attributed to two factors: first, the presence of calcium diphoshate phases, which contain the pyrophosphate group that inhibits the crystallization of hydroxyapatite *in vitro* [19]; second, the low ionic concentration of silicon observed in Fig. 8, which plays an important role in the bioactivity mechanism. This mechanism has been previously described, and proposes that Si–O–Si bonds are broken and form two Si–OH groups, one of which is released to the medium and the other is maintained on the sample surface to act as the apatite nucleation point. At these nucleation points, the exchange with the calcium and phosphorus ions of SBF occurs to form Ca–P precipitates [31].

Although the core is not bioactive, bioactivity can be modulated with external layers doped with small amounts of iron, as seen in Figs. 6 and 7.

The precipitation of apatites on the surface of samples C/EL-1Fe and C/EL-3Fe is related to the ionic exchange observed in Fig. 8. At the initial contact times (6 h and 9 h) for both samples, a slight dissolution of the outer coating layers occurred. The most significant changes took place from day 1, which begin to appear precipitated on the material's surface. This corresponded to ionic silicon release and calcium and phosphorus adsorption (see Fig. 8).

In sample C/EL-1Fe, the precipitate continued to grow until a cauliflower-like morphology appeared on the whole surface after 13 days (Fig. 6(C–F)). The ionic behavior noted between days 1 and 13 showed the release of silicon ions and phosphorus and calcium adsorption that the sample performed. This implies that the Ca–P precipitate was formed on the sample's surface by following the above-described bioactivity behavior. EDX revealed that these precipitates had a Ca/P ratio like apatite ratios. The stoichiometric hydroxyapatite ratio is 1.67

102
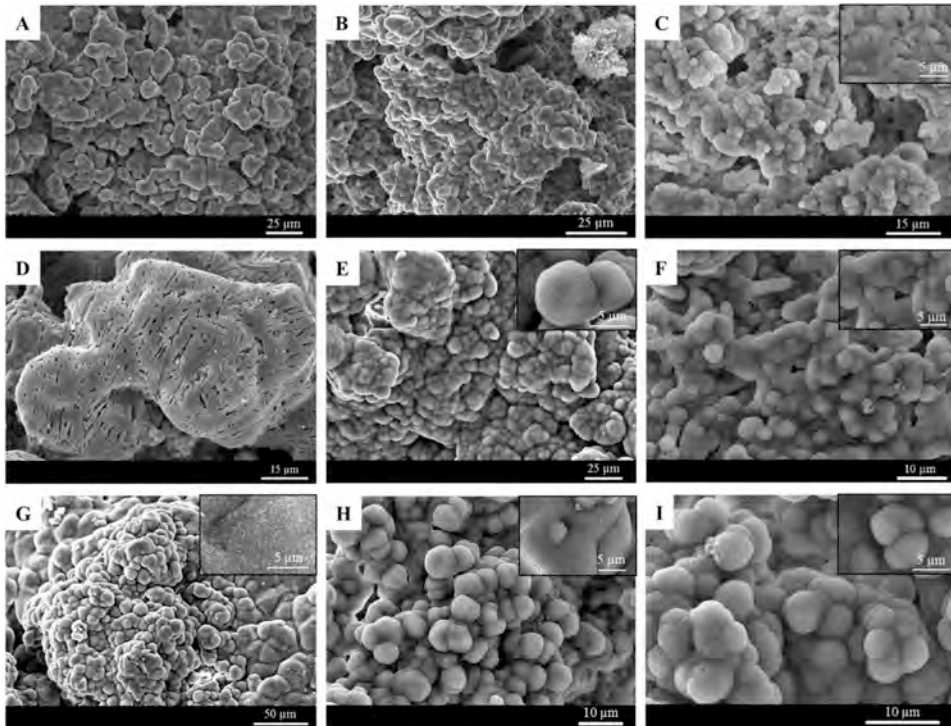
Fig. 7. SEM images of sample C/EL-3Fe soaked in SBF for: (A) 6 h; (B) 9 h; (C) 1 day; (D) 3 days; (E) 8 days; (F) 13 days; (G) 18 days; (H) 23 days; (I) 28 days.

and can reach lower values for calcium-deficient hydroxyapatite Ca_{10-x} $(PO_4)_{6-x}(HPO_4)$ $(OH)_{2-x}$ [32]. Values below 1.67 have also been reported, which correspond to hydroxyapatites combined with β-$Ca_3(PO_4)_2$. Values of 1.71 correspond to hydroxyapatite with excess calcium [32]. However, the formed precipitates were unstable and part of the precipitate disappeared after 18 days (Fig. 6G), which coincided with the silicon adsorption and calcium and phosphorus release performed by the sample (Fig. 8). At 23 and 28 days, apatite once again precipitated and dissolved (Fig. 6 (H–I)). The nature of sample C/EL-1Fe was generally bioactive and varied with time. The ICP-OES curves indicated that the sample adsorbed calcium ions from SBF, but silicon and phosphorus ions were released and adsorbed differently while the study was underway. Silicon and phosphorus ions exhibited an opposite release and adsorption behavior, and a maximum point of silicon release by the sample meant minimal phosphorus adsorption and, in turn,

apatite precipitates appeared on the surface.

The precipitate of sample C/EL-3Fe disappeared after 1 day and once again precipitated on day 8 to remain even until day 28 (Fig. 7 (D-I)). As in the previous case when the precipitate disappeared, then ionic adsorption of silicon and calcium and phosphorus release occurred. The opposite ionic behavior occurred when the apatite precipitated. As precipitates were maintained from day 8 to day 28, slight or insignificant changes in ionic concentrations were observed. The only variation in the phosphorus concentration took place from day 23 to day 28, when the almost total adsorption of this ion present in SBF occurred.

The iron detection range in the ICP-OES equipment is 0.1–100.0 mg/L. However, given the low concentrations at which this element was added to the external scaffold layers, it was impossible to detect its concentration in SBF.

The difference in bioactive behavior of samples C/EL-1Fe and C/EL-
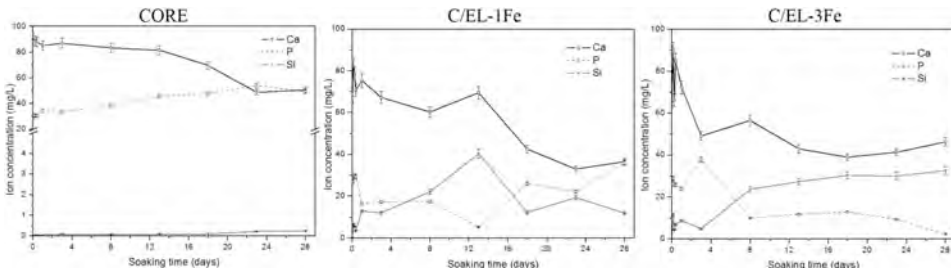
Fig. 8. Variation in the concentrations of the calcium (Ca), phosphorous (P) and silicon (Si) ions in SBF after the interaction with the core and samples C/EL-1Fe and C/EL-3Fe at different times.

103

3Fe can be attributed to sample C/EL-3Fe presenting a larger amount of iron and, therefore, a bigger amount of the $Ca_{9.33}Fe_{1.167}(PO_4)_7$ phase. This nonstoichiometric phase could have led to a different ion exchange with SBF to allow the stabilization of the apatite precipitate after 8 days.

Recent research has guided the use of ceramic doping with iron ions to provide magnetic properties that can be used in hyperthermia treatments and to, thus, combat diseases like cancer [33]. Baino et al. prepared bio-glass scaffolds both with and without iron by sol-gel foaming (60SiO$_2$-40CaO, 60SiO$_2$-38CaO-2Fe$_2$O$_3$ and 60SiO$_2$-30CaO-10Fe$_2$O$_3$). They reported that regardless of the amount of iron employed, the materials were very well able to form globular apatite with a cauliflower-like morphology. They proposed that these bioactive materials with ferromagnetic properties would be excellent candidates to regenerate bone affected by cancer [23].

However, iron not only provides magnetic benefits, but is also an essential element in our body and forms part of vital biological processes. The incorporation of iron into bone implants not only involves the release of iron ions to the body, but also improves the implant's biological properties. Pon-On et al. demonstrated that substituting iron in hydroxyapatite improved the implant's biological activity, and observed how this better adsorbed protein like bovine serum albumin [34]. Their results also showed that their iron-doped material was not only an excellent bone tissue regeneration candidate, but also a potential protein-releasing agent.

The scaffold herein manufactured revealed that the amount of dopant modified the materials' bioactive behavior, with C/EL-1Fe displaying variable bioactivity over time and C/EL-3Fe exhibiting stable bioactivity after 8 days. To date, the *in vivo* benefits of this variation in precipitation and apatite dissolution on the scaffold surface have not yet been demonstrated. However, this behavior might imply that the implant can be used in accordance with patient requirements.

It is known that bone tissue does not remain the same throughout an individual's life because factors like bone mineral content and bone mineral density (hydroxyapatite (g/cm^2)), and cellular processes, differ from the first months of life to adulthood [35, 36]. Bone modeling and remodeling processes occur in the first years of life (balance between the bone's resorption and formation) due to considerable cellular activity with less bone mineral content. However, adults display less cellular activity and higher bone density [37–39]. For this reason, it is estimated that possible bone implant requirements should change.

Accordingly, sample C/EL-1Fe (noncontinuous bioactivity) and sample C/EL-3Fe (stable bioactivity) may be an excellent candidate for individuals in early life stages and for adults, respectively. Future studies will attempt to demonstrate how variation in an implant's bioactivity can benefit the regenerative process of tissue and be used in a particular way with each patient.

As far as we are aware, there are no known materials with layers of different compositions capable of presenting variable bioactivity. For this reason, it would be interesting to study the effect of other ions as dopants of external layers and their interference with bioactivity.

5. Conclusions

Multilayer ceramic scaffolds doped with small amounts of iron were successfully prepared. Scaffolds presented adequate porosity, mechanical resistance and surface chemical composition, and were capable of promoting apatite precipitation on the surface, which make it a bioactive material. Sample C/EL-1Fe's bioactivity varied with time, with precipitates on its surface after 3 days that appeared and disappeared even after 28 days. Sample C/EL-3Fe's bioactivity appeared after 8 days and remained stable with time. The differences in these samples' bioactive behavior were attributed to the changes in the crystalline phases that took place when replacing iron in the material's crystalline network. Both samples can be potentially used as specialized implants in line with patient requirements. Our study results

demonstrate the need to continue studying the advantages and disadvantages of materials that exhibit variable bioactivity *in vitro* and *in vivo*.

Declaration of competing interest

None.

References

[1] S.V. Dorozhkin, Current state of bioceramics, J. Ceram. Sci. Technol. 9 (2018) 353–370.
[2] U. Ripamonti, L.C. Roden, C. Ferretti, R.M. Klar, Biomimetic matrices self-initiating the induction of bone formation, J. Craniofac. Surg. 22 (2011) 1859–1870.
[3] W. Paul, C.P. Sharma, Bioceramic scaffold-bone tissue engineering, in: G. Khang (Ed.), Handbook of Intelligent Scaffolds for Tissue Engineering and Regenerative Medicine, Pan Stanford Publishing Pte Ltd, Singapore, 2012, pp. 83–95.
[4] J.Y. Rho, L. Kuhn-Spearing, P. Zioupos, Mechanical properties and the hierarchical structure of bone, Med. Eng. Phys. 20 (1998) 92–102.
[5] J.R. Caeiro, P. Gonzalez, D. Guede, Biomechanics and bone (& II): trials in different hierarchical levels of bone and alternative tools for the determination of bone strength, Rev. De Osteoporos. Metab. Miner. 5 (2013) 99–108.
[6] N. Eliaz, N. Metoki, Calcium phosphate bioceramics: a review of their history, structure, properties, coating technologies and biomedical applications, Materials 10 (2017) 1–104.
[7] I. Denry, L.T. Kuhn, Design and characterization of calcium phosphate ceramic scaffolds for bone tissue engineering, Dent. Mater. 32 (2016) 43–53.
[8] P. Ros-Tarraga, N.A. Mata, A. Murciano, P. Velasquez, P.N. De Aza, Multilayer ceramic materials: a method to link bioactivity and durability, Ceram. Int. 45 (2019) 23611–23618.
[9] N.A. Mata, P. Ros-Tarraga, P. Velasquez, A. Murciano, P.N. De Aza, Synthesis and characterization of 3D multilayer porous Si-Ca-P scaffolds doped with Sr ions to modulate in vitro bioactivity, Ceram. Int. 46 (2020) 968–977.
[10] A. Hoppe, N.S. Gueldal, A.R. Boccaccini, A review of the biological response to ionic dissolution products from bioactive glasses and glass-ceramics, Biomaterials 32 (2011) 2757–2774.
[11] M. Jimenez, C. Abradelo, J. San Roman, L. Rojo, Bibliographic review on the state of the art of strontium and zinc based regenerative therapies. Recent developments and clinical applications, J. Mater. Chem. B. 7 (2019) 1974–1985.
[12] S. Gomes, A. Kaur, J.M. Greneche, J.M. Nedelec, G. Renaudin, Atomic scale modeling of iron-doped biphasic calcium phosphate bioceramics, Acta Biomater. 50 (2017) 78–88.
[13] P.T. Lieu, M. Heiskala, P.A. Peterson, Y. Yang, The roles of iron in health and disease, Mol. Aspect. Med. 22 (2001) 1–87.
[14] V.S. Chandra, G. Baskar, R.V. Suganthi, K. Elayaraja, M.I.A. Joshy, W.S. Beaula, et al., Blood compatibility of iron-doped nanosize hydroxyapatite and its drug release, ACS Appl. Mater. Interfaces 4 (2012) 1200–1210.
[15] S. Vahabzadeh, S. Bose, Effects of iron on physical and mechanical properties, and osteoblast cell interaction in beta-tricalcium phosphate, Ann. Biomed. Eng. 45 (2017) 819–828.
[16] R.K. Singh, M. Srivastava, N.K. Prasad, S. Awasthi, A. Dhayalan, S. Kannan, Iron doped beta-Tricalcium phosphate: synthesis, characterization, hyperthermia effect, biocompatibility and mechanical evaluation, Mat. Sci. Eng. C-Mater. 78 (2017) 715–726.
[17] C.T. Wu, W. Fan, Y.F. Zhu, M. Gelinsky, J. Chang, G. Cuniberti, et al., Multifunctional magnetic mesoporous bioactive glass scaffolds with a hierarchical pore structure, Acta Biomater. 7 (2011) 3563–3572.
[18] T. Kokubo, H. Takadama, How useful is SBF in predicting in vivo bone bioactivity? Biomaterials 27 (2006) 2907–2915.
[19] H. Fleisch, S. Bisaz, Mechanism of calcification - inhibitory role of pyrophosphate, Nature 195 (1962) 911.
[20] R.D. Shannon, Revised effective ionic-radii and systematic studies of interatomic distances in halides and chalcogenides, Acta Crystallogr. Sect. A 32 (1976) 751–767.
[21] F. Baino, E. Fiume, M. Miola, F. Leone, B. Onida, F. Laviano, et al., Fe-doped sol-gel glasses and glass-ceramics for magnetic hyperthermia, Materials 11 (2018) 1–15.
[22] M. Thommes, K. Kaneko, A.V. Neimark, J.P. Olivier, F. Rodriguez-Reinoso, J. Rouquerol, K.S.W. Sing, Physisorption of gases, with special reference to the evaluation of surface area and pore size distribution (IUPAC Technical Report), Pure Appl. Chem. 87 (2015) 1051–1069.
[23] F. Baino, E. Fiume, M. Miola, F. Leone, B. Onida, E. Verné, Fe-doped bioactive glass-derived scaffolds produced by sol-gel foaming, Mater. Lett. 235 (2019) 207–211.
[24] M.P. Ginebra, M. Espanol, Y. Maazouz, V. Bergez, D. Pastorino, Bioceramics and bone healing, EFORT Open Rev 3 (2018) 173–183.
[25] L.E. Rustom, M.J. Poellmann, A.J.W. Johnson, Mineralization in micropores of calcium phosphate scaffolds, Acta Biomater. 83 (2019) 435–455.

104

[26] K.S. Lew, R. Othman, K. Ishikawa, F.Y. Yeoh, Macroporous bioceramics: a re-markable material for bone regeneration, J. Biomater. Appl. 27 (2012) 345–358.

[27] I. Bruzauskaite, D. Bironaite, E. Bagdonas, E. Bernotiene, Scaffolds and cells for tissue regeneration: different scaffold pore sizes-different cell effects, Cytotechnology 68 (2016) 355–369.

[28] P. Ros-Tarraga, A. Murciano, P. Mazon, S.A. Gehrke, P.N. De Aza, In vitro behaviour of sol-gel interconnected porous scaffolds of doped wollastonite, Ceram. Int. 43 (2017) 11034–11038.

[29] P. Ros-Tarraga, A. Murciano, P. Mazon, S.A. Gehrke, P.N. De Aza, New 3D stratified Si-Ca-P porous scaffolds obtained by sol-gel and polymer replica method: micro-structural, mineralogical and chemical characterization, Ceram. Int. 43 (2017) 6548–6553.

[30] F. Gervaso, F. Scalera, S.K. Padmanabhan, A. Sannino, A. Licciulli, High-perfor-mance hydroxyapatite scaffolds for bone tissue engineering applications, Int. J. Appl. Ceram. Technol. 9 (2012) 507–516.

[31] A.H. De Aza, P. Velasquez, M.I. Alemany, P. Pena, P.N. De Aza, In situ bone-like apatite formation from a Bioeutectic((R)) ceramic in SBF dynamic flow, J. Am. Ceram. Soc. 90 (2007) 1200–1207.

[32] S. Raynaud, E. Champion, D. Bernache-Assollant, P. Thomas, Calcium phosphate apatites with variable Ca/P atomic ratio I. Synthesis, characterisation and thermal

[33] stability of powders, Biomaterials 23 (2002) 1065–1072.

M. Miola, Y. Pakzad, S. Banijamali, S. Kargozar, C. Vitale-Brovarone, A. Yazdanpanah, et al., Glass-ceramics for cancer treatment: so close, or yet so far? Acta Biomater. 83 (2019) 55–70.

[34] W. Pon-On, N. Charoenphandhu, J. Teerapornpuntakit, J. Thongbunchoo, N. Krishnamra, I.M. Tang, Physicochemical and biochemical properties of iron-loaded silicon substituted hydroxyapatite (FeSiHAp), Mater. Chem. Phys. 141 (2013) 850–860.

[35] L.D. Rio, A. Carrascosa, F. Pons, M. Gusinyé, D. Yeste, F.M. Domenech, Bone mi-neral density of the lumbar spine in white mediterranean Spanish children and adolescents: changes related to age, sex, and puberty, Pediatr. Res. 35 (1994) 362–365.

[36] J. Latifa, Physiology and bone physiopathology, An. Sist. Sanit. Navar. 26 (2003) 7–15.

[37] J.H. Davies, Bone mass acquisition in healthy children, Arch. Dis. Child. 90 (2005) 373–378.

[38] M.A. Levine, Assessing bone health in children and adolescents, Indian J. Endocrinol. Metab. 16 (2012) 205–212.

[39] G. Saggese, G.I. Barocelli, S. Bertelloni, Puberty and bone development, Best Pract. Res. Clin. Endocrinol. Metabol. 16 (2002) 53–64.

105

Apéndice D

Artículo 4

Original

3D multiphasic porous scaffolds of calcium phosphates doping with silicon and magnesium

Nayarit A. Mata [a,*], *Patricia Ros-Tárraga* [a], *Pablo Velasquez* [a], *Angel Murciano* [b], *Piedad N. De Aza* [a]

[a] *Instituto de Bioingeniería, Universidad Miguel Hernández, Elche, Alicante, Spain*
[b] *Departamento de Materiales, Óptica y Tecnología Electrónica, Universidad Miguel Hernández, Elche, Alicante, Spain*

ABSTRACT

In this work it is demonstrated the capacity of the sol–gel process to obtain materials with different phases, using the same chemical composition, and modifying only the conditions of hydrolysis and condensation. This method combined with the polymer sponge replica technique allowed to obtain a porous and three-dimensional scaffold, called core, consisting mainly of calcium phosphates. Additionally, due to the versatility of the sol–gel process, this core was coated with additional phases, constituted by silicon and magnesium, obtaining multilayer scaffolds. The scaffolds were physically and chemically characterized and the *in vitro* bioactivity was evaluated by immersion in simulated body fluid. The results of *in vitro* bioactivity showed that the core revealed a lamellar microstructure with some apatite precipitates after 14 days, while the multilayer scaffolds presented precipitates over the whole surface in only 3 days. The accelerated bioactivity and the general properties of the multiphase and multilayer scaffolds show the potential of this material in the area of tissue engineering.

© 2021 SECV. Published by Elsevier España, S.L.U. This is an open access article under the CC BY-NC-ND license (http://creativecommons.org/licenses/by-nc-nd/4.0/).

Andamios porosos multifásicos 3D de fosfatos cálcicos dopados con silicio y magnesio

RESUMEN

Palabras clave:
Sol-gel
Síntesis
Bioceramics
Multifásico
Fosfato cálcico

En este trabajo se demuestra la capacidad del proceso sol-gel en la obtención de materiales con diferentes fases, usando la misma composición química, y modificando únicamente las condiciones de hidrólisis y condensación. Este método combinado con la técnica de réplica de esponja polimérica permitió obtener un andamio poroso y tridimensional, llamado núcleo, constituido principalmente por fases de fosfatos de calcio. Adicionalmente, debido a la versatilidad del proceso sol-gel, este núcleo fue recubierto con fases adicionales,

constituidas por silicio y magnesio, obteniendo andamios multicapa. Los andamios fueron caracterizados física y químicamente y la bioactividad *in vitro* evaluada mediante inmersión en suero fisiológico artificial. Los resultados de bioactividad *in vitro* mostraron que el núcleo reveló una microestructura lamelar con algunos precipitados de apatito después de 14 días, mientras que los andamios multicapa presentaron precipitados sobre la superficie en solo 3 días. La bioactividad acelerada y las propiedades generales del andamio multifásico y multicapa, demuestran el potencial de este material en el área de ingeniería de tejido.

Introduction

Ceramics are an outstanding alternative in the repair or replacement of damaged bone. Specially, calcium phosphates stand out for their similarity to the mineral component of bone and have demonstrated excellent biocompatibility [1,2]. However, the success of an implant does not depend only on biocompatibility, other requirements are also necessary. Some of these requirements are bioactivity, osteoconductivity, osteoinductivity, biodegradability, mechanical properties, and porous structure [3,4].

It is difficult for an implant with a single calcium phosphate phase to satisfy all these characteristics. For example, tricalcium phosphate (TCP) is biocompatible and is best known for its resorbability, however, presents poor mechanical resistance [1,5,6].

In view of this problem, materials with more than one calcium phosphate phase (biphasic, triphasic and multiphasic) receive a special interest, because they can combine the advantages of individual phases [1,7].

There are many techniques to obtain multiphasic calcium phosphate materials, such as solid-state reaction, spray pyrolysis, sol–gel, hydrothermal treatments, and mechanical mixing [7]. Of all these techniques, sol–gel has the advantage of synthesizing ceramic materials at relatively low temperatures. Recently it has been used in the preparation of bioactive glass, being able to obtain crystalline phases by controlling the heat treatment [8]. The control of crystallinity is important as it will influence the mechanical properties and degradation of the material [3].

In this research, the sol–gel and polymer sponge replica techniques will be used to obtain a three-dimensional porous material (core of the scaffold). The gelation time of the sol–gel will be varied to developed different crystalline phases of calcium phosphate and other phases formed by the incorporation of silicon and lithium. The presence of silicon is due to the fact that it has been shown to influence the differentiation and proliferation of osteoblasts, that are the cells responsible for bone regeneration [9]. Instead, lithium has been added in tricalcium phosphates and has shown improved mechanical properties [10].

The core with more phases will be coated with a second chemical composition (multilayer scaffold) to improve bioactivity. This second composition will have a lower percentage of phosphorus and a higher percentage of silicon with respect to the chemical composition of the core. In addition, the calcium ions will be doped with magnesium in three different percentages to improve the cellular behaviour [11,12]. Gu et al. [11]

demonstrated that TCP scaffolds doped with 1% MgO could improve the migration and spreading of cells such as human bone marrow mesenchymal stem cells and human umbilical vein endothelial cells. They also observed that magnesium induces the mineralization of the extracellular matrix and favors the increase of biomarkers such as Runx2, Col-I, ALP, OCN and BSP that regulate osteogenic differentiation. Additionally, Ke et al. [12] demonstrated that the presence of MgO and SiO$_2$ in TCP scaffolds significantly improved formation of new bone after 16 weeks of implantation compared to TCP without dopants.

Previously, multilayer scaffolds have been developed, but by doping with strontium and iron [13,14]. These ions also have positive effects during the bone regeneration process and their incorporation at low concentrations in the scaffolds accelerated *in vitro* bioactivity.

As far as we know, there are materials of various calcium phosphates, but no scaffold with multilayer configuration that combines a multiphasic core with outer layer containing a higher percentage of silicon and magnesium. In this study, different characterization techniques and *in vitro* bioactivity tests will be used to evaluate the potential of this material as a future bone implant.

Experimental part

Ceramic scaffolds were prepared following the methodology in Fig. 1. The preparation process was divided into stage 1 (cores preparation) and stage 2 (core coatings).

Table 1 shows the reagents and quantities used for the scaffold core and the external coatings doped with magnesium in three different concentrations. All reagents were supplied by Sigma-Aldrich, except the magnesium carbonate from ACROS organics.

Stage 1, the cores were obtained by following these steps: (i) mixing of the reagents, (ii) agitation to produce the hydrolysis, (iii) addition of the carbonates, (iv) heating the solution to 100 °C for 1 h (solution A) and 15 min (solution B), (v) immersion of the polyurethane sponge (20 ppi, 13 mm Ø × 10 mm long), (vi) centrifugation of the sponge at 200 rpm to remove the excess solution, (vii) drying in the oven, and (viii) sintering at 950 °C. Given the gelation level of the solutions, and to ensure the template's macroporosity, steps (v–vii) were repeated 10 times for solution A and 30 times for solution B.

Stage 2, the core coating was made following these steps: (i) mixing of the reagents, (ii) immersion of the cores, (iii) centrifugation, (iv) drying in the oven and (v) sintering at 950 °C. Steps (ii–iv) were repeated 6 times for each type of coating.

109
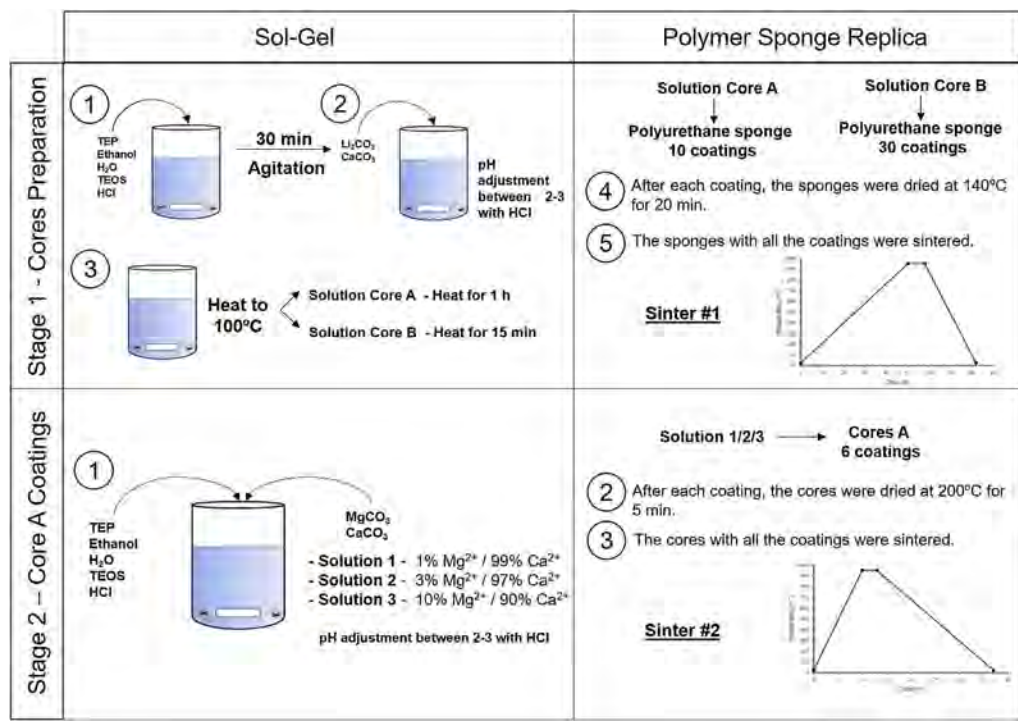
Fig. 1 – Schematic representation of the multilayer scaffolds preparation.

The X-ray diffraction (XRD) technique was followed to evaluate the crystalline phases of the ceramic scaffolds. The Bruker – AXR D8 Advance diffractometer was used with secondary graphite monochromator and Cu Kα radiation (1.5418740 Å) with Bragg–Brentano thetha–2thetha geometry. The X-ray tube operating conditions were 40 kV and 30 mA, and the test conditions were angles 2θ from 10° to 40° with 0.02 steps by counting 8 s per step. The diffractograms were analyzed with the Match! Software, version 3.11.2.188, using the database provided by the Crystallography Open Database (COD).

A scanning electron microscope with energy dispersive X-ray spectroscopy (SEM-EDX) (Hitachi S-3500N and INCA system by Oxford Instrumental Analytical) was used to evaluate the microstructure and qual-itatively the chemical composition of the scaffold surface.

Raman spectra were acquired by a LabRAM HR 800 Raman system brand Horiba-Jobin Yvon with an integrate Olympus BX41 confocal microscope. Spectra were collected between 300 and 1300 cm^{-1} at a resolution of 1 cm^{-1} using a 514 nm laser.

The mercury porosimetry technique was followed to determine pore distribution and porosity <300 μm. A Poromaster 60 GT Quantachrome instruments was used, with pressure between 0.851 psi and 59153.25 psi. The pycnometer with water, followed by the application of Archimedes' principle, was employed to determine porosity >300 μm.

A total of 15 samples of each type (8.5 mm diameter and 7.0 mm high) were tested in compression using a Simple Manual Test Stand (NEURTEK instruments SVL-1000N). Force was

Table 1 – Chemical composition and reagents used in the preparation of the cores and external coatings.[a]							
Scaffold	Chemical composition (mol%)	Triethyl phosphate TEP (ml)	Tetraethyl orthosilicate TEOS (ml)	Li_2CO_3 (g)	$CaCO_3$ (g)	$MgCO_3$ (g)	Substitution of Ca^{2+} by Mg^{2+}
Core A/B	SiO_2–25P_2O_5–6Li_2O–68CaO	10.2	0.38	0.5	8.04	–	–
CoreA-1Mg	29SiO_2–3P_2O_5–67.3CaO–0.7MgO				11.2	0.1	1%
CoreA-3Mg	29SiO_2–3P_2O_5–66CaO–2MgO	1.63	11.03	–	11	0.3	3%
CoreA-10Mg	29SiO_2–3P_2O_5–61CaO–7MgO				10	1	10%

[a] All the preparations were carried out with 20 ml of distilled water, 5 ml of ethanol and 10 ml of HCl to obtain 10 g of sol.

110
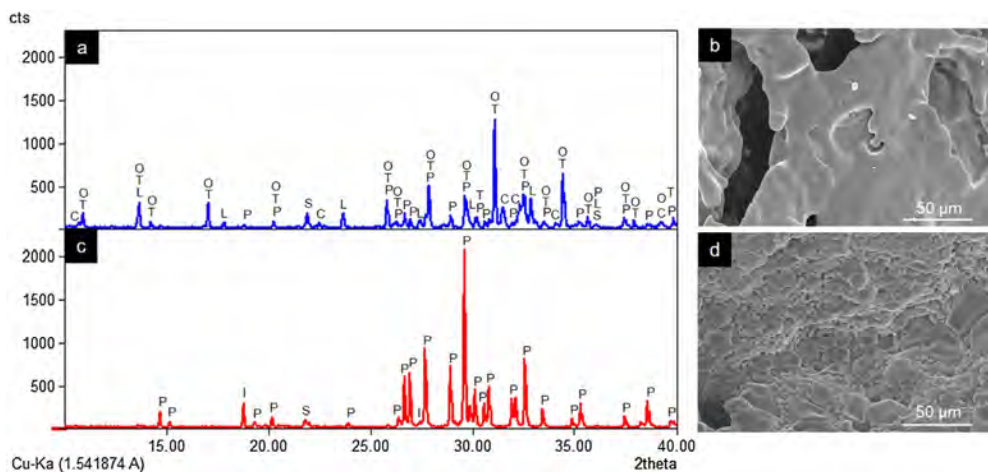
**Fig. 2 – Diffractograms and SEM images of Core A (a and b) and Core B (c and d) (P: $Ca_2P_2O_7$, I: $Li(PO_3)$, S: SiO_2, T: β-$Ca_3(PO_4)_2$, L: $LiCa(PO_4)$, O: $Ca_{9.95}Li_{1.05}(PO_4)_7$, C: $Ca_5(PO_4)_3Cl$).**

applied constantly over the entire sample surface. A digital force gauge dst/dsv SERIES was employed to record force until the scaffold completely broke.

Porosity and compressive strength tests were performed on the Core A and CoreA-10Mg scaffolds as representative samples of the other scaffolds.

Scaffolds' *in vitro* bioactivity was evaluated by soaking them in simulated body fluid (SBF) from 3 days to 28 days at 37 °C according to Standard ISO/FDIS 23314:2014 [15]. The sample was evaluated by SEM-EDX after each testing time. Ion exchange was evaluated by inductively coupled plasma optical emission spectrometry (ICP-OES) with Thermo iCAP 6500 DUO equipment. For this purpose, an aliquot of the resulting SBF was taken for the analysis. The remaining chloride ions in the SBF aliquot were analyzed by the ion chromatography technique (IC) using Metrohm equipment.

Results

Characterization of cores

The crystalline phases formed in Cores A and Core B are seen in Fig. 2, together with the surface images obtained by SEM.

Core A (Fig. 2(a) and (b)) presented mostly the β-TCP phase (COD 96-151-7239), and the phases with the phosphate group $(PO_4)^{3-}$, but with lithium and chlorine: $Ca_{9.95}Li_{1.05}(PO_4)_7$ (COD 96-152-6054); $LiCa(PO_4)$ (COD 96-722-2995); $Ca_5(PO_4)_3Cl$ (COD 96-101-917, COD 96-210-5266). The other phase that Core A less intensely presented was the calcium pyrophosphate phase ($Ca_2P_2O_7$ – CPP) (COD 96-100-1557) and the SiO_2 phase (COD 96-900-8225). This core had a smooth surface, and the edges of a possible hexagonal grain were noticed in some areas. The Ca/P ratios on the sample surface were 1.06 and 1.40. The presence of chlorine and silicon was also detected, but the latter was zero on some surface points.

Core B (Fig. 2(c) and (d)) presented mostly the $Ca_2P_2O_7$ phase, followed by the $Li(PO_3)$ phase (COD 96-210-2137) and the SiO_2 phase. This core was characterized by a surface made up of different sized hexagonal grains measuring ~10–15 μm on average. The Ca/P ratios on the sample surface were 0.93 and 1.09. Silicon was also detected, but only on some surface points.

Fig. 3 shows the Raman spectra of both cores. Table 2 indicates the vibration groups assigned to each frequency. In Core A, the characteristic bands of the PO_4^{3-} group of the TCP phase appeared, including calcium phosphate substituted for lithium and chloroapatite. In Core B, the vibrations of the P–O–P and PO_3 groups corresponding to the CPP phase, or even the $Li(PO_3)$ phase, were identified.

Characterization of the CoreA-XMg scaffolds

Fig. 4 presents the diffractograms of the CoreA-XMg scaffolds. These samples showed the following phases: β-TCP (COD 96-151-7239); $Ca_{10.115}Mg_{0.385}(PO_4)_7$ (COD 96-901-2137); $LiCa(PO_4)$ (COD 96-722-2995); $Ca_{9.95}Li_{1.05}(PO_4)_7$ (COD 96-152-6054); $Ca_5(PO_4)_3Cl$ (COD 96-101-917, COD 96-210-5266); SiO_2 (COD 96-900-8228).

When Core A was coated, the CPP phase peaks completely disappeared, while the phase of the calcium phosphate substituted for magnesium appeared. Moreover, when magnesium doping increased, the phase of calcium phosphate substituted for magnesium also increased, while the phase chloroapatite decreased. During intermediate doping (CoreA-3Mg), the intensity of these peaks was equal and inversed during the minimum (CoreA-1Mg) and maximum (CoreA-10Mg) doping.

Fig. 5 shows the SEM images of the CoreA-XMg scaffolds. Two images are presented per scaffold: one with low magnification, where the microstructure of the new coatings made on Core A are seen; the second images are presented at high magnification, where these coatings can be seen in more detail. On

111
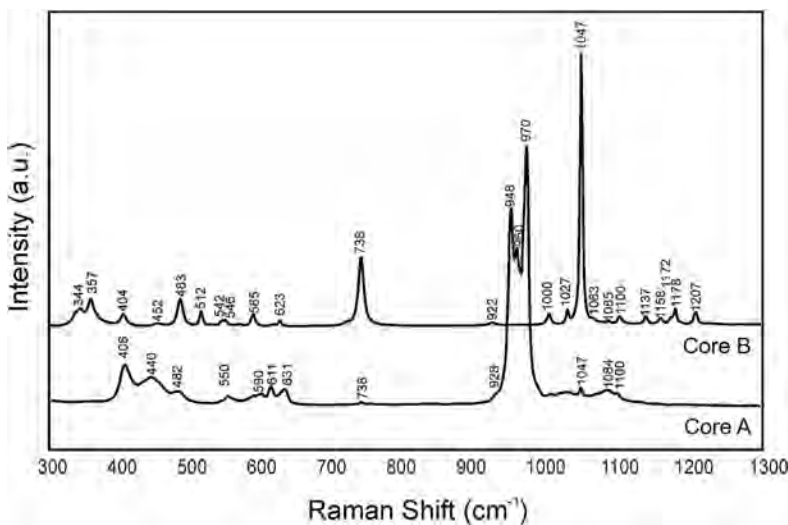
Fig. 3 – Raman spectra of Core A and Core B.

Table 2 – Frequencies of the bands observed in the Raman spectra of Core A and Core B.			
Raman shift (cm^{-1})		Vibrational group	Ref.
Core A	Core B		
–	344	δ (PO$_3$) sym stret	[16]
–	357	δ (PO$_3$) sym stret	[16,17]
–	404	δ (PO$_3$) sym stret	[16]
406	–	ν_2 (PO$_4$)$^{3-}$	[17]
440	–	ν_2 (PO$_4$)$^{3-}$	[17]
482	483	δ (PO$_3$) sym stret	[16]
–	512	δ (PO$_3$) sym stret	[16,17]
–	542	δ (PO$_3$) asym stret	[16]
550	–	ν_4 (PO$_4$)$^{3-}$	[17]
–	585	δ (PO$_3$) asym stret	[16]
590	–	ν_4 (PO$_4$)$^{3-}$	[17]
611	–	ν_4 (PO$_4$)$^{3-}$	[17]
–	623	δ (PO$_3$) asym stret	[16]
631	–	ν_4 (PO$_4$)$^{3-}$	[17]
738	738	ν(P-O-P) sym stret	[16,17]
928	922	ν(P-O-P) asy stret	[16]
948	–	ν_1 (PO$_4$)$^{3-}$	[17]
960	–	ν_1 (PO$_4$)$^{3-}$	[17]
970	–	ν_1 (PO$_4$)$^{3-}$	[17]
–	1000	ν(PO$_3$) sym stret	[16]
–	1027	ν(PO$_3$) sym stret	[16]
1047	1047	ν(PO$_3$) sym stret	[16,17]
–	1063	ν(PO$_3$) sym stret	[18]
1084	1085	ν(PO$_3$) asym stret	[18]
1100	1100	ν(PO$_3$) asym stret	[16]
–	1137	ν(PO$_3$) asym stret	[16,17]
–	1158	ν(PO$_3$) asym stret	[18]
–	1172	ν(PO$_3$) asym stret	[16]
–	1178	ν(PO$_3$) asym stret	[17]
–	1207	ν(PO$_3$) asym stret	[16]

112
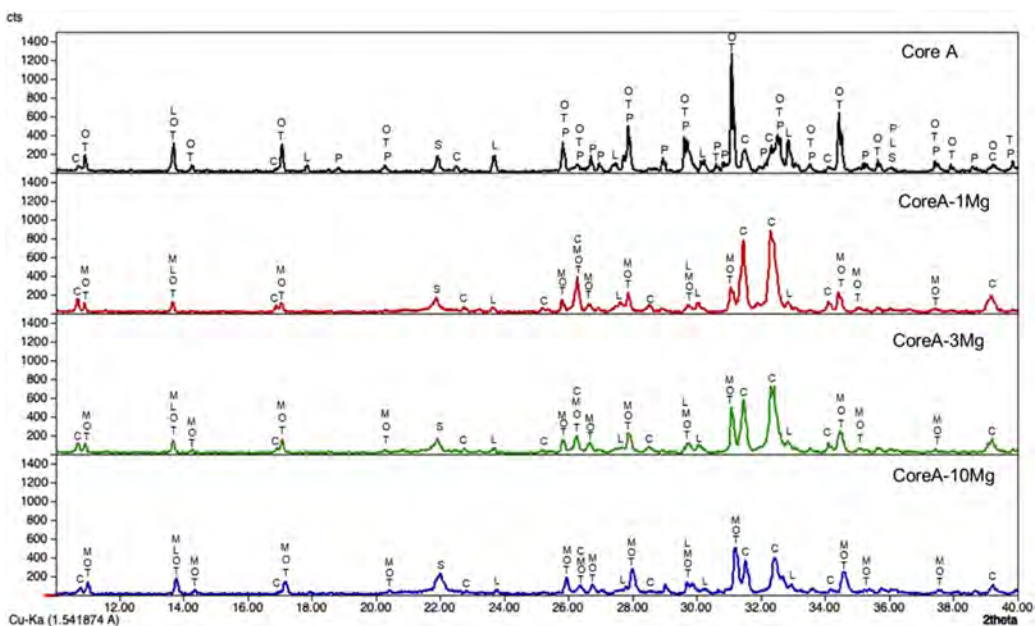
**Fig. 4 – Diffractograms of the Core A and CoreA-XMg scaffolds: P: $Ca_2P_2O_7$, S: SiO_2, T: β-$Ca_3(PO_4)_2$, M: $Ca_{10.115}Mg_{0.385}(PO_4)_7$, L: $LiCa(PO_4)$, O: $Ca_{9.95}Li_{1.05}(PO_4)_7$ and C: $Ca_5(PO_4)_3Cl$.**

the CoreA-1Mg and CoreA-3Mg scaffolds, the coating-formed plates are distributed over the entire Core A surface. The CoreA-10Mg scaffold coating presented no defined plates like the previous scaffolds. In this case, different sized particles covered the entire surface.

The EDX performed on the surface of these coatings revealed the presence of calcium, phosphorus, chlorine, magnesium and silicon. The atomic percentage averages of magnesium and silicon at the different points were 0.45% and 15.15% for the CoreA-1Mg scaffold, 1.42% and 21.27% for the CoreA-3Mg scaffold and 4.75% and 16.09% for the CoreA-10Mg scaffold, respectively.

On scaffolds' porosity, the mercury porosimetry technique and pycnometer allowed information on both micro- and macroporosity to be acquired. Fig. 6 shows the mercury porosimetry curves and Table 3 presents the total microporosity, which is divided into intra- and interparticle porosity. Core A presented more interparticle pores compared to intraparticle ones. The CoreA-10Mg scaffold displayed the same mercury intrusion behavior, but despite the percentage of intraparticle pores being approximately the same, the percentage of interparticle pores was higher compared to Core A. As a result, the total microporosity of Core A was 57.46% and that of CoreA-10Mg was 65.49%. The pore distribution curve shows that Core A had the most pores, approximately between 250 μm and 1.7 μm, with a mean value of 121 μm. The pore distribution of CoreA-10Mg was roughly between 173 μm and 0.5 μm, with a mean value of 38 μm.

Table 3 also shows scaffolds' macroporosity obtained by pycnometry and Archimedes' principle. For Core A it was

72.50% and 53.29% for the CoreA-10Mg scaffold. Finally, the compressive strength presented in Table 3 falls within a range of 0.38–1.84 MPa for the Core A and one of 0.40–2.00 MPa for the CoreA-10Mg scaffolds.

Evaluation of the in vitro bioactivity of the Core A and CoreA-XMg scaffolds

Fig. 7 shows the SEM images obtained after the *in vitro* bioactivity evaluation of Core A. Fig. 7(a) depicts how the surface presented no morphological changes up to 7 days immersed in SBF, when the original smooth scaffold surface (Fig. 2(b)) began to dissolve, shown by the arrow in Fig. 7(b). After 14 days in SBF (Fig. 7(c)), the zone observed at 7 days resembled a lamellar structure surrounded by the original microstructure. Additionally, spheres with an apatite-like appearance precipitated on the entire surface. On the following days (21 and 28) the lamellar structure continued to evolve until it occupied most of the surface which was, in turn, covered by a bigger number of precipitates (Fig. 7(d) and (e)). On average, the Ca/P ratios of lamellas were (1.34 ± 0.24) in the middle and (1.53 ± 0.16) on the edge of lamellas. For precipitates, the Ca/P ratio was (1.31 ± 0.12), and other elements like silicon and chlorine were also detected.

Fig. 8 shows the SEM images obtained after the *in vitro* bioactivity evaluation of CoreA-1Mg, CoreA-3Mg and CoreA-10Mg. The three afore-mentioned scaffolds presented precipitates after 3 days in SBF and even remained until 28 days (image not shown). These precipitates distributed over the

113
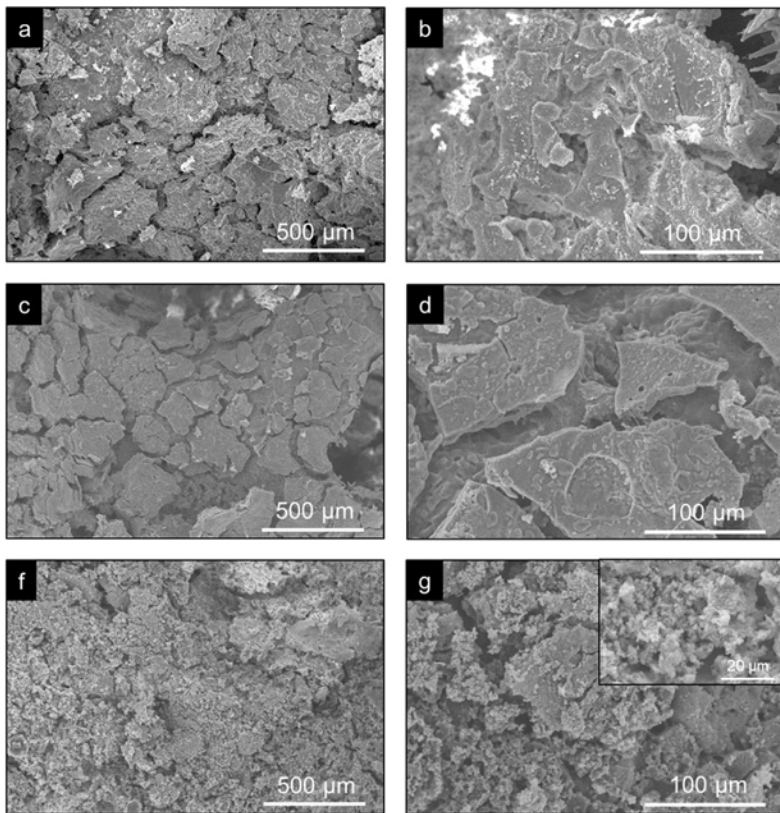
Fig. 5 – SEM images of (a and b) the CoreA-1Mg, (c and d) CoreA-3Mg and (f and g) CoreA-10Mg scaffolds.

sample' entire surfaces were globular in shape with needle-like structures.

The Ca/P ratio of precipitates changed over time and, due to magnesium doping, the (Ca + Mg)/P ratio was also considered. From 3 to 21 days, the CoreA-1Mg scaffold presented an average Ca/P ratio of (1.21 ± 0.13) and a (Ca + Mg)/P ratio of (1.31 ± 0.16). However, at 28 days, the Ca/P ratio changed to (1.52 ± 0.03) and the (Ca + Mg)/P ratio to (1.57 ± 0.04).

The CoreA-3Mg scaffold presented a Ca/P ratio of (1.46 ± 0.18) and a (Ca + Mg)/P ratio of (1.54 ± 0.22). Finally, the
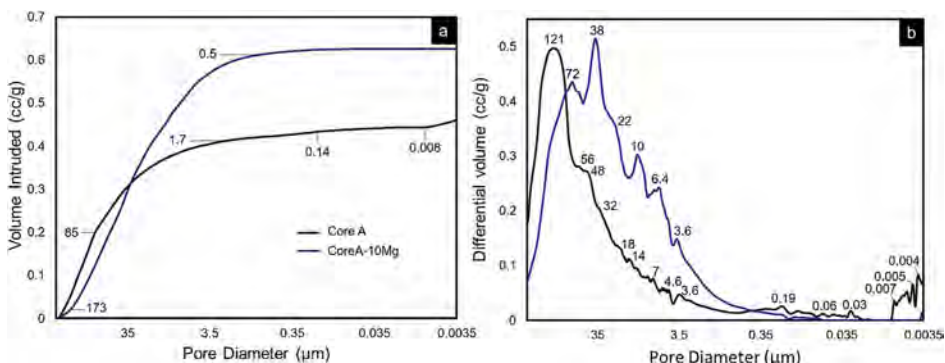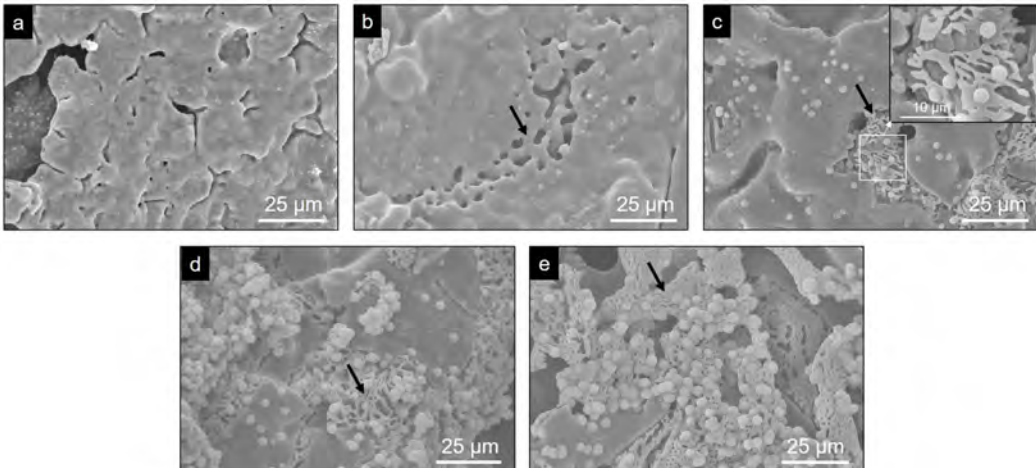
Fig. 6 – Mercury porosimetry curves: (a) cumulative and (b) differential volume intruded *vs.* pore diameter of the Core A and CoreA-10Mg scaffolds.

Table 3 – Summary of the porosity and compressive strength of the Core A and CoreA-10Mg scaffolds.					
Sample	Interparticle porosity (%)[a]	Intraparticle porosity (%)[b]	Scaffold microporosity (%)	Scaffold macroporosity (%)	Compressive strength (MPa)
Core A	50.11	7.35	57.46	72.50	0.38–1.84
CoreA-10Mg	58.37	7.13	65.49	53.29	0.40–2.00

[a] Corresponding to pores between 1 μm and 300 μm.
[b] Corresponding to pores <1 μm.

Fig. 7 – SEM images obtained by SEM after the *in vitro* bioactivity evaluation of the Core A scaffold: (a) 3 days, (b) 7 days, (c) 14 days, (d) 21 days and (e) 28 days.

CoreA-10Mg scaffold had a Ca/P ratio of (1.64 ± 0.22) and a (Ca + Mg)/P ratio of (1.77 ± 0.22).

Fig. 9 presents the curves obtained by ICP-OES and IC for the different scaffolds. It shows the concentration of ions in SBF during the evaluation of the *in vitro* bioactivity. The ionic behavior in the SBF that was in contact with Core A (Fig. 9(a)) showed: (i) calcium concentration generally lowered from the first day to 28 days, and displayed oscillatory behavior at intermediate times; (ii) phosphorous concentration lowered on day 3, but this concentration rose at other times; (iii) silicon whose initial concentration in SBF was zero, remained the same for the rest of the study time; (iv) lithium whose initial concentration was also zero, progressively increased during the rest of the study time; and (v) chloride concentration rose on day 7, and lowered to the initial concentration values for longer immersion times.

Fig. 9(b)–(d) shows the curves of the CoreA-1Mg, CoreA-3Mg and CoreA-10Mg scaffolds. In summary, the ionic behavior was as follows: (i) chloride ions showed similar behavior to the core but rose on day 3; (ii) calcium ions concentration in the CoreA-1Mg scaffold lowered until 21 days when it rose, while the other scaffolds showed opposite behavior; (iii) silicon concentration rose in the early day, except for the CoreA-10Mg scaffold which showed a slight adsorption after 28 days; (iv) phosphorous concentration generally lowered in the SBF, (v) lithium concentration rose over time and finally (vi) part

of the magnesium ions from the SBF was adsorbed by the scaffolds after 28 days, mainly on the CoreA-10Mg scaffold.

Discussion

Characterization of cores

Cores A and B were manufactured by the same method. The only difference between the two cores was the heating time of the sol solution (Fig. 1). This variation led to both cores presenting a different chemical phase, according to the XRD and Raman characterization results.

While preparing cores, the hydrolysis of TEOS and TEP first occurred, and then condensation was activated by adding carbonates. An acid catalyst was used to accelerate the hydrolysis reaction and, at the same time, to avoid rapid gelation in the condensation reaction. Fig. 10 summarizes the hydrolysis and condensation reactions of TEP. It is worth mentioning that although complete TEP hydrolysis can be seen, it rarely occurs. Therefore during condensation, water or alcohol can be obtained as a product of the reaction depending on the degree of TEP molecule hydrolysis. The reaction that took place while adding calcium carbonate is also shown. Note that it was the majority carbonate in the reaction, and that lithium carbonate was also added. As all these processes occurred

115
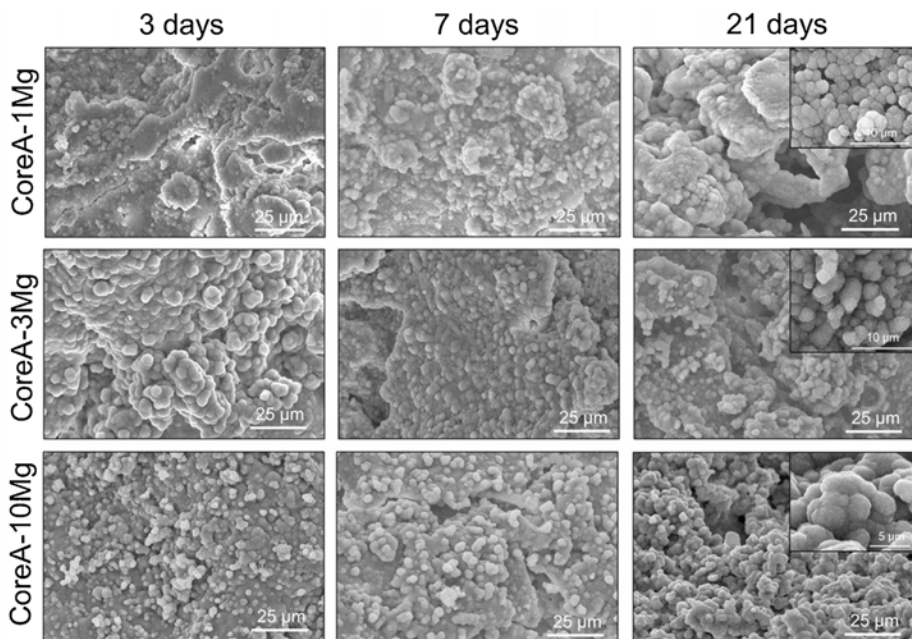
Fig. 8 – SEM images obtained after the *in vitro* bioactivity evaluation of the CoreA-XMg scaffold at 3 days, 7 days, and 21 days.

simultaneously, calcium ions were incorporated into the reaction, interfered with condensation, and could form TCP and/or CPP molecules.

The extension of the reactions (see Fig. 10) was modified according to heating time to generate the solution of Cores A and B. The difference in the two solutions was the amount of water in the final solution, which modified the condensation process. In solution A, and after heating for 1 h, all the water had evaporated and, therefore, all the added calcium ions came into contact with the hydrolyzed and condensed molecules, which favored the formation of TCP (Ca/P = 1.5). Solution B, with a 15-min heating time, still held most of the initial water. Visually, the solution separated into two phases: one oily and one liquid. The oily phase contained the molecules produced by hydrolysis and condensation, and the liquid phase was water. Thus, water molecules tended to dissolve calcium ions and leave the oily phase with a calcium deficit, which favored CPP formation (Ca/P = 1).

In the presence or absence of water molecules, this mechanism of action of calcium, explains the existence of two cores with different phases. The formation of the TCP or CPP phases, due to the deficiency (or not) of calcium ions, has also been observed by other authors [19]. In Core A, the other phases containing the PO_4^{3-} group formed along with the TCP phase, but were combined with other ions like lithium and chlorine. These ions were in the solution and, like calcium, they can form part of condensation. Consequently, other phases were obtained. In sol–gel synthesis is usual to find the formation of additional or residual phases to those desired [20].

Both cores were constituted of calcium phosphates, which are interesting as biomaterials. The main components were TCP and CPP, which are biocompatible [1,21]. Another phase present as chloroapatite, is not a good biomaterial at high concentration because it acidifies the environment, however, thanks to this, it can help in the dissolution of alkaline salts, digest the organic matrix and activate the bone resorption process produced by osteoclasts [22,23]. The phases of calcium phosphate substituted for lithium are phases that, as far as we know, have barely been studied. However, it is known that lithium is found in small traces in the human body and it stimulates the proliferation of certain cells and bone densification, as well as improving the mechanical properties by adding it to TCP [10,23].

The presence of a high number of phosphate phases in the Core A, makes it an ideal material to study the synergistic effects between the phases. Additionally, in order to improve the behavior of the core, it is coated with phases constituted of silicon and magnesium, obtaining a multilayer scaffold. The study of Core B under the same conditions is proposed for a future work.

Characterization of the CoreA-XMg scaffolds

The increase in intensity of the silica peaks in the three diffractograms in Fig. 4 corroborates the presence of the external coatings, which presents more silicon than the core. The decrease in the CPP phase was attributed to the diffusion processes that occur during the second sintering where the

116
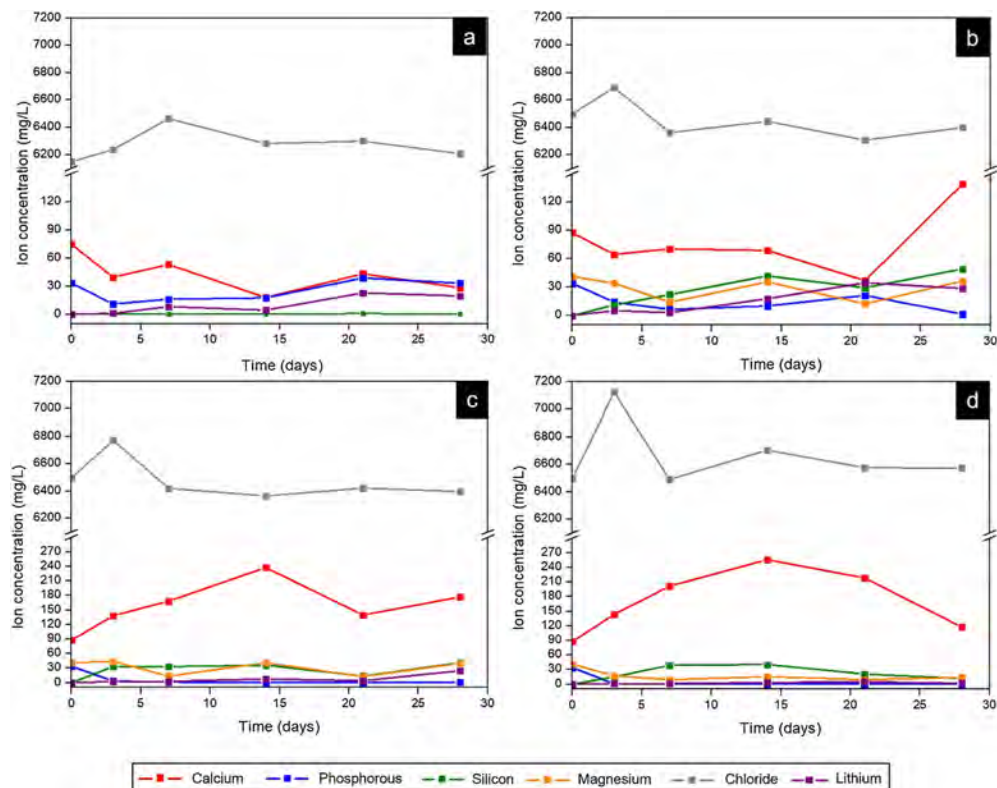
Fig. 9 – The ion concentration in SBF at different times after soaking scaffolds: (a) Core A, (b) CoreA-1Mg, (c) CoreA-3Mg, and (d) CoreA-10Mg.
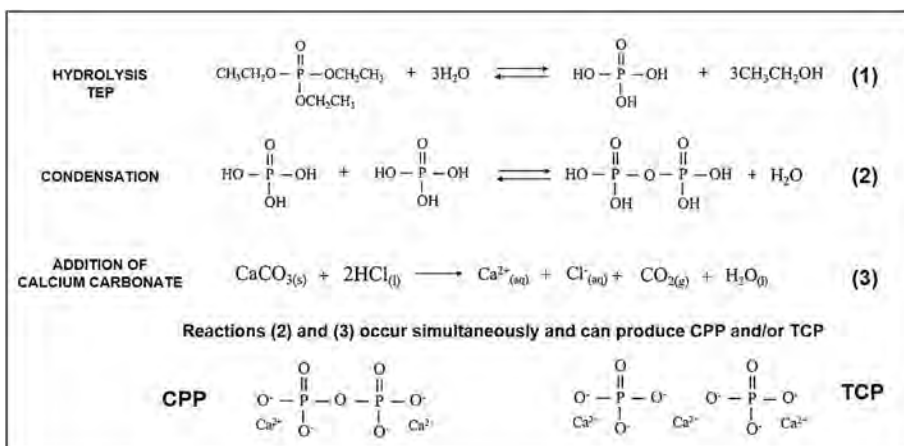

Fig. 10 – TEP hydrolysis and condensation reactions in the presence of calcium during core preparation.

117

pyrophosphate was redistributed to form a phase with a Ca/P ratio above 1. The presence of magnesium also explained the disappearance of CPP. Different studies have shown that it tends to preferentially stabilize the TCP phase [24]. The intensity of the XRD peaks decreased with increased magnesium, which could imply loss of crystallinity.

Competition occurs between the formation of calcium phosphate with magnesium and chloroapatite. Compared to Core A, the intensity of the phase chloroapatite increased with coatings. However, this phase decreased with increased of magnesium because the formation of calcium phosphate substituted for magnesium phase was favored.

The coated scaffoldsśurface changed (Fig. 5) compared to the Core A surface (Fig. 2(b)). The coating of the CoreA-1Mg and CoreA-3Mg scaffolds formed separate plates that covered the core surface. The fact that was no continuous layer could be attributed to the contractions that occurred during heat treatment. The reason why the CoreA-10Mg scaffold coating did not form plates, but different sized precipitates instead, could be due to the amount of magnesium that now competed with calcium. According to the studies by Zhou and co-workers, Ca^{2+} and Mg^{2+} ions can react with PO_4^{3-} to form needle and plate particles, but when both ions coexist in the PO_4^{3-} reaction, they form a mesoporous structure [24].

The atomic percentage of silicon was practically the same in all three scaffolds. Thus the difference in peak intensity, observed by XRD, could be due to the difference between the crystalline and amorphous phases, which was not detected. The percentage of magnesium consistently rose with the increase in doping.

During the bone growth, the porosity is fundamental for defining the cells/scaffold interaction. In this work, pores larger than 300 μm were designated as macropores, while those smaller than 300 μm as micropores. Although an ideal pore size has not yet been established, it is known that both types are fundamental. Microporosity favors cells/material interaction as they are responsible for protein adsorption and retention, which will later interact with cells promote their adhesion [25]. Macroporosity is responsible for enabling cells to penetrate and migrate throughout the scaffold [25].

Microporosity increased with the coatings on the core because CoreA-10Mg scaffold surface was more porous (Fig. 5(f) and (g)) than Core A (Fig. 2). In the case of macroporosity, this decreased due to the coatings on Core A, which closed the original template pores. Despite the decreased macroporosity, another property was favored: compressive strength. As a result of increased compressive strength, the CoreA-10Mg scaffold could be compared to cancellous bone which, according to Polo-Corrales et al. [26], lies between 2 MPa and 4 MPa.

Evaluation of the in vitro bioactivity of the Core A and CoreA-XMg scaffolds

The *in vitro* evaluation of Core A showed that the material generally behaved by dissolving its original microstructure to form a lamellar structure which was, in turn, colonized by precipitates. After 7 days the lamellas appeared together with a release of chlorides, calcium and lithium. According to the released ions, the dissolved phases could the chloroapatite

and lithium phases. The average Ca/P ratio was (1.53 ± 0.16) on the edge of lamellae, which indicates the presence of the β-TCP phase, it would suggest that the dissolved phases were the CPP, lithium phases or chloroapatite. The dissolution of the CPP phase cannot be ionically verified as other phases also contained calcium and phosphorus. However, lithium release was evident. After 14 days, precipitates appeared and adsorption of chloride and calcium occurred that could be incorporated into the new precipitates.

Globular apatite-like precipitates had an average Ca/P ratio of (1.31 ± 0.12). Although this would not correspond to the Ca/P ratio of hydroxyapatite, the presence of both silicon and chlorine retained in the precipitate could affect hydroxyapatite detection or formation. The mechanism by which these precipitates appeared on the material's surface, together with lamellae formation, can be attributed to the presence of the β-TCP phase, according mechanism proposed by Kim et al. [27].

The *in vitro* behavior displayed by the CoreA-XMg scaffolds was different compared to Core A, but similar to each other. After only 3 days of being in contact with SBF, the three scaffolds showed precipitates, which covered the entire surface, and even remained until 28 days.

From the analysis done of scaffolds' ionic behavior, it was concluded that chloride ions influenced the appearance of precipitates as this was released after 3 days (Fig. 10), which coincided with their appearance (Fig. 9). The phosphorous concentration always lowered in the three scaffolds; that is, phosphorous was adsorbed by the sample until all the phosphorus present in SBF was consumed. This adsorption is associated with the formation of precipitates.

The ionic behavior of calcium and magnesium was different in the three scaffolds. In the CoreA-1Mg scaffold, in the first days the sample adsorbed calcium and then released it after 28 days. The other two scaffolds released calcium until 14 days and then adsorbed it. This behavior is due to the doping with magnesium. The scaffolds with the highest percentage of doping initially formed the precipitates with magnesium, even adsorbing the magnesium ions from the SBF. On the contrary, the scaffold with lower percentage of magnesium formed the precipitates with calcium adsorbed from SBF. In general, lithium was released by all the scaffolds, indicating the dissolution of the coating and contact with the core. Likewise, silicon was released by scaffolds and it is suggested that the bioactivity of these is due to the greater amount of silica in the external coatings, following the mechanism proposed by Hench [28].

The Ca/P and (Ca + Mg)/P ratios in the initial times do not correspond to the hydroxyapatite ratio (1.67). However, with the immersion time this ratio increased, reaching the ratio of calcium deficient hydroxyapatite. Only the CoreA-10Mg scaffold presented hydroxyapatite ratios.

In short, the sol–gel method's versatility was demonstrated by obtaining a multiphase material of calcium phosphates. This method allowed different elements to be incorporated to form complex and varied phases. The different phases conferred Core A a bioactive characteristic, but also the development of a lamellar structure when it came into contact with SBF. By incorporating the second coatings on Core A, a multilayer scaffold with a marked bioactivity character was

118

created. The bioactivity of the multiphase core was improved with coatings that accelerated bioactive behavior after being in contact with SBF for only 3 days. Previously, Ciro et al. [29] improved the bioactivity of material with crystalline phases of α/β-TCP, CPP and CaHPO$_4$, by adding 10 and 15% of bioglass with composition 31SiO$_2$–56CaO–2MgO–11P$_2$O$_5$. However, with the development of multilayer scaffold, besides promoting the bioactivity with the external layer, it is proposed to maintain the characteristics such as porosity and mechanical resistance provided by the composition of the core.

Previously, multilayer scaffolds doped with strontium and iron were studied, which also showed an acceleration of *in vitro* bioactivity [13,14]. In the case of strontium, the ion substituted the calcium silicate phase, while iron and magnesium substituted the calcium phosphate phase. Although all three studies show positive effects on bioactivity, the core of the strontium and iron doped scaffolds are different from the one used in this study and therefore cannot be directly compared.

The presence of magnesium on apatite precipitates might promote tissue growth than to its good interaction with cells, and silicon release may contribute to this process, as discussed above. Although the three doped scaffolds presented precipitates at only 3 days, the CoreA-10Mg scaffold could prove the most favorable for cells given the larger amount of magnesium contained on the surface. It is worth highlighting that, although doped coatings provide bioactivity, the core presented a chemical composition that was capable of mimicking cancellous bone with macroporosity and compressive strength.

Conclusions

In this work, it was demonstrated the versatility of the sol–gel process in obtaining multiphase materials. Using a single chemical composition and varying the heating time of the solution, three-dimensional porous scaffolds with different crystalline phases were obtained. Additionally, through this method it was possible to obtain multilayer structures doped with silicon and magnesium in the outer layers. The multilayer scaffold developed in this work combines several chemical compositions that provide different characteristics such as mechanical strength, porosity, and *in vitro* bioactivity, which are difficult to obtain in scaffolds of a single chemical composition. Silicon accelerated bioactivity and the presence of magnesium in apatite precipitates can enhance cellular processes.

Conflicts of interest

None declared.

Acknowledgement
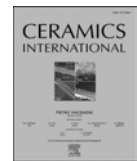
REFERENCES

[1] M. Canillas, et al., Calcium phosphates for biomedical applications, Bol. Soc. Esp. Cerám. Vidr. 53 (2017) 91–112.

[2] E. Champion, Sintering of calcium phosphate bioceramics, Acta Biomater. 9 (2013) 5855–5875.

[3] N. Eliaz, et al., Calcium phosphate bioceramics: a review of their history, structure, properties, coating technologies and biomedical applications, Materials 10 (334) (2017) 1–104.

[4] B. Thavornyutikarn, et al., Bone tissue engineering scaffolding: computer-aided scaffolding techniques, Prog. Biomater. 3 (2014) 61–102.

[5] N. Kondo, et al., Bone formation and resorption of highly purified β-tricalcium phosphate in the rat femoral condyle, Biomaterials 26 (2005) 5600–5608.

[6] M. Ebrahimi, et al., Biphasic calcium phosphates bioceramics (HA/TCP): concept, physicochemical properties and the impact of standardization of study protocols in biomaterials research, Mater. Sci. Eng. C 71 (2017) 1293–1312.

[7] S.V. Dorozhkin, Multiphasic calcium orthophosphate (CaPO$_4$) bioceramics and their biomedical applications, Ceram. Int. 42 (2016) 6529–6554.

[8] Q. Nawaz, et al., New insights into the crystallization process of sol–gel-derived 45S5 bioactive glass, J. Am. Ceram. Soc. 103 (2020) 4234–4247.

[9] A.M. Pietak, et al., Silicon substitution in the calcium phosphate bioceramics, Biomaterials 28 (2007) 4023–4032.

[10] C.Q. Zhao, et al., Doping lithium element to enhance compressive strength of b-TCP scaffolds manufactured by 3D printing for bone tissue engineering, J. Alloys Compd. 814 (2020) 152327.

[11] Y. Gu, et al., Three-dimensional printed Mg-doped b-TCP bone tissue engineering scaffolds: effects of magnesium ion concentration on osteogenesis and angiogenesis in vitro, Tissue Eng. Regen. Med. 16 (4) (2019) 415–429.

[12] D. Ke, et al., Effects of MgO, ZnO, SrO, and SiO$_2$ in tricalcium phosphate scaffolds on in vitro gene expression and in vivo osteogenesis, Mater. Sci. Eng. C 96 (2019) 10–19.

[13] N.A. Mata, et al., Synthesis and characterization of 3D multilayer porous Si–Ca–P scaffolds doped with Sr ions to modulate in vitro bioactivity, Ceram. Int. 46 (2020) 968–977.

[14] N.A. Mata, et al., New iron-doped multilayer ceramic scaffold with noncontinuous bioactive behavior, Ceram. Int. 46 (2020) 16388–16396.

[15] ISO/FDIS 23317: 2007, Implants for surgery – in vitro evaluation for apatite-forming ability of implant materials.

[16] D. De Waal, et al., Vibrational spectra of a solid solution of cadmium and calcium pyrophosphate, Mater. Res. Bull. 29 (1994) 1129–1135.

[17] G. Cheng, et al., Effects of Mn-doping on the structural evolution of β-tricalcium phosphate by Rietveld refinement and Raman spectroscopy, Mater. Lett. 235 (2019) 236–238.

[18] B.C. Cornilsen, R.A. Condrate, The vibrational spectra of β-Ca$_2$P$_2$O$_7$ and γ-Ca$_2$P$_2$O$_7$, J. Inorg. Nucl. Chem. 41 (1979) 602–605.

[19] Z.Z. Zyman, A.V. Goncharenko, D.V. Rokhmistrov, Phase evolution during heat treatment of amorphous calcium phosphate derived from fast nitrate synthesis, Process. Appl. Ceram. 11 (2017) 147–153.

[20] C. Ruiz-Aguilar, et al., Characterization of β-tricalcium phosphate powders synthesized by sol–gel and mechanosynthesis, Bol. Soc. Esp. Cerám. Vidr. 57 (2018) 213–220.

[21] S.R. Vasant, M.J. Joshi, A review on calcium pyrophosphate and other related phosphate nano bio-materials and their applications, Rev. Adv. Mater. Sci. 48 (2017) 44–57.

[22] P.H. Schlesinger, et al., Characterization of the osteoclast ruffled border chloride channel and its role in bone resorption, J. Biol. 272 (1997) 18636–18643.

[23] M. Šupová, Substituted hydroxyapatites for biomedical applications: a review, Ceram. Int. 41 (2015) 9203–9231.

[24] H. Zhou, et al., Synthesis of β-TCP and CPP containing biphasic calcium phosphates by a robust technique, Ceram. Int. 42 (2016) 11032–11038.

[25] R.A. Perez, et al., Role of pore size and morphology in musculo-skeletal tissue regeneration, Mater. Sci. Eng. C 61 (2016) 922–939.

[26] L. Polo-Corrales, et al., Scaffold design for bone regeneration, J. Nanosci. Nanotechnol. 24 (2014) 15–56.

[27] H. Kim, et al., Process and kinetics of bonelike apatite formation on sintered hydroxyapatite in a simulated body fluid, Biomaterials 26 (2005) 4366–4373.

[28] L.L. Hench, Bioceramics: from concept to clinic, J. Am. Ceram. Soc. 74 (1991) 1487–1510.

[29] E. Ciro, et al., Elaboración de un cemento óseo de fosfato de calcio con una adición de biovidrio, Bol. Soc. Esp. Cerám. Vidr. 54 (2015) 84–92.

Apéndice E

Artículo 5

Multilayer Mg-pyrophosphate glass ceramic with discontinuous bioactivity. Physicochemical characterization

Nayarit A. Mata [a], Pablo Velasquez [a], Angel Murciano [b], Piedad N. De Aza [a],*

[a] Instituto de Bioingeniería, Universidad Miguel Hernández, Avda. Ferrocarril S/n, Elche, Alicante, 03202, Spain
[b] Departamento de Materiales, Óptica y Tecnología Electrónica, Universidad Miguel Hernández, Avda. Universidad S/n, Elche, Alicante, 03202, Spain

ABSTRACT

Novel pyrophosphate glass ceramic scaffolds (3D-Ca-P_2) were fabricated and coated with several layers of CaO-P_2O_5-SiO_2-MgO [3D-[Ca/P/Si]-XMg (X = 1,3 and 10 mol%)] as potential bioactive scaffolds for bone regeneration. The core scaffolds present a homogeneous distribution of polygonal grains consisting of 97% $Ca_2P_2O_7$ with CaO-P_2O_5 glass as the matrix phase. Incorporating MgO into coatings led to extremely porous layers, assembled by nanosized equiaxed particles, which favoured the formation of different phases of tricalcium phosphate instead of pyrophosphate. Possible applications were determined based on Standard ISO/FDIS 23317:2014 for ceramics and powder samples. The 3D-Ca-P_2 scaffolds' non-bioactivity was modulated by coatings of different bioactivity behaviours depending on MgO contents. 3D-[Ca/P/Si]-10Mg was the best scaffold as precipitated hydroxyapatite (HA), was more amorphous than in the other scaffolds because Mg was incorporated into the HA network, which could favour subsequent cell adhesion. The multilayer scaffold provides advantages over others developed until now because in a unique structure all the characteristics required for an implant are combined. On a physical level, mechanical resistance, and porosity, and on a chemical level, a combination of calcium phosphate phases, similar to the mineral phase of bone, doped with Mg ions, which are capable of being transformed into HA in different periods of time.

1. Introduction

The incentive of the present work resulted from the authors making longstanding efforts to develop: (i) unconventional CaO-P_2O_5-SiO_2 scaffolds as bone substitutes; (ii) the full-bodied synthesis of such biomaterials. Traditionally, CaO-P_2O_5-SiO_2 system compositions have been developed as monophasic [1,2], biphasic materials [3,4] and multiphase materials [5,6]. Moreover, the incorporation of silicon into calcium phosphate in an optimal composition can control the material's biodegradability and bioactivity [7,8]. However, the main phases are noticeably orthophosphates, while calcium pyrophosphate (Ca-P_2) remains relatively unexplored. Pyrophosphate is an essential molecule for the body and is present in plasma, teeth and bone [9–11].

Calcium phosphate solids formation is essentially relevant as calcium phosphate that comes in the calcium hydroxyapatite (HA) form is the main skeletal system constituent. Calcium phosphate deposition in body regions that ought not to calcify takes place under many pathological conditions: e.g., arthritis, bursitis, dental calculus, other ectopic calcification forms, etc. [12]. Several authors have clearly demonstrated the role of tripolyphosphate, pyrophosphate and long-chain phosphates to inhibit HA formation both in vitro and in vivo [13,14].

Most of the materials developed show good biocompatibility, but few are developed as three-dimensional scaffolds with excellent physical characteristics such as mechanical strength and porosity. For this reason, our most recent idea was to fabricate a multilayer of stratified materials, where each layer would provide the final material a combination of different requirements. We propose manufacturing a material of non-bioactive behaviour to bioactive, or even intermittent bioactive behaviour, depending on the needs of the implantation site or the patient's health. We hypothesised that by simply modifying the technique used in our above work would lead to a new full-bodied synthesis of CaO-P_2O_5-SiO_2 scaffolds consisting of cristobalite, calcium pyrophosphate and different tricalcium phosphate phases as the main phases. An extensive literature search did not detect any previous works along these lines which is, hence, the choice of topic for the present study. Another effort herein made is to assess the possible effects of Mg^{2+} as an additive during the synthesis process and on bioactivity behaviour. We have several reasons for choosing Mg^{2+}. First of all, Mg^{2+} is the fourth most

---

* Corresponding author. Instituto de Bioingenieria, Universidad Miguel Hernandez, 03202, Elche, Alicante, Spain.
  E-mail addresses: nmata@umh.es (N.A. Mata), pavelasquez@umh.es (P. Velasquez), amurciano@umh.es (A. Murciano), piedad@umh.es (P.N. De Aza).

abundant ion in the human body, mainly in bones [15]. Secondly, Mg^{2+} tends to help retain the amorphous phase of calcium phosphates [16]. Thirdly, cell adhesion and proliferation are favoured by amorphous hydroxyapatite [17]. Finally, Mg^{2+} tends to help stabilise tricalcium phosphate (TCP) as opposed to pyrophosphate [18].

2. Materials and methods

In order to obtain pyrophosphate 3D scaffolds (3D-Ca-P_2), 20 ppi-Polyurethane foams (Eurofoam-Germany-PU) of 13 mm Ø x 10 mm long were coated with a sol-solution composed mainly of: 98% Tetraethyl Orthosilicate, Aldrich (TEOS) as a silicon source; ≥ 99.8% Triethy Phosphate, Aldrich (TEP) as a phosphorus source; ≥ 99% calcium carbonate, Sigma, as a calcium source. Finally, 99% lithium carbonate, Sigma-Aldrich, was added as a reinforcing agent. In order to obtain an oily solution that was viscous enough to wet the PU foams and would not drip, it was adjusted with 37% hydrochloric acid, Ensure, until pH 2–3, followed by heating for 15 min at 100 °C. Table 1 shows the amount of the different reagents used to obtain the sol-solution. Finally, 30 impregnations of the PU foam in sol-solution were necessary to create a thick enough coating before burning the PU foam and sintering the 3D-Ca-P_2 ceramic at 950 °C/8 h.

In order to improve the bioreabsorption and osteogenesis of the sintered pyrophosphate glass ceramic scaffold, it was coated with silicon and magnesium. New sol-solutions with 1, 3 and 10 mol% MgO were prepared according to Table 1. The 3D-Ca-P_2 ceramic scaffolds were coated 6 times in each new sol-solution and dried at 200 °C for 5 min. Finally, the new 3D-[Ca/P/Si]-XMg-coated scaffolds were sintered at 950 °C/3 h.

Based on Standard ISO/FDIS 23317:2017 for ceramics and powder samples [19], the possible bone tissue repair application of both the 3D-Ca-P_2 scaffolds and 3D-[Ca/P/Si]-XMg coated scaffolds was determined. The 3D scaffolds were immersed in simulated body fluid (SBF) up to 28 days at 37 °C.

The composition and crystalline phases of the manufactured 3D-Ca-P_2 scaffolds and 3D-[Ca/P/Si]-XMg-coated scaffolds were evaluated by X-Ray Diffraction (XRD, Bruker-AXR D8Advance) using Cu-K_α radiation (1.5418740 Å). Data were collected between 10° and 50° (2θ) at 0.02 steps, counting 8 s per step. The X-Ray tube was operated at 40 kV and 30 mA. Version 3.7.1.132 of Software Match! was used for the Rietveld analysis of difractograms and the database provided by the Inorganic Crystal Structure Database (ICSD) and the Crystallography Open Database (COD). Next the Fourier-Transform Infrared Spectra (FTIR, Thermo Scientific Nicolet iS5, equipped with iD5 ATR) were collected between 1500 cm^{-1} and 450 cm^{-1} at a resolution of 4 cm^{-1} and room temperature by employing 64 scans.

The physical characterization of the scaffolds was performed on the manufactured 3D-Ca-P_2 and 3D-[Ca/P/Si]-10Mg scaffolds as a representative sample. The porosity and distribution of the pores between 300 μm and 0.004 μm was evaluated by the Mercury Porosimetry Technique using a Poremaster 60 GT Quantachrome instruments, with a pressure between 6.789 KPa and 407,031 KPa. The total porosity of the scaffold was evaluated by pycnometer with water following the Archimedes principle. Compressive strength was evaluated by crushing until rupture with a Microtest SCM3000 instrument. The force was applied axially to the cylindrical scaffolds at a speed of 1.00 mm/min.

The morphology of the uncoated and Mg-coated scaffolds before and

after soaking in SBF was characterised by Scanning Electron Microscopy with Energy Dispersive X-Ray Spectroscopy (SEM-EDX) using a Hitachi S-3500 N and the INCA system by Oxford Instruments Analytical. Scaffolds were electron beam conductive by coating with palladium prior to the SEM study.

To determine the bioactivity and/or biodegradability of the 3D-Ca-P_2 scaffold and 3D-[Ca/P/Si]-XMg-coated scaffolds, changes in the ionic concentration in SBF were established by ICP-OES (inductively-coupled plasma atomic emission spectroscopy; PerkinElmer Optima 2000). Scaffolds were extracted from SBF and examined by SEM-EDX at regular time points.

3. Results

The mineralogical study of the 3D-Ca-P_2 and 3D-[Ca/P/Si]-XMg-coated scaffolds after milling displayed several crystalline phases. The XRD pattern of the 3D-Ca-P_2 scaffold (see Fig. 1) displayed the typical peaks in these phases; e.g., cristobalite-SiO_2 (COD 96-900-8225), calcium diphosphate-$Ca_2P_2O_7$ (COD 96-100-1557) and $Li(PO_3)$ (COD 96-210-7073). The 3D-[Ca/P/Si]-XMg-coated scaffolds showed non-stoichiometric Mg-Tricalcium phosphate (Mg-TCP) $Ca_{10.115}Mg_{0.385}P_7O_{28}$ (COD 96-901-2137), non-stoichiometric Li-Tricalcium phosphate (Li-TCP) $Ca_{9.95}Li_{1.05}(PO_4)_7$ (COD 96-152-6054) and $LiCaPO_4$ (COD 96-722-2995). The Rietveld Analysis provided in Table 2 displayed calcium diphosphate from the 3D-Ca-P_2 scaffold as the main phase, followed by non-stoichiometric Mg-TCP in the 3D-[Ca/P/Si]-1Mg and 3D-[Ca/P/Si]-3Mg-coated scaffolds and non-stoichiometric Li-TCP in 3D-[Ca/P/Si]-10Mg.

Fig. 2 depicts the FTIR of the 3D-Ca-P_2 scaffold, along with the spectrum of the 3D-[Ca/P/Si]-10Mg as being representative of all the 3D-[Ca/P/Si]-XMg-coated scaffolds. The Si-O-Si and PO_4^{3-} groups overlapped, and the $P_2O_7^{4-}$ and PO_2 groups were present.

The vibration of the PO_4^{3-} groups in the scaffolds was denoted by several peaks that grouped in three main zones: (i) asymmetric bending modes by several well-resolved peaks between 526 cm^{-1} and 610 cm^{-1}; (ii) the symmetric stretching vibration mode by several peaks between 920 cm^{-1} and −970 cm^{-1}; (iii) the asymmetric stretching vibration mode by another group of several peaks between 1000 cm^{-1} and 1084 cm^{-1} [20]. According to several studies [21,22], the peak at around 800 cm^{-1} was for HPO_4^-, which is characteristic of non-stoichiometric calcium phosphates.

The Si-O-Si vibration groups were also found in two main regions: (i) symmetrical stretching or bending, 800–970 cm^{-1} and (ii) asymmetrical stretching, 1000–1207 cm^{-1}. However, the presence of alkali-earth elements, like magnesium and calcium, modified these structures and a new band that corresponded to Si-O-NBO appeared at 920 cm^{-1} [23,24].

The pyrophosphate group ($P_2O_7^{4-}$) was present and detected by signals at 725 cm^{-1}, 920 cm^{-1} and 1207 cm^{-1} [25] in both scaffolds. Nonetheless, these peaks were much larger in the 3D-Ca-P_2 scaffold.

Finally, the presence of glass in the 3D-Ca-P_2 scaffold was observed by the signals of the PO_2 groups at 1155 cm^{-1} asymmetric and 1065 cm^{-1} symmetric, and the PO group at 970 cm^{-1} and (P=O) at 1280 cm^{-1} [26]. All these peaks were much smaller in the coating scaffolds. Moreover, the fact that 1280 cm^{-1} disappeared was noteworthy.

The SEM-EDX examination of the microstructure of the 3D-Ca-P_2 and 3D-[Ca/P/Si]-XMg-coated scaffolds is shown in Fig. 3. The 3D-Ca-P_2 scaffolds' microstructure is provided in Fig. 3A–C, which depicts a

Table 1
Chemical composition for manufacturing the glass ceramic and coatings.

	TEP (ml)	TEOS (ml)	CaCO₃ (g)	Li₂CO₃ (g)	H₂O (ml)	Ethanol (ml)	HCl (ml)	MgCO₃ (g)
3D-Ca-P₂	10	0.5	8	0.5	20	5	10	-
3D-[Ca/P/Si]-1Mg	1.6	11	11.2	-	20	5	10	0.1
3D-[Ca/P/Si]-3Mg	1.6	11	11	-	20	5	10	0.3
3D-[Ca/P/Si]-10Mg	1.6	11	10	-	20	5	10	1.0

123
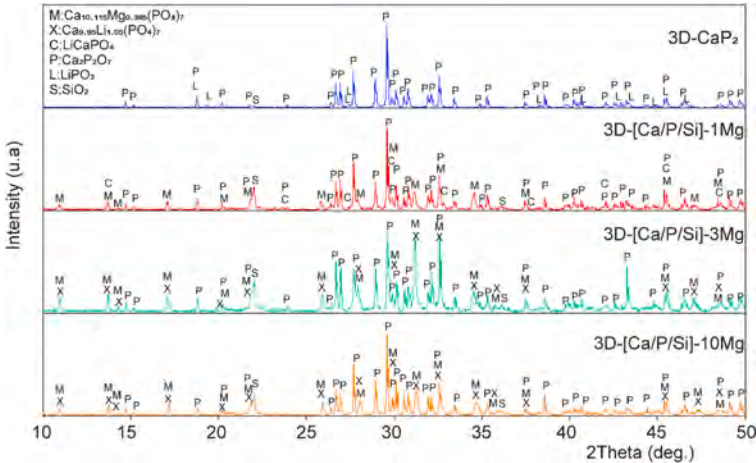
Fig. 1. XRD of the 3D-Ca-P$_2$ and 3D-[Ca/P/Si]-XMg-coated scaffolds.

Table 2
Rietveld analysis.

Sample	Phase (%)		χ^2
3D-Ca-P$_2$	Ca$_2$P$_2$O$_7$	97.1	2.0
	Li(PO$_3$)	1.7	
	SiO$_2$	1.1	
3D-[Ca/P/Si]-1Mg	Ca$_2$P$_2$O$_7$	61.3	2.0
	Ca$_{10.115}$Mg$_{0.385}$P$_7$O$_{28}$	19.3	
	SiO$_2$	14.2	
	LiCa(PO$_4$)	4.5	
3D-[Ca/P/Si]-3Mg	Ca$_2$P$_2$O$_7$	57.5	2.5
	Ca$_{10.115}$Mg$_{0.385}$P$_7$O$_{28}$	29.7	
	Ca$_{9.95}$Li$_{1.05}$(PO$_4$)$_7$	7	
	SiO$_2$	5.8	
3D-[Ca/P/Si]-10Mg	Ca$_2$P$_2$O$_7$	58.6	2.0
	Ca$_{9.95}$Li$_{1.05}$(PO$_4$)$_7$	27	
	Ca$_{10.115}$Mg$_{0.385}$P$_7$O$_{28}$	8.7	
	SiO$_2$	5.6	

highly porous structure (porosity $\sim$ 70% and pore size $\sim$400–700 μm) obtained by the sol-gel processing route. Fig. 3A depicts a low-magnification microstructure of the 3D-Ca-P$_2$ scaffolds. At increasing magnification, a microstructure, performed by the homogeneous distribution of polygonal grains with $0.93 <$ Ca/P < 1.06, was distinguished and came very close to the Ca/P ratio of the main phase in the Rietveld analysis (97% of Ca$_2$P$_2$O$_7$). Bordering these polygonal crystals appeared a glassy phase, mainly in triple points (arrows in Fig. 3B and C), with a $0.25 <$ Ca/P < 0.35 ratio. The XRD did not show the typical broadband when glass is present in material. So the amorphous glass phase was not enough to be detected by the XRD, but conferred the scaffold a whitish vitreous appearance.

Fig. 3D–F shows the 3D-[Ca/P/Si]-XMg-coated scaffolds' microstructure. As magnesium content increase, the coated layers became bigger and covered a larger surface of the 3D-Ca-P$_2$ scaffolds. The coated layers related to non-stoichiometric Mg-TCP and the Li-TCP phases were found to be extremely porous materials, which were assembled by nanosized equiaxed particles (Fig. 3G). The EDX results revealed that Mg content only came to 25% of (Ca + Mg). The Ca/P or (Ca + Mg)/P ratio in the 3D-[Ca/P/Si]-XMg-coated scaffolds respectively came close to 1 and 1.5, which matched the chemical formulae of Ca$_2$P$_2$O$_7$ from the
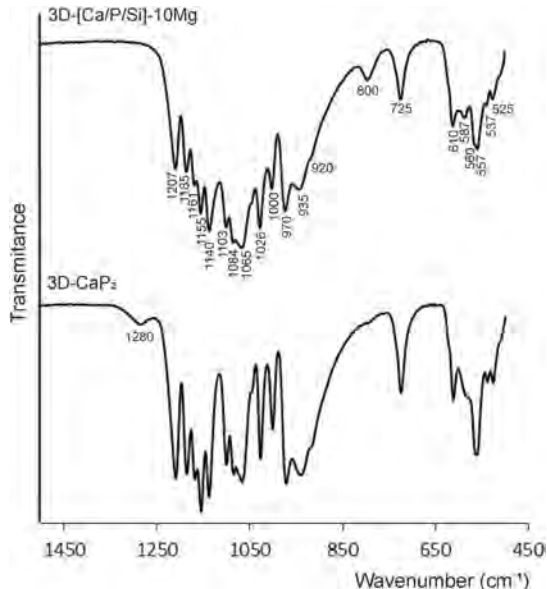

Fig. 2. The ATR-FTIR spectra of the 3D-Ca-P$_2$ scaffold and 3D-[Ca/P/Si]-10Mg as being representative of all the coated scaffolds.

bottom scaffold and those of Ca$_{10.115}$Mg$_{0.385}$P$_7$O$_{28}$ from the coating. The Li$^+$ content in the 3D-[Ca/P/Si]-XMg coatings was negligible as it went below the limit of detection for SEM.

Fig. 4 shows the results obtained by Mercury Porosimetry Technique. According to the volume of the intruded mercury, the curves show (Fig. 4A-B) that the uncoated scaffold (3D-Ca-P$_2$) had a greater number of intraparticle pores, with a pore distribution of approximately 0.1 μm–0.004 μm, and less interparticle pores between 200 μm and 10 μm. On the contrary, this same sample, but now coated (3D-[Ca/P/Si]-10Mg), presented mostly interparticle pores, with two important ranges of intruded mercury. The first of these ranges was between 200 μm and 35 μm and the second between 33 μm and 4.5 μm. Table 3 shows the

124
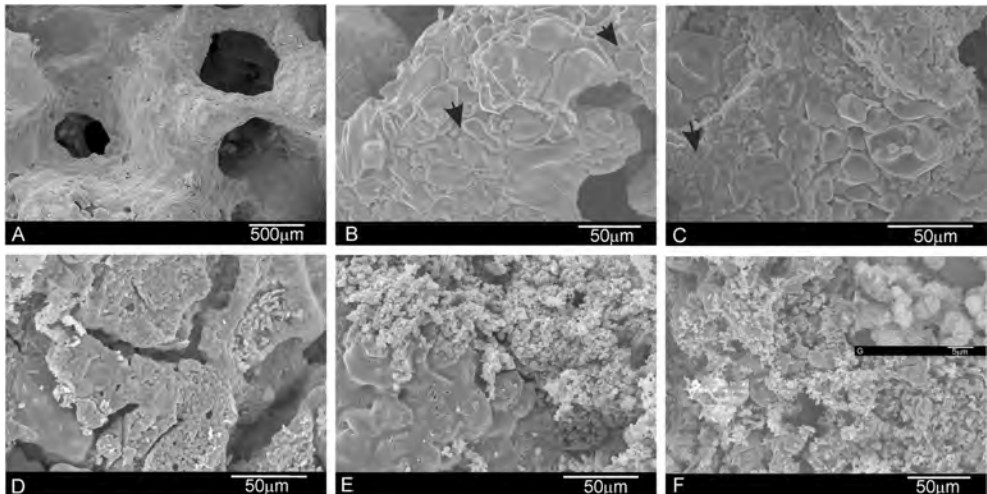
Fig. 3. SEM micrographs of the 3D-Ca-P$_2$ (A–C) and 3D-[Ca/P/Si]-XMg-coated scaffolds with 1 mol%Mg (D), 3 mol%Mg (E) and 10 mol%Mg (F) [arrows in B and C denote the glass phase].
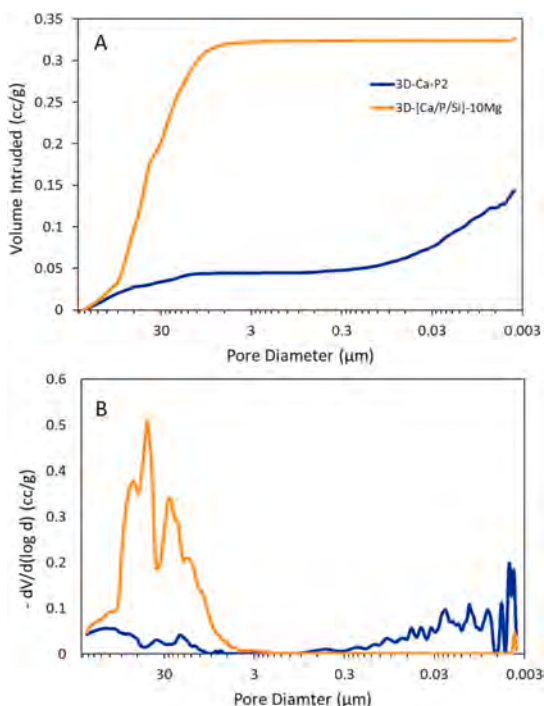

Fig. 4. Mercury porosimetry curves of the 3D-Ca-P$_2$ and 3D-[Ca/P/Si]-10Mg scaffold. (A) differential and (B) cumulative volume intruded versus pore diameter.

percentages of both types of pores as well as other physical properties of these scaffolds. The total porosity of the material network was 23.76% for sample 3D-Ca-P$_2$ and 49.50% for sample 3D-[Ca/P/Si]-10Mg. The

porosity of the scaffolds and compressive strength were 42% and 2.87 MPa for 3D-Ca-P$_2$ scaffold and 34% and 3.38 MPa for 3D-[Ca/P/Si]-10Mg scaffold.

Figs. 5 and 6 show the surface morphology changes of the 3D-Ca-P$_2$ and 3D-[Ca/P/Si]-XMg-coated scaffolds, respectively, after being soaked in SBF for different times.

No morphological changes were observed at the beginning of the assay in the 3D-Ca-P$_2$ microstructure (Fig. 5A). After 7 soaking days, the polygonal grains of calcium diphosphate appeared to be more individualised due to glass phase degradation (Fig. 5B). After 21 soaking days, the polygonal grains had rounded edges and the glass phase did not completely dissolve as the 3D structure remained throughout the test (Fig. 5C). At high magnification, the polygonal grains were glued by the rest of glass phase that acts a bonding agent. A small white precipitate, composed mainly of silicon, was also observed sporadically after 28 testing days (Fig. 5D).
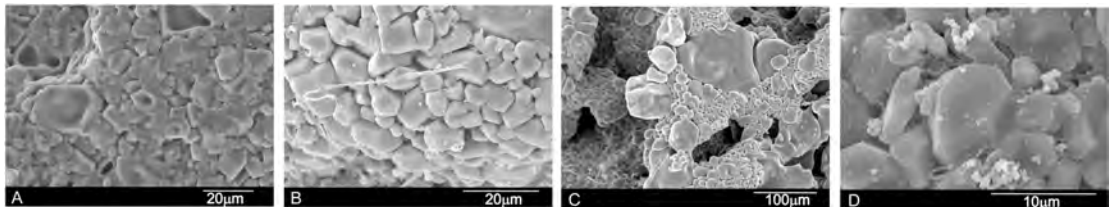
After 3 soaking days, the morphology of the 3D-[Ca/P/Si]-1Mg-coated scaffolds completely differed from the original one (Fig. 1D). A dense spherical precipitate layer coated the whole scaffold surface which, at high magnification, was formed by needle-like crystals. The EDX analysis revealed that these spherical precipitates gave $1.36 < Ca/P < 1.50$. After 7 and 14 soaking days, the new spherical layer seemed to disappear. At low magnification, the image taken on day 7 revealed the bottom 3D-Ca-P$_2$ microstructure with some minor remains of the precipitate dispersed on the surface. Details of the remaining phase were observed at high magnification on day 7. On day 21, the surface was once again coated with a spherical precipitate. At high magnification, it was formed by needle-like crystallites. The EDX done of the spherical precipitate on day 21 gave $1.11 < Ca/P < 1.39$ or $1.15 < (Ca + Mg)/P < 1.46$, and $1.30 < Ca/P < 1.44$ or $1.40 < (Ca + Mg)/P < 1.54$ on day 28. At 14 and 21 days, small conglomerates of white cauliflower-like precipitates were dispersed on the surface (arrow for days 14 and 21). EDX indicated a composition made up mainly of silicon. On day 28, the new precipitate's morphology did not change.

On soaking days 3 and 7, the 3D-[Ca/P/Si]-3Mg-coated scaffolds' morphology showed polygonal grains of the calcium diphosphate from the 3D-Ca-P$_2$ scaffold, together with some remains of the 3D-[Ca/P/Si]-3Mg coating scattered on the scaffold surface. After 14 soaking days, morphology drastically changed with the appearance of a new spherical precipitate coating with $1.23 < Ca/P < 1.31$ or $1.33 < (Ca + Mg)/P <$

125

Table 3
Summary of the physical characterization of the scaffolds.

Sample	Interparticle Porosity (%)[a]	Intraparticle Porosity (%)[b]	Total Porosity Network (%)	Apparent Density Network (g/cc)	Scaffold Porosity (%)	Compressive strength (MPa)
3D-Ca-P$_2$	7.38	16.38	23.76	1.66	42	2.87
3D-[Ca/P/Si]-10Mg	48.85	0.65	49.50	1.52	34	3.38

[a] Corresponding to pores between 1 μm–300 μm.
[b] Corresponding to pores <1 μm.

Fig. 5. SEM micrographs of the 3D-Ca-P$_2$ scaffolds after (A) 3 days, (B) 7 days, (C) 21 days and (D) 28 days of SBF soaking.

1.36. On day 21, the spherical precipitate coating neither seemed as dense as the 14-day precipitate, nor formed a continuous layer on the entire surface. At the end of the 28-day soaking time, the spherical precipitate formed again. Although it still did not cover the whole sur-face, it seemed denser than the 21-day layer. A lamellar microstructure was observed beneath the new precipitate given the partial dissolution of the glass from the 3D-Ca-P$_2$ scaffold (28 days, inner).

After 3 and 7 soaking days, the 3D-[Ca/P/Si]-10Mg-coated scaffold showed a similar microstructure to the 3D-[Ca/P/Si]-3Mg scaffold and at the same soaking time. This indicated the grains of the 3D-Ca-P$_2$ scaffold with rounded edges given their partial dissolution and the dissolution of the glass phase. Sporadically, part of the coating remained on the rounded calcium pyrophosphate grains. After 14 and 21 days of soaking, a dense globular precipitate layer coated the scaffold surface which, at high magnification, had a cotton-like morphology. The EDX analysis revealed that these globular precipitates had 1.18 < Ca/P < 1.21 or 1.21<(Ca + Mg)/P < 1.31. At the end of the soaking time, the new precipitate had partially dissolved to reveal rounded grains beneath the 3D-Ca-P$_2$ scaffold.

The ion changes in SBF, due to the different scaffolds' behaviours after several soaking times in SBF, are presented in Fig. 7. We can see that the behaviour of the calcium, phosphorous and silicon ions vastly differed depending on the scaffold type being tested.

The 3D-Ca-P scaffolds showed calcium ion adsorption from SBF as it was depleted in the surrounding medium. Phosphorous ions were released from the scaffold to SBF. Finally, the silicon ion concentration did not change while the study was underway.

In contrast, the changes in the 3D-[Ca/P/Si]-XMg-coated scaffolds were more drastic and sinusoidal behaviour was noted throughout the trial. For the 3D-[Ca/P/Si]-XMg scaffold, silicon and phosphorous be-haviours displayed the inverse behaviour when the silicon concentration rose and the phosphorus one lowered, except at the beginning of the trial (day 3), when P rose in 3D-[Ca/P/Si]-3Mg and slightly lowered in 3D-[Ca/P/Si]-10Mg.

4. Discussion

The 3D-Ca-P$_2$ scaffolds were obtained by immersing polyurethane foams in sol-solutions followed by heat treatment [27]. In order to obtain a 3D material consisting of Ca$_2$P$_2$O$_7$ crystals, crystals should be dispersed in a matrix phase. Ca$_2$P$_2$O$_7$ crystals reinforced with CaO-P$_2$O$_5$ glass matrix materials are believed to be good candidates for developing 3D scaffolds with excellent mechanical strength, because viscosity and proportion of glass phase, at the desired temperature, vary with composition [28]. According to the CaO-P$_2$O$_5$ phase diagram, Ca$_2$P$_2$O$_7$ firstly presents the appearance of the liquid phase at 950 °C [29]. For this reason, the 3D material consisted of Ca$_2$P$_2$O$_7$ crystals, in which a small amount of CaO-P$_2$O$_5$ glass was intentionally prepared. The 3D-Ca-P$_2$ scaffold had a vitreous appearance related to the glass phase, which was not enough to detect a broadband in XRD, and its presence was determined by the 155 cm^{-1}, 1065 cm^{-1} and 970 cm^{-1} signals in FTIR [26] (Fig. 2).

3D-Ca-P$_2$ scaffold densification took place during heating, with a maximum shrinkage of ~30%. Glass acted as a bonding agent to inter-link the Ca$_2$P$_2$O$_7$ polygonal crystals in the 3D-Ca-P$_2$ scaffold (Fig. 2B and C). The glass phase did not crystallise upon cooling. The final micro-structure comprised grains with a broad size distribution ranging from relatively small (10–15 μm) to quite large (70–75 μm). The micro-structure reflected the liquid-phase sintering process by the dissolution/crystallization mechanism, when bigger grains further enlarged and smaller grains were dissolved during the CaO-P$_2$O$_5$ melt. The XRD pattern of the milled 3D-Ca-P$_2$ scaffold after sintering included 97.1% Ca$_2$P$_2$O$_7$, 1.7% Li(PO$_3$) and 1.1% cristobalite (Table 2).

The 3D-Ca-P$_2$ scaffolds were coated with 3D-[Ca/P/Si]–XMg and developed a scaffold with a high porous coatings. The porosity of the coatings was verified with the curves in Fig. 4 and the data reported in Table 3. The intra- and interparticle porosity is the total microprosity of the scaffolds (pores < 300 μm) and for the 3D-[Ca/P/Si]−10Mg scaffold it was much higher compared to the same uncoated scaffold as a consequence of the superficial change observed between both (Fig. 3). The 3D-Ca-P$_2$ scaffold originally had mostly intraparticle pores and by coating it with the second composition the interparticle pores increased. At macro level (pores > 300 μm), the opposite happened, the decrease of the total porosity of the 3D-Ca-P$_2$ scaffold with respect to the 3D-[Ca/P/Si]−10Mg scaffold was due to the fact that the coatings made on the porous scaffold reduced the diameter of the big pores originally found in the polyurethane sponge. The presence of submicron and nanosized pores gives the scaffold excellent characteristics for future applications. This means they can be suitably used as both bone substitutes and bimolecular carriers [30]. Although there is no consensus on the ideal pore size of a scaffold, both macro- and microporosity are necessary. According to Rustom et al. pores larger than 100 μm are required for

126
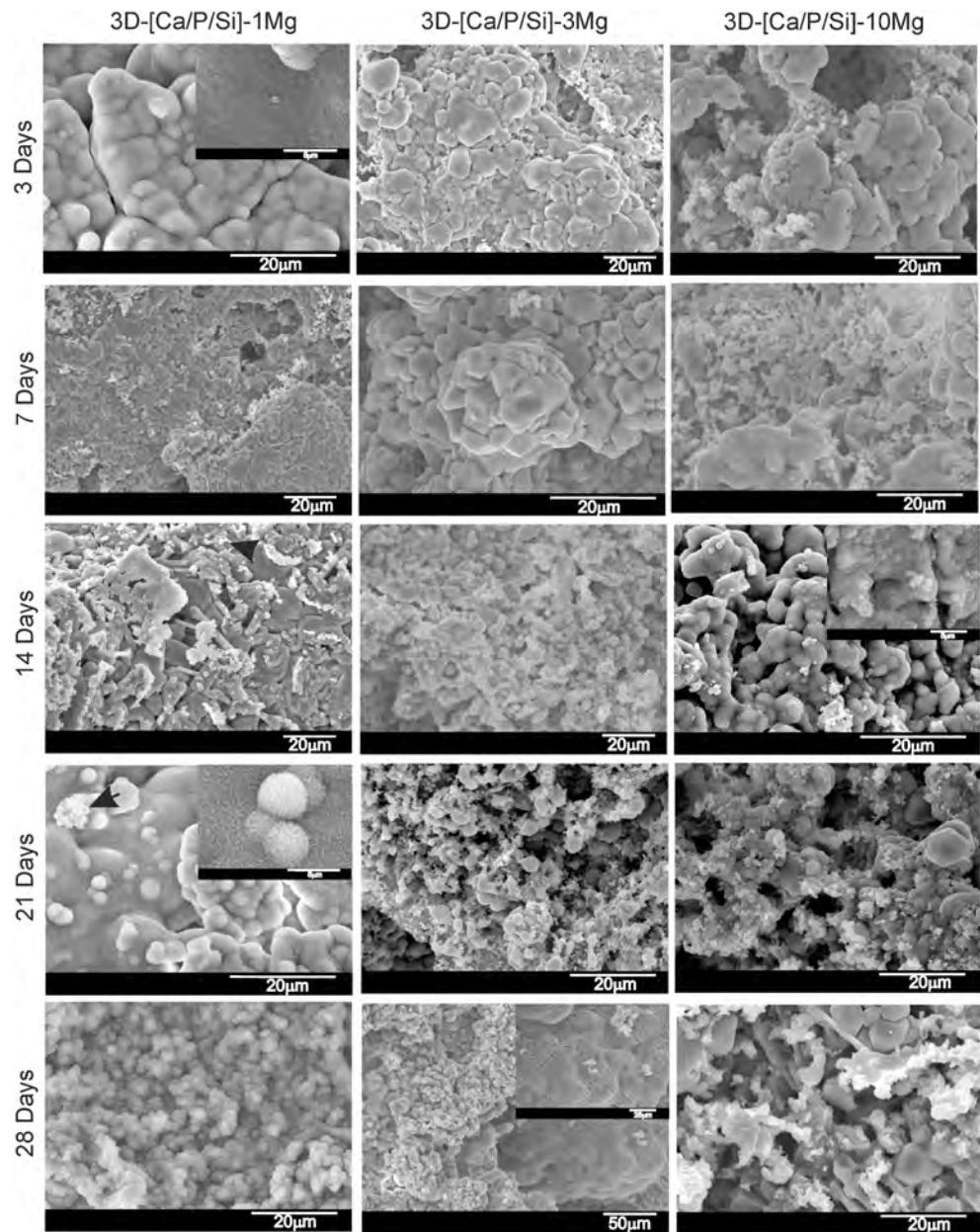
Fig. 6. SEM micrographs of the 3D-[Ca/P/Si]-XMg-coated scaffolds after different soaking times in SBF.
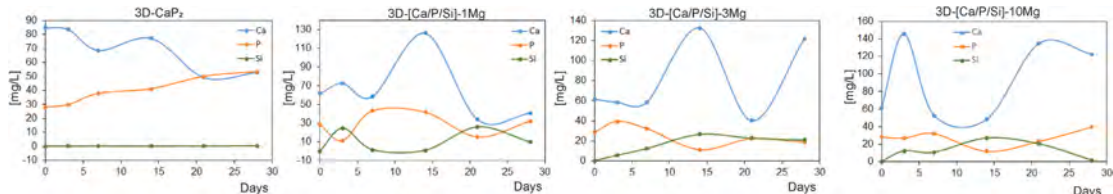
Fig. 7. Ion concentration changes in SBF during the soakings of the 3D-Ca-P$_2$ and 3D-[Ca/P/Si]-XMg-coated scaffolds.

bone growth, but also pores smaller than 50 μm because they provide additional spaces for bone growth and contribute to the improvement of mechanical strength as a result of filling those spaces [31].

The compression strength of the 3D-Ca-P$_2$ scaffold was high but increased with the coatings. This is due to the reduced macroporosity presented by the 3D-[Ca/P/Si]−10Mg scaffolds. However, despite the decrease, both scaffolds showed a compressive strength comparable to trabecular or spongy bone. According to Caeiro et al., depending on the region of the skeleton, the compressive strength of the trabecular bone varies between 1.5 and 9.3 MPa [32]. While Gibson et al., presented a compressive strength between 0.2 and 4 MPa when the relative density is around 0.1 [33].

Given the EDX and XRD results, the 3D-[Ca/P/Si]–XMg scaffolds included the Ca$_2$P$_2$O$_7$ and SiO$_2$ phases of the 3D-Ca-P$_2$ scaffold, plus Ca$_{10.115}$Mg$_{0.385}$P$_7$O$_{28}$, Ca$_{9.95}$Li$_{1.05}$(PO$_4$)$_7$, and LiCaPO$_4$. The different TCP-containing phases increased as the sol-solution rose from 1 mol% Mg to 10 mol% Mg. (Fig. 1, Table 2). The Mg^{2+} with an ionic radius (0.65 Å) smaller than Ca^{2+} (0.99 Å) allowed Ca^{2+} to be replaced with Mg^{2+} in TCP. The EDX results indicated that Mg^{2+} content only amounted to 25% of (Ca + Mg). This finding agrees with Zhou et al. [34], who reported up to 22% Mg^{2+} of Ca^{2+} replacement in calcium pyrophosphate, and agrees with Yasukawa et al. [35], who reported 30% Mg^{2+}.

When the Ca^{2+} and Mg^{2+} contents from the 3D-[Ca/P/Si]–XMg sol-solution increased, two processes occurred at the same time: (i) part of the glass began to dissolve (the FTIR peaks related to the glass phase were much smaller; Fig. 2), and reacted with the coating to give rise to new Li$^+$ phases; (ii) the Ca$_2$P$_2$O$_7$ phase started to transform into TCP (Ca/P increased from 1 to ~1.5). So that Ca^{2+} and Mg^{2+} concentrations rose, the Ca$_2$P$_2$O$_7$ phase decreased and the non-stoichiometric-TCP phases increased, as observed in the Rietveld analysis of the 3D-[Ca/P/Si]–XMg scaffolds (Table 2). The formation kinetics of the highly porous coat (Fig. 3D–G) is complex and unclear. It has been suggested that the formation of a nano-sized equiaxed crystals structure from the coating is related to a battle of free Ca^{2+} and Mg^{2+} to bind to PO$_4^{3-}$. This battle between Ca^{2+} and Mg^{2+} ions has been reported by several authors, who describe how, depending on the type/s of calcium phosphate phase/s present in the material, needle-like and plate-like particles [36],

and even amorphous spheres [37,38], can be generated. The 3D-Ca-P$_2$ scaffolds presented no bioactivity at any assay time point. The 3D-[Ca/P/Si]–XMg-coated scaffolds displayed intermittent bioactivity, which meant that the amount of Mg-dopant modified scaffolds' *in vitro* behaviour. Fig. 8 shows a summary of the different bioactivity kinetics of the glass-ceramics studied.

The non-bioactive behaviour of pyrophosphate is well-documented given the presence of P$_2$O$_7^{4-}$ groups that inhibit hydroxyapatite precipitation [39–41]. Conversely, all the 3D-[Ca/P/Si]–XMg scaffolds exhibited intermittent bioactivity at different testing times. What they all have in common is that when there is an incorporation of silicon and decrease in phosphorus into the medium, HA precipitation occurs (Figs. 5 and 6). For example, on days 3, 21 and 28 in the 3D-[Ca/P/Si]–1Mg scaffolds; on days 14 and 28 in the 3D-[Ca/P/Si]–3Mg scaffolds; on days 14 and 21 in the 3D-[Ca/P/Si]−10Mg scaffolds (Figs. 5 and 6). On the contrary, when P increases and Si decreases in the medium, the dissolution of HA takes place (HA previously precipitated on scaffold surfaces), and starts to precipitate to a phase rich in Si (probably Si-OH) by generating possible anchor points on the surface so that the new HA precipitate can nucleate and grow. This was seen on days 7 and 14 in the 3D-[Ca/P/Si]–1Mg scaffolds; on day 21 in the 3D-[Ca/P/Si]–3Mg scaffolds; on day 28 in the 3D-[Ca/P/Si]−10Mg scaffolds. Some remains of the previously precipitated HA layer were observed on the scaffolds, together with a new white silicon-rich precipitate (34.22 > Si > 1.89). The polygonal grains from the 3D-Ca-P$_2$ scaffold were visible underneath.

In order to explain the dissolution of the HA precipitate layer in scaffolds, it is necessary to contemplate the dissolution of glass. The glass presents in the material that came into contact with SBF was hydrolysed and produced the dissolution of the glass phase of the 3D-Ca-P$_2$ scaffold by releasing groups (P$_2$O$_7^{4-}$) to the medium. The chelating effect of polyphosphates present in glasses on divalent cations is well-known [42], which can react vigorously with the Ca^{2+} of the precipitated HA to break the crystalline structure of (Ca$_{10}$(PO$_4$)$_6$(OH)$_2$). As far as we know, this is the first bioactivity mechanism based on the competitive process between a core generator of pyrophosphate and the coating source of HA.

The incorporation of Mg into the HA network leads to HA precipitate crystallinity. This network distortion is not so marked for low Mg^{2+} concentrations and, consequently, HA is more crystalline (3D-[Ca/P/Si]–1 Mg at 21 days) than for high Mg^{+2} concentrations, where HA is more amorphous (3D-[Ca/P/Si]–10 Mg at 14 days). This favours subsequent cell adhesion because cells are favoured by amorphous HA, as in human bone, than with crystalline HA [43].

The scaffold obtained in this study stands out for (i) having a multilayer structure that allowed combining the benefits of two different chemical compositions, (ii) presenting a core mainly constituted by the calcium pyrophosphate phase, which inhibits the crystallization of HA *in vitro*, but provides mechanical resistance and (iii) presenting external coatings that provided bioactivity, with magnesium ions that improve cell adhesion.

These three characteristics allowed the scaffold to present a bioactivity mechanism promoted by the vitreous phase of the core and the external layers. In addition, depending on the magnesium
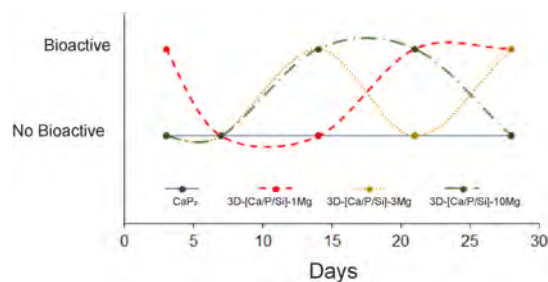

Fig. 8. Bioactivity kinetics of the 3D-Ca-P$_2$ scaffold and 3D-[Ca/P/Si]-XMg coated scaffolds.

128

concentration, the HA precipitate was formed at different times and with different morphologies.

In general, the scaffold presents characteristics difficult to obtain in a single structure such as mechanical resistance, porosity and modulated bioactivity.

5. Conclusions

Novel pyrophosphate glass ceramic scaffolds containing polygonal grains of calcium pyrophosphate with $CaO-P_2O_5$ glass as the matrix phase were manufactured and coated with several $CaO-SiO_2-MgO$ [3D-[Ca/P/Si]-XMg (X = 1, 3 and 10 mol%)] layers by sol-gel and the polymer replication method. The core of multilayer scaffold provided a three-dimensional structure with mechanical resistance and porosity to support the external coatings that provided the bioactivity.

We were able to modulate scaffolds' bioactivity from a non-bioactive material like the 3D-Ca-P_2 core to scaffolds with intermittent bioactivity depending on the coating's magnesium content. Of all the coated scaffolds that we prepared, in our view that with the best bioactivity was 3D-[Ca/P/Si]-10Mg because the formed HA was more amorphous due to the incorporation of Mg^{2+} into the HA lattice. This made the precipitated HA similar to the biological HA of human bone, which would allow cells to adhere better. This means that we can produce materials according to the specific needs of each application.

Declaration of competing interest

The authors declare that they have no known competing financial interests or personal relationships that could have appeared to influence the work reported in this paper.

Acknowledgements

References

[1] S. Xu, Q. Wu, Y. Guo, C. Ning, K. Dai, Copper containing silicocarnotite bioceramic with improved mechanical strength and antibacterial activity, Mater. Sci. Eng. C 118 (2021) 111493, https://doi.org/10.1016/j.msec.2020.111493.

[2] G. Dong, Y. Zheng, L. He, G. Wu, C. Deng, The effect of silicon doping on the transformation of amorphous calcium phosphate to silicon-substituted α-tricalcium phosphate by heat treatment, Ceram. Int. 42 (1) (2016) 883–890, https://doi.org/10.1016/j.ceramint.2015.09.013. Part A.

[3] S. Ramezani, R. Emadi, M. Kharaziha, F. Tavangarian, Synthesis, characterization and in vitro behavior of nanostructured diopside/biphasic calcium phosphate scaffolds, Mater. Chem. Phys. 186 (2017) 415–425, https://doi.org/10.1016/j.matchemphys.2016.11.013.

[4] B. Jokic, I. Stamenkovic, M. Zrilic, K. Obradovic-Djuricic, R. Petrovic, D. Janackovic, Silicon-doped biphasic α-calcium-phosphate/hydroxyapatite scaffolds obtained by a replica foam method using uniform pre-annealed spherical particles, Mater. Lett. 74 (2012) 155–158, https://doi.org/10.1016/j.matlet.2012.01.081.

[5] S. Hesaraki, H. Nazarian, M. Alizadeh, Multi-phase biocomposite material in-situ fabricated by using hydroxyapatite and amorphous nanosilica, Int. J. Mater. Res. 102 (5) (2011) 494–503, https://doi.org/10.3139/146.110397.

[6] N.A. Mata, P. Ros-Tárraga, P. Velasquez, A. Murciano, P.N. De Aza, Synthesis and Characterization of 3D multilayer porous Si-Ca-P scaffolds doped with Sr ions to modulate in vitro bioactivity, Ceram. Int. 46 (1) (2020) 968–977, https://doi.org/10.1016/j.ceramint.2019.09.058.

[7] J.H. Shepherd, D.V. Shepherd, S.M. Best, Substituted hydroxyapatites for bone repair, J. Mater. Sci. Mater. Med. 23 (2012) 2335–2347, https://doi.org/10.1007/s10856-012-4598-2.

[8] A.V. Zanfir, N. Nenu, G. Voicu, A.I. Badanoiu, C.D. Ghitulica, F. Iordache, Modified calcium silicophosphate cements with improved properties, Mater.s Chem. Phy. 238 (1) (2019) 121965, https://doi.org/10.1016/j.matchemphys.2019.121965.

[9] I.S. Kulaev, V. Vagabov, T. Kulakovskaya, The Biochemistry of Inorganic Polyphosphates, second ed., John Wiley, Chichester, 2004.

[10] A. Kornberg, N.N. Rao, D. Ault-Riché, Inorganic polyphosphate: a molecule of many functions, Annu. Rev. Biochem. 68 (1999) 89–125, https://doi.org/10.1146/annurev.biochem.68.1.89.

[11] Inorganic polyphosphates; biochemistry, biology, biotechnology, in: H.C. Schröder, W.E.G. Müller (Eds.), Progress in Molecular and Subcellular Biology, vol. 23, Springer Verlag, Berlin, 1999.

[12] R.A. Terkeltaub, Inorganic pyrophosphate generation and disposition in pathophysiology, Am. J. Physiol. Cell Physiol. 281 (1) (2001) C1–C11, https://doi.org/10.1152/ajpcell.2001.281.1.C1.

[13] H. Fleisch, R.G.G. Russell, F. Straumann, Effect of pyrophosphate on hydroxyapatite and its implications in calcium homeostasis, Nature 212 (23) (1966) 901–903.

[14] R.G. Russell, R.C. Muhlbauer, S. Bisaz, D.A. Williams, H. Fleisch, The influence of pyrophosphate, condensed phosphates, phosphonates and other phosphate compounds on the dissolution of hydroxyapatite in vitro and on bone resorption induced by parathyroid hormone in tissue culture and in thyroparathyroidectomised rats, Calcif. Tissue Res. 6 (1970) 183–196, https://doi.org/10.1007/BF02196199.

[15] W. Jahnen-Dechent, M. Ketteler, Magnesium basics (suppl1), i3–i14, Clin. Kidney J. (2012) 5, https://doi.org/10.1093/ndtplus/sfr163.

[16] M. Supová, Substituted hydroxyapatites for biomedical applications: a review, Ceram. Int. 41 (8) (2015) 9203–9231, https://doi.org/10.1016/j.ceramint.2015.03.316.

[17] A. Gozalian, A. Behnamghader, M. Daliri, A. Moshkforoush, Synthesis and thermal behavior of Mg-doped calcium phosphate nanopowders via the sol gel method, Sci. Iran. 18 (2011) 1614–1622, https://doi.org/10.1016/j.scient.2011.11.014.

[18] P.M.C. Torres, J.C.C. Abrantes, A. Kaushal, S. Pina, N. Döbelin, M. Bohner, J.M. F. Ferreira, Influence of Mg-doping, calcium pyrophosphate impurities and cooling rate on the allotropic α⇔β-tricalcium phosphate phase transformations, J. Eur. Ceram. Soc. 36 (2016) 817–827, https://doi.org/10.1016/j.jeurceramsoc.2015.09.037.

[19] ISO/FDIS 23317, Implants for Surgery- in Vitro Evaluation for Apatite-Forming Ability of Implant Materials, 2007.

[20] P.N. De Aza, F. Guitian, C. Santos, S. De Aza, R. Cusco, L. Artus, Vibrational properties of calcium phosphate compounds. II comparison between hydroxyapatite and β-tricalcium phosphate, Chem. Mater. 9 (1997) 916–922, https://doi.org/10.1021/cm9604266.

[21] L. Berzina-Cimdina, N. Borodajenko, Research of calcium phosphates using Fourier transform infrared spectroscopy, Infrared Spectroscopy-Materials Science, Engineering and Technology 12 (7) (2012 Apr 25) 251–263.

[22] A.R. Toibah, I. Sopyan, Y.M. Yuhazri, R.A. Jeefferie, O. Nooririnah, FTIR study on phase behavior of magnesium-doped biphasic calcium phosphate synthesized via sol-gel method, in: InAIP Conference Proceedings 2nd, vol. 1455, American Institute of Physics, 2012 Jun 29, pp. 97–103, https://doi.org/10.1063/1.4732476. No. 1.

[23] H. Aguia, J. Serra, P. Gonzalez, B. Leon, Structural study of sol-gel silicate glasses by IR and Raman spectroscopies, J. Non-Cryst. Solids 355 (8) (2009) 475–480, https://doi.org/10.1016/j.jnoncrysol.2009.01.010.

[24] P. Innocenzi, Infrared spectroscopy of sol-gel derived silica-based films: a spectra-microstructure overview, J. Non-Cryst. Solids 316 (2003) 309–319, https://doi.org/10.1016/S0022-3093(02)01637-X.

[25] S. Raynaud, E. Champion, D. Bernache-Assollant, P. Thomas, Calcium phosphate apatites with variable Ca/P atomic ratio I. Synthesis, characterisation and thermal stability of powders, Biomaterials 23 (4) (2002) 1065–1072, https://doi.org/10.1016/S0142-9612(01)00218-6.

[26] R. Hussin, M.A. Salim, N.S. Alias, M.S. Abdullah, S. Abdullah, S.A.A. Fuzi, S. Hamdan, M.N. Md Yusuf, Vibrational studies of calcium magnesium ultraphosphate glasses, J. Fundamental Science 5 (2009) 41–53, https://doi.org/10.11113/mjfas.v5n1.286.

[27] P. Ros-Tárraga, N.A. Mata, A. Murciano, P. Velasquez, P.N. De Aza, Multilayer materials: a method to link bioactivity and durability, Ceram. Int. 45 (17) (2019) 23611–23618, https://doi.org/10.1016/j.ceramint.2019.08.072.

[28] T. Kasuga, Y. Ota, K. Tsji, Y. Abe, Preparation of High-stregh calciumphosphate ceramics with low modulus of elasticity containing β-Ca(PO3)2 fibers, J. Am. Ceram. Soc. 79 (7) (1996) 1821–1824, https://doi.org/10.1111/j.1151-2916.1996.tb08001.x.

[29] W.L. Hill, G.T. Faust, D.S. Reynolds, The binary system P2O5 -2CaO-P2O5, Am. J. Sci. 242 (9) (1944) 457–477, https://doi.org/10.2475/ajs.242.9.457.

[30] Xi Wang, H.C. Schröder, W.E.G. Müller, Amorphous polyphosphate, a smart bioinspired nano-/bio-material for bone and cartilage regeneration: towards a new paradigm in tissue engineering, J. Mater. Chem. B 6 (2018) 2385–2412, https://doi.org/10.1039/C8TB00241J.

[31] L.E. Rustom, M.J. Poellmann, A.J.W. Johnson, Mineralization in micropores of calcium phosphate scaffolds, Acta Biomater. 83 (2019) 435–455, https://doi.org/10.1016/j.actbio.2018.11.003.

[32] J.R. Caeiro, P. Gonzalez, D. Guede, Biomechanics and bone (& II): trials in different hierarchical levels of bone and alternative tools for the determination of bone strength, Rev. De Osteoporos. Metab. Miner. 5 (2013) 99–108.

[33] L.J. Gibson, M.F. Ashby, Cellular Solids: Structure and Properties, second ed., Pergamon, Oxford, 1999, pp. 429–452.

[34] H. Zhou, S. Hou, M. Zhang, H. Chai, Y. Liu, S B Bhaduri, L. Yang, L. Deng, Synthesis of β-TCP and CPP containing biphasic calcium phosphates by a robust technique, Ceram. Int. 42 (2016) 11032–11038, https://doi.org/10.1016/j.ceramint.2016.03.244.

[35] A. Yasukawa, S. Ouchi, K. Kandori, T. Ishikawa, Preparation and characterization of magnesium–calcium hydroxyapatites, J. Mater. Chem. 6 (1996) 1401–1405, https://doi.org/10.1039/JM9960601401.

[36] F. Tamimi, D.L. Nihouannen, D.C. Bassett, S. Ibasco, U. Gbureck, J. Knowles, A. Wright, A. Flynn, S.V. Komarova, J.E. Barralet, Biocompatibility of magnesium

phosphate minerals and their stability under physiological conditions, Acta Biomater. 7 (2011) 2678–2685, https://doi.org/10.1016/j.actbio.2011.02.007.

[37] H. Zhou, S. Bhaduri, Novel microwave synthesis of amorphous calcium phosphate nanospheres, J. Biomed. Mater. Res. B Appl. Biomater. 100B (2012) 1142–1150, https://doi.org/10.1002/jbm.b.32681.

[38] A.C. Tas, Submicron spheres of amorphous calcium phosphate forming in a stirred SBF solution at 55 1C, J. Non-Cryst. Solids 400 (2014) 27–32, https://doi.org/10.1016/j.jnoncrysol.2014.04.031.

[39] H. Fleisch, R.G.G. Russell, S. Bisaz, P.A. Casey, R.C. Muehlbauer, The influence of pyrophosphate analogues (diphosphonates) on the precipitation and dissolution of calcium phosphate in vitro and in vivo, Calcif. Tissue Res. 2 (1968), 10-10A.

[40] H. Fleisch, J. Maerki, R.G.G. Russell, Effect of pyrophosphate on dissolution of hydroxyapatite and its possible importance in calcium homeostasis, Proc. Soc. Exp. Biol. Med. 122 (1966) 317–320, https://doi.org/10.3181/00379727-122-31123.

[41] A. Jung, S. Bisaz, P. Bartholdi, H. Fleisch, Influence of pyrophosphate on the exchange of calcium and phosphate ions on hydroxyapatite, Calcif. Tissue Res. 13 (1973) 27–40, https://doi.org/10.1007/BF02015393.

[42] H. Gao, T. Tan, D. Wang, Dissolution mechanism and release kinetics of phosphate controlled release glasses in aqueous medium, J. Contr. Release 96 (2004) 29–36, https://doi.org/10.1016/j.jconrel.2003.12.031.

[43] N.J. Lakhkar, I.H. Lee, H.W. Kim, V. Salih, I.B. Wall, J.C. Knowles, Bone formation controlled by biologically relevant inorganic ions: role and controlled delivery from phosphate-based glasses, Adv. Drug Deliv. Rev. 65 (4) (2013) 405–420, https://doi.org/10.1016/j.addr.2012.05.015.
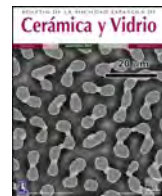
130

Apéndice F

Artículo 6

Original article

Effect of Sr, Mg and Fe substitution on the physico-chemical and biological properties of Si—Ca—P multilayer scaffolds

Nayarit A. Mata [a,*], Marcela Arango-Ospina [b], Pablo Velasquez [a], Angel Murciano [c], Piedad N. De Aza [a], Aldo R. Boccaccini [b]

[a] *Institute of Bioengineering, Miguel Hernandez University, Avda. Universidad s/n, 03202 Elche, Spain*
[b] *Institute of Biomaterials, University of Erlangen-Nuremberg, Cauerstr. 6, 91058 Erlangen, Germany*
[c] *Department of Materials, Optical and Electronic Technology, Miguel Hernandez University, Avda. Universidad s/n, 03202 Elche, Spain*

ARTICLE INFO

ABSTRACT

In this work, a new combination of ceramic materials is proposed for bone tissue engineering applications. Multilayer scaffolds consisting of a core composed mainly of calcium pyrophosphate and external coatings of silica and calcium doped with Fe^{3+}, Sr^{2+} and Mg^{2+} were prepared. To study the influence of the arrangement of dopant ions in the external coatings, two different scaffolds were developed: scaffolds 3J consisting of a single external coating with 9 mol% of Fe^{3+}, Sr^{2+} and Mg^{2+} ions; and scaffolds 3S comprising three external coatings, each containing 3 mol% of Fe^{3+}, Sr^{2+} and Mg^{2+} ions. Scaffolds were physicochemically characterized and evaluated for *in vitro* bioactivity and cellular response in the presence of MG-63 cells. The results showed that the core scaffold displayed no *in vitro* bioactivity or good cellular response, but served as a support for the external coatings given its mechanical resistance. The cell viability of scaffolds 3J and 3S increased more than 100% in relation to the core, and also improved cell proliferation and adhesion resulting in a dense layer of cells that covered the scaffolds' entire surface. The arrangement of ions in the external coatings did not influence the cellular response, but determined the bioactivity rate.

132

Efecto de la sustitución de Sr, Mg y Fe en las propiedades físico-químicas y biológicas de andamios multicapa de Si-Ca-P

R E S U M E N

Palabras clave:
Biocerámicas
Sol-gel
Andamios
Dopaje iónico

En este trabajo se propone una nueva combinación de materiales cerámicos para aplicaciones en ingeniería de tejido óseo. Se prepararon andamios multicapa formados por un núcleo principalmente de pirofosfato cálcico y recubrimientos externos de sílice y calcio dopados con Fe^{3+}, Sr^{2+} y Mg^{2+}. Para estudiar la influencia de la disposición de los iones dopantes en los recubrimientos externos, se desarrollaron dos andamios diferentes: andamios 3J con un recubrimiento externo con 9 mol% de Fe^{3+}, Sr^{2+} y Mg^{2+}; y andamios 3S con tres recubrimientos externos, cada uno con 3 mol% de Fe^{3+}, Sr^{2+} y Mg^{2+}. Posteriormente, se realizó caracterización fisicoquímica, se evaluó su bioactividad *in vitro* y respuesta celular en presencia de células MG-63. Los resultados mostraron que el núcleo del andamio no presentaba bioactividad ni buena respuesta celular, pero servía de soporte para los recubrimientos externos debido a la resistencia mecánica. La viabilidad celular de los andamios 3J y 3S aumentó en más de 100% respecto al núcleo y mejoró la proliferación y adhesión celular, dando lugar a una densa capa de células en la superficie de los andamios. La disposición de los iones en los recubrimientos externos no influyó en la respuesta celular, pero determinó la tasa de bioactividad.

© 2021 SECV. Publicado por Elsevier España, S.L.U. Este es un artículo Open Access bajo la licencia CC BY-NC-ND (http://creativecommons.org/licenses/by-nc-nd/4.0/).

Introduction

Tissue engineering is a multidisciplinary field that uses engineering tools and health science to solve tissue degradation and regeneration problems [1]. This field involves three indispensable components: (i) cells; (ii) scaffolds and (iii) biological factors [2–5]. Scaffolds play an important role because they act as the physical matrix where biological entities are deposited to promote the integration and/or restoration of damaged tissue. For this reason, the choice of the scaffold's biomaterial must be in accordance with the tissue type to be treated.

In recent years, bone has become one of the most replaced tissues, mainly by the increase in skeletal system trauma due to motor vehicle use and degenerative diseases as a result of increased life expectancy [6,7]. The selection of a biomaterial that mimics bone is complicated because of the hierarchical structure and the biological processes that occur in this kind of tissue [8,9].

Ceramic materials are an excellent choice for restoring hard tissues for their similarity to the bone mineral component [10–12]. Although ceramic materials are able to chemically imitate bone and provide biocompatibility, a scaffold with a single chemical composition is not sufficient to fulfill all the requirements that a scaffold must meet: good mechanical strength, porous structure, osteoconductivity, osteoinductivity, biodegradability, among others [8,13,14]. For this reason, previous studies have proposed creating multilayer scaffolds consisting of coatings with different chemical compositions to provide several characteristics [15–18].

The present research work proposes creating a core formed by a chemical composition that confers mechanical resistance, and it is subsequently coated by bioactive compositions doped with ions like Fe^{3+}, Sr^{2+} and Mg^{2+}. Naturally, these ions are found in bone and participate in different processes, which

is why these ions have been widely incorporated into various ceramic and glass materials [19–22]. Strontium behaves similarly to calcium, stimulates osteoblast activity and restricts osteoclast differentiation [19,23]. Magnesium stimulates new bone formation and increases cell adhesion [24]. Iron participates in tissue growth and blood vessel formation [19]. These ions have been previously incorporated individually into external coatings of multilayer scaffolds to present apatite precipitates during *in vitro* bioactivity evaluations [16–18].

Hence this research work aims to integrate these three ions (in the ideal ionic concentration obtained in the previous studies) into a unique scaffold to enhance the benefits of each ion. Multilayer scaffolds were prepared with the same calcium phosphate core but were coated by external coatings of mainly calcium silicate doped with Fe^{3+}, Sr^{2+} and Mg^{2+} in two different configurations. The first configuration included a single external coating with 3 mol% of each ion (Fe^{3+}, Sr^{2+} and Mg^{2+}); *i.e.* 9 mol% doping in relation to the total calcium moles. In the second configuration, coatings of 3 mol% of each ion were incorporated into three different layers; *i.e.* the first was a iron-doped coating, the next was a strontium-doped coating, and the most external was a magnesium-doped coating. Scaffolds were physico-chemically characterized. Subsequently, the *in vitro* bioactivity and behavior in cell culture were evaluated by indirect (extracts of material powder) and direct (scaffold) assays.

Materials and methods

Scaffold preparation

Scaffolds were prepared by sol-gel and the polymer replica method. The reagents used to prepare the sol-gel solution were tetraethyl orthosilicate (TEOS – $Si(OC_2H_5)_4$) as a source

Table 1 – Formulations of ceramics (mol%).

Formulation	SiO$_2$	P$_2$O$_5$	CaO	Li$_2$O	SrO	MgO	Fe$_2$O$_3$
Formulation 1	1	25	68	6	–	–	–
Formulation 2	29	3	63		2	2	1
Formulation 3	29	3	67	–	–	–	1
Formulation 4	29	3	66	–	2	–	
Formulation 5	29	3	66	–	–	2	

of silicon, triethyl phosphate (TEP – (C$_2$H$_5$)$_3$PO$_4$) as a source of phosphorous, and calcium carbonate as a source of calcium. They were all provided by Sigma–Aldrich. The reagents used to introduce ions into the sol–gel solution were lithium carbonate (Li$_2$CO$_3$), strontium carbonate (SrCO$_3$) and magnesium carbonate (MgCO$_3$), all provided by Sigma-Aldrich, and ferrous sulfate heptahydrate (FeSO$_4$·7H$_2$O) supplied by Merck. Solutions were prepared in a medium with distilled water, 37% hydrochloride acid (HCl – Ensure) and 97% ethanol (C$_2$H$_5$OH – Guimana). Table 1 shows all formulations made by this method. The employed polymer template was a polyurethane sponge with 20 pores per inch, 12.7 mm diameter and 10 mm high.

Multilayer scaffolds were constituted by a core and external layers. Core composition was SiO$_2$—25P$_2$O$_5$—68CaO—6Li$_2$O mol% (Formulation 1) and the composition of external coatings was 29SiO$_2$—3P$_2$O$_5$—68CaO mol%. To introduce the dopant, the latter composition was modified to obtain formulations 2–5. Based on these formulations, two different configurations were selected for the scaffolds.

Core

The solution of formulation 1 was prepared with 11.4 ml of TEP, 20 ml of distilled water, 5 ml of ethanol, 0.36 ml of TEOS, 10 ml of HCl, 0.5 g of Li$_2$CO$_3$ and 8.38 g of CaCO$_3$. Before adding carbonates, the solution was stirred for 30 min. Drops of HCl were added to keep the solution's pH between 2 and 3. The solutions with all the reagents were heated for 30 min at 100 °C with stirring. After this time, the solution formed an oily phase capable of covering the polymeric sponge. The polyurethane templates where immersed into the solution 30 times. After each immersion, sponges were centrifuged at 500 rpm and oven-dried at 140 °C to ensure the formation of a coating. Finally, the green bodies were sintered at 950 °C at a heating rate of 18 °C/h and maintained for 8 h.

Scaffold configuration 1 (scaffold 3J)

The configuration 1 (labeled 3J) consisted of a core scaffold coated with Formulation 2. In this formulation, 9% of the original total calcium moles were substituted by 3% of each doping ion (Fe^{+2}, Mg^{+2} and Sr^{+2}). The solution was prepared with 11.01 ml of TEOS, 20 ml of distilled water, 5 ml of ethanol, 1.64 ml of TEP, 10 ml of HCl, 0.5 g of SrCO$_3$, 0.29 g of MgCO$_3$, 0.94 g of FeSO$_4$.7H$_2$O and 10.3 g of CaCO$_3$. Core scaffolds were immersed in this solution 6 times. After each immersion, samples were centrifuged and oven-dried. Finally, samples were sintered at 950 °C at a heating rate of 92.5 °C/h and maintained for 3 h.

Scaffold configuration 2 (scaffold 3S)

The configuration 2 (labeled 3S) consisted of a core scaffold coated with Formulations 3, 4 and 5. In all these formulations, 3% of the total calcium moles were substituted by Fe^{+2}, Sr^{+2} and Mg^{+2}, respectively. The first coating layer was doped with iron. Subsequently, it was coated with the strontium-doped coating and finally by the magnesium-doped coating. The amounts of ions were selected so that the ion concentrations were the same. Three solutions were prepared with 11.01 ml of TEOS, 20 ml of distilled water, 5 ml of ethanol, 1.64 ml of TEP, 10 ml of HCl, 11 g CaCO$_3$, and each solution with 0.5 g of SrCO$_3$, 0.29 g of MgCO$_3$ and 0.94 g of FeSO$_4$·7H$_2$O, respectively. For each layer, the sample was immersed 6 times in solution. Before coating with the next layer, the sample was sintered at 950 °C at a heating rate of 92.5 °C/h and maintained for 3 h.

Scaffolds characterization

Mineralogical characterization by X-ray diffraction
The chemical and mineralogical characterizations of scaffolds were evaluated by X-ray diffraction (XRD). A Bruker AXR D8 Advance equipment was used with a secondary graphite monochromator and Cu-Kα radiation (1.5418740 Å). The X-ray tube operated at 40 kV and 30 mA with 0.02 steps by counting 8s per step. Data were collected between 20 and 40 degrees (2θ). The software Match!, version 3.9.0.158, was used for the analysis, and diffractograms were compared to the Crystallography Open Database (COD).

Microstructural characterization
The microstructure and morphology of scaffolds were studied by Scanning Electron Microscopy with Energy Dispersive X-ray (SEM-EDX). A Hitachi S-3500N with INCA system by Oxford Instruments Analytical was used. Samples were gold- and palladium-coated prior to evaluation.

Physical characterization
Ten scaffolds of each type were employed to study physical properties (8.5 mm diameter and 7.0 mm high). Scaffolds' porosity was measured by a pycnometer according to Arquimedes' principle. Scaffolds' maximum compressive strength was measured by a Simple Test Stand (NEURTEK instruments SVL-1000N). Force was applied to the scaffolds surface until total failure and the maximum force was recorded with a digital force gauge dst/dsv SERIES. Maximum compressive strength was calculated according to the following equation:

$$\sigma_m = \frac{F_m}{A}$$

where σ_m (MPa) is maximum compressive strength, F_m (N) is maximum force and A (mm^2) is the area perpendicular to the applied force.

In vitro bioactivity evaluation
Scaffolds' *in vitro* bioactivity was evaluated by the ability to precipitate apatite on the surface when immersed in simulated body fluid (SBF). Scaffolds 3J and 3S were soaked in SBF prepared according to Standard ISO/FDIS 23317:2017 for

134

ceramics and powder samples during different periods. The ceramic scaffolds (8.5 mm diameter and 7.0 mm high) were immersed in 50 ml of SBF and kept for 3, 14 and 21 days in water bath at 37 °C.

After each period, a sample was evaluated by SEM-EDX and the SBF aliquot was assessed by inductively coupled plasma optical emission spectrometry (ICP-EOS). In the last test, a Thermo iCAP 6500 DUO equipment was used to analyze the ionic element concentration in the resulting SBF. The *in vitro* bioactivity of the scaffolds' core has been previously studied [18].

Indirect cell culture

Ion release

In order to study the influence of the ions released by materials with cells, the powder from each scaffold was put into contact with cell culture medium (CCM) before seeding cells. The core and scaffolds 3J and 3S were ground using an agate mortar and sterilized at 160 °C for 2 h. Powders at 10 mg/ml and 100 mg/ml were brought into contact with Dulbecco's modified Eagle Medium (DMEM – Gibco) supplemented with 10% Fetal Bovine Serum (FBS – Corning) and 1% penicillin/streptomycin (PS – Gibco) in 15 ml falcon tubes for 24 h, and then for 96 h in a shaking incubator at 90 rpm and 37 °C.

Analysis of the released ions

An aliquot of the CCM, which was brought into contact with the powder of each scaffold at both concentrations for 24 h and 96 h, was analyzed by ICP-OES to know which ions were released by each material. The pH of the CCM was measured with a Mettler Toledo instrument (FiveEasy Plus).

Cell culture

Cell assays were performed using osteosarcoma cell line MG-63. Cells were cultured in 75 cm^2 culture flasks with DMEM supplemented with 10% FBS and 1% PS and incubated at 37 °C in a humidified atmosphere with 5% CO_2 and in a 95% air environment. Every 2 days, cells were passaged when 80% confluency had been reached. During the passage, the medium was removed to eliminate non-adherent cells, washed with Dulbecco's Phosphate Buffered Saline (DPBS – Gibco) and, finally, cells were collected using trypsin-EDTA (Gibco). Cells were counted using trypan blue and a hemocytometer. One day before the indirect assay, cells were seeded in 24-well plates at a concentration of 100,000 cells/ml. After 24 h and 96 h, the falcon tubes with the CCM and powders were centrifuged at 2000 rpm for 5 min. Then the CCM supernatants were transferred to the 24-well plates with the previously seeded cells and incubated at 37 °C in a humidified atmosphere with 5% CO_2. The control for this assay was cells brought into contact with the non-conditioned CCM.

Cell viability

After incubating for 1 day (D1) and 3 days (D3), cell viability was studied by the cell-counting kit containing water-soluble tetrazolium salt (WST-8). This salt reduces cell dehydrogenase, which results in a water-soluble formazan that is characterized as being yellow-colored and is proportional to the number of viable cells. For this assay, the CCM of each well

was transferred to Eppendorf tubes and reserved at incubator conditions during the analysis. Subsequently, 500 μl of a solution containing 1 vol% WST-8 and 99 vol% of the CCM were added to each well. After a 2 h incubation at 37 °C, 100 μl of each well were transferred to a 96-well plate and the absorbance was measured at 450 nm (FLUOstar Omega, BMG LABTECH). The absorbance value of the 1 vol% WST-8 solution was subtracted from all the absorbance values. After a 1-day analysis, the solution was removed from the 24-well plate, washed with DPBS, and the previously reserved CCM was returned to each well to continue the incubation period until day 3, time at which the procedure was repeated.

LDH activity

Lactate dehydrogenase (LDH) activity was studied after 3 days. LDH is an enzyme that is found inside cells and is released when cell membrane damage occurs. LDH activity is used to not only study cytotoxicity, but also to measure the number of cells that remain until the end of the assay by rupturing the membrane so they can be released. The LDH enzyme catalyzes the conversion of lactate and pyruvate by reducing NAD to NADH, which is then detected by absorbance. For this assay, the CCM was removed, washed with DPBS and 1 ml of lysis buffer (containing 0.1 wt% Triton X, 20 mM TRIS, 1 mM $MgCl_2$ and 0.1 mM $ZnCl_2$) was added to each well and left for 30 min. Subsequently, the lysis buffer was transferred from each well to Eppendorf tubes and centrifuged at 2000 rpm for 5 min. 140 μl of the supernatant from each Eppendorf tube and 60 μl of the LDH solution were added (containing 20 μl of the LDH assay substrate solution, 20 μl of the LDH assay dye and 20 μl of the LDH assay cofactor solution) to a 48-well plate. Finally, the well plate was incubated in the dark for 30 min, the reaction was stopped with 300 μl of HCl 1 M, and the absorbance was measured at 490 nm.

Direct cell culture

Sample preparation and cell seeding.

The core and scaffolds 3J and 3S were sterilized at 160 °C for 2 h. Samples were pre-conditioned to wet the scaffold surface and prepare it for cell attachment. For this purpose, scaffolds were placed inside a 24-well plate together with 1.5 ml of the CCM and were incubated for 30 min at 37 °C and 5% CO_2. After the pre-conditioning time, the CCM was removed and seeding was performed with the previously cultured MG-63 cells in a drop-wise manner by placing a drop of 25 μl containing 50,000 cells on the surface of each scaffold to be incubated for 30 min at 37 °C and 5% CO_2. This procedure was repeated once again. After the last 30-minute period, the CCM was added to each well. Samples were incubated for 1, 3, 7, 14 and 21 days. The CCM was refreshed every 2 days.

Cell viability

The viability of the cells in each scaffold was studied by WST-8. After each assay time (1, 3, 7, 14 and 21 days), the CCM was removed and scaffolds were transferred to a new 24-well plate to avoid considering the cells at the bottom of wells. Subsequently, 1.5 ml of a solution containing 1 vol% WST-8 and 99 vol% CCM was added to each well and incubated for 3 h at 37 °C and 5% CO_2. Afterward, 100 μl of each well were

135

transferred to a 96-well plate and absorbance was measured at 450 nm.

LDH activity

After 7, 14 and 21 days, scaffolds were transferred to a new 24-well plate and cells were lysed with 1.5 ml of lysis buffer to each sample. After 30 min, the procedure described above for the indirect assay was repeated.

Cell morphology evaluation

The evaluation of cell morphology, adhesion and proliferation on scaffolds' surface was performed by fluorescence staining and SEM. Fluorescence staining was carried out using rhodamine phalloidin red staining to observe the cytoplasm and DAPI (4′,6-diamidino-2′-phenylindole, dihydrochloride) blue staining to view cell nuclei. Images were obtained with a fluorescence microscope (Axio Scope A.1, Carl Zeiss).

For SEM, the cells on the surface of samples were fixed with two solutions for 1 h, the first containing glutaraldehyde and sodium cacodylate and the second with glutaraldehyde, sodium cacodylate and paraformaldehyde. Next a dehydration process was carried out with a series of alcohols from 30% to 99.5% ethanol, and each alcohol was brought into contact with the samples for 30 min. Finally, samples were dried at the critical point (Leica EM CPD300) and viewed by SEM (Auriga CrossBeam, Carl Zeiss).

Statistics

The results are shown as the mean values and standard deviation. The significant difference between values was calculated with the Origin software and the one-way analysis of variance ANOVA by a Tukey test. The significance level is given by a p-value of $p < 0.05 = *$.

Results

Scaffold characterization

Ceramic scaffolds obtained after the sintering process maintained the cylindrical shape with 8.5 mm diameter and 7.0 mm high approximately, as well as a weight of (0.35 ± 0.10) g.


Fig. 1 – (A) The XRD patterns of the core and scaffolds 3J and 3S. (B) Details of the principal peaks. P: $Ca_2P_2O_7$, S: SiO_2, L: $Li(PO_3)$, H: $Mg_2P_2O_7$, F: $Ca_{9.333}Fe_{1.167}(PO_4)_7$, M: $Ca_{10.115}Mg_{0.385}(PO_4)_7$, E: $Ca_{0.1}Fe_{0.6}Mg_{1.3}(SiO_3)_2$, C: $Ca_{0.90}Mg_{0.71}Fe_{0.25}(SiO_3)_2$, D: $Ca_{1.65}Sr_{0.35}(SiO_4)$, N: $CaLi(PO_4)$.

The mineralogical characterization carried out by XRD to study the scaffolds crystalline phases is shown in Fig. 1. In this figure, it is observed that the core is formed mainly by calcium pyrophosphate ($Ca_2P_2O_7$ – COD 96-100-1557) and by a minority of silicon dioxide (SiO_2 – COD 96-101-0939) and $Li(PO_3)$ (COD 96-210-7073). Additionally, the principal peaks of $Ca_2P_2O_7$ phase reported at 2θ 29.57° and 29.65° were slightly shifted to 2θ 29.60° and 29.68°.

Subsequently, the diffractograms of scaffolds 3J and 3S were analized. The following changes can be distinguished in the diffractograms:

(i) The diffractograms of scaffolds 3J and 3S are shifted to the right in relation to the core, as shown in detail in Fig. 1(B). The main peaks shifted to 2θ 29.68° and 29.76°. This means that ions entered the crystalline structure of calcium pyrophosphate. Specifically, phase $Mg_2P_2O_7$ (COD 96-201-7953) was identified. At these peaks


Fig. 2 – SEM-EDX images of the core (A, B), and scaffolds 3J (C, D) and 3S (E, F).

136

new phases were identified and corresponded to non-stoichiometric calcium silicate substituted for iron and magnesium ions ($Ca_{0.1}Fe_{0.6}Mg_{1.3}(SiO_3)_2$ – COD 96-152-9618 and $Ca_{0.90}Mg_{0.71}Fe_{0.25}(SiO_3)_2$ – COD 96-153-0360).

(ii) The calcium pyrophosphate phase peaks of the core decreased, and new phases appeared that corresponded to tricalcium phosphate (TCP) substituted for iron ($Ca_{9.333}Fe_{1.167}(PO_4)_7$ – COD 96-400-2456, TCP-Fe) and magnesium ($Ca_{10.115}Mg_{0.385}(PO_4)_7$ – COD 96-901-2137, TCP-Mg). In both scaffolds, the two phases were identified but not in the same proportion. In scaffolds 3J, the main phase was the TCP-Fe phase, whereas in scaffolds 3S the TCP-Mg phase was identified.

(iii) The peak corresponding to SiO_2 phase identified at 2θ 22.02° increased, especially in scaffolds 3S.

(iv) A minor strontium silicate phase ($Ca_{1.65}Sr_{0.35}(SiO_4)$ – COD 96-153-5820) was identified in both scaffolds at 2θ 32.90°.

(v) A TCP phase substituted for lithium ($CaLi(PO_4)$ – COD 96-722-2995, TCP-Li) was identified at 2θ 23.63° and 32.89° in scaffolds 3S.
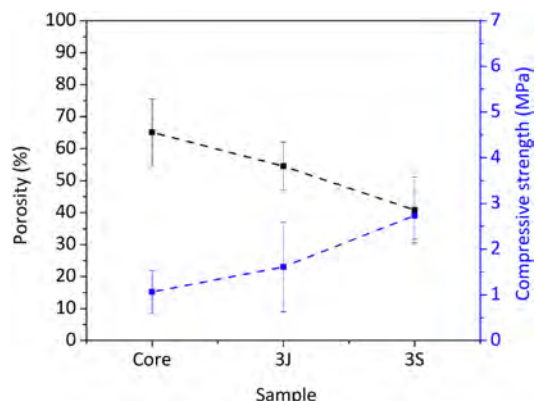

Fig. 3 – Porosity and compressive strength representation of the core and scaffolds 3J and 3S.
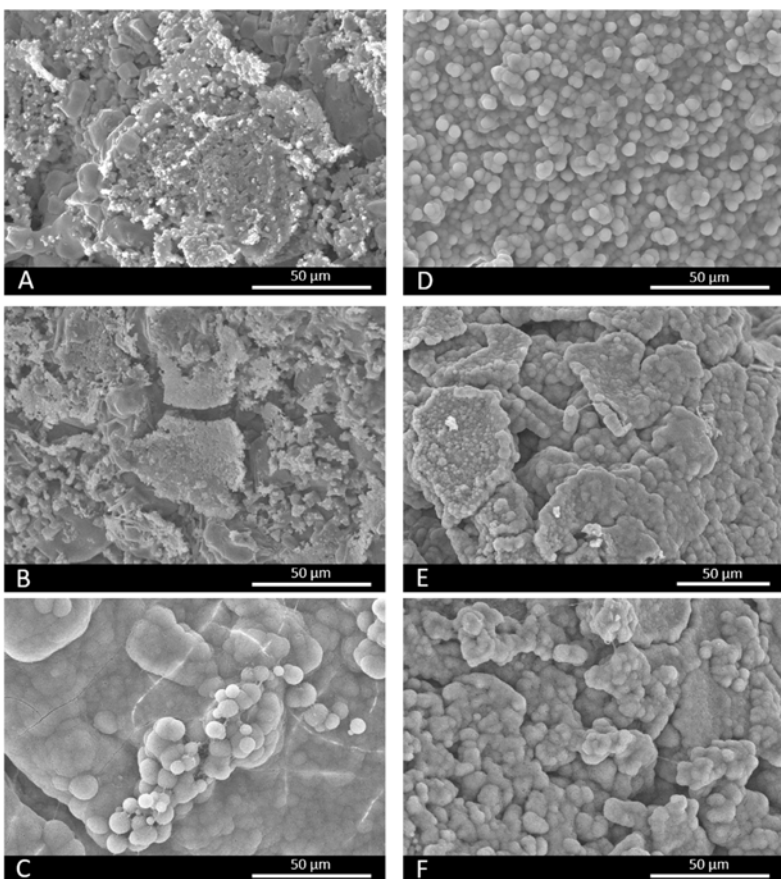

Fig. 4 – SEM images of scaffolds 3J (A-C) and 3S (D-F) after 3, 14 and 21 days of immersion in SBF.
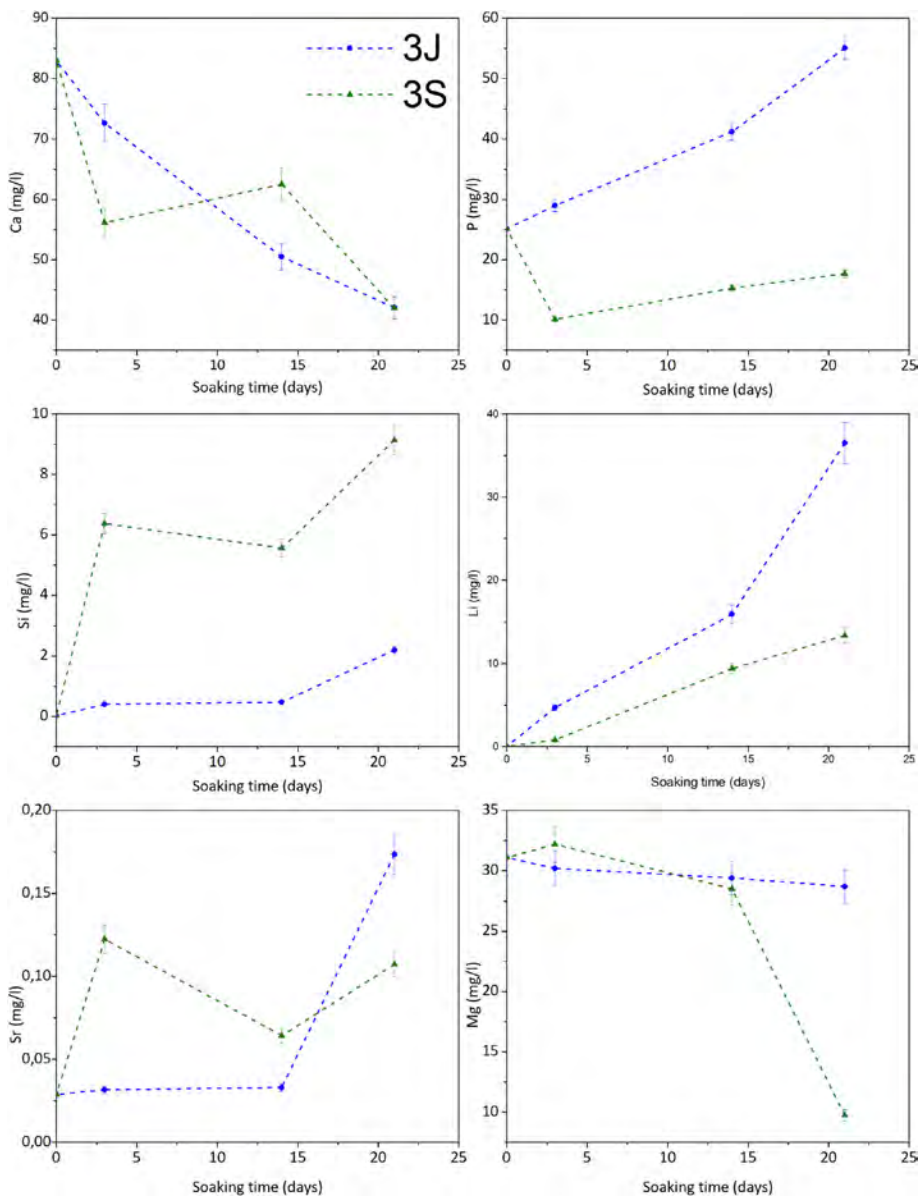
Fig. 5 – Variation in the ionic concentration in SBF after the immersion of scaffolds 3J and 3S at different times.

Fig. 2 (A, B) illustrates the core's microstructure formed by grains of different sizes and shapes. Fig. 2(C–F), which corresponds to the surfaces of scaffolds 3J and 3S, depicts the plates of coatings (marked by dotted lines) over the core. For scaffolds 3J, the core's microstructure lies underneath plates. For scaffold 3S, the previous Sr coating lies beneath the external Mg coating. The EDX analysis on the surface is inserted into the images of each scaffold. This analysis confirmed that the core contained mainly calcium and phosphorus. In addition to calcium and phosphorus, scaffolds 3J contained silicon, strontium, iron and magnesium. In scaffolds 3S, in addition to calcium, phosphorus and silicon, the presence of the dopant ions was detected depending on the surface point.

Fig. 3 shows the scaffolds' physical characteristics, such as compressive strength and porosity. The core's porosity was 65%, which decreased to 40% due to the coatings in scaffolds

138
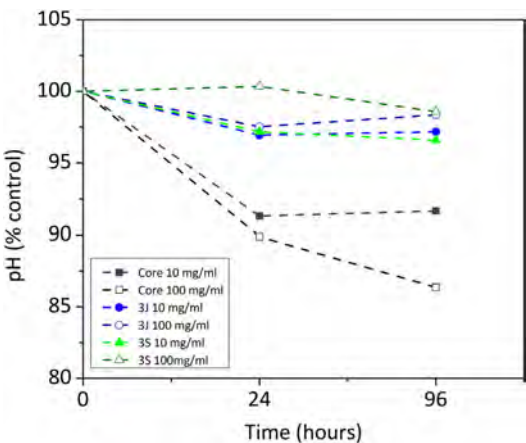
Fig. 6 – Variation in pH in the CCM (pH 8.5) after coming into contact with the core, 3J and 3S powders at 10 mg/ml and 100 mg/ml for 24 h and 96 h.

3S. Mechanical strength rose from (1.00 ± 0.47) MPa in the core to (2.74 ± 0.52) MPa in scaffolds 3S (see Fig. 3).

In vitro bioactivity evaluation

Fig. 4 shows the SEM images of scaffolds 3J and 3S after immersion in SBF. Fig. 4(A, B) depict how scaffolds 3J still have part of the coating after 3 and 14 immersion days. However, after 21 days (Fig. 4C), spherical precipitates were observed on the surface. In contrast, after 3 days the scaffolds 3S showed these precipitates on the surface (Fig. 4D), which remained even up to 21 days (Fig. 4F). The EDX analysis revealed that these precipitates were apatite-like.

Fig. 5 illustrates the study of the ionic interaction between scaffolds 3J/3S and SBF. Scaffolds 3J showed calcium adsorption and phosphorus release during the test, while silicon and strontium started to be released from the beginning of the test with a significant release at 21 days. In contrast, scaffold 3S displayed strong calcium and phosphorus adsorption and the release of silicon and strontium at the beginning of the test. The release of lithium took place in both scaffolds. In relation to magnesium, only scaffold 3S showed adsorption at 21 days. No iron ions were detected.

Indirect cell culture

The indirect cell assay revealed how the ions released by the scaffolds influenced cell behavior. Fig. 6 shows the first parameter herein considered, the variation in pH after 24 h and 96 h of exposing the powder of each scaffold with CCM. The powder of scaffolds 3J and 3S at concentrations of 10 and 100 mg/ml brought about a slight drop in the medium's pH after 96 h, but no more than 3.5%. In contrast, the core powder at a 10 mg/ml and 100 mg/ml concentration lowered the pH by 8.4%, and 13.7%.

The release of ions in the CCM for each material at both concentrations, and after 24 h and 96 h, is shown in Fig. 7. In the core material, at both concentrations, the release of phosphorus, lithium and silicon ions took place. At the 10 mg/ml concentration, the supernatant of the scaffolds 3J showed only silicon release. When the concentration rose to 100 mg/ml, the release of silicon, calcium and strontium became greater. Finally, at the above-mentioned concentrations, only significant silicon release was observed for scaffold 3S.

The viability of the cells incubated with the different conditioned CCMs is shown in Fig. 8. After 1 day (D1), the viability of the cells corresponding to the core's medium, and at both concentrations (10 mg/ml and 100 mg/ml) and times (24 h and 96 h), significantly decreased compared to the control. After 3 days (D3), the viability of the cells in contact with the core's medium at 10 mg/ml and both times increased to values that equaled the control. In contrast, the cells in contact with the core's medium at 100 mg/ml and both times were lower than the control. The viability of the cells in contact with the media of 3J and 3S at both concentrations and times also equaled the viability of the control or was slightly higher, which was the case of the cells in contact with the media of 3J and 3S at 10 mg/ml and both times.

The number of cells after 3 days in each case is shown in Fig. 9. Although a slight decrease in the number of cells was observed in relation to the control, no significant difference appeared.

Direct cell culture

After evaluating the influence of the released ions on cells, the behavior of the cells that came into direct contact with the scaffold was studied. Fig. 10 shows the results of the viability of the cells in contact with the core and scaffolds 3J and 3S. The viability of cells in contact with the core increased over time, with no significant difference from day 1 to day 21. In contrast, the cell viability of scaffolds 3J and 3S increased with time, with a significant difference from day 1. After 14 and 21 days, the viability of the cells in scaffolds 3J and 3S was significantly higher compared to the core. Cell viability after 21 days increased by approximately 110% in scaffold 3J and by 130% in scaffold 3S compared to the core.

Fig. 11 shows the results obtained from analyzing LDH activity. The number of cells in scaffolds 3J and 3S was nearly the same after 7, 14 and 21 days. In contrast, the number of cells in the core significantly decreased after 14 days.

Regarding the visual evaluation of the cells on the scaffolds, Figs. 12 and 13 show images of the surface obtained by fluorescence microscopy and SEM.

Fig. 12 depicts the surface of the core (Fig. 12A, B) and scaffolds 3J (Fig. 12C, D) and 3S (Fig. 12E, F) after 3 and 7 days. Due to staining, cell nuclei are denoted in blue and the cytoskeleton in red. On the core's surface, single round cells were observed, while others formed agglomerates. No difference in cell development appeared between days 3 (Fig. 12A) and 7 (Fig. 12B). With scaffolds 3J (Fig. 12C) and 3S (Fig. 12E), after 3 days a higher number of round-shaped cells were observed on the surface. Some of these cells spread as indicated by the arrow. After 7 days (Fig. 12D, F), cell proliferation was observed due

139
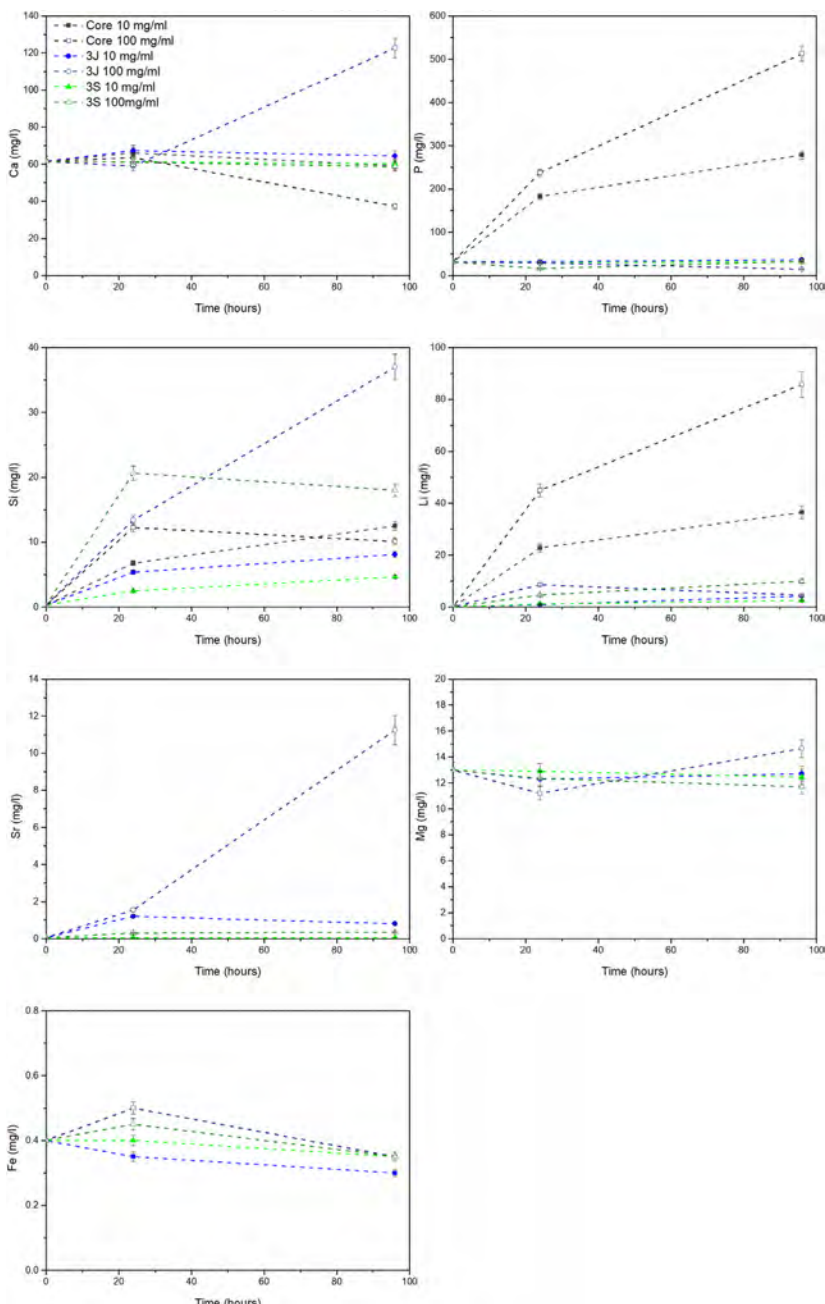
Fig. 7 – Variation of the ionic concentration in the CCM after coming into contact with the core, 3J and 3S powders at 10 mg/ml and 100 mg/ml for 24 h and 96 h.
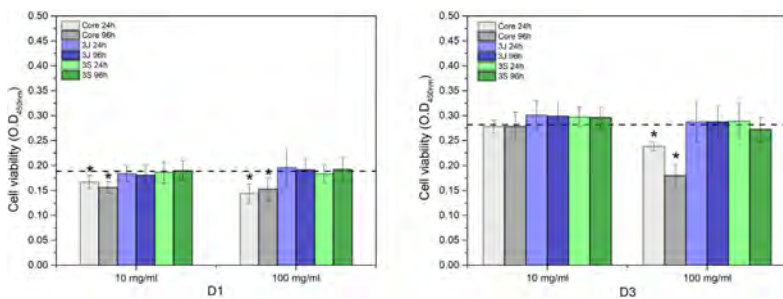
Fig. 8 – Cell viability of the MG-63 cells after 1 day (D1) and 3 days (D3) incubated with the CCM that had been previously in contact with the core, 3J and 3S powders at 10 mg/ml and 100 mg/ml for 24 h and 96 h. * means a significant difference ($p < 0.05$) compared to the control.
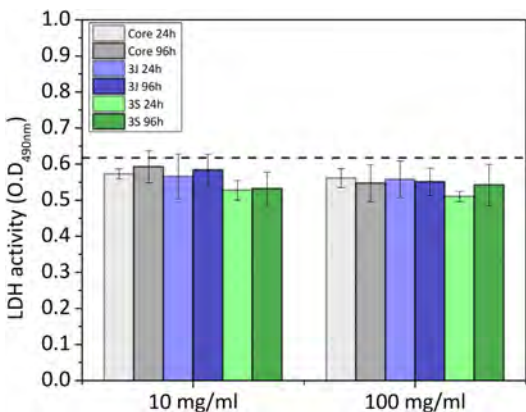

Fig. 9 – LDH activity of the MG-63 cells after 3 days incubated with the CCM that had previously been in contact with the core, 3J and 3S powders at 10 mg/ml and 100 mg/ml for 24 h and 96 h.


Fig. 10 – Cell viability of the MG-63 cells in contact with the core and scaffolds 3J and 3S between 1 and 21 days. * means a significant difference ($p < 0.05$) compared to the core.

to the formation of new cell colonies. Some cells were still round-shaped, but others had partially expanded.

Fig. 13 illustrates the SEM images. At 3 days, some cells were observed on the core's surface (Fig. 13A), but more cells were noted on the surface of scaffolds 3J (Fig. 13B) and 3S (Fig. 13C). The cells observed on the surface of scaffold 3J started to expand (dotted line), while those cells on the surface of scaffold 3S were more elongated. After 14 days on scaffolds 3J (Fig. 13E) and 3S (Fig. 13F), a dense and large layer of cells covering the entire scaffold surface formed, which became denser after 21 days (Fig. 13H–I). In contrast, on the core surface, a layer of cells began to form after 21 days (Fig. 13G).

Discussion

In order to implement new strategies to cover bone-implant demands, this research work proposes a new combination of ceramic materials. These new multilayer ceramic scaffolds,

doped with iron, strontium and magnesium in two different configurations, allowed to cover the following properties in a single scaffold: mechanical strength, porosity, bioactivity, and good interaction with cells.

First, the core of the scaffold was obtained and the most outstanding characteristic was the mechanical resistance. The compressive strength of the scaffold's core, constituted mainly by calcium pyrophosphate (Fig. 1), was close to the lower trabecular bone strength limit reported as 1.5–7.5 MPa (Fig. 3) depending on the body area [25]. The lithium added in the core formulation contributes to this mechanical strength, as was reported in another study with TCP materials [26].

As regards *in vitro* bioactivity, it has been previously found that this scaffold did not present *in vitro* bioactivity due to the inhibitory effect of pyrophosphate [18,27]. In fact, the silicon added to promote ion exchange and generate nucleation points was not enough to overcome the effect of pyrophosphate.

141
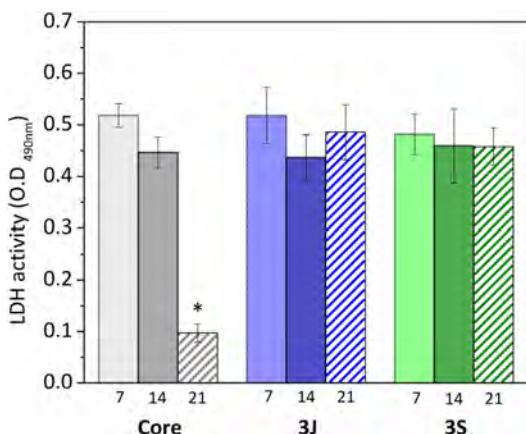
Fig. 11 – LDH activity of the MG-63 cells in contact with the core and scaffolds 3J and 3S after 7, 14 and 21 days. * means a significant difference (p < 0.05) compared to the control.

However, the present study demonstrates its behavior in the presence of cells. By an indirect cell culture assay, the ions released by the core lowered the pH (Fig. 6), which acidified the medium and, therefore, decreased cell viability (Fig. 8). The most significant ionic variation in the core was the release of phosphorus, lithium, and silicon (Fig. 7). The release of lithium and silicon to the medium created attraction points for the protons of water molecules, which led to the release of OH^- that was unable to explain the drop in pH. This suggests that medium acidification resulted from the breaking of P—O—P bonds due to the attack of water molecules, which caused $2PO_4^{3-} + 2H^+$ to form and, consequently, the release of H^+ protons to the medium. Due to the excessive release of phosphorus, a drop in pH was the predominant effect. Despite diminished cell viability, no significant cytotoxic effects were evidenced in the indirect assay in relation to the control (Fig. 9).

Although cell viability remained practically constant over time in the direct assay (Fig. 10), a drop in the number of cells was observed after 21 days (Fig. 11). The viability and cytotox-

icity assays complement each other. The first one only shows the mitochondrial activity of the cells in the material and the second one effectively demonstrates how many cells remain in contact with the material. In this case, the lower amount of cells observed after 21 days, indicates the consequences of prolonged medium acidification.

In addition, nor were cell adhesion and proliferation on the surface favored (Figs. 12 and 13). This behavior has also been reported by Banerjee et al., who compared the TCP surface and attributed this behavior to the interface's instability and to lack of apatite precipitates, which beneficially interact with cells [28].

The core's negative response in the presence of cells differed from that indicated by other studies that have reported calcium pyrophosphate as a biocompatible material [29–31]. However, when comparing other studies to the present work, we found that none of them analyzed pH variations in cell culture medium over time, and the material concentrations were low (1000 µg/ml) compared to those herein employed [29,31]. In addition, calcium pyrophosphates reported in other research works were prepared by different methods. The materials obtained by the sol-gel process, as in this work, were characterized by a large specific surface area and were, therefore, more reactive [32]. In any case, material acidification, which triggers reduced cell activity, is an effect that can take place thanks to the static conditions in the study, but in dynamic conditions, *in vivo*, this might not be an inconvenience. Calcium pyrophosphate occurs naturally in the organism and is a bone mineralization regulator together with the action of other enzymes [33].

Despite the drawbacks presented by the core in the cellular assays *in vitro*, it served as a support for the external coatings with a higher percentage of silicon and dopant ions. The scaffolds' mechanical strength doubled after coatings (Fig. 3) and overcame the lower compressive strength limit reported for trabecular bone [25]. Consequently, porosity decreased by approximately 25% in relation to the core due to the pore plugging caused by the more viscous coatings (Fig. 3). The SEM images illustrate the presence of coating layers. By analyzing surface areas by EDX, the presence of dopant ions was confirmed (Fig. 2).

Although the coatings of scaffolds 3J and 3S were constituted by the same ions, the sintering thermal treatments
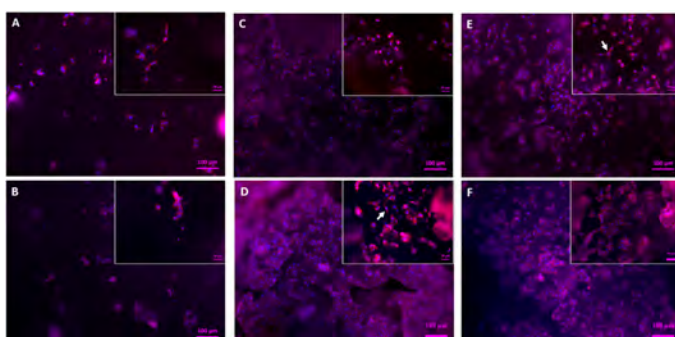

Fig. 12 – Fluorescence staining of the nuclei (blue) and cytoskeleton (red) of the MG-63 cells on the surface of the core (A, B), and scaffolds 3J (C, D) and 3S (E, F) after 3 and 7 days.
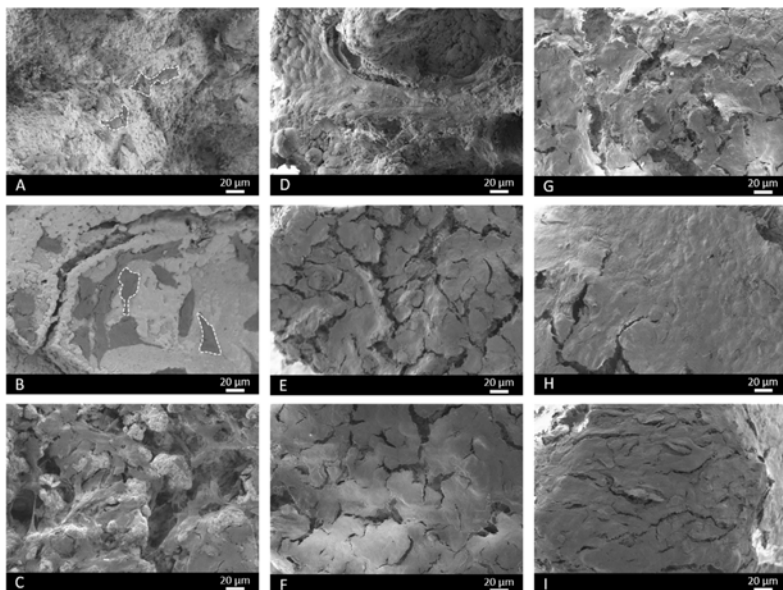
Fig. 13 – SEM images of the core (A, D, G) and scaffolds 3J (B, E, H) and 3S (C, F, I) after 3 (A–C), 14 (D–F) and 21 days (G–I) of immersion in the CCM with MG-63 cells.

differed. Scaffolds 3J were resintered after coating, while scaffolds 3S had three different coatings and were sintered 3 more times. These processes allowed the dopant ions to be distributed differently in each scaffold as evidenced by XRD (Fig. 1). The first noteworthy behavior was the shift in peak at 29.57°, which corresponded to calcium pyrophosphate. This meant that a distortion occurred in the crystal lattice from substituting calcium ions for smaller ions that tensed the lattice. The ionic radius of Ca^{2+} was 1.00 Å [34] and that of dopant ions Sr^{2+} was 1.18 Å [34], with 0.72 Å for Mg^{2+} [34] and 0.64 Å for Fe^{3+} [35]. This suggests that ions smaller than calcium moved to the crystal lattice, such as magnesium, because the magnesium-substituted calcium pyrophosphate ($Mg_2P_2O_7$) was identified. This shift has also been reported by Kim et al. when doping calcium pyrophosphate with 1, 3 and 5 wt% Mg^{2+} [34].

Another change observed by XRD was the tendency to form phases substituted by ions smaller than calcium such as iron and magnesium. Sintering processes in the presence of dopant ions promoted the conversion of calcium pyrophosphate into TCP.

Due to the presence of a higher silicon content in external coatings, new combined phases were formed, such as silica, strontium silicate and non-stoichiometric silicates with magnesium, iron and calcium. The combined phases with iron and magnesium showed that the competitive behavior of both ions was smaller in size than calcium, while strontium was bigger and formed an independent phase. Although a small amount was identified from the strontium silicate phase, it was assumed that the remaining species formed an amorphous phase. The peak corresponding to silica increased in

scaffolds 3S compared to scaffolds 3J because having three coatings presented 3-fold the amount of silicon.

Although scaffolds 3J and 3S had the same phases, as expected because both contained the same ions, the proportion of each phase differed. With each sintering process, calcium pyrophosphate decreased and non-stoichiometric TCP increased with different ions. It is even observed that TCP-Mg phase was the main phase in relation to the TCP-Fe phase confirming that magnesium ions tended to stabilize TCP, as reported by Torres et al. and Zhou et al. [36,37].

The lithium ions introduced into the core formed the $Li(PO_3)$ phase and were introduced into the calcium pyrophosphate lattice given the peak shift. Due to coatings and heat treatments, these lithium ions subsequently formed part of the diffusion processes that led to the TCP-Li phase in scaffold 3S. In the 3J scaffold this phase was not observed since having only one sintering process compared to the 3S scaffold, the reduced diffusion did not allow the formation of any crystalline phase. Therefore, the lithium remained forming amorphous phase or within the crystalline lattice of the calcium pyrophosphate. All these changes between scaffolds 3S and 3J are summarized insofar as scaffolds 3S formed more TCP phases and possessed a larger amount of silicon.

The *in vitro* bioactivity evaluation showed that scaffolds 3J exhibited bioactive behavior at 21 days, while scaffold 3S did so at 3 days (Fig. 4), due to the presence of precipitates with a typical apatite morphology [38,39]. On the first testing days, dissolution of coating layers was observed on the surface of scaffolds 3J, which was also evidenced by the release of phosphorus to SBF (Fig. 5) and calcium adsorption on the scaffold surface. After 21 days, when silicon and strontium were

143

released, apatite precipitation occurred. Conversely, scaffold 3S released silicon and strontium on day 3, which led to the adsorption of calcium and phosphorus from SBF to apatite precipitate.

Due to the number of crystalline and non-crystalline phases in scaffolds, establishing a mechanism to explain the bioactivity is complicated. However, due to the amount of silicon in external coatings and the formation of new non-stoichiometric TCP phases, bioactivity could be explained by the mechanisms already proposed by Hench for bioactive glass ceramics and calcium phosphates [40,41]. Scaffolds 3S had more silicon and its release on day 3 created nucleation points for apatite precipitates. This confirmed the rapid decrease of calcium and phosphorus on day 3. Strontium was released simultaneously with silicon, which could be related to either the dissolution of the strontium silicate phase identified by XRD or the amorphous phase between silicon and strontium. The bioactivity of scaffolds 3S could also be due to the TCP phases. It is known that given its negative surface, TCP attracts Ca^{2+} ions from SBF and creates a nucleation point for apatite precipitates [28,41]. Zhou et al. have confirmed that the TCP-Mg surface is more negative than TCP and can, therefore, more strongly attract ions, and can even adsorb magnesium ions from SBF, which occurred at 21 days [37]. Both effects provided scaffolds 3S a significant bioactive behavior. In contrast, as scaffolds 3J did not have many silicon and TCP phases, the mechanisms were delayed until 21 days when silicon was released. Moreover, it also had larger amounts of calcium pyrophosphate and magnesium pyrophosphate phases in the inner part, which are known to inhibit apatite precipitation *in vitro* due to the P-O-P bond of the pyrophosphate group [18,27].

Regarding the interaction between scaffolds 3J and 3S and MG-63 cells, the ions released by the materials in the indirect assay slightly increased cell viability after 3 days (Fig. 8). The analysis of the ionic concentrations indicated that the release of silicon could be primarily responsible for the slight increase in viability as the dopant ions of strontium, iron and magnesium were not significantly released during the study time, except for the extracts of scaffolds 3J at 100 mg/ml (Fig. 7). Silicon plays a key role in cellular response. Han et al. have demonstrated that silicon enhances cell proliferation, differentiation and mineralization [42]. This could be another reason for the better performance of scaffolds 3J and 3S compared to the core. Xing et al. utilized the benefits of silicon and strontium to demonstrate the synergistic effect when combining both ions in a single structure, and they observed the stimulation of cell proliferation and osteogenic differentiation [43]. The release of silicon is closely related to the presence of strontium, as demonstrated by Yin et al. when doping boron bioglasses with strontium, these authors noted a faster release of silicon and the increased proliferation of MG-63 cells [44]. This could explain the joint release of silicon and strontium herein evidenced.

The effect of dopants and their arrangement on viability were studied by the direct assay. When cells were evaluated directly on the scaffolds surface, cell viability increased with time, and increased by more than 100% compared to the core after 21 days (Fig. 10). In relation to cell morphology,

cell proliferation on the surfaces of scaffolds 3J and 3S was greater than on the core's surface (Figs. 12 and 13). The cell colonies in the core were initially more agglomerated, while cells were more spread out and adhered to the surface of scaffolds 3J and 3S. The dense and continuous layers of the cells that formed on the surface of scaffolds 3J and 3S after 14 days demonstrated not only the positive effect of ions on the surface that had not yet been released, but also the influence of the silicon released to the medium.

The dopant ions herein used had positive effects on cellular response. Strontium and iron ions possess angiogenic, osteogenic and antibacterial properties, and strontium is widely used to treat osteoporosis [19,22,45]. Magnesium influences the activity of osteoblasts and osteoclasts [19]. To our knowledge, however, there is no material that combines strontium, iron and magnesium ions. Some studies have reported the combination of two of these ions. For example, Kim et al. have demonstrated that calcium pyrophosphate doped with strontium and magnesium is a biocompatible material [34]. The same has been observed by Singh et al. and Vahabzadeh et al. when doping tricalcium phosphate with iron ions [46,47]. Tricalcium phosphate has been doped with magnesium at different concentrations, and Gu et al. have reported how magnesium not only increases cell proliferation, but also improves cell morphology and viability [48]. During the cell culture assays in the above study, the authors observed how magnesium and calcium ions decreased in the medium over time (which was also the case in our work), and they attributed this behavior to apatite deposition and mineralization. Although no release of magnesium ions was seen, these ions may enhance cell adhesion by influencing the interaction with integrin that acts as an adhesion protein [24,49]. Lithium was also one of the ions released mainly by the core. This ion has long since been used to treat mental disorders but has recently been employed to improve compressive strength and has positive effects on angiogenesis [26,50]. However, the influence of this ion on the cells that came into contact with the core was not observed in our work due to the effect of lowering the pH, while the release of lithium in scaffolds 3J and 3S could enhance the effect of the other ions.

It was generally found that the behavior of the cells that came into contact with scaffolds 3J and 3S was similar, with no direct influence of ion arrangement on the interaction with cells. On the contrary, the ion arrangement affected crystalline phases and their *in vitro* bioactivity behavior.

It is possible to consider that the core, being the common base of the scaffolds 3J and 3S, may cause cytotoxic effects when the coatings dissolve. However, the indirect cell assays revealed that the core's acidification effect disappeared after crushing the scaffolds and mixing the core material with outer coatings. This could be due to the decrease in the calcium pyrophosphate phase which, as sintering proceeded was transformed into TCP phases, and would mean that the amount of calcium pyrophosphate would not be sufficient to cause acidification. As previously mentioned, acidification is a negative effect in static *in vitro* tests, but should not be a drawback *in vivo* because pyrophosphate is a natural bone mineralization regulator.

Conclusions

In this research work, multilayer ceramic scaffolds were developed as a future alternative for bone tissue engineering applications. The scaffold's core, constituted mainly by calcium pyrophosphate, did not show a good cellular response, but its structure exhibiting mechanical resistance served as a support to apply the external coatings constituted mainly by calcium and silicon, and doped with iron, strontium and magnesium ions (3J and 3S). Cell viability in scaffolds 3J and 3S increased by more than 100% *vs.* the core, and cell proliferation and adhesion improved by the formation of a dense layer of cells that covered the entire surface after 21 days. In cellular terms, there was no significant difference between the arrangement of dopant ions. In bioactivity terms, however, scaffolds 3S (ions in separate coatings) presented bioactivity at 3 days, while scaffolds 3J (ions in the same coating) did so at 21 days, which was attributed to the larger amount of silicon in the external coatings.

Conflict of interest

None.

Acknowledgements

REFERENCES

[1] P. Verma, V. Verma, Concepts of tissue engineering, Anim. Biotechnol. (2020) 295–307, http://dx.doi.org/10.1016/B978-0-12-811710-1.00013-6, Elsevier.

[2] A. Przekora, The summary of the most important cell-biomaterial interactions that need to be considered during in vitro biocompatibility testing of bone scaffolds for tissue engineering applications, Mater. Sci. Eng. C 97 (2019) 1036–1051, http://dx.doi.org/10.1016/j.msec.2019.01.061.

[3] J.J. Li, D.L. Kaplan, H. Zreiqat, Scaffold-based regeneration of skeletal tissues to meet clinical challenges, J. Mater. Chem. B 2 (42) (2014) 7272–7306, http://dx.doi.org/10.1039/c4tb01073f.

[4] H. Qu, H. Fu, Z. Han, Y. Sun, Biomaterials for bone tissue engineering scaffolds: a review, RSC Adv. 9 (45) (2019) 26252–26262, http://dx.doi.org/10.1039/c9ra05214c.

[5] Pearlin, S. Nayak, G. Manivasagam, D. Sen, Progress of regenerative therapy in orthopedics, Curr. Osteoporos. Rep. 16 (2) (2018) 169–181, http://dx.doi.org/10.1007/s11914-018-0428-x.

[6] M.P. Murphy, M.R. Borrelli, D.T. Montoro, M.T. Longaker, D.C. Wan, Skeletal tissue engineering, Princ. Tissue Eng. (2020) 1007–1021, http://dx.doi.org/10.1016/B978-0-12-818422-6.00057-5, Elsevier.

[7] S.V. Dorozhkin, Current state of bioceramics, J. Ceram. Sci. Technol. 9 (4) (2018) 353–370, http://dx.doi.org/10.4416/JCST2018-00026.

[8] A. Wubneh, E.K. Tsekoura, C. Ayranci, H. Uludağ, Current state of fabrication technologies and materials for bone tissue engineering, Acta Biomater. 80 (2018) 1–30, http://dx.doi.org/10.1016/j.actbio.2018.09.031.

[9] W. Wang, K.W.K. Yeung, Bone grafts and biomaterials substitutes for bone defect repair: a review, Bioact. Mater. 2 (4) (2017) 224–247, http://dx.doi.org/10.1016/j.bioactmat.2017.05.007.

[10] Y. Yang, Y. Kang, M. Sen, S. Park, Biomaterials in tissue engineering, Biomater. Tissue Eng. Appl. A Rev. Past Futur. Trends (2011) 1–564, http://dx.doi.org/10.1007/978-3-7091-0385-2, Springer-Verlag.

[11] G.M. Raghavendra, K. Varaprasad, T. Jayaramudu, Biomaterials: design, development and biomedical applications, Nanotechnol. Appl. Tissue Eng. (2015) 21–44, http://dx.doi.org/10.1016/B978-0-323-32889-0.00002-9, Elsevier.

[12] N. Eliaz, N. Metoki, Calcium phosphate bioceramics: a review of their history, structure, properties, coating technologies and biomedical applications, Materials 10 (4) (2017), http://dx.doi.org/10.3390/ma10040334.

[13] I. Denry, L.T. Kuhn, Design and characterization of calcium phosphate ceramic scaffolds for bone tissue engineering, Dent. Mater. 32 (1) (2016) 43–53, http://dx.doi.org/10.1016/j.dental.2015.09.008.

[14] S. Bose, M. Roy, A. Bandyopadhyay, Recent advances in bone tissue engineering scaffolds, Trends Biotechnol., 30(10) 546–554, doi:10.1016/j.tibtech.2012.07.005.

[15] P. Ros-Tárraga, N.A. Mata, Á. Murciano, P. Velasquez, P.N. De Aza, Multilayer ceramic materials: a method to link bioactivity and durability, Ceram. Int. 45 (17) (2019) 23611–23618, http://dx.doi.org/10.1016/j.ceramint.2019.08.072.

[16] N.A. Mata, P. Ros-Tárraga, P. Velasquez, A. Murciano, P.N. De Aza, Synthesis and characterization of 3D multilayer porous Si–Ca–P scaffolds doped with Sr ions to modulate in vitro bioactivity, Ceram. Int. 46 (1) (2020) 968–977, http://dx.doi.org/10.1016/j.ceramint.2019.09.058.

[17] N.A. Mata, P. Ros-Tárraga, P. Velasquez, A. Murciano, P.N. De Aza, New iron-doped multilayer ceramic scaffold with noncontinuous bioactive behavior, Ceram. Int. 46 (10) (2020) 16388–16396, http://dx.doi.org/10.1016/j.ceramint.2020.03.198.

[18] N.A. Mata, P. Velasquez, A. Murciano, P.N. De Aza, Multilayer Mg-pyrophosphate glass ceramic with discontinuous bioactivity. Physicochemical characterization, Ceram. Int. 47 (10) (2021) 14612–14620, http://dx.doi.org/10.1016/j.ceramint.2021.02.044.

[19] V.M. Schatkoski, et al., Current advances concerning the most cited metal ions doped bioceramics and silicate-based bioactive glasses for bone tissue engineering, Ceram. Int. 47 (3) (2021) 2999–3012, http://dx.doi.org/10.1016/j.ceramint.2020.09.213.

[20] S. Meininger, et al., Effect of strontium substitution on the material properties and osteogenic potential of 3D powder printed magnesium phosphate scaffolds, Mater. Sci. Eng. C 98 (2019) 1145–1158, http://dx.doi.org/10.1016/j.msec.2019.01.053.

[21] D. Ke, S. Tarafder, S. Vahabzadeh, S. Bose, Effects of MgO, ZnO, SrO, and SiO$_2$ in tricalcium phosphate scaffolds on in vitro gene expression and in vivo osteogenesis, Mater. Sci. Eng. C 96 (2019) 10–19, http://dx.doi.org/10.1016/j.msec.2018.10.073.

[22] M. S. Araujo, A. C. Silva, B. Cabal, J. F. Bartolomé, and S. Mello-Castanho, In vitro bioactivity and antibacterial capacity of 45S5 Bioglass®-based compositions containing alumina and strontium, J. Mater. Res. Technol., 13, 154–161. doi:10.1016/j.jmrt.2021.04.053.

[23] S.M. Rabiee, N. Nazparvar, M. Azizian, D. Vashaee, L. Tayebi, Effect of ion substitution on properties of bioactive glasses: a review, Ceram. Int. 41 (6) (2015) 7241–7251, http://dx.doi.org/10.1016/j.ceramint.2015.02.140.

[24] A. Hoppe, N.S. Güldal, A.R. Boccaccini, A review of the biological response to ionic dissolution products from bioactive glasses and glass-ceramics, Biomaterials 32 (11) (2011) 2757–2774, http://dx.doi.org/10.1016/j.biomaterials.2011.01.004.

[25] G. Kaur, et al., Mechanical properties of bioactive glasses, ceramics, glass-ceramics and composites: state-of-the-art review and future challenges, Mater. Sci. Eng. C 104 (2019), http://dx.doi.org/10.1016/j.msec.2019.109895, 109895.

[26] C.Q. Zhao, et al., Doping lithium element to enhance compressive strength of β-TCP scaffolds manufactured by 3D printing for bone tissue engineering, J. Alloys Compd. 814 (2020), http://dx.doi.org/10.1016/j.jallcom.2019.152327.

[27] H. Fleisch, S. Bisaz, Mechanism of calcification: inhibitory role of pyrophosphate, Nature 195 (4844) (1962) 911, http://dx.doi.org/10.1038/195911a0.

[28] S.S. Banerjee, A. Bandyopadhyay, S. Bose, Biphasic resorbable calcium phosphate ceramic for bone implants and local alendronate delivery, Adv. Eng. Mater. 12 (5) (2010) 148–155, http://dx.doi.org/10.1002/adem.200980072.

[29] E. Alsubhe, et al., Analysis of the osteogenic and mechanical characteristics of iron (Fe^{2+}/Fe^{3+})-doped β-calcium pyrophosphate, Mater. Sci. Eng. C 115 (2020) 111053, http://dx.doi.org/10.1016/j.msec.2020.111053.

[30] S.R. Vasant, M.J. Joshi, A review on calcium pyrophosphate and other related phosphate nano bio-materials and their applications, Rev. Adv. Mater. Sci. 49 (1) (2017) 44–57.

[31] A.D. Anastasiou, et al., β-Pyrophosphate: a potential biomaterial for dental applications, Mater. Sci. Eng. C 75 (2017) 885–894, http://dx.doi.org/10.1016/j.msec.2017.02.116.

[32] G.J. Owens, et al., Sol–gel based materials for biomedical applications, Prog. Mater. Sci. 77 (2016) 1–79, http://dx.doi.org/10.1016/j.pmatsci.2015.12.001.

[33] I.R. Orriss, T.R. Arnett, R.G.G. Russell, Pyrophosphate: a key inhibitor of mineralisation, Curr. Opin. Pharmacol. 28 (2016) 57–68, http://dx.doi.org/10.1016/j.coph.2016.03.003.

[34] D.W. Kim, J.S. An, I.S. Cho, Effects of Mg and Sr co-addition on the densification and biocompatible properties of calcium pyrophosphate, Ceram. Int. 44 (8) (2018) 9689–9695, http://dx.doi.org/10.1016/j.ceramint.2018.02.198.

[35] I. Ullah, et al., Simultaneous co-substitution of Sr^{2+}/Fe^{3+} in hydroxyapatite nanoparticles for potential biomedical applications, Ceram. Int. 44 (17) (2018) 21338–21348, http://dx.doi.org/10.1016/j.ceramint.2018.08.187.

[36] P.M.C. Torres, et al., Influence of Mg-doping, calcium pyrophosphate impurities and cooling rate on the allotropic α↔β-tricalcium phosphate phase transformations, J. Eur. Ceram. Soc. 36 (3) (2016) 817–827, http://dx.doi.org/10.1016/j.jeurceramsoc.2015.09.037.

[37] H. Zhou, et al., Synthesis of β-TCP and CPP containing biphasic calcium phosphates by a robust technique, Ceram. Int. 42 (9) (2016) 11032–11038, http://dx.doi.org/10.1016/j.ceramint.2016.03.246.

[38] F.E. Ciraldo, et al., Fabrication and characterization of Ag- and Ga-doped mesoporous glass-coated scaffolds based on natural marine sponges with improved mechanical properties, J. Biomed. Mater. Res. – Part A (2020) 1–19, http://dx.doi.org/10.1002/jbm.a.37123.

[39] M. Arango-Ospina, K. Lasch, J. Weidinger, A.R. Boccaccini, Manuka Honey and Zein coatings impart bioactive glass bone tissue scaffolds antibacterial properties and superior mechanical properties, Front. Mater. 7 (2021) 1–12, http://dx.doi.org/10.3389/fmats.2020.610889.

[40] L.L. Hench, Bioceramics: from concept to clinic. J. Am. Ceram. Soc. 72 (1993) 93–98. J. Am. Ceram. Soc., 74 (1991) 1487–1510.

[41] H.M. Kim, T. Himeno, T. Kokubo, T. Nakamura, Process and kinetics of bonelike apatite formation on sintered hydroxyapatite in a simulated body fluid, Biomaterials 26 (21) (2005) 4366–4373, http://dx.doi.org/10.1016/j.biomaterials.2004.11.022.

[42] P. Han, C. Wu, Y. Xiao, The effect of silicate ions on proliferation, osteogenic differentiation and cell signalling pathways (WNT and SHH) of bone marrow stromal cells, Biomater. Sci. 1 (4) (2013) 379–392, http://dx.doi.org/10.1039/c2bm00108j.

[43] M. Xing, X. Wang, E. Wang, L. Gao, J. Chang, Bone tissue engineering strategy based on the synergistic effects of silicon and strontium ions, Acta Biomater. 72 (2018) 381–395, http://dx.doi.org/10.1016/j.actbio.2018.03.051.

[44] H. Yin, et al., Fabrication and characterization of strontium-doped borate-based bioactive glass scaffolds for bone tissue engineering, J. Alloys Compd. 743 (2018) 564–569, http://dx.doi.org/10.1016/j.jallcom.2018.01.099.

[45] S.H. Lin, W.J. Zhang, X.Q. Jiang, Applications of bioactive ions in bone regeneration, Chin. J. Dent. Res. 22 (2) (2019) 93–104, http://dx.doi.org/10.3290/j.cjdr.a42513.

[46] R.K. Singh, M. Srivastava, N.K. Prasad, S. Awasthi, A. Dhayalan, S. Kannan, Iron doped β-tricalcium phosphate: synthesis, characterization, hyperthermia effect, biocompatibility and mechanical evaluation, Mater. Sci. Eng. C 78 (2017) 715–726, http://dx.doi.org/10.1016/j.msec.2017.04.130.

[47] S. Vahabzadeh, S. Bose, Effects of iron on physical and mechanical properties, and osteoblast cell interaction in β-tricalcium phosphate, Ann. Biomed. Eng. 45 (3) (2017) 819–828, http://dx.doi.org/10.1007/s10439-016-1724-1.

[48] Y. Gu, J. Zhang, X. Zhang, G. Liang, T. Xu, W. Niu, Three-dimensional printed Mg-doped β-TCP bone tissue engineering scaffolds: effects of magnesium ion concentration on osteogenesis and angiogenesis in vitro, Tissue Eng. Regen. Med. 16 (4) (2019) 415–429, http://dx.doi.org/10.1007/s13770-019-00192-0.

[49] H. Zreiqat, et al., Mechanisms of magnesium-stimulated adhesion of osteoblastic cells to commonly used orthopaedic implants, J. Biomed. Mater. Res. 62 (2) (2002) 175–184, http://dx.doi.org/10.1002/jbm.10270.

[50] L. Liu, et al., Lithium-containing biomaterials stimulate bone marrow stromal cell-derived exosomal miR-130a secretion to promote angiogenesis, Biomaterials 192 (2019) 523–536, http://dx.doi.org/10.1016/j.biomaterials.2018.11.007.

146

Agradecimientos

En primer lugar, me gustaría agradecer a la Conselleria de Innovación, Universidades y Sociedad Digital de la Generalitat Valenciana por la concesión de la subvención del programa Santiago Grisolía (GRISOLÍAP/2018/037), con la cual ha sido posible desarrollar el presente trabajo doctoral, incluido el apoyo para estancias predoctorales en centros fuera de la Comunidad Valenciana (BEFPI/2021/056). Así como a la Agencia Estatal de Investigación y el Ministerio de Ciencia e Innovación (MCIN/AEI/10.13039/501100011033) por el proyecto PID2020-116693RB-C21.

En segundo lugar, me gustaría agradecer a los profesores encargados de esta subvención, la profesora Piedad N. De Aza y los profesores Pablo Velásquez y Ángel Murciano, por haber confiado en mi para la realización de esta Tesis Doctoral y brindarme la oportunidad de venir a España en condiciones excepcionales.

Especialmente, a mi directora de tesis, la profesora Piedad N. De Aza debo agradecerle por todo el apoyo ofrecido desde antes de mi llegada. Así como la confianza brindada durante todos estos años, junto con los conocimientos transmitidos sobre el área de biomateriales y las orientaciones recibidas entorno al mundo de la investigación.

A mi co-director de tesis, el profesor Ángel Murciano le agradezco enormemente por inspirarme con su pasión por la investigación. Sin duda alguna, ha sido un excelente guía, no solo por los conocimientos transmitido sino también por involucrarse y enfrentar conmigo en primera línea las dificultades que surgieron en el desarrollo experimental, incluso durante las largas jornadas en el laboratorio. Su entrega es lo que realmente lo define como un verdadero mentor y para mi vale más que todos los logros que alcanzamos a nivel académico. Por último, debo agradecerle por los conocimientos culturales y gastronómicos que nos enseñó a mi y a mis compañeros que sin duda nunca olvidaremos.

Igualmente me gustaría agradecer al profesor Pablo Velásquez, por quien tengo un gran aprecio. Gracias por haber estado dispuesto ayudarme en todo momento, por la confianza brindada en todo lo relacionado con el manejo del laboratorio y por ayudarme en el desarrollo de mi tesis doctoral. Pero sobre todo, gracias por su amistad y por aconsejarme en muchos aspectos.

También me gustaría agradecer especialmente a la profesora Delia Gutiérrez, porque sin ella todo esto no hubiese sido posible. Gracias por confiar en mi y por el inmenso apoyo brindado durante el proceso inicial. Principalmente me gustaría agradecerle por ser ejemplo de constancia y por formar parte del conjunto de profesores de la Universidad Simón Bolívar, a quienes debo gran

parte de mi formación profesional y por quienes siento una profunda admiración por su vocación, por su compromiso, por su valentía pero sobre todo por enseñarnos que se puede hacer MUCHO partiendo de muy poco. A todos ustedes, cuyo ejemplo llavaré a todos los rincones que visite, infinitas gracias.

Agradezco también al profesor Aldo R. Boccaccini por darme la oportunidad de realizar una estancia en el Instituto de Biomateriales de la Universidad de Erlangen-Nuremberg en Alemania. Por su rápida aceptación y por darme la oportunidad de explorar nuevas áreas de investigación que enriquecieron enormemente mi formación. De esta experiencia, me gustaría también agradecer a Marcela Arango Ospina por orientarme durante mi estancia, por su paciencia, por su apoyo experimental y por todos los conocimientos compartidos.

También me gustaría agradecer a mis compañeros de laboratorio Anabel Díaz y Carlos Navalón, en primer lugar por los conocimientos transmitidos, pero sobre todo por brindarme su amistad y por haber hecho que mis días en el laboratorios fuesen más amenos. Simplemente gracias porque cada uno me enseñó algo, me llevo grandes experiencias, momentos de infinitas risas y otros no tan alegres pero que siempre recordaré con gran cariño. También debo agradecer a Patricia Ros porque aunque fue poco el tiempo que compartimos en el laboratorio es inmenso y enriquecedor el legado que me ha dejado para realizar esta tesis doctoral. Gracias por siempre estar dispuesta ayudarme en cualquier momento aún estando fuera del laboratorio y por supuesto por la bonita amistad que hemos formado durante estos años.

Por último, me gustaría agradecer inmensamente a toda mi familia, especialmente a mis padres y a mi hermana por todo el amor y por todo el apoyo que me han dado no solo en esta etapa sino también en las anteriores. Desde la distancia han sabido levantarme en los momentos más difíciles y han estado ahí para ayudarme a volar cada vez más alto. Finalmente, me gustaría agradecer a Abián, mi compañero desde el inicio de este proceso y quien sin duda ha sido un pilar fundamental. Gracias por ayudarme a alcanzar este logro, por escucharme con paciencia y ayudarme a enfrentar todas las adversidades, pero sobre todo por enseñarme a ver las cosas desde una mejor perspectiva.

Indudablemente mi estancia en España ha estado marcada por todos ustedes pero también por muchas otras personas que aunque no menciono directamente, al cruzarse en mi camino de una u otra forma aportaron un granito de arena. A todos ustedes, gracias.